



**HAL**  
open science

# Magnetic fluidized beds in microfluidic: application to ultrasensitive detection for bioanalysis

Lucile Fanny Tse dey Alexandre

## ► To cite this version:

Lucile Fanny Tse dey Alexandre. Magnetic fluidized beds in microfluidic: application to ultrasensitive detection for bioanalysis. Analytical chemistry. Université Paris Sciences & Lettres, 2018. English. NNT: . tel-03704660

**HAL Id: tel-03704660**

**<https://hal.science/tel-03704660>**

Submitted on 25 Jun 2022

**HAL** is a multi-disciplinary open access archive for the deposit and dissemination of scientific research documents, whether they are published or not. The documents may come from teaching and research institutions in France or abroad, or from public or private research centers.

L'archive ouverte pluridisciplinaire **HAL**, est destinée au dépôt et à la diffusion de documents scientifiques de niveau recherche, publiés ou non, émanant des établissements d'enseignement et de recherche français ou étrangers, des laboratoires publics ou privés.

# THÈSE DE DOCTORAT

de l'Université de recherche Paris Sciences et Lettres  
PSL Research University

Préparée à l'Institut Curie

Magnetic fluidized beds in microfluidic:

Application to ultrasensitive detection for bioanalysis

Ecole doctorale n°388

Chimie physique et chimie analytique de Paris Centre

**Spécialité** Chimie Physique

## COMPOSITION DU JURY :

Mme. TALY Valéry  
Université Paris Descartes,  
Présidente du jury

Mme. FRENEA ROBIN Marie  
Université Claude Bernard Lyon 1,  
Rapporteur

M. LAURELL Thomas  
Faculty of Engineering LTH,  
Rapporteur

Mme. DU ROURE Olivia  
ESPCI,  
Examineur

M. FRESNAIS Jérôme  
Sorbonne Université,  
Examineur

Mme. DESCROIX Stéphanie  
Institut Curie,  
Directrice de thèse

M. MALAQUIN Laurent  
LAAS - CNRS,  
Co-directeur de thèse  
Invité

Soutenue par Lucile  
**ALEXANDRE**  
le 04 Octobre 2018

Dirigée par **Stéphanie DESCROIX**  
et **Laurent MALAQUIN**



*Magnetic fluidized beds in microfluidic: Application to ultrasensitive detection for bioanalysis*  
*PhD thesis of L. Alexandre*

## Abstract

To tackle new challenges in trace analysis, a new generation of microfluidic magnetic fluidized has been developed. This system is based on a suspension of magnetic beads inside a microfluidic channel. Particles are in suspension between two forces: the drag force created by the flow of liquid and the magnetic force due to addition of a permanent magnet to the system. In order to increase the flow rate of work, the height of the chip has been increased by five. We were able to work at 15  $\mu\text{L}/\text{min}$  and the efficiency of the new system was improved by addition of a vibrator motor and a bimodal support. A proof of concept was performed on capture of biotin and DNA.

A second part of my PhD work was dedicated to the application of the fluidized bed module for bioanalysis. First, extraction, pre-concentration and detection of bacteria on chip have been performed with a significant decrease of the limit of detection and of the time scale compared to usual methods. Then the system of fluidized bed was used as a platform to tests new ligands in order to perform a competitive bioassay in the context of preeclampsia. Finally, an ELISA was integrated on the fluidized bed with promising results.

Those results proved the efficiency of the microfluidic magnetic fluidized bed to work as a module for extraction, pre-concentration and detection of target of low concentration.

## Résumé en français

Un système de lit fluidisé magnétique microfluidique a été développé pour répondre aux besoins d'extraction et de préconcentration nécessaire comme première étape de bioanalyse. Ce système se base sur le même concept que les lits fluidisés macroscopiques en remplaçant la gravité par une force magnétique. Un nouveau module a été développé au court de ma thèse afin d'aborder de nouveaux défis en terme de détection à très basse concentration. Une augmentation de la hauteur de la puce nous a permis de travailler à hauts débits (15  $\mu\text{L}/\text{min}$ ). Un premier travail sur l'homogénéisation de la répartition des billes à l'intérieur de la puce microfluidique a été effectué grâce à l'implémentation d'un système de vibration et d'une matrice bimodale. Cette approche a prouvé son efficacité sur des modèles de capture de protéines et d'ADN.

En parallèle, une seconde partie de mon travail a porté sur l'application du système de lit fluidisé à différents défis analytiques. Dans un premier temps, nous avons montré son potentiel pour l'analyse bactérienne. Le lit fluidisé peut aussi être utilisé comme plateforme de tests pour ligands pour la prise en charge de patientes souffrant de pré-éclampsie au cours de leur grossesse. Enfin un immuno-dosage de type ELISA a été réalisé entièrement dans ce système de lit fluidisé.

Ces résultats montrent l'adaptabilité de ce système au-delà de ses capacités à travailler à haut débit, bas coût, en consommant peu d'échantillon, et avec une grande sensibilité.



*Magnetic fluidized beds in microfluidic: Application to ultrasensitive detection for bioanalysis*  
*PhD thesis of L. Alexandre*

---

## Remerciements

C'est un exercice bien difficile de remercier toutes les personnes qui ont participé, encouragé, supporté cette thèse. Lorsque j'ai débuté, je me doutais déjà que trois ans de thèse ne peuvent pas être réalisés seule, que ce serait d'abord un exercice de travail en groupe. Mais je n'imaginai pas combien ces interactions, ces conseils allaient me construire, tout ce qu'ils allaient m'apporter.

Mes premiers remerciements vont à Stéphanie Descroix, qui a encadré ce travail. Merci ! Merci tout d'abord pour la confiance que tu m'as accordée. Que ce soit au tout début, en me confiant ce travail, mais aussi jour après jour, expérience après expérience. Tu m'as encouragée, tu m'as poussée, tu m'as fait grandir. Et surtout, pendant les coups durs de la thèse aussi bien que pendant les difficultés plus personnelles de ces trois ans, tu as été à mes côtés quand j'en ai eu besoin, tu m'as écoutée, tu m'as épaulée. Je ne pense pas pouvoir te remercier suffisamment en seulement quelques mots à l'intérieur d'un manuscrit, l'écriture est bien incomplète pour dire merci, mais je suis fière que ces remerciements commencent par toi.

Merci à Laurent Malaquin, qui a co-encadré cette thèse, et qui m'a aussi permis de découvrir la ville de Toulouse. Merci pour ton soutien, pour ton aide et pour les nombreuses corrections de thèse, d'abstracts, de dossiers que tu as effectuées au cours de ces trois années.

Je souhaite aussi remercier Jean-Louis Viovy, tout d'abord pour m'avoir accueillie dans son équipe, mais aussi pour son aide et pour ses conseils qui ont su donner un élan particulier à ma thèse. Merci aussi à Catherine Villard, qui m'a écoutée et conseillée avec toujours beaucoup de sagesse.

Merci aux membres du jury, qui ont pris le temps de relire, de discuter et de compléter ce travail, avec une grande bienveillance.

Iago Pereiro a été mon encadrant en stage de master avant de prendre le rôle de mentor dans la thèse. Il m'a fait confiance pour reprendre son sujet de thèse, au moment où j'avais besoin d'un nouveau projet. Un grand merci pour tous tes conseils, aussi bien sur le travail que sur quantité de sujets philosophiques. Promis, je vais essayer la méditation, et je te fais signe dès que je commence le chamanisme.

Le début de ma thèse a aussi été mené avec l'aide d'Amel Bendali, dont la précision et l'écoute m'ont aidée à rendre mon travail plus efficace, mais aussi à surmonter les moments parfois un peu difficile de la thèse. Merci de m'avoir montré qu'on peut être une femme épanouie en science tout en construisant sa vie de famille.

Cette thèse a été réalisée en même temps que quatre autres thèses dans le laboratoire. Ismail et Lauriane ont été deux piliers dans ce travail, deux soutiens. Vous m'avez tous les deux beaucoup appris, que ce soit à travers cette belle amitié qui s'est bien développée en trois ans, mais aussi dans les moments durs ou à travers les confrontations. Lauriane, tu es la personne la plus humaine que je connaisse. Tu as un cœur immense, toujours plus grand

que ce que je devinais. Garde le ! Il te rend tellement belle. Ismail, qu'est-ce que tu m'as fait grandir en trois ans ! J'aime le fait que tu me pousses toujours plus loin, à réfléchir toujours un peu plus, à remettre encore en questions une autre certitude. Ton calme face à toute situation et ta faculté à analyser avant de réagir m'intriguent toujours, mais qu'est ce qu'ils sont agréables à vivre ! Miza a été ma personne de confiance dans les moments de doute, une oreille attentive, sans aucun jugement. Tu me manques ! Et même si le Singapour que tu nous as fait découvrir semble génial, n'oublie pas de revenir en France nous voir. Floriane, j'espère qu'on continuera la zumba !

Mais l'équipe ne s'arrête pas à cinq thèses. Marco, on peste souvent contre tes chansons italiennes, mais au fond elles nous manquent quand tu n'es pas au labo. Davide, merci pour tous tes conseils, j'espère qu'ils se rendent compte en Italie de la chance qu'ils ont de t'avoir. Sarah, ces années ensemble nous font de beaux souvenirs, merci pour tes gentilles attentions. Corentin, merci pour ton écoute, et pour ta vision éclairée des relations sociales. Merci Elodie d'être passée pendant toute l'écriture de ce manuscrit dans mon bureau pour que je continue à parler à des gens. J'espère qu'un jour tu viendras au labo avec ton épée. Merci Moencopi pour le coup de main en manips. Merci à tous ceux qui ont rendu plus facile le fait de se lever le matin, Mathilde, Marine, Céline, Cécile, Renaud, Bastien, Théo, Emile. Et le meilleur pour la fin, merci Charles pour les discussions et les conseils scientifiques.

Merci à ceux qui ont travaillé dans l'équipe lit fluidisé. Simon, Madad, Laura, Manh, Julie, c'était un plaisir de travailler avec vous. Vous m'avez tous appris, à votre façon, à travailler en groupe, merci !

Merci à l'ensemble des collaborateurs des projets présentés dans cette thèse.

Merci à tous mes amis, qui m'ont encouragée et soutenue pendant ses trois ans, en acceptant mon manque de disponibilité. Merci à Laurie, Marion et Anahid. Merci à Héloïse, Matthieu, Sophie, Romain et Amélie. Merci à Olivia, à Maxime, à Elsa, à Benoit, à Vanessa et à Lucie. Merci à toute la makia !

Merci à ma famille, qui m'a épaulé tout le long du chemin. Merci pour les petits messages, pour les colis, et pour toutes les ondes positives ! Merci à Raphaël et Guilaine pour les petits restos, merci à Orianne et Laurie pour les appels et les vidéos de chat. Merci à mes parents, qui ne sont pas toujours les premiers à apprendre les nouvelles mais qui sont ceux à qui je les annonce avec tout mon cœur. Merci d'avoir participé à cette belle aventure.

Et pour finir, merci à Nico. Merci d'être à mes côtés jour après jour. Tu me soutiens, tu m'écoutes, tu m'épaules. Mais pas seulement, tu me pousses à réfléchir, tu me pousses à donner le meilleur de moi-même. Tu me guides quand je suis perdue, tout en me laissant m'épanouir. Tu fais de moi quelqu'un de meilleur. Merci d'être dans ma vie, merci pour ta présence dans tous nos moments heureux comme dans ceux plus difficiles. C'était une belle expérience à vivre à deux, et j'ai hâte de découvrir la suite à tes côtés.

## Table of Contents

Abstract.....	1
Résumé en français.....	1
Remerciements.....	1
<b>General Introduction.....</b>	<b>1</b>
<b>Introduction .....</b>	<b>3</b>
<b>Solid phase extraction on micro-particles in microfluidics.....</b>	<b>3</b>
1. Fundamentals on microfluidics and magnetic beads.....	3
a) <i>Introduction to microfluidics.....</i>	3
b) <i>Specificity of microfluidics devices.....</i>	4
2. Particles handling in microfluidic devices.....	5
a) <i>Mechanical trapping.....</i>	6
b) <i>Chemical interaction with a surface and directed assembly.....</i>	8
c) <i>Optical tweezers .....</i>	10
d) <i>Dielectrophoresis-based beads manipulation .....</i>	12
e) <i>Acoustic waves.....</i>	14
f) <i>Magnetic handling of particles.....</i>	16
3. Magnetic support in microfluidics and super-paramagnetic particles.....	20
a) <i>Magnetic properties materials .....</i>	20
b) <i>Super-paramagnetic beads from Dynabeads™ .....</i>	25
c) <i>Organization and handling of superparamagnetic beads in a magnetic field.....</i>	27
d) <i>Functionalization.....</i>	30
4. Micrometric magnetic beads in microfluidic systems for extraction, pre-concentration and detection.....	30
a) <i>Analytical Challenge.....</i>	31
b) <i>Magnetic beads involved in extraction and detection .....</i>	32
c) <i>Digital, plasmon resonance or photonic crystal enhanced detection.....</i>	34
5. Conclusion.....	37
Bibliography .....	38
<b>Chapter 1.....</b>	<b>47</b>
<b>The fluidized bed concept: from basic system to the new generation .....</b>	<b>47</b>
1. Fluidized bed: working principle .....	47
2. First generation of microfluidic magnetic fluidized bed .....	52
a) <i>Development of a fluidized bed at micro scale.....</i>	52
b) <i>Miniaturization of the fluidized bed concept.....</i>	53
c) <i>Geometry of the chip.....</i>	54
d) <i>Operating regimes .....</i>	56
e) <i>Magnetic interactions in the fluidized bed.....</i>	58
f) <i>Recirculation and mixing of particles within the fluidized bed.....</i>	61
g) <i>Application of fluidized bed to biological analysis.....</i>	62
3. Evolution of the fluidized concept for high throughput analysis.....	62
a) <i>Fluidized bed characterization as function of the chamber height.....</i>	63

b) Capture efficiency as function of the chamber height.....	65
4. Conclusion and perspectives.....	67
5. Materials and methods.....	68
Bibliography.....	69
<b>Note on the vocabulary.....</b>	<b>71</b>
<b>Part A.....</b>	<b>73</b>
<b>Development and physical characterization of a new generation of fluidized bed.....</b>	<b>73</b>
<b>Chapter 2.....</b>	<b>75</b>
<b>Passive mixing in a fluidized matrix of beads based on Herringbones design.....</b>	<b>75</b>
1. Introduction.....	75
a) Passive mixing.....	77
b) Operating conditions.....	82
c) Herringbones design to create mixing.....	84
d) Fluidized bed and Herringbone design.....	85
2. Description of the adaption of the Herringbone design to the fluidized bed chip.....	87
3. Efficiency of mixing using Herringbones design in the microfluidic magnetic fluidized bead.....	90
a) Visualization of flow path deformation.....	90
b) Effect on the bead mobility.....	91
c) Quantification of the mixing through biotin capture.....	92
d) Influence of the design of the grooves.....	94
e) Influence of the depth of the grooves.....	96
f) Inversion of the place of Herringbones to avoid anchoring.....	97
4. Perspectives.....	100
5. Material and method.....	101
Bibliography.....	102
<b>Chapter 3.....</b>	<b>107</b>
<b>Active mixing in microfluidic fluidized bed.....</b>	<b>107</b>
1. Introduction.....	107
2. Alternation of regimes of fluidization.....	118
a) Observations of the movement induced on the matrix of beads.....	118
b) Quantification using a streptavidin-biotin capture model.....	120
3. Increase of the mobility of the beads at high frequencies.....	122
a) How to create movement of beads on a microfluidic chamber?.....	122
b) Characterization of the vibration motor and observations of the movement induced on the matrix of beads.....	123
c) Quantification using a streptavidin-biotin model.....	126
d) Bio-application: influence on the capture of DNA.....	127
4. Conclusion and perspectives.....	130
a) Control of the frequency and the amplitude.....	130
b) Ultrasounds to move particles.....	131
5. Material and method.....	133

Bibliography .....	134
<b>Chapter 4.....</b>	<b>139</b>
<b>Modulating the fluidized bed behavior by controlling magnetic particles properties and dimensions .....</b>	<b>139</b>
1. Bimodal matrices to enhance mixing.....	139
a) <i>Fluidized bed in industry</i> .....	139
b) <i>Particles segregation in complex mixture</i> .....	140
c) <i>Increasing mixing by adding different size of particles</i> .....	141
d) <i>Theoretical model of bimodal matrices in fluidization</i> .....	143
2. Integration of bimodal matrix in magnetic micro fluidized beds .....	144
a) <i>Bimodal fluidized bed – qualitative approach</i> .....	144
b) <i>Influence of beads composition on the expansion of the micro-fluidized bed</i> .....	148
c) <i>Model of interaction</i> .....	149
d) <i>Proof of concept with capture of biotinylated DNA on Streptavidin beads</i> .....	150
3. Evaluation of the 250 $\mu\text{m}$ chip with vibration and bimodal matrix.....	155
a) <i>Proof of concept with streptavidin/biotin model</i> .....	155
b) <i>Validation of the model on DNA hybridization</i> .....	156
4. Conclusion and Perspectives.....	159
a) <i>Conclusion</i> .....	159
b) <i>Perspectives to further improve the bed homogeneity</i> .....	159
5. Material and method .....	162
Bibliography .....	163
Transition .....	165
<b>Part B .....</b>	<b>167</b>
<b>Application of the first generation of fluidized bed to bio-analytical challenges .....</b>	<b>167</b>
<b>Chapter 5.....</b>	<b>169</b>
<b>A microfluidic fluidized bed to capture, amplify and detect bacteria from raw samples .....</b>	<b>169</b>
1. Introduction .....	169
a) <i>Health standards in food poisoning</i> .....	169
b) <i>Microfluidics for the capture and detection of bacteria</i> .....	170
2. New module of extraction and pre-concentration of bacteria using a moving magnetic matrix of beads .....	174
a) <i>Microfluidic magnetic fluidized bed as a platform of capture, extraction and detection of bacteria</i> .....	174
b) <i>Article</i> .....	175
c) <i>Versatility of the system toward bacteria strain</i> .....	184
d) <i>A further development of the fluidized bed platform towards antibiotic susceptibility investigation</i> .....	186
3. Perspectives .....	191
Bibliography .....	192

**Chapter 6 .....195**

**The fluidized bed as a miniaturized extra-corporeal platform - New therapeutic strategy against preeclampsia .....195**

1. Introduction.....	195
a) <i>Epidemiology of pre-eclampsia.....</i>	195
b) <i>Diagnostic of preeclampsia based on growth factors balance.....</i>	197
c) <i>Pre-eclampsia treatment and sFlt-1 depletion.....</i>	198
d) <i>Fluidized bed as a test platform.....</i>	200
e) <i>New ligands to restore the angiogenic balance.....</i>	201
2. Preliminary proof of concept.....	201
a) <i>Materials and method.....</i>	201
b) <i>Proof of concept of the detection by immunoassay in chip.....</i>	201
c) <i>Preliminary results.....</i>	204
d) <i>Going forward to optimization and clinical samples test.....</i>	206
3. Article.....	207
4. Perspectives.....	227
a) <i>Conclusion on the first results.....</i>	227
b) <i>Going to extracorporeal blood- cleaning: the strategy of animal model.....</i>	227
Bibliography.....	229

**Chapter 7 .....231**

**Extraction, preconcentration and detection of proteic biomarker by immunoassay in continuous flow .....231**

1. Introduction.....	231
2. Materials and methods.....	236
<i>Reagents and chemicals.....</i>	236
<i>Chip fabrication.....</i>	237
<i>Microfluidic Setup.....</i>	237
<i>Operating process.....</i>	237
<i>Fluorescence detection.....</i>	238
3. Optimization of the support.....	238
a) <i>Optimization of the immune-capture support functionalization.....</i>	239
b) <i>Optimization of the buffer composition.....</i>	240
4. Two methods of operation: manual in-tube labeling versus sequential injection.....	242
5. Influence of the enzymatic step: “stop and go” versus “continuous in flow” processes	245
a) <i>Detection protocol.....</i>	245
b) <i>Signal analysis.....</i>	246
6. Evaluation of the bioassay performances.....	248
a) <i>Optimization of the concentration of detection antibody on the immunoassay performances.....</i>	248
b) <i>Influence of the capture flow rate on the immunoassay performances.....</i>	250
c) <i>Influence of the volume of the sample on the immunoassay performances.....</i>	251
d) <i>Calibration curve.....</i>	252
7. Perspectives.....	255

Bibliography .....	257
<b>Conclusion .....</b>	<b>263</b>
<b>Appendixes.....</b>	<b>265</b>
<b>Résumé en français.....</b>	<b>283</b>
<b>Développement (et compréhension) de lits fluidisés magnétiques en microfluidique : .....</b>	<b>283</b>
<b>Application à la détection ultrasensible en bio-analyse.....</b>	<b>283</b>
1. Introduction générale .....	285
2. Description du système de lit fluidisé microfluidique et magnétique .....	286
3. Développement des aspects physiques du lit fluidisé en vue de travailler à haut débit 289	
1. <i>Implémentation de rainures de type « Herringbones ».....</i>	<i>290</i>
2. <i>Ajout de vibrations par système actif.....</i>	<i>293</i>
3. <i>Travail avec un support magnétique bimodal .....</i>	<i>295</i>
4. Applications biologiques du système de lits fluidisés microfluidiques magnétiques ...	296
a. <i>Capture et culture de bactéries in situ .....</i>	<i>297</i>
b. <i>Traitement par aphérèse de la pré-éclampsie.....</i>	<i>299</i>
c. <i>Intégration d'un test ELISA en puce .....</i>	<i>303</i>
5. Conclusion.....	305





---

## General Introduction

The development of new systems for trace analysis remains critical in many fields such as bio-medical analysis, food safety and environment monitoring. A large variety of biomarkers such as nucleic acids, proteins and even cells require detection at low concentrations in complex matrices. Hence, this still remains a challenge for many conventional approaches available.

In order to tackle this challenge, one of the proposed methods by conventional approaches usually requires an initial solid phase pre-concentration step prior to extraction step. These conventional approaches perform this step using particles or monolith columns. In this context, Microfluidics may appear as a promising alternative to further meet this challenge. Although bearing its own challenges, Microfluidics has the potential to improve the robustness, reproducibility and capacity of integration of capture and extraction steps. In this manuscript, a new technique based on suspension of particles in a flow-through of magnetic forces will be introduced. Drawn from the macroscopic fluidized bed commonly used in industries, the dynamic distribution of the beads within flow was downscaled to a micro level. This system is called microfluidic magnetic fluidized bed for the integration of steps and improved performance.

The first part of the manuscript focuses on a more detailed introduction on the usage and handling of microparticles in microfluidics for analytical applications. Different possibilities to handle particles in microfluidics and their involvement in analytical challenges will be described. A special attention will be given to super-paramagnetic beads.

Then, the concept of fluidized beds at the microscale, the first optimizations and the achieved results in the team will be presented (chapter 1). A new generation of fluidized bed has been developed during my PhD and, its advantages and limitations will be reviewed. In particular, we will explore our interest in the spatial distribution of particles, their mobility, the resulting surface to volume ratio and its influence on the capture efficiency. The improvement of beads distribution in this new generation of fluidized bed will be addressed more particularly in the second part of the manuscript.

The second part of the manuscript that consists of three chapters, presents new concepts to improve the homogeneity of the fluidized bed. First, approaches to enhance mixing in microfluidics channel will be investigated with a special attention given to methods that can be translated to agitation of particles. We will first consider the passive mixing methods (chapter 2), then active ones (chapter 3), and how those techniques can be applied to a matrix of beads. In particular, herringbones grooves and the implementation of vibration to the flow will be adapted to the fluidized bed, and their effect on the bed features will be discussed. Second, an approach on influencing the particle homogeneity and mobility using a bimodal distribution of particles as a support for extraction (chapter 4) will be focused. All approaches will be combined and its proof of concept on the capture of biomolecules will be reported.

In parallel to the development of this new generation of microdevice, the fluidized bed's ability for several bio-applications will be discussed. Those results were obtained with the first generation of fluidized bed chip. First, the capture of bacteria was explored and an efficiency of 90% was attained (chapter 5). This method was developed with a detection module based on the multiplying of bacteria capture on the surface of the beads in a nutritive medium. The potential of this integrated approach will be investigated for low concentrated sample.

The following chapter presents the results obtained as part of a project for treatment of pre-eclampsia (chapter 6). This project was conjointly set up with the Faculty of Pharmacy and the Cochin Hospital. The fluidized bed was used as a miniaturized platform mimicking extra-corporeal circulation to test ligands to restore the angiogenic balance of two growth factors of interest. The potential of this approach will be tested both with cell media and plasma samples.

Finally, the possibility to integrate ELISA in the fluidized will be evaluated in the microfluidic chip (chapter 7). The proof of concept was performed with interleukin IL-6 as the target. IL-6 was chosen as the interleukin target because it is involved in responses of the human immune system to infection and cellular injury. The optimization of the fluidized bed-based ELISA and the assay performances will be represented.

## Introduction

### Solid phase extraction on micro-particles in microfluidics

#### 1. Fundamentals on microfluidics and magnetic beads

##### a) Introduction to microfluidics

Microfluidics is defined as the science and technology of manipulation and control of fluids (from microliters ( $10^{-6}$  L) to picoliters ( $10^{-12}$  L)) in designs with dimensions from tens to hundreds of micrometers.

In 1959, Richard P. Feynman announced in his speech 'There's plenty of Room at the Bottom' that "What I would like to suggest is the possibility of training an ant to train a mite to do this. What are the possibilities of small but movable machines? They may or may not be useful, but they surely would be fun to make." (Feynman, 1960). Following this speech, the field of Micro Electro Mechanical Systems (MEMS) appeared as a technological revolution which paved the way for microfluidics during the nineties. The first micro-motor was built in 1989, with a limited speed of up to 500 rpm (Fan et al., 1989).

The appeal of miniaturization stemmed from curiosity, as Feynman suggested, but also from multiple needs: 1) the need for new tools (i.e. pumps, surgical micro-instruments and micro-needles) in the biomedical fields to manipulate or analyze cells, DNA and proteins that could be observed easily; 2) the need to decrease the cost of experiments and analysis (airbag sensors are a good example); and 3) the necessity to develop more precise technologies at lower costs (inkjet technology).

Microfluidics was born on those concepts and it evolved drastically since its first faltering steps in the early seventies. For example, the first functional micro-system ever built was a gas chromatograph on silicon wafer in 1972 (Terry, 1972). Between 1980 and 1995, many actuators such as valves or micro-pumps were developed to simplify the construction of micro-systems (MEMS Technologies). In 1993, Manz and Harrison published a pioneering work on electrophoresis on chip (Manz et al., 1993). In 1998, G. Whitesides simplified the micro-fabrication processes by developing soft lithography based on the use of poly(dimethylsiloxane) to fabricate PDMS chips (Duffy et al., 1998). Ever so complex microfluidic devices were developed since then (such as multiplexing, mixers, digital microfluidic), paving the way to innovative approaches in a wide variety of fields (food safety, environment control and medicine to name a few).

#### **b) Specificity of microfluidics devices**

Compared to traditional fluid studies or technics, microfluidics offers several advantages such as low cost experiments, small volumes consumption, reduction of analysis/reaction time due to the decrease of diffusion distances, an increase of the surface to volume ratio, multiplexing, portability, versatility in design for integration, reproducibility and automation. However, hydrodynamics rules established at the macro-scale have to be re-considered at the micro-scale. From past knowledge, Newton laws break down at microscopic levels. For example, gravity forces become negligible in front of forces such as capillary forces (Stone et al., 2004; Tabeling, 2005). Moreover, at the micro-scale, the impact of surfaces becomes predominant. In such conditions, viscosity predominates over inertial forces which give rise to laminar flows. It means that turbulences do not occur spontaneously and that two liquids injected side by side will mix only by diffusion on a direction perpendicular to the flow.

To describe physical phenomena in microfluidics, dimensionless numbers are generally used. These numbers allow us to compare forces at play in microfluidics. Among them, the most commonly used is the Reynolds number,  $Re$ . The Reynolds number reports on the ratio of inertial over viscous forces. It can be defined as:

$$Re = \frac{\rho_f v l}{\eta}$$

Equation 1

With  $\rho_f$  the fluid density ( $\text{kg}\cdot\text{m}^{-3}$ ),  $v$  the velocity of fluidic phase ( $\text{m}\cdot\text{s}^{-1}$ ),  $l$  is the characteristic channel dimension (m) and  $\eta$  is the dynamic viscosity of fluidic phase ( $\text{Pa}\cdot\text{s}$ )

For  $\text{Re} > 1$ , turbulences can appear while for  $\text{Re} < 1$ , laminar regimes predominate. For channels with micrometer-scale dimensions, as  $\text{Re} \sim 1$ , the Reynolds number is usually smaller than 1. In micro-channels, the flows are mostly laminar, with ordered and regular streamlines. In these conditions, mixing is driven by diffusion only. This statement should be moderated by considerations on the conditions of the flow since the limits of regimes (laminar or turbulent) can be described by more than one dimensionless parameters (Squires et al., 2008).

## 2. Particles handling in microfluidic devices

Homogeneous reactions (liquid-liquid) have proven their efficiency, especially regarding clinical applications. In order to expand the range of possible bioassays (extraction, purification and detection), heterogeneous reactions (solid-liquid for example) have been explored. A common approach is to use nano- or micro-particles and to manipulate them with actuators. For example, magnetic solid phase extraction is a system of extraction and purification of specific molecules using a magnet and magnetic particles that are adapted for multistep protocols. Microfluidic systems working with particles have many advantages such as 1) the simplicity of handling, 2) an increase in specific surface area in comparison to channel coating, and 3) a high loading capacity (Serra et al., 2017). Moreover, beads confer a chemical stability to the experiment that reduces variability, leading to more reliable and reproducible results.

Micro-particles have mostly been used to increase the ratio of the surface of capture to the volume of analyzed sample. The use of solid suspensions in biological and bioanalytical protocols has become common due to its simplicity and efficiency. The use of micro-particle relies on the possibility to functionalize the surface of those particles providing high versatility and on the high surface/volume ratio due to their size (Nilsson et al., 2009; Serra et al., 2017).

In this context, we will first focus on the manipulation of small particles: the advantages they provide and how microfluidic systems handle them. Then, we will focus on

superparamagnetic particles at the micro-scale. Finally, we will see how they can be used in bio-applications to extract, pre-concentrate and detect molecules of interest.

### a) Mechanical trapping

To maintain particles in place inside a microchannel under flow, a simple solution is to mechanically trap them within geometrical patterns. Micro-particles are smaller than the size of the channel where samples are injected. They are sensitive to shear-stress which makes them easier to be manipulated under flow but more difficult to be confined. In order to trap micro-particles, micro-pattern structures can be microfabricated inside microchannels. Once the beads are mechanically trapped, reactions on their surfaces can take place.

One of the first groups to develop this approach was the team of Takehiko Kitamori (Sato et al., 2000). As presented on Figure 1 (a and b), they trapped 45  $\mu\text{m}$ - wide beads inside a glass channel using a constriction. The sample and buffer were percolated at 2  $\mu\text{L}/\text{min}$  through the immobilized bed of beads. Immunosorbent assay was performed on the surface of the beads through the absorption of human secretory immunoglobulin A (s-IgA) and the creation of a complex with a colloidal gold conjugated anti-s-IgA antibody. These reactions were detected using thermal lens microscopy. A comparison study between microtiter plates (Figure 1 c) and microbeads (Figure 1 d) was performed. This study reported that the microfluidic system allowed a decrease of analysis time from 24 h to 1 h and a lowered limit of detection at 1  $\mu\text{g}/\text{mL}$  (dozens of times lower than conventional Elisa). Moreover, these improvements were achieved at a lower cost and with easier procedures.

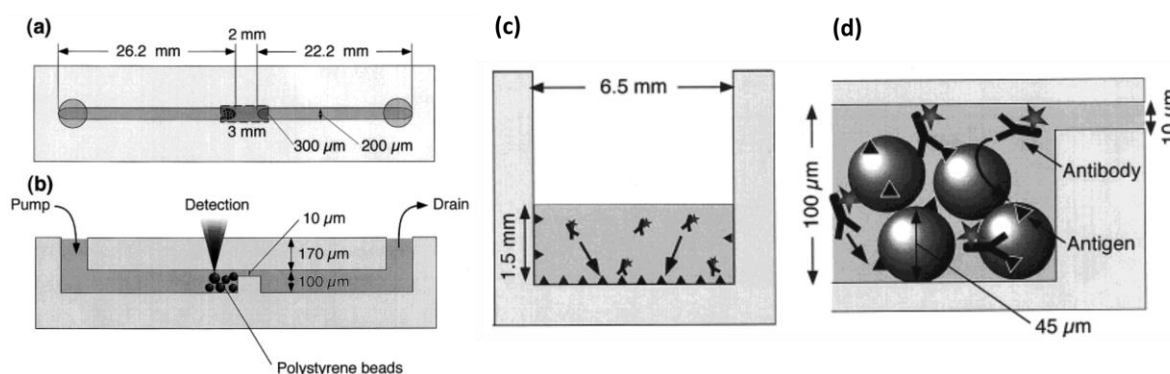


**Figure 1** Layout of the glass microchip for immunosorbent assay (a) overview (b) a cross section and illustrations of the antigen-antibody reaction in (c) a microtiter plate (d) the microchip (Sato et al., 2000)

Different strategies have been rolled out to overcome the issue of back pressure in micro-fabricated constrictions (Koh et al., 2017), using distinct traps (Chen et al., 2013; Di Carlo et al., 2006), array of micro-holes (Han et al., 2015; Thompson and Bau, 2010) and other confinement techniques (Yu and Kornelsen, 2003; Zhang et al., 2012). Andersson et al. refined this process in order to increase the interactions between the beads and the liquid. A filter chamber was introduced to immobilize microbeads (Andersson et al., 2000). Inside their micro-device, a comb-like structure with 50  $\mu\text{m}$  height pillars that were evenly spaced with a 2  $\mu\text{m}$  separation, was built as a square to avoid clogging (Figure 2 A and B). Beads were trapped inside the square pillar area, and the sample could flow through the beads. Courtesy of this geometry, the flow rate was dropped by only 40% for a given pressure when all beads were inside the chamber. Thus, interaction with the surface of the beads could be performed directly during the percolation of a given solution in flow without any limitation on its volume.

A similar approach was developed by Fu et al. They fabricated an array of pillars that could be shifted by a pneumatic micro-valve (Figure 2 (A-C), Fu et al., 2011). In this case, pillars were 20  $\mu\text{m}$  X 50  $\mu\text{m}$  in dimension with a height of 45  $\mu\text{m}$  that were spaced by 5  $\mu\text{m}$ . The chamber was 75  $\mu\text{m}$  high, and could be closed by the pillars when the valve was actuated (Figure 2 C and D). Flow rates of work were between 0.5 and 5  $\mu\text{L}/\text{min}$ . This system was tested on a competitive immunoassay (Figure 2 E) performed on human plasma with an analytical recovery between 81 and 110 % of the spiked target (3,5,6-trichloropyridinol or TCP). The linear reachable range was from 1 to 50  $\text{ng}/\text{mL}$  with a limit of detection of 0.080  $\text{ng}/\text{mL}$ .



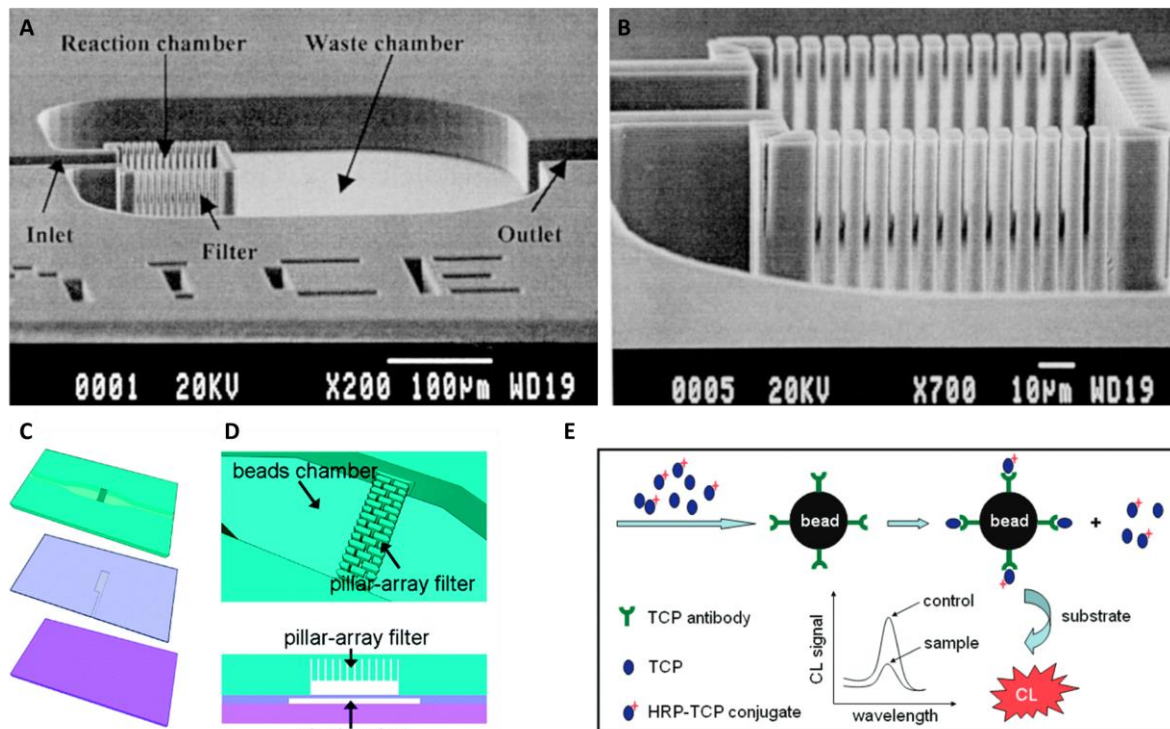


**Figure 2 (A) and (B) SEM images of the main chamber and the filtration system of the chip in (Andersson et al., 2000) (C) Schematic representation of the three layers of the chip: the beads chamber, the pneumatic control and the glass substrate (D) schematic view of the main chamber (E) diagram of the working principle of the TCP competitive immunoassay performed on the beads (Fu et al., 2011)**

Mechanical trapping is a simple approach, but it requires specific microfabrication. As beads are confined in the trap, the interactions between the surface of the beads and the flowing solution are not maximal. Moreover, flow rates are limited by back pressure generated by the geometry.

#### **b) Chemical interaction with a surface and directed assembly**

To manipulate micro-particles in microfluidic devices, chemical interactions can be used to control particle movements. By functionalizing the particles' surfaces, it is possible to control the beads functionalization as well as the interaction with the channel's surface. Such an approach has been developed by Andersson et al.. They developed a strategy to chemically pattern a silicon-based channel so that micro- and nano-beads could be maintained as pictured in Figure 3 (Andersson et al., 2001). The surface channel was locally modified using biotin by micro-contact printing. They were able to reach a patterning resolution of about 5 µm for streptavidin beads with diameters of 2.8 and 5.5 µm as well as

to work with a density of binding that ranged from tens (micro-beads) to hundreds (nanometers beads) of beads within a surface of  $100 \mu\text{m}^2$ . While different chemistry immobilization techniques were investigated, biotin-streptavidin showed the best resolution and adherence to the beads (Figure 3 B). This patterning was able to withstand a flow of liquid in the channel of up to a pressure drop of 3 kPa, which corresponds to common pressures in microfluidics.

This method can be extended to bio-applications. Lee et al. used chemical patterning to develop a microarray of beads in order to perform an immunoassay (Lee et al., 2009). A surface adhesive layer was created by spin coating a UV-curable acrylate adhesive layer in order to regulate the pattern of  $30 \mu\text{m}$  wide micro-beads that were functionalized with elastin-like polypeptide (ELP). ELP is a smart bio-polymer that is sensitive to temperature, pH, light and ionic strength. They used its properties to specifically capture, extract and release a cancer biomarker, namely a prostate-specific antigen (PSA). Moreover, an immunoassay by sandwich ELISA could be performed on the surface of the beads for detection (limit of detection of  $0.05 \text{ ng/mL}$  and saturation of the surface of the beads above  $10 \mu\text{g/mL}$ ). One limitation of this approach is that the functionalization occurs only at the bottom part of the channel.

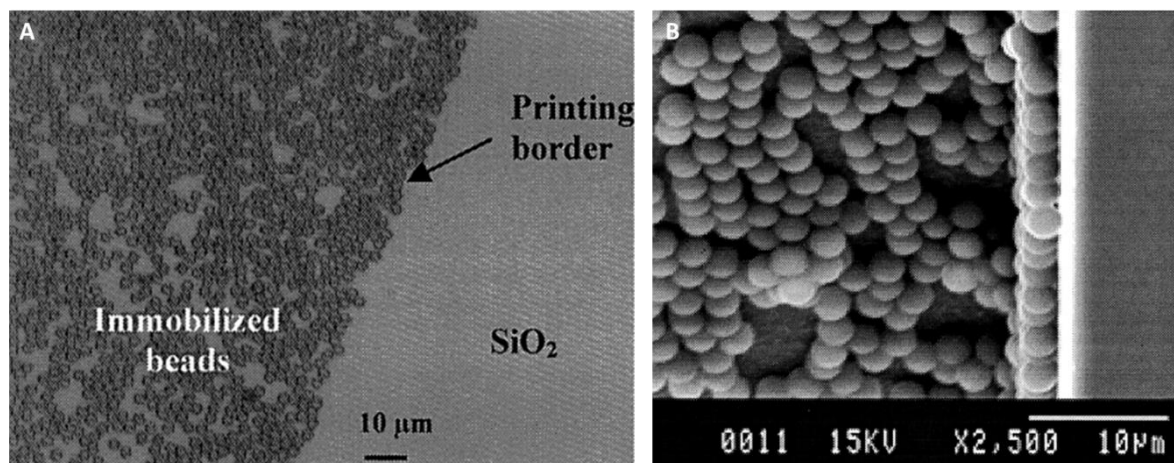


**Figure 3 (A) immobilized 2.8 Streptavidin beads on a biotin coated surface by micro-contact (B) SEM image of a monolayer of amino-functionalized beads immobilized on an anhydride coated channel with a density of surface coverage reach 15 beads/ $100 \mu\text{m}^2$ . (Andersson et al., 2001)**

Directed-assembly of beads is also another possibility to explore. L. Malaquin et al. published a controlled particle assembling on surface (Malaquin et al., 2007). Capillary forces and convective flows were exploited to create monolayers or arrays of beads (Figure 4). Immobilization and organization were controlled through hydrodynamic forces and

adjustment of the evaporation process. Surface tension, velocity, pattern and size were also investigated to improve the quality of the structures. Three parameters were essential to control the assembly regimes: the substrate temperature, the contact angle and the particle concentration. Delapierre et al. focused on coupling this technology with micro-patterned obstacles (Delapierre et al., 2017). Capillary assembly was optimized for cell deposition. Preparation of an array of 10 000 cell spots could be ready in less than 1 hour.

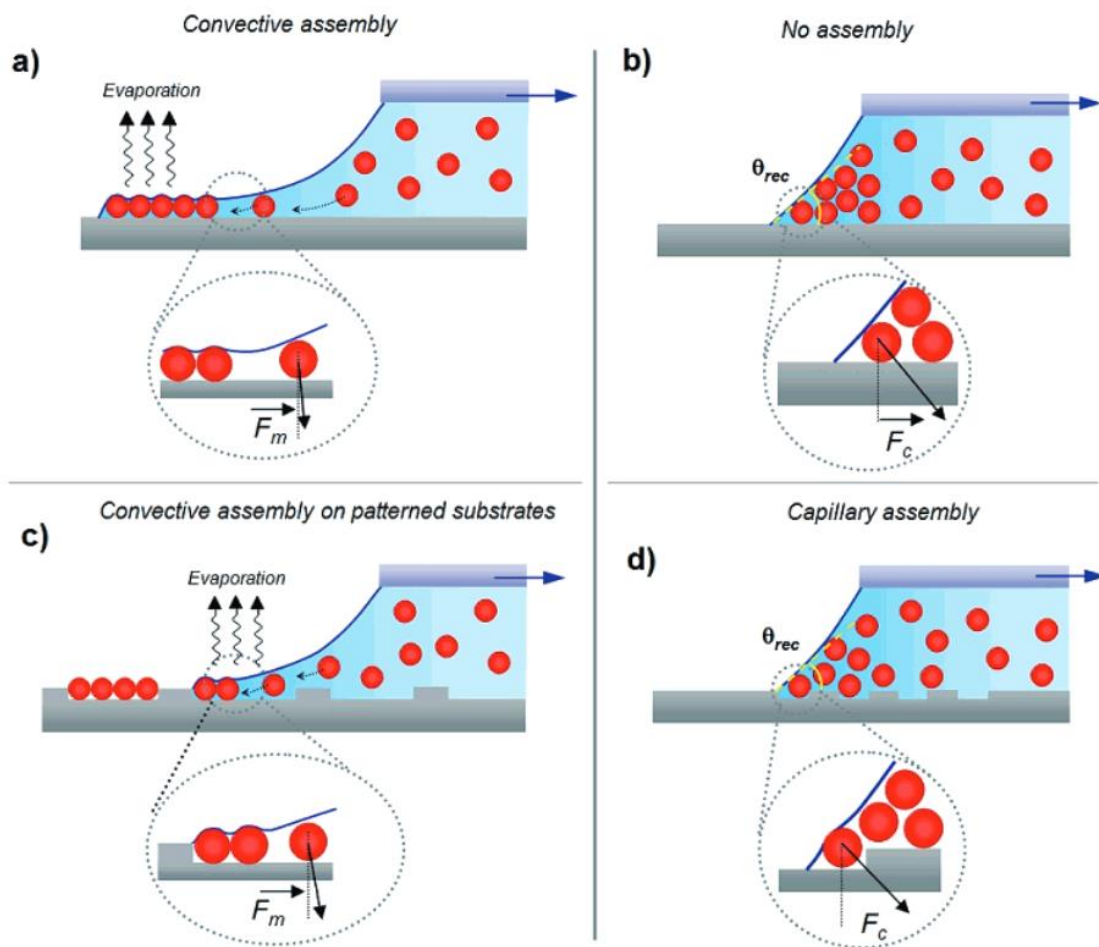


**Figure 4** Assembly mechanisms based on particle confinement at the contact line of a droplet (Malaquin et al., 2007)

These methods are simple, acute and easy to realize. However, immobilization on a 2D surface limits the available surface for interaction, and the achievable flow rates.

### c) Optical tweezers

Optical tweezers are a technology used to manipulate small objects with light in three dimensions. It has been demonstrated that a focalized laser beam was able to exert (either

attractive or repulsive) forces in the range of 0.1 to 200 pN on single micrometric particles and to move them in the three dimensions of space. Not only that particles from few angstroms up to 10  $\mu\text{m}$  can be handled, individual atoms can be handled too. A spatial resolution down to the nanometer can be achieved with a time resolution that is around  $10^{-4}$  s (Laurent et al., 2002; Neuman and Nagy, 2008).

One of the first publications on optical trap based on forces of radiation pressure was reported by Ashkin in 1970 (Ashkin, 1970). First experiments were conducted with a single  $2.68\mu\text{m}$  bead in a beam with a power in the order of the mW. The bead was drawn along the axis of the beam and accelerated in the direction of the light. Next, he created an optical trap by combining two identical laser beams. Eventually, he used a pair of infrared lights to generate forces under damage free conditions in light of the possible biological applications (Ashkin et al., 1987).

Optical tweezers can be easily combined with microfluidic systems such as hydrogel encapsulation (Arai et al., 2005), computer spatial light modulator (Rodrigo et al., 2002), DNA stretching (Smith et al., 1996) and mechanical trapping (Burger et al., 2014). Burger et al. presented a system where beads ( $20\ \mu\text{m}$  in diameter) were first captured by centrifugation on 'V-cup' (traps designed in the PDMS chamber) in the main chamber of a PDMS disc. Then they were fluorescently labeled before being re-organized by optical tweezers in order to discriminate the labeled from the unlabeled beads as presented on Figure 5 A and B. Labeled beads could then be collected in an adjacent chamber, while others were flushed away. This set-up allowed an optimization of the capture and selection parameters in order to adapt the system to living cells.

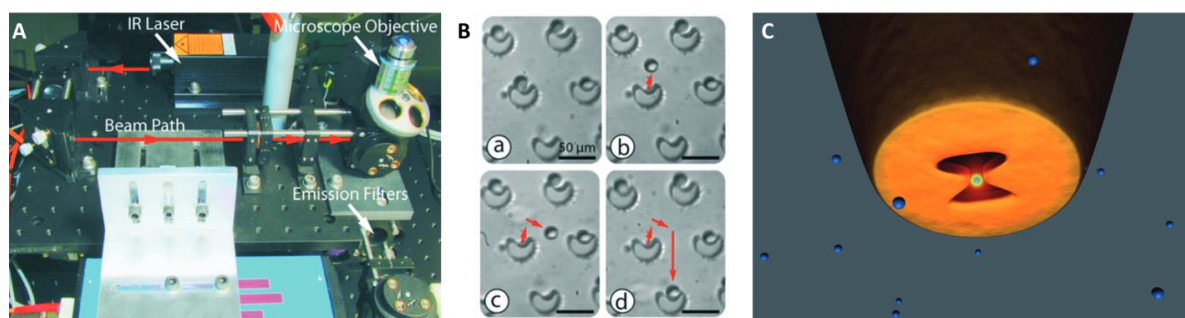


**Figure 5** *A Set-up of Burger et al. of the implementation of optical tweezers and B manipulation of microbeads in the 'V-cup' (Burger et al., 2014) C Schematic representation of nano-optical tweezers with the antenna illuminated by a laser beam at 1.064 nm and focused through the 40 X objective (Berthelot et al., 2014)*

One of the major issues in manipulating metallic particles in a liquid phase was the elevation of temperature (the force applied on the particle being proportional to the power of the laser and to the distance particle-center of the trap) leading to bubbles formation. It would in turn damage biological tissues. This issue was addressed by using plasmonic tweezers (Tsuboi, 2016) or nano-optical tweezers (Berthelot et al., 2014) as shown on Figure 5 C.

This low-noise and low-drift approach to move particles was non-invasive but brought constraints on the construction of the set-up as the distance between the microscope objective and the particle was below 200  $\mu\text{m}$ . Magnetic tweezers usually allowed the manipulation of only one particle at a time, even if this limitation can be bypassed by complex optical patterns (Grier, 2003). This is a major bottleneck for analytical applications. Moreover, applications for biological samples were also limited due to the aforementioned heating effects and the biological response to laser beam that could alter the experiment, causing photo-damage.

#### **d) Dielectrophoresis-based beads manipulation**

Dielectrophoresis (DEP) regroups technologies inducing movements of a particle in a non-uniform electric field through the interaction of the particle's dipole and spatial gradient of the electric field. DEP is a powerful technology to manipulate particles in micro-devices (Çetin and Li, 2011; Demircan et al.; Dürr et al., 2003; Zhang et al., 2010).

DEP forces are useful tools for manipulating biological particles such as regular cells (Frénéa et al., 2003; Menad et al., 2015), cancer cells (Pethig and Markx, 1997; Yang et al., 1999a), leukocytes (Yang et al., 1999b), DNA (Asbury et al., 2002), bacteria (Brown et al., 1999), yeast (Wang et al., 1993), viruses (Schnelle et al., 1996), and biological agents (Huang et al., 2003). We will focus on the techniques of DEP on beads, a domain that has been widely covered by literature (Auerswald and Knapp, 2003; Gawad et al., 2010; Jung and Kwak, 2007).

Tirapu-Azpiroz et al. presented a system to mechanically trap micro-beads assisted by dielectrophoresis (Tirapu-Azpiroz et al., 2015). Planar electrodes were integrated in a PDMS chamber (Figure 6 A), allowing the guidance, trapping, and release of micro-beads. The constant flow rate in the device was controlled by a capillary pump. Channel walls were transparent and hydrophilic. The main channel was composed of a  $420 \times 420 \mu\text{m}^2$  area made of 96 traps. Planar metallic electrodes were lithographically patterned below the chip. The electrodes created DEP forces on micro-beads (10  $\mu\text{m}$  in diameter) to dock them inside



designed traps. As shown on Figure 6 B, the dielectrophoresis effect was combined with the drag force (resulting in a constant flow rate  $\sim 80$  nL/min) induced by the flow to reach an optimal efficiency: they demonstrated a capture of 63 % (7 V) and a release of 98 % (voltage turned off).

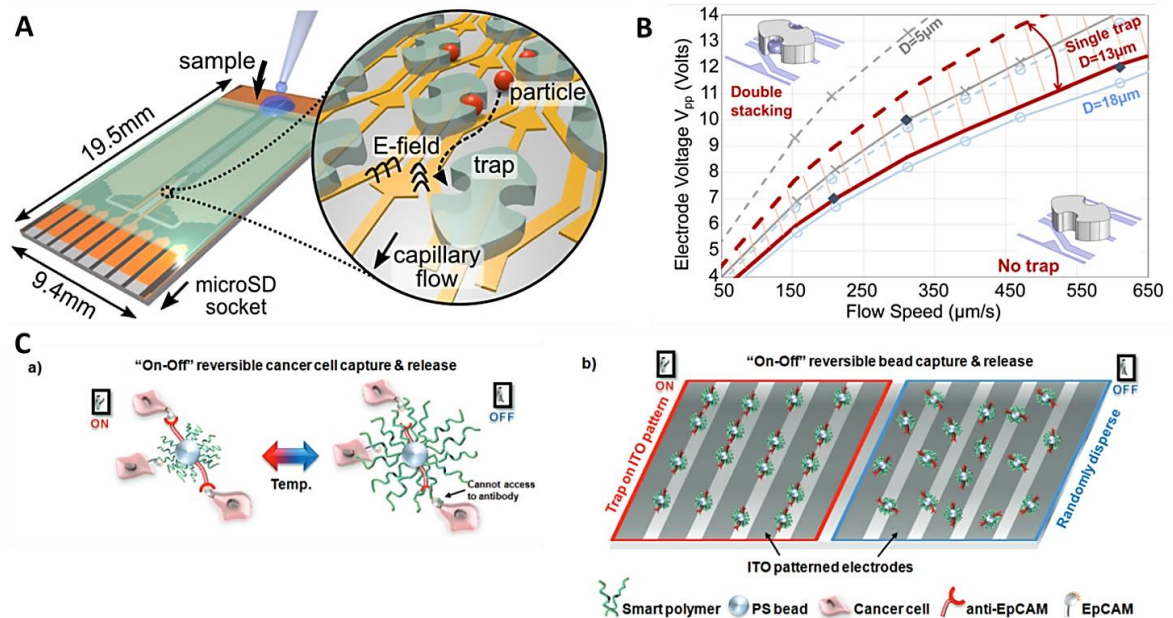


**Figure 6** (A) Schematic representation of the chip and the trapping process (B) representation of the computed relation between the flow speed and voltage applied on the electrode (Tirapu-Azpiroz et al., 2015) (C) representation of the 'on-off' manipulation of smart beads to capture and release tumor cells (a) but also to manipulate them (b) (Kim et al., 2016)

In 2016, Kim et al. introduced the concept of 'smart beads' (Kim et al., 2016) that combined temperature activation of the beads and dielectrophoresis. Those beads were coated with poly(N-isopropylacrylamide), a temperature responsive polymer with a sharp reversible hydrophilic-hydrophobic transition (lower critical solution temperature at  $32^\circ\text{C}$ ), and functionalized with an antibody targeting tumor cells. The properties of the polymer were used to capture and release tumor cells as shown on Figure 6 C a. Dielectrophoresis was then involved to manipulate and position the particle/cell complex. Indium tin oxide (ITO)-pattern glass allowed an induction of an electric field and a force on the beads, at an electric potential of  $5 V_{pp}$  at 100 Hz. This force was used to position the beads and the tumor cell (placed above 80 % of attached beads), and to control the pattern of the beads for further analysis, as illustrated on Figure 6 c. DEP was also used to eliminate the beads or the cells that were not responding to the electrical field.

Dielectrophoresis is a label-free non-invasive bio-compatible method as both particles and cells can be manipulated using this technology without physically touching them. However, it only works in certain medium conditions and it requires complex micro-fabrication steps.

#### e) Acoustic waves

Forces generated by ultrasonic standing waves can also be applied to manipulate particles in suspension. When a high frequency acoustic wave propagates in a fluidic phase, it loses its energy through viscous damping of the waves. This phenomenon induces an acoustic streaming flow and, in presence of particles in suspension, it induces an acoustic radiation force on the particles. This force is proportional to the diameter of the particle, to the frequency of the acoustic waves and to the speed of the sound in the fluid (Destgeer and Sung, 2015; Laurell and Lenshof, 2014). It can be used to move particles, to sort them and even to rotate them (Ahmed et al., 2016).

Thomas Laurell's team developed an acoustic control of particles movements in a buffer solution as shown in Figure 7 (Laurell et al., 2007; Nilsson et al., 2004). 90 % of separation and pre-concentration in 67 % of the initial volume of 5  $\mu\text{m}$  wide beads was achieved at 2 MHz, 22 V and 0.3 mL/min.

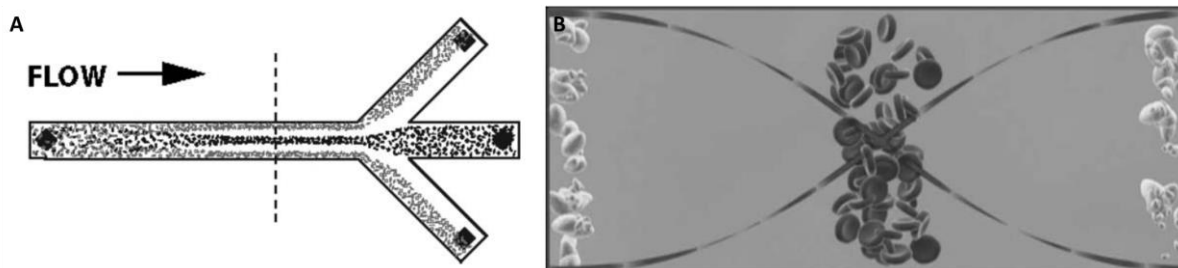


**Figure 7 (A) Illustration of separation of negative acoustic contrast factor ( $\varphi$ ) particles (black-centre outlet) and positive  $\varphi$ -factor particles (grey-side outlets) in 45° design chip (B) Illustrated cross-section of a separation channel showing negative  $\varphi$ -factor particles (e.g. lipid particles) collected in the pressure antinodes by the side walls and positive  $\varphi$ -factor particles (i.e. red blood cells) in the pressure node (Laurell et al., 2007)**

This sorting technique was then extended to mixtures of different sizes of beads, ranging from 2 to 10  $\mu\text{m}$  particles inside a 350  $\mu\text{m}$  wide channel as shown on Figure 8 A (Pettersson et al., 2007). This system has proven to be highly efficient in sorting various blood components (red blood cells, platelets and leukocytes) at a flow rate of 0.10 mL/min (Figure

8 B). Sorting was further extended to particles of equal size, but having different densities (Figure 8 C).

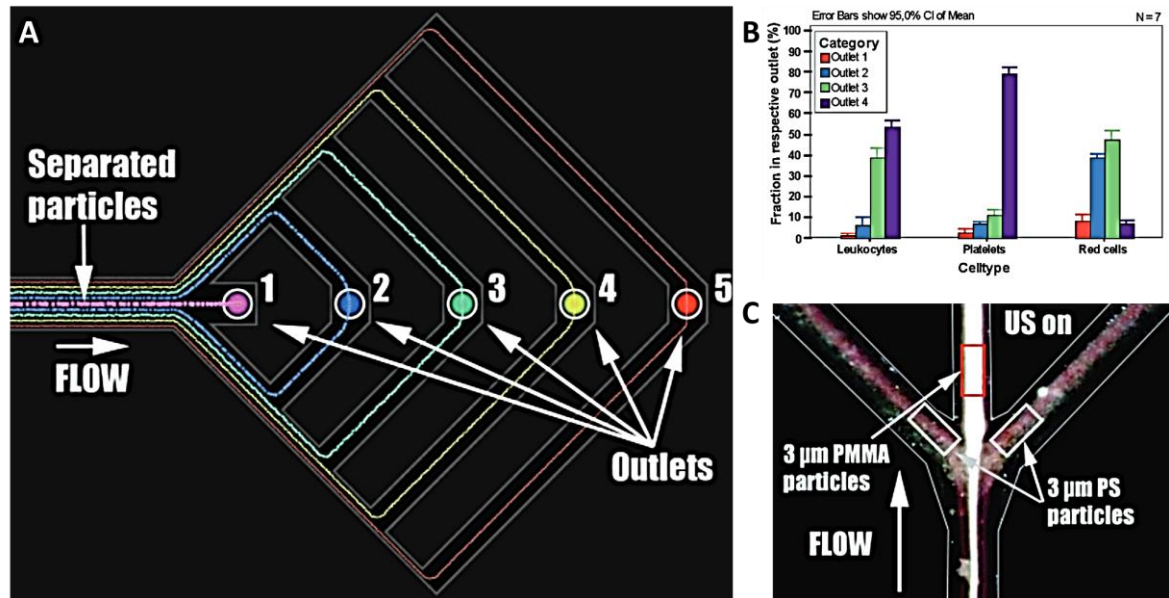


**Figure 8** A) Illustration of the fractionation of the separated particles at the end of the separation channel: in this case, through five consecutive outlets/fractions. Since the separation is symmetrical along the center of the channel; eight of the fractionation outlet channels are pairwise connected B) Separation of platelets, red cells, and leukocytes with CsCl (0.22 g/mL) added to the suspending medium (Petersson et al., 2007) C) 3 µm red PS and white PMMA particles with different densities could be separated

Recently, Destgeer et al. published on the sorting of micro-particles by traveling surface acoustic waves (TSAW) in a PDMS chip using acoustic waves for sorting beads with sizes ranging from 3 to 10 µm in diameter (Destgeer et al., 2013). They were able to show a 100 % efficiency of sorting on specificity (absence of contamination between the sub-population) at 100 µL/min (3.5 mm/s) using a power of 55 mW and a 40 µm X 200 µm channel.



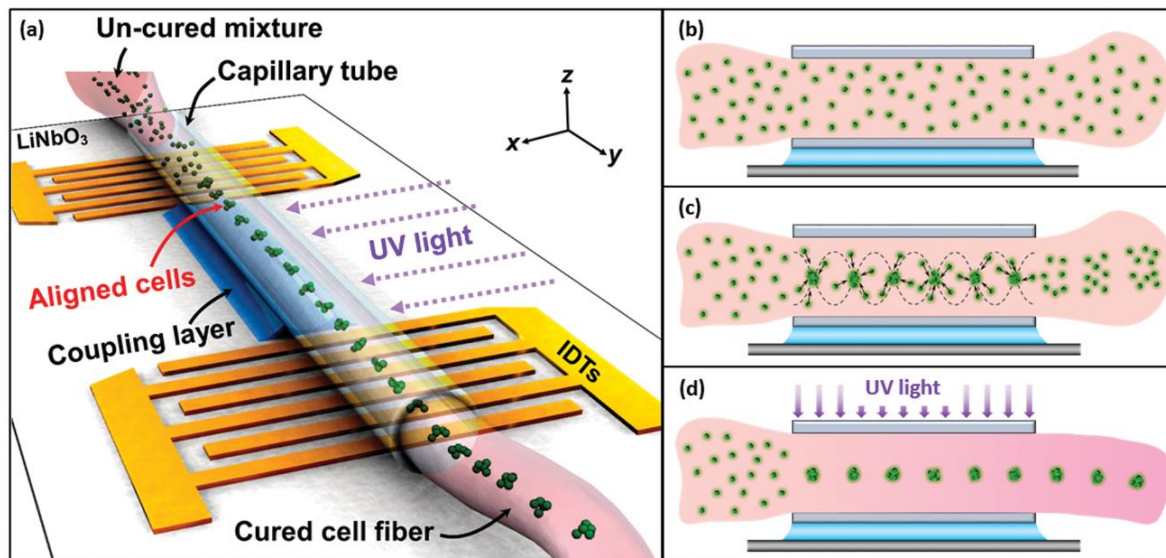


**Figure 9** a) Schematic representation of the entire process for generating a patterned cell fiber in the perpendicular orientation using SAWs. b) The photosensitive polymer and cell solution are added to a tube placed above a piezoelectric substrate containing two parallel IDTs with a water-coupling layer. c) IDTs are activated and produced SAWs that align the cells. d) Following IDT deactivation, the fiber is polymerized with UV light and extracted, retaining cell patterns. (Lata et al., 2016)

Lata et al. implemented this technology to control the spatial distribution of beads or cells in a channel in order to polymerize hydrogel around their surface (Lata et al., 2016). They used surface acoustics waves (SAWs) to arrange particles or cells in highly viscous liquids such as PEGDA (Figure 9 a) where Reynolds number can fall down to  $10^{-3}$  (Wexler et al., 2013). The process is fully biocompatible as they were able to show a cell survival rate of 100% measured within a short time frame (24h).

#### f) Magnetic handling of particles

To control the movement of particles, an easy and simple approach is to use magnetic particles that can be influenced by a magnetic field. Magnetic particles, as will be further discussed in the third part of this introduction, are usually made of magnetic powder/nanoparticle encapsulated in a polymer matrix resistant to oxidation, and their surface can be functionalized for the purpose of bio-applications. Their sizes vary across four orders of magnitude, ranging from a few nanometers to dozens of micrometers. Under a magnetic field  $\vec{B}$ , the force  $\vec{F}_{mag}$  applied on the magnetic particles can be written as

$$\vec{F}_{mag} = \frac{V \Delta\chi}{\mu_0} (\vec{B} \cdot \vec{\nabla}) \vec{B}$$

Equation 2

Where  $V$  is the volume of the particle,  $\Delta\chi$  is the difference of magnetic susceptibility between the medium and the particle and  $\mu_0$  is the vacuum permeability. The full demonstration will be performed in chapter 1.

As shown in this equation, particles are sensitive to the gradient of the magnetic field. The magnetic force applied on them is within the range of a few up to tens of pN depending on the parameters appearing in Equation 2.

More specifically, superparamagnetic particles are of particular interest for biological analysis. These particles are composed of individual paramagnetic nanoparticles that are generally composed of only one magnetic domain. These nanoparticles exhibit a magnetic moment that spontaneously flips with the Néel relaxation time as characteristic period. Thus it gives rise to zero magnetization in the absence of a magnetic field. When submitted to an external magnetic field, each domain self-orientates and provides a magnetization to the particle (Ruffert, 2016).

In microfluidics, different approaches based on permanent or electro- magnet have been proposed to control and manipulate magnetic particles. Electromagnets offer the possibility to switch off the magnetic field, which is a property that can be used to release magnetic particles. Such property allows a more flexible manipulation and the liberty to preset multiple poles. However, permanent magnets are still very common as they have the benefits of simplicity and portability without any temperature rise. Moreover, they can reach stronger magnetic forces compared to electromagnets (Gijs, 2004).

Patterning precision depends on the size of magnetic particles and on the geometry of the magnetic field, as shown in Figure 10. A high precision in positioning magnetic beads, at the micron scale, was demonstrated (Zanini et al., 2012) by adjusting the geometry of the magnetic field using micro-magnets. The interactions between beads appear on those pictures as the chains were created (Figure 10 b, c and d) which will be an issue for our system as developed further. Individual particle positioning was achieved with magnets of the size of the particle, as well as magnetically functionalized cells, making this magnetic array relevant for bio-applications such as cell purification (Osman et al., 2013).

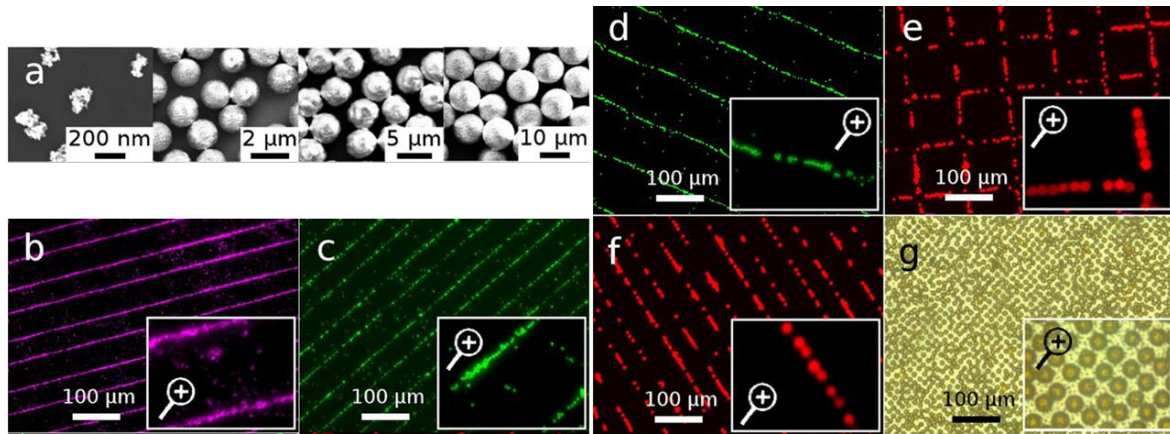


**Figure 10 (Color online)** (a) SEM images of the superparamagnetic particles; (b)–(f): Fluorescence images of the superparamagnetic particles trapped by micromagnets [(b): 200 nm above out-of-plane magnetized NdFeB film; (c): 1.4 μm above out-of-plane magnetized NdFeB film; (d): 1.4 μm above in-plane magnetized SmCo film; (e), (f): 4.9 μm above out-of-plane magnetized NdFeB film; (g) 10.3 μm particles individually positioned in a square lattice above an out-of-plane magnetized NdFeB film (the reversed magnets are  $7 \times 7 \mu\text{m}^2$  in surface area, separated by 5 μm). The insets in (b)–(g) present a zoom on the particles positioned above each magnetic configuration (Zanini et al., 2012)

This ability to precisely control the movement of magnetic beads can be used to control bioassay on the surface of particles. Magnetophoresis is based on a gradient of field used to deflect the trajectory of beads. Peyman et al. demonstrated the performance of a multi-step biochemical assay in continuous flow (15 μL/h or 350 μm/s), first with a biotin-streptavidin model, and then with a sandwich immunoassay (Peyman et al., 2009). As shown in Figure 11 a and b, magnetic particles (2.8 μm in diameter) were injected inside a micro-channel and then deflected in the flow by a magnetic force. Reagents and buffers were flowed through the channel in parallel flows. Detection was performed by fluorescence. The assay was performed using a flow ranging from 0.1 to 10 μg/mL for one minute with only 7.5 μL of reagents.

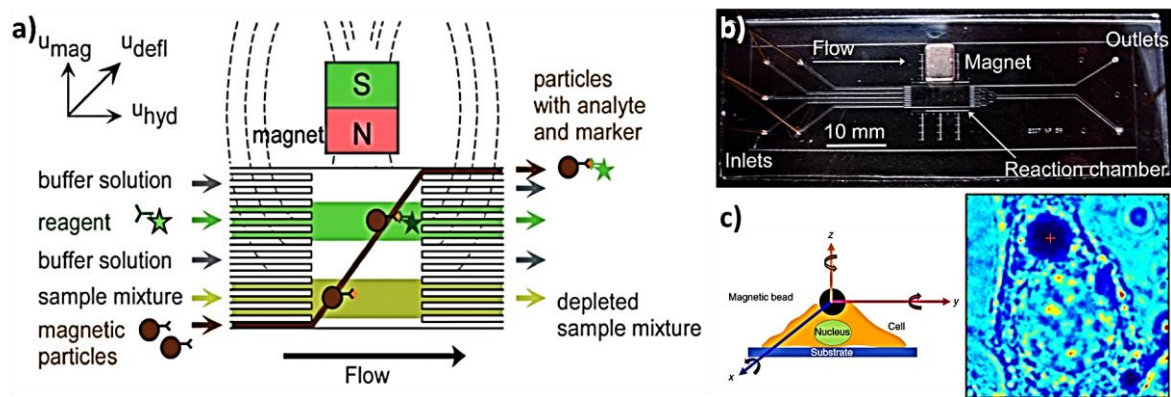


**Figure 11 a)** The principle of the continuous flow reactor: magnetic particles are deflected through multi-laminar reagent streams and consecutive binding and washing steps are performed on their surface in continuous flow **b)** picture of the chip (Peyman et al., 2009) **c)** representation of a cell and micro-magnetic bead and picture of particle tracking inside an elongated melanoma cell (Zhang et al., 2017)

More complex situations can be considered notably by changing the geometry of the magnetic field. Deng et al. constructed a filtration system for magnetic beads made of nickel posts of 7  $\mu\text{m}$  high that were magnetized in the presence of a permanent magnet (Deng et al., 2002). Working with magnetic beads of 4.5  $\mu\text{m}$  in diameter, each post could capture around 50 beads. Their results revealed a separation efficiency from non-magnetic beads of 95% after release (stop of the external magnetic field).

This approach is compatible with any medium, even with cells. Magnetic beads can be bound to the surface of a cell via surface receptors (Figure 11 c). A magnetic field is then used to control the movements of the magnetic beads and to apply a local mechanic stress on the living cell. This 3D magnetic twisting cytometry has been recently presented by Zhang et al. (Zhang et al., 2017).

Magnetic handling of particles has the advantages to be easily automated (through electromagnet), bio-compatible, precise, and non-invasive. In the next paragraphs, we will focus on magnetic particles and their use in microfluidics.

### 3. Magnetic support in microfluidics and super-paramagnetic particles

#### a) Magnetic properties materials

The use of magnetic support for sample preparation and for diagnostic purposes has increased over the last 30 years (Olsvik et al., 1994; Tartaj et al., 2003). Magnetic support has been developed based on different materials such as iron oxides, chromium dioxides and barium ferrites to name a few. Iron oxides have the advantage of better stability against oxidation (Ozaki, 2004).

Magnetic properties are related to the spin of electrons. The spin is a quantic property of a particle, usually related to its own magnetic moment induced by the orbital motion of the electrons around the nucleus. However, spin is the only quantic value without any equivalent in classic point of view. The spin of an electron creates a magnetic moment, and the gathering of these magnetic moments gives rise to the magnetic properties of a material (note: a magnetic field can also be created by the movement of electrons in atoms).

If a material is placed in a magnetic field of a strength  $\vec{H}$ , the individual atomic moments will organize themselves to answer and create a magnetic moment  $\vec{M}$ . This answer is proportional to the magnetic field  $\vec{H}$  as:

$$\vec{M} = \chi_r \vec{H}$$

Equation 3

$\chi_r$  is a constant dependent of the intrinsic characteristics of the material. This constant can be positive or negative, and is named the magnetic susceptibility.  $\chi_r = 0$  if the material does not respond to any magnetization.

The global magnetic field inside the magnetic material is

$$\vec{B} = \mu_0 (\vec{H} + \vec{M}) = \mu_0 (1 + \chi_r) \vec{H} = \mu_0 \mu_r \vec{H}$$

Equation 4

With  $\mu_0$  the vacuum permeability ( $4\pi \cdot 10^{-7} \text{ N/A}^2$ ) and  $\mu_r$  the magnetic permeability.

The intrinsic organization of a material to answer to a magnetic field is related to the magnetic susceptibility,  $\chi_r$ . According to the value of the magnetic susceptibility  $\chi_r$ , a material can be considered as diamagnetic, paramagnetic or ferromagnetic (Pamme, 2006a).

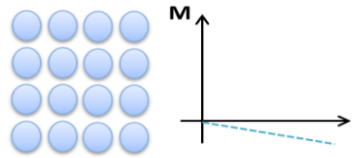
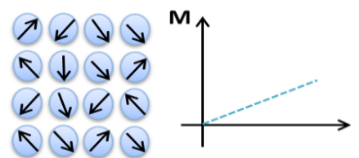
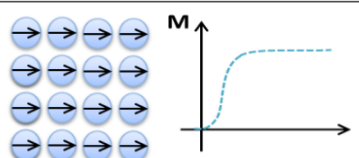
Most materials are weakly diamagnetic, with  $\chi_r < 0$  (i.e. water, proteins, DNA, cells, polymers, wood, glass). Their direction of polarization is opposite to the external field. They are repelled from magnetic field and forced toward the minima of magnetic field. Such materials are called non-magnetics.

Paramagnetic materials have a positive magnetic susceptibility  $\chi_r > 0$  (i.e. oxygen, platinum and manganese salts, organic free radicals). When placed inside a magnetic field, they organize themselves, align with the field direction and are weakly attracted toward zones of high magnetic field. However, in the absence of a magnetic field, no distinct organization is shown, and magnetic moments organize themselves randomly without any neighboring effect resulting in an absence of magnetization.

Ferromagnetic materials present a high positive magnetic susceptibility  $\chi_r \gg 1$  (i.e. iron, cobalt, nickel). These materials are usually organized into magnetic or Weiss domains with the magnetization in opposite directions in each domain. This allows the minimization of the magnetostatic energy of the system. Upon external magnetic field, the domain walls can move, causing the domains aligned with the external field to grow and the other domains to shrink. This order is not disrupted by thermal agitation up to the critic temperature  $T_c$  named Curie temperature, above which agitation is strong enough to disorient and randomize the magnetic moment.

Other configurations are possible such as anti-ferromagnetism and ferrimagnetism, but are less usual.

**Table 1 Comparison of the three most important types of magnetism (Tabnaoui, 2012).**

Magnetism Type	Magnetic Susceptibility ( $\chi$ )	Atomic and Magnetic Behaviour	
<i>Diamagnetism</i>	- small $\chi < 0$ - negative (repulsion) H <sub>2</sub> O, ( $-9.048 \cdot 10^{-6}$ ) Cu, ( $-0.77 \cdot 10^{-6}$ )	Atoms have no magnetic moment.	
<i>Paramagnetism</i>	- small $\chi > 0$ - positive (attraction) Na, ( $-8.6 \cdot 10^{-6}$ ) Al, ( $-2.2 \cdot 10^{-5}$ )	- Without magnetic field: random orientation of magnetic moments (no-interaction between neighbouring atoms).  - In a magnetic field: parallel alignment of magnetic moments.	
<i>ferromagnetism</i>	- large $\chi \gg 1$ - positive (attraction) - function of applied field Fe, (1000)	Atoms have parallel aligned magnetic moments within domains.	

Even without external magnetic field, the ferromagnetic particles can be divided in areas where electron spin are all oriented in the same direction. Those areas are called magnetic domains. In the presence of multiple domains, the magnetization answer of the material to a magnetic field is nonlinear as shown on Figure 12. When a magnetic field is moved towards an unmagnetized ferromagnetic material, magnetization is increased inside the material (dashed line). When the external magnetic field is decreased and reduced to zero, an internal magnetization still exists inside the material (b and e), called remanent magnetization. In order to completely switch off the internal magnetization an external magnetic field named coercive field has to be applied (c and f) (Pamme, 2006b; Tabnaoui, 2012).



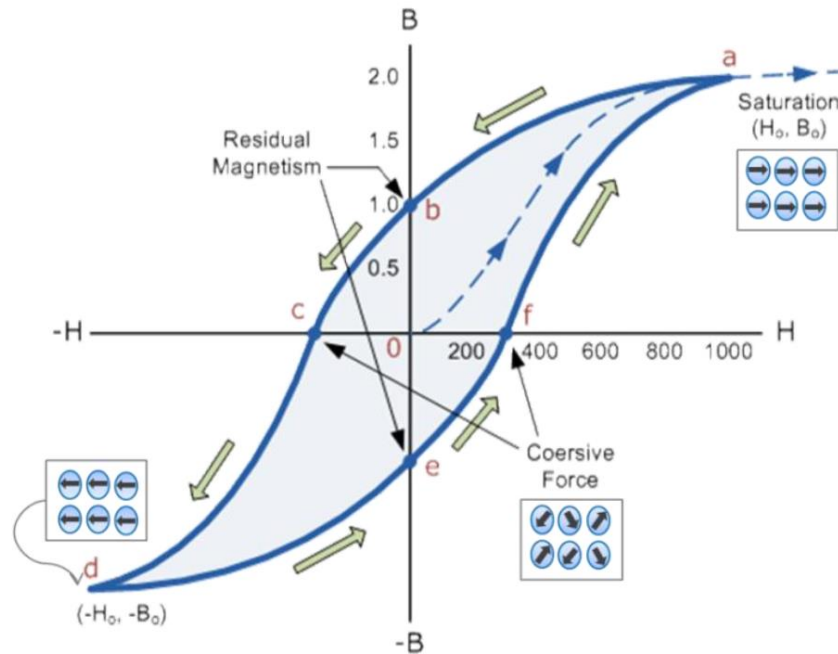


**Figure 12 Influence of the external magnetic field  $H$  on the magnetic answer of a ferromagnetic material (Tabnaoui, 2012).**

For particles of smaller sizes, the number of domains is reduced and it can go down to 1. The single domain magnetic particles tend to align with the direction of the minimum energy. A change of direction requires additional energy  $\Delta E = KV$ , with  $K$  the magnetic anisotropy and  $V$  the volume of the particle. This energy  $\Delta E$  is the energy barrier of a non-interacting single domain particle with uniaxial anisotropy (Matijević and Borkovec, 2004). This energy has the same order of magnitude as the thermal agitation ( $k_B T$ ). In the absence of an external magnetic field, the direction of the magnetization changes in a random fashion. This change can be modeled by the Néel-Arrhenius relaxation time:

$$\tau = \tau_0 \exp\left(\frac{\Delta E}{k_B T}\right)$$

Equation 5

Where  $\tau_0$  is the characteristic time of the material (typically  $10^{-9} - 10^{-10}$  s),  $\Delta E$  the energy barrier as previously described,  $k_B$  the Boltzmann constant and  $T$  the temperature.

Super paramagnetic particles are composed of single domain particles where the magnetization reverses on a characteristic that is the Néel relaxation time. In the absence of an external magnetic field, the global magnetization of the system is nullified. Hence, no



interaction among beads can be observed. There is neither coercive field nor remanent magnetization, which is a huge advantage.

When a magnetic field is applied to the system, there is an alignment of the directions of all the magnetization of magnetic nanoparticles within the beads. The field ( $B$ ) applied on the magnetic beads induces a magnetization ( $M$ ), as shown on Figure 13. In this thesis, there will be no focus on the beads magnetization at smaller values ( $< 10\text{mT}$ ) of the field  $B$  (small frame on each graphs of Figure 13) as they do not represent the framework of the study. For fields between  $10\text{ mT}$  and  $2\text{ T}$ , the magnetization of superparamagnetic particles can be written as:

$$M = M_0 \left(1 - \frac{k_B T}{M_s \bar{V} B}\right)$$

Equation 6

Where  $M_0$  is the magnetization at saturation of the particle,  $M_s$  is the intrinsic spontaneous magnetization,  $\bar{V}$  the mean volume and  $B$  the magnetic field (Fonnum et al., 2005). The general equation is a Langevin function ( $L(x) = \coth(x) - \frac{1}{x}$ ). In the article, the cotangent is approximate as 1 as  $\frac{k_B T}{M_s \bar{V} B} \ll 1$ .

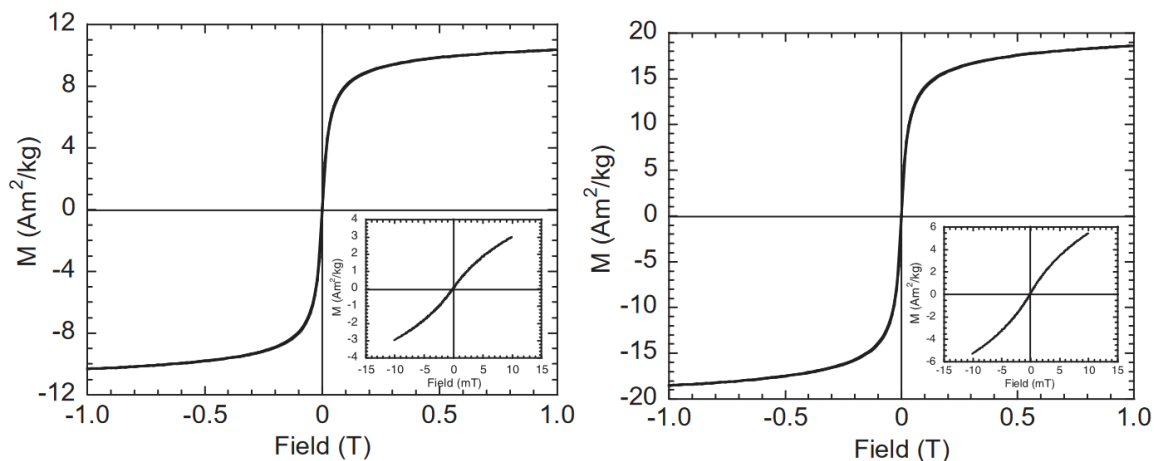


**Figure 13** Values of magnetization of *M-280* (left) and *M450* (right) beads as a function of the external electric field (Fonnum et al., 2005)

As shown on Figure 13, the magnetization of the particles can be considered as saturated almost as  $B > 0.2\text{ T}$ . This assumption will be considered as true for the rest of the demonstration.

When a magnetic particle is brought within the proximity of a magnetic field ( $B$ ), a force ( $\overrightarrow{F_{mag}}$ ) is applied on it. This force depends on the gradient of the magnetic field  $\vec{B}$  and of the magnetic moment of the bead  $\vec{m}_b$ .

$$\overrightarrow{F_{mag}} = \nabla(\vec{m}_b \vec{B}) = (\vec{m}_b \nabla) \vec{B} + (\vec{B} \nabla) \vec{m}_b$$

Equation 7

In a first approximation, the beads are considered saturated, so  $\nabla \vec{m}_b = 0$ .

$$\overrightarrow{F_{mag}} = (\vec{m}_b \nabla) \vec{B}$$

Equation 8

The magnetic moment of the bead  $\vec{m}_b$  can be written as the magnetization of the material reported to the volume  $V$  of one particle  $\vec{m}_b = V\vec{M}$  and using Equation 3  $\vec{m}_b = \chi_r V \vec{H}$ . The expression of the magnetic force can thus be written as:

$$\overrightarrow{F_{mag}} = \frac{V \chi_r}{\mu_0} (\vec{B} \nabla) \vec{B}$$

Equation 9

With  $V$  the volume of the particle,  $\chi_r$  the difference in magnetic susceptibilities between the particle and the surrounding media,  $\mu_0$  the vacuum permeability.

### b) Super-paramagnetic beads from Dynabeads™

Many commercial products have been developed in the field of superparamagnetic beads. Exemples of these suppliers are: Creative Diagnostics® with particles ranging 50 nm to 6  $\mu\text{m}$  in diameter, they have enhanced magnetic properties with the addition of magnetic particles to the iron oxides center; AbraMag® Magnetic beads from Abraxis with superparamagnetic non aggregating iron oxides microspheres of 0.5  $\mu\text{m}$  in diameter and PureProteome™ Magnetics beads from Merck ranging from 300 nm to 2.5  $\mu\text{m}$  in diameter that are dedicated for bioapplications. The well-known Dynabeads© from Thermofischer is also another good example of the success of this technology. Beads are made by the incorporation of iron oxides in an envelope of porous polymer. These beads exist in diameters of 1, 2.8 and 4.5  $\mu\text{m}$ , have superparamagnetic properties and uniformity in size (Fonnum et al., 2005). Several protocols to create magnetic particles have been tested, such

as emulsion or dispersion polymerization. We will focus on Dynabeads, as they are the main type of particles used in this work.

In 1979, John Ugelstad produced perfectly spherical monosized particles in a range of 0.5 to 100 microns (Haukanes and Kvam, 1993). These particles were synthesized by emulsion and polymerization of a monomer in a mixture of sodium hexadecyl sulphate and hexadecanol in order to form submicron sized droplets (Hansen et al., 1976). The fabrication process had two steps: activation of the polymer particles in water, and subsequent absorption by those polymers of water-soluble organic compounds in order to increase their volume more than 1000 times. The size of the pre-emulsion droplets and the monomer swelling ratio were the essential parameters for the determination of the mean particle size (Sæthre et al., 1995). Their first use was essential for fast protein liquid chromatography systems (Ugelstad et al., 1983). Porous beads covered with oxidative groups were dispersed in aqueous solution of  $Fe^{2+}$  with salts. Reaction induced the formation of fine grains of magnetic oxides, inside and outside the beads. Thus, the particles acquired superparamagnetic properties.

In 1984, John Ugelstad published a paper on a sensitive, specific and reproducible concept to remove tumor cells from bone marrow using beads of  $3\mu m$  in diameter. The beads were made of polymerized hydrophilic styrene divinylbenzene, which had 19.4% of magnetite and were functionalized with six monoclonal antibodies (Treleaven et al., 1984). They proved that the magnetic approach was more efficient than simple microspheres coated with antibodies by showing an extraction of 99.9% of the tumor cells.

Nowadays, those beads are commonly used in laboratories to perform immunoassays, extraction, pre-concentration and detection. The latter will be discussed in the next section. This success is due to the following main advantages:

- A high surface to volume ratio that allows an improved kinetics of capture at their surface (Teste et al., 2011a, 2011b)
- Availability of a wide variety of chemistry and functionalization such as minimizing particles aggregation, limiting non-specific binding and controlling ligand density
- The facility to handle the particles for separating molecules of interest from complex matrices without centrifugation step

Nonetheless, these particles also exhibit several drawbacks that have to be considered for analytical applications:

- Most of these particles have porous surfaces that induce non-specific capture resulting in lower specificity.
- The sedimentation of the particles that reduces the possibility of injection and transport may impede the experimental reproducibility

### c) Organization and handling of superparamagnetic beads in a magnetic field

In the presence of a magnet, superparamagnetic particles behave as magnetic dipoles (Martinez-Pedrero and Tierno, 2015) that interact with each other due to attractive forces. The magnetic interaction potential ( $U_{dd}$ ) between two dipoles (i,j) can be described at a distance  $r$  as :

$$U_{dd} = \frac{\mu_0}{4\pi} \left\{ \left( \frac{\vec{m}_i \vec{m}_j}{r^3} \right) - \left[ \frac{(\vec{m}_i \vec{r})(\vec{m}_j \vec{r})}{r^5} \right] \right\}$$

Equation 10

With  $\vec{m}_i$  and  $\vec{m}_j$  the dipole moments of the particles,  $\mu_0$  the vacuum permeability and  $\vec{r}$  the distance vector between the two particles.

Under an external magnetic field, superparamagnetic beads tend to align along the magnetic field lines (Li et al., 2016). Their magnetization enables them to interact as dipole-dipole and self-assemble into stable chains (Singh et al., 2005). As shown on Figure 14 A, the columns orient themselves along the magnetic field lines. In the absence of magnetic field, the particles lose their magnetization causing disassembly of the formed chains and clusters. This property has already been observed in several designs (Doyle et al., 2002; Guo et al., 2006; Morimoto et al., 2009; Weddemann et al., 2011).

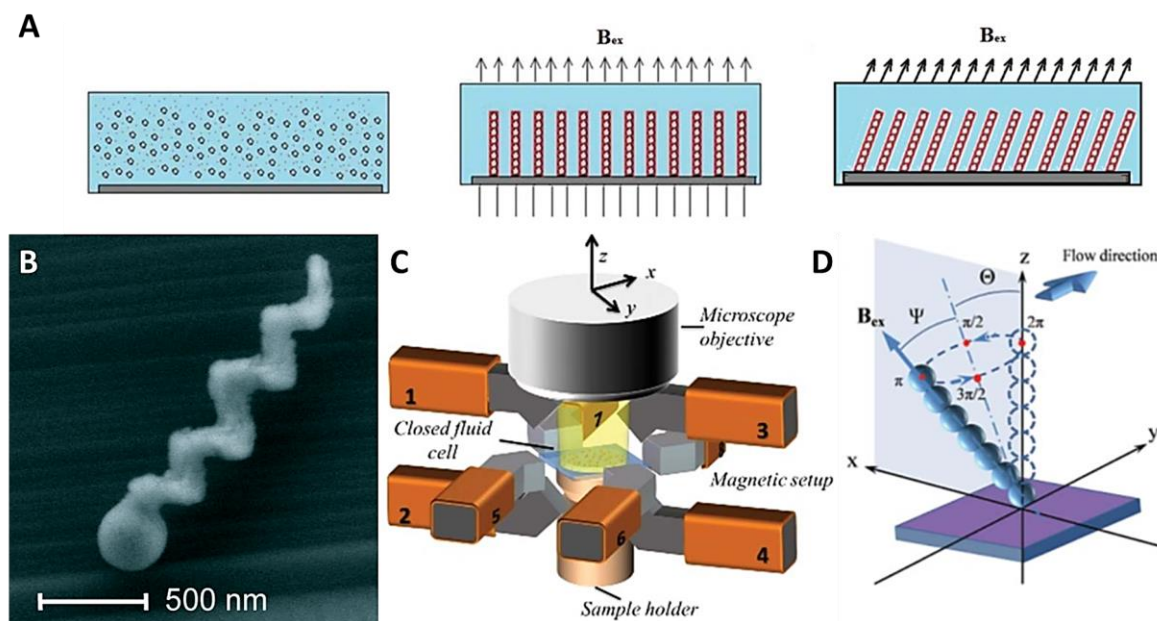


**Figure 14** A) creation and movement of artificial cilia made of  $2.7\ \mu\text{m}$  spherical magnetic beads (white) and poly(butylacrylate) latex nanoparticles (red) B) SEM picture of a nano-swimmer made of glass ( $\text{SiO}_2$ ) with  $200\text{-}300\ \text{nm}$  in width and  $1\ \text{to}\ 2\ \mu\text{m}$  long and were able to move in a rotational magnetic field with a precision of trajectory of the micrometer (Ghosh and Fischer, 2009). C) Representation of a eight poles electromagnet allowing the controlled handling of artificial cilia D) movement of the artificial cilia (Wang et al., 2013).

The shape and the length of the columns depend on the size of the particles and on the magnitude of the magnetic field. The velocity of a chain a micro-beads is proportional to the velocity of a single beads with an enhancement factor that is dependent on the fluidic characteristic around the material and logarithmically dependent on the length of the chain (Derks et al., 2007). As expected, those chain formations are more stable in less viscous media (Lin et al., 2014). This property of self-assembly has been used in different configurations particularly to develop moving structures and control their movement thanks to the magnetic field. Ghosh and Fischer reported the creation of fully controlled artificial swimmer (Figure 14 B), with a precision of trajectory at the micrometer (Ghosh and Fischer, 2009). Wang et al. created an artificial cilia controlled by multiple electromagnets (Figure 14 C). Using chains of micro magnetic beads and poly(butylacrylate) latex nanoparticles that provided flexibility, they were able to vary the length and the density of the cilia with the number of beads as well as the density of the magnetic field (aspect ratio up to 11). Furthermore, they were able to manipulate the structure in order to create a flow velocity of  $3\ \mu\text{m/s}$  at a frequency of  $5\ \text{Hz}$ . The same idea was developed by Coq

et al. to investigate the collective dynamics of actuated microcilia in a viscous fluid (Coq et al., 2011; Wang et al., 2013).

Self-assembly of magnetic particles can also be used to generate and measure forces of single cells or molecules. Bauer et al. presented a technique based on the assembly of self-organization of magnetic micro-cylinders that can generate higher forces than optical traps (limited to 100pN) without dependence on the micro-pattern or the cantilever as observed in atomic force microscopy (Bauër et al., 2017). Construction of super paramagnetic micro-cylinders (6 $\mu\text{m}$  in diameter and 12 $\mu\text{m}$  in length) was reported in which, Arp2/3 actin networks were grown by functionalization of the particles surface. As they self-assemble, those cylinders interact with each other in a homogenous field forming lines. Forces generated between the cylinders could reach several nN. Thus, actin networks development could be observed under pressure up to a hundred Pa. Stress performed between the cylinders was fully controlled by the external field applied. Bauer et al. were able to show a decrease of the growth speed that is linear up to the maximum stress of 100 Pa.

This method easily allows multiplexing and it is free from the complexity of usual forces measurement techniques. It is a low cost, handling friendly alternative.

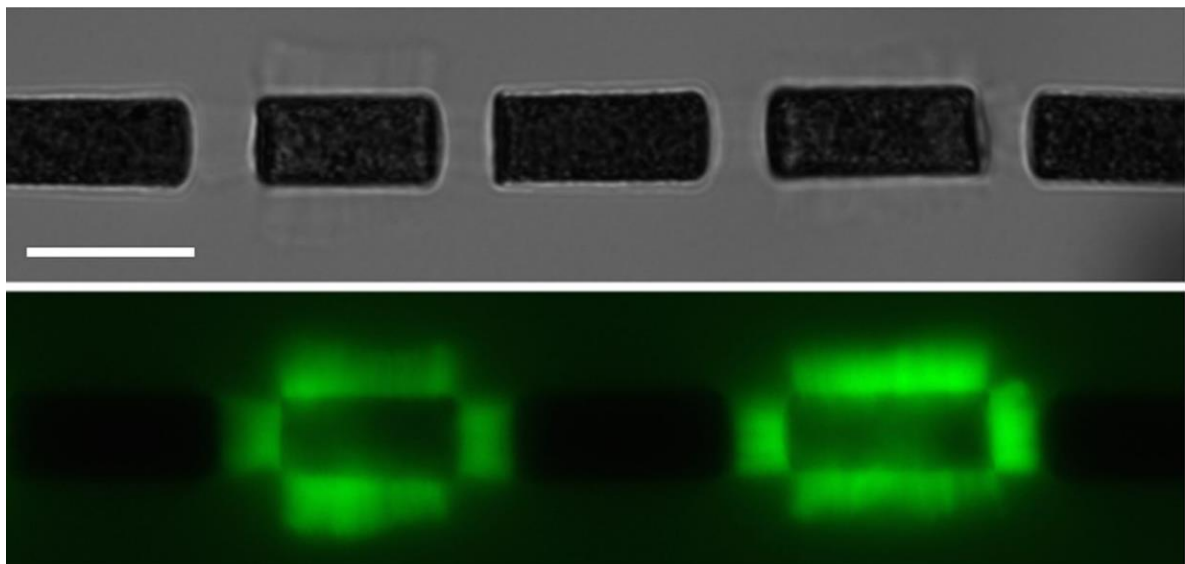


**Figure 15** Chain of magnetic cylinders (6 $\mu\text{m}$  in diameter) in an horizontal magnetic field. Top: Bright field image, bottom, Fluorescent image (actin is labelled). Actin networks have grown from cylinders covered by the activator of the polymerization for around 15 minutes. Non actin-covered cylinders have been passivated by BSA. The cylinders are seen from the side, the circular faces being perpendicular to the image. Scale bar 10  $\mu\text{m}$  (Bauër et al., 2017).

#### d) Functionalization

Functionalization of beads has always been a critical step to develop applications in separation, diagnostics and catalysis. The versatility in various functionalizations of magnetic beads is a great advantage. Nowadays, most of commonly used functions for biomolecular functionalization are available commercially (i.e. amino group, carboxylic acid, epoxy, tosyl, streptavidin, protein A and G, antibodies). These functions can be used to graft the ligands of interest at the beads surface. Some beads are directly functionalized with specific biomolecule, as shown in Figure 16 (Pamme, 2006a).

Micro-particles can be used for ion exchange separations based on a functionalization of the surface of the beads using weakly acidic (COOH), weakly (NH<sub>2</sub>) and strongly basic groups (N<sup>+</sup>(CH<sub>3</sub>)<sub>3</sub>). For separations based on affinity interactions, Microbeads coated with specific antibody, lectin, nucleic acid, protein, enzyme or biotin are usually involved (Horák et al., 2007).

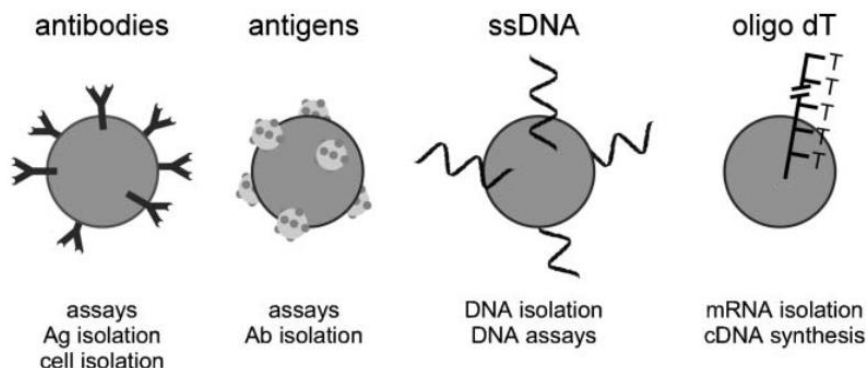


**Figure 16** Examples of surface functionalization for micro-particles (Pamme, 2006)

The functionalization of beads will not be developed in this manuscript as all of the beads functionalization have already been performed by commercial means or collaborators.

#### 4. Micrometric magnetic beads in microfluidic systems for extraction, pre-concentration and detection

### a) Analytical Challenge

There is a strong need for new technologies to tackle the challenge of trace analysis in various fields such as environment monitoring, food safety or biomedical analysis. Indeed, in current diagnosis (especially cancer diagnosis) new biomarkers (protein, DNA, cell) have emerged and are mostly present at very low concentrations in complex matrix. Similarly, in food safety, the presence of one pathogenic bacterium in food or water can be dramatic. In this context, Microfluidics is now considered as the technology of choice to meet this challenge. Droplet Microfluidics, for instance, has paved the way for circulating tumor DNA analysis (Pekin et al., 2011; Taly et al., 2013) as well as the emerging field of single cells analysis (Brouzes et al., 2009; Mazutis et al., 2013).

However, to address the question of trace analysis, we still need to improve the current technologies. The main bottleneck still remains the extraction and preconcentration of the targeted analytes. In the macro-world, this first step is often performed by solid phase extraction (SPE) through SPE columns that accommodate a few hundreds of milliliters. Being able to integrate this step in Microfluidics remains a challenge both in terms of performance and integration. Among the different approaches of microfluidic SPE, most of them rely on micrometric particles or monolith directly polymerized on chip (Svec, 2006). In section 2, we have described the different ways to manipulate microparticles on chip. The first approach for SPE on chip was mainly based on mechanical trapping. However, the issue of backpressure and the necessity to work with a homogeneous packing of beads were the main limitations to this solution.

Extraction and pre-concentration are also performed with magnetic microparticles. This type of methods is easy to integrate into the microfluidic workflow and it can even be combined with detection techniques. It has led to the development of portable platforms or devices that are fully automated to perform particularly immunoassay on chip (Ducrée et al., 2007; Pereiro et al., 2017; Sasso et al., 2012; Sista et al., 2008). Each step has to be integrated from sample collection and preparation to processing and analysis. To integrate these different steps, microfluidic devices have to integrate valves, mixers, pumps and sensors. In the next section, we will discuss sensors that can be combined to micro-beads processes.

To address new development in extraction, capture and immunoassay, we will describe devices involving magnetic beads for ultrasensitive detection.



## **b) Magnetic beads involved in extraction and detection**

Not only that magnetic beads can be used as a support for the capture but they are also used to enhance the detection signal. They are an ideal candidate for extraction of molecules of interest, with the possibility of full automation. A step of detection can be directly integrated inside the system, by taking advantage of the properties of magnetic beads.

For example, in the case of sandwich assay, beads are coated with an antibody or an aptamer (for their temperature stability, long shelf life and easy synthesis) to capture the antigen and a second antibody specific to the antigens is linked to an enzyme. The enzyme is further reacting with a substrate to produce fluorescence. Chang et al. presented a chip to produce all of the steps of an immunoassay on magnetic beads (Chang et al., 2015). Figure 17 presents the capture inside the microfluidic chip. Using several entrances that are organized around the main chamber, antigen, secondary antibody, enzyme and substrate are sequentially injected on the beads. All of the steps profited from the high surface to volume ratio due to the use of a suspension of beads. The fluorescence signal analysis is then monitored with a portable detection module (GloMaxs 20/20 Luminometer, Promega, USA). Araci et al. They developed a digital biological platform that is able to monitor fluids at picoliter volumes based on a density of 2000 micromanipulators/mm<sup>2</sup> such as mixing or compartmentalization valves (Araci et al., 2016). They used this device for single molecule detection and ELISA tests on magnetic beads like TNF- $\alpha$  immunoassay. They evaluated the LOD at 10 fM with the possibility to reach the sub-femtomolar and a background noise of 4%. Moreover, this platform could provide access to protein association dynamic with magnetic beads as the fluorescent signal provides an estimation of the number of proteins on a single bead.

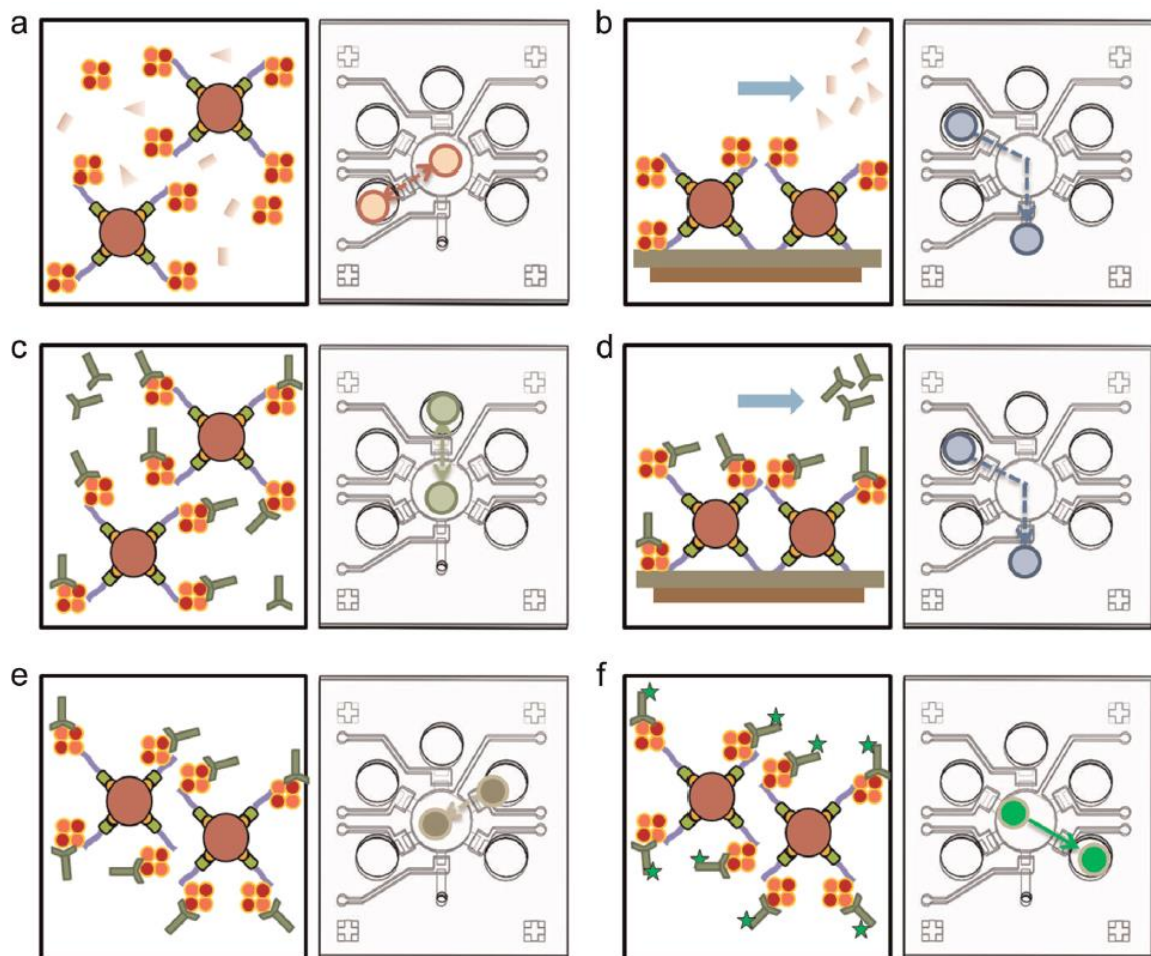


**Figure 17** Schematic representation of the different steps of the immunoassay in chip with the incubation of the blood sample (orange-red) with beads (pink circles) coated with specific aptamers (a) washing step in phosphate buffer where beads are immobilized by a permanent magnet (b) the binding of the secondary acridinium specific antibody (green Y) (c) another washing step is performed as the previous one (d) a solution of  $H_2O_2$  is injected in the main chamber and incubated (e) beads are transported and detection of the chemiluminescent signal is performed (f) (Chang et al., 2015)

Magnetic beads can also be used with redox labels or optical labels (Bange et al., 2005). This solution can be adapted to a high number of processes based on magnetic beads such as electrochemical immunosensor (D. Tang et al., 2008), chemiluminescent metal immunoassay (Aiping Fan et al., 2005), and magnetic sensor (S. G. Grancharov et al., 2005). Based on the same extraction principle as described above, Krause et al. performed an electrochemical analysis (Krause et al., 2015). The detection was not directly performed on the beads but through a process involving a function that was grafted on the surface of the bead. As described in Figure 18, the sandwich bioassay can be performed with primary

antibody on Ag/AgCl electrodes and beads linked to the secondary antibody. Those beads are also labeled by a ferrioxo HRP function that can be reduced by a solution of hydroquinone (HQ) and  $H_2O_2$ . Amperometric signals were recorded in the detection chamber in the presence of HQ and  $H_2O_2$ . HQ reduced ferrioxo HRP, and the signal measured the reduction of oxidized mediator (benzoquinone) on the electrodes (Figure 18 II c). The limits of detection were around tens of fg/mL (18 fg/mL for IL-6, 10 fg/mL for TNF- $\alpha$ , 15 fg/mL for CRP, and 40 fg/mL for IL-1 $\beta$ ). Such a system is portable, easy to integrate and allows the use for multiplexing.

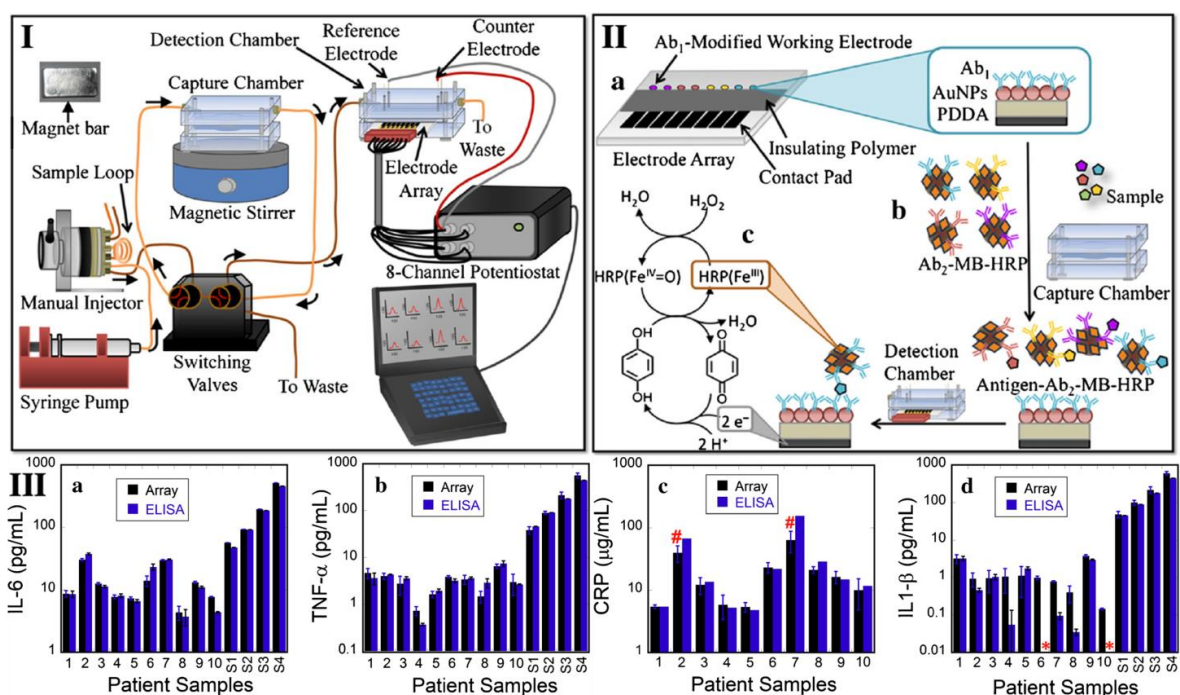


**Figure 18 (I) presentation of the modular microfluidic electrochemical immunoarray system (II) protocol of detection of proteins with (a) the electrodes coated with the primary antibody (b) the formation of the complex antigen and micro-beads inside the microfluidic chamber (c) quantitative detection by amperometric signal III immunoassay and ELISA assay results from serum samples of cancer patients for IL-6 (a), TNF- $\alpha$  (b), CRP(c) and IL-1 $\beta$  (d) (Krause et al., 2015)**

Properties of magnetic beads can be profited in the integration of the detection step inside the system that is used for extraction and pre-concentration. Therefore, magnetic beads appear as the ideal candidate for full automation of microfluidic trace analysis systems.

**c) Digital, plasmon resonance or photonic crystal enhanced detection**

Some systems of detection can be coupled to digital microfluidics. Digital microfluidics offers the possibility to integrate each step of the process. Advantages are vast: multistep protocol automatization, encapsulation of single cell/beads/particle, high throughput analysis, low processing time, high binding kinetic, and decrease of the limit of detection (Cretich et al., 2015; Serra et al., 2017)

This method can be coupled to substrate (Shim et al., 2013) or label (Zhao et al., 2011) detection with amplification of the signal, as every droplet can be measured. As shown on Figure 19, analog detection is dependent on the increase of intensity that is linked to the concentration of the sample, whereas digital measurement is only dependent on the signal and not in each droplet (Walt, 2013)

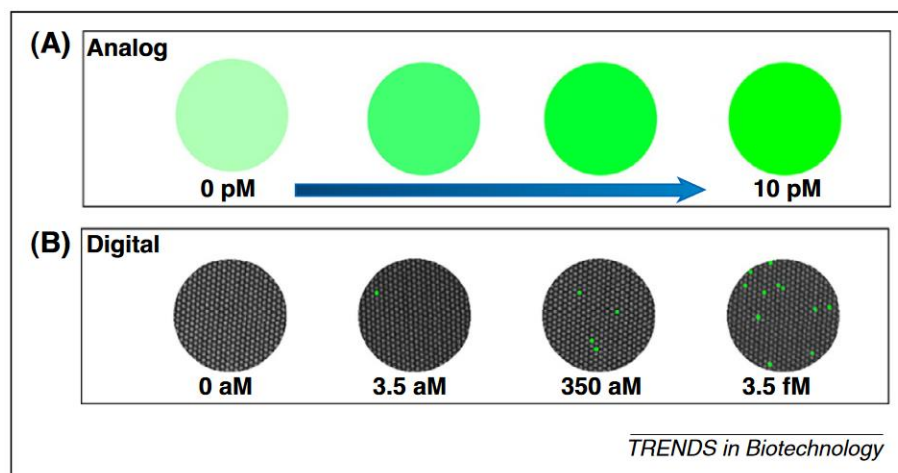


**Figure 19 Comparison between the analog and the digital detection (Walt, 2013)**

Particles detection could also be coupled to less usual systems of detection such as surface plasmon resonance microscopy. Halpern et al. adapted this technique to the detection of hybridization on DNA-functionalized particles as presented on Figure 20 A (Halpern et al., 2014). This method gave an access to real-time measurement of the absorption of the particle as shown on Figure 20 B.

Photonic crystal enhanced microscopy was also adapted to single particle detection (Zhuo et al., 2014). The operating principle was based on surface attachment detection through a shift of the photonic crystal resonant reflection as shown on Figure 20 C. This method could be adapted to dielectric and magnetic particles, without a restriction on their form or their functionalization. Distance between particles had to be at least 4  $\mu\text{m}$ . Hence, this solution could not have worked with too high concentration of particles.

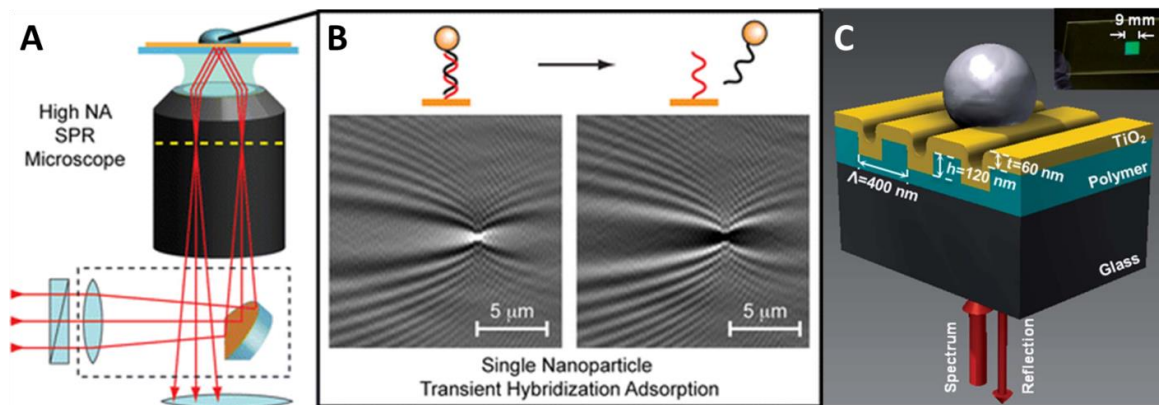


**Figure 20** A Schematic representation of the near-infrared, objective-coupled, high numerical aperture surface plasmon resonance microscope utilizing a knife-edge mirror B Schematic representation of the operating principal of photonic crystal enhanced microscopy with a nanoparticle attached to a photonic crystal and a picture of a glass cover slip made of photonic crystal (Zhuo et al., 2014)

More exotic detections can be performed such as magneto-resistance (Megens and Prins, 2005) This type of micro-system put forth the versatility of detection with magnetic beads.

Microfluidic methods based on magnetic beads take advantage of the high surface/volume ratio in order to reach high performance and counter analytical challenges. Those systems can be easily coupled to detection methods and even directly on beads.

## 5. Conclusion

Microfluidics has already demonstrated its potential in order to perform analysis at small scale, low costs and with small amounts of reagents. In this context, the use of microparticles emerged as an interesting approach to further improve the surface to volume ratio for the enhancement of interactions between a solid surface and a volume of sample. Micro-particles offer a high surface-to-volume ratio to work, easy handling and high loading capacity. They can be used to tackle new challenges in trace analysis due to their simple integration into microfluidics systems. Several technics have been developed to automatize the movement of particles, based on mechanic, chemistry, optic, dielectrophoresis, acoustic, droplets, or magnetism. In this study, we chose to focus on magnetic beads, which present superparamagnetic properties. These beads can be easily handled with a magnetic field. In order to use them as immunosupport, their surface can be functionalized with bio-molecules. These properties make magnetic beads ideal in tackling new challenges of trace analysis. Furthermore, these magnetic beads can be involved in extraction and detection steps of protocols for measurements of low concentrations. Beads can either be the support of the production of signal, or be directly used for recognition and measure.

In the following section, I will introduce a new technology, the microfluidic fluidized bed, that has been recently pioneered by our team. This technology allows the performance of an on chip solid phase extraction at moderate flow rate coupled with high capture efficiency. During my PhD project, I have designed and characterized a new generation of fluidized bed that is able to accommodate higher flow rate and thus, able to analyze larger sample volume in given analysis time. Developing this new generation of fluidized bed has also proven new challenges especially regarding the homogenization of the beads inside the fluidized bed. In particular, as they will be described in the following chapters, different approaches either passive or active will be discussed. In the second part of the manuscript, bioanalytical applications of the microfluidic fluidized will be presented. The first one deals with bacteria capture and detection, while the two last chapters reports on the use of this bed for molecules capture.



## Bibliography

- Ahmed, D., Ozcelik, A., Bojanala, N., Nama, N., Upadhyay, A., Chen, Y., Hanna-Rose, W., and Huang, T.J. (2016). Rotational manipulation of single cells and organisms using acoustic waves. *Nat. Commun.* 7, 11085.
- Aiping Fan, Choiwan Lau, and Lu\*, J. (2005). Magnetic Bead-Based Chemiluminescent Metal Immunoassay with a Colloidal Gold Label.
- Andersson, H., van der Wijngaart, W., Enoksson, P., and Stemme, G. (2000). Micromachined flow-through filter-chamber for chemical reactions on beads. *Sens. Actuators B Chem.* 67, 203–208.
- Andersson, H., Jönsson, C., Moberg, C., and Stemme, G. (2001). Patterned self-assembled beads in silicon channels. *ELECTROPHORESIS* 22, 3876–3882.
- Araci, I.E., Robles, M., and Quake, S.R. (2016). A reusable microfluidic device provides continuous measurement capability and improves the detection limit of digital biology. *Lab. Chip* 16, 1573–1578.
- Arai, F., Ng, C., Maruyama, H., Ichikawa, A., El-Shimy, H., and Fukuda, T. (2005). On chip single-cell separation and immobilization using optical tweezers and thermosensitive hydrogel. *Lab. Chip* 5, 1399–1403.
- Asbury, C.L., Diercks, A.H., and Engh, G. van den (2002). Trapping of DNA by dielectrophoresis. *ELECTROPHORESIS* 23, 2658–2666.
- Ashkin, A. (1970). Acceleration and Trapping of Particles by Radiation Pressure. *Phys. Rev. Lett.* 24, 156–159.
- Ashkin, A., Dziedzic, J.M., and Yamane, T. (1987). Optical trapping and manipulation of single cells using infrared laser beams. *Nature* 330, 769–771.
- Auerswald, J., and Knapp, H.F. (2003). Quantitative assessment of dielectrophoresis as a micro fluidic retention and separation technique for beads and human blood erythrocytes. *Microelectron. Eng.* 67–68, 879–886.
- Bange, A., Halsall, H.B., and Heineman, W.R. (2005). Microfluidic immunosensor systems. *Biosens. Bioelectron.* 20, 2488–2503.
- Bauër, P., Tavecchi, J., Pujol, T., Planade, J., Heuvingh, J., and Roure, O. du (2017). A new method to measure mechanics and dynamic assembly of branched actin networks. *Sci. Rep.* 7, 15688.
- Berthelot, J., Aćimović, S.S., Juan, M.L., Kreuzer, M.P., Renger, J., and Quidant, R. (2014). Three-dimensional manipulation with scanning near-field optical nanotweezers. *Nat. Nanotechnol.* 9, 295–299.
- Brouzes, E., Medkova, M., Savenelli, N., Marran, D., Twardowski, M., Hutchison, J.B., Rothberg, J.M., Link, D.R., Perrimon, N., and Samuels, M.L. (2009). Droplet microfluidic technology for single-cell high-throughput screening. *Proc. Natl. Acad. Sci.* 106, 14195–14200.
- Brown, A.P., Betts, W.B., Harrison, A.B., and O'Neill, J.G. (1999). Evaluation of a dielectrophoretic bacterial counting technique. *Biosens. Bioelectron.* 14, 341–351.

Burger, R., Kurzbuch, D., Gorkin, R., Kijanka, G., Glynn, M., McDonagh, C., and Ducreé, J. (2014). An integrated centrifugo-opto-microfluidic platform for arraying, analysis, identification and manipulation of individual cells. *Lab. Chip* 15, 378–381.

Çetin, B., and Li, D. (2011). Dielectrophoresis in microfluidics technology. *ELECTROPHORESIS* 32, 2410–2427.

Chang, K.-W., Li, J., Yang, C.-H., Shiesh, S.-C., and Lee, G.-B. (2015). An integrated microfluidic system for measurement of glycosylated hemoglobin levels by using an aptamer–antibody assay on magnetic beads. *Biosens. Bioelectron.* 68, 397–403.

Chen, X., Shojaei-Zadeh, S., Gilchrist, M.L., and Maldarelli, C. (2013). A lipobead microarray assembled by particle entrapment in a microfluidic obstacle course and used for the display of cell membrane receptors. *Lab. Chip* 13, 3041–3060.

Coq, N., Bricard, A., Delapierre, F.-D., Malaquin, L., du Roure, O., Fermigier, M., and Bartolo, D. (2011). Collective Beating of Artificial Microcilia. *Phys. Rev. Lett.* 107.

Cretich, M., Daaboul, G.G., Sola, L., Ünlü, M.S., and Chiari, M. (2015). Digital detection of biomarkers assisted by nanoparticles: application to diagnostics. *Trends Biotechnol.* 33, 343–351.

Delapierre, F.-D., Mottet, G., Taniga, V., Boisselier, J., Viovy, J.-L., and Laurent Malaquin (2017). High throughput micropatterning of interspersed cell arrays using capillary assembly. *Biofabrication* 9, 015015.

Demircan, Y., Özgür, E., and Külah, H. Dielectrophoresis: Applications and future outlook in point of care. *ELECTROPHORESIS* 34, 1008–1027.

Deng, T., Prentiss, M., and Whitesides, G.M. (2002). Fabrication of magnetic microfiltration systems using soft lithography. *Appl. Phys. Lett.* 80, 461–463.

Derks, R.J.S., Dietzel, A., Wimberger-Friedl, R., and Prins, M.W.J. (2007). Magnetic bead manipulation in a sub-microliter fluid volume applicable for biosensing. *Microfluid. Nanofluidics* 3, 141–149.

Destgeer, G., and Sung, H.J. (2015). Recent advances in microfluidic actuation and micro-object manipulation via surface acoustic waves. *Lab. Chip* 15, 2722–2738.

Destgeer, G., Lee, K.H., Jung, J.H., Alazzam, A., and Sung, H.J. (2013). Continuous separation of particles in a PDMS microfluidic channel via travelling surface acoustic waves (TSAW). *Lab. Chip* 13, 4210–4216.

Di Carlo, D., Aghdam, N., and Lee, L.P. (2006). Single-Cell Enzyme Concentrations, Kinetics, and Inhibition Analysis Using High-Density Hydrodynamic Cell Isolation Arrays. *Anal. Chem.* 78, 4925–4930.

Dianping Tang, Ruo Yuan, \* and, and Chai, Y. (2008). Ultrasensitive Electrochemical Immunosensor for Clinical Immunoassay Using Thionine-Doped Magnetic Gold Nanospheres as Labels and Horseradish Peroxidase as Enhancer.

Doyle, P.S., Bibette, J., Bancaud, A., and Viovy, J.-L. (2002). Self-Assembled Magnetic Matrices for DNA Separation Chips. *Science* 295, 2237–2237.



- Ducrée, J., Haeberle, S., Lutz, S., Pausch, S., Stetten, F. von, and Zengerle, R. (2007). The centrifugal microfluidic Bio-Disk platform. *J. Micromechanics Microengineering* 17, S103.
- Duffy, D.C., McDonald, J.C., Schueller, O.J., and Whitesides, G.M. (1998). Rapid Prototyping of Microfluidic Systems in Poly(dimethylsiloxane). *Anal. Chem.* 70, 4974–4984.
- Dürr, M., Kentsch, J., Müller, T., Schnelle, T., and Stelzle, M. (2003). Microdevices for manipulation and accumulation of micro- and nanoparticles by dielectrophoresis. *ELECTROPHORESIS* 24, 722–731.
- Fan, L.-S., Tai, Y.-C., and Muller, R.S. (1989). IC-processed electrostatic micromotors. *Sens. Actuators* 20, 41–47.
- Feynman, R.P. (1960). There's Plenty of Room at the Bottom. *Eng. Sci.* 23:5, 13.
- Fonnum, G., Johansson, C., Molteberg, A., Mørup, S., and Aksnes, E. (2005). Characterisation of Dynabeads® by magnetization measurements and Mössbauer spectroscopy. *J. Magn. Magn. Mater.* 293, 41–47.
- Frénéa, M., Faure, S.P., Le Pioufle, B., Coquet, P., and Fujita, H. (2003). Positioning living cells on a high-density electrode array by negative dielectrophoresis. *Mater. Sci. Eng. C* 23, 597–603.
- Fu, Z., Shao, G., Wang, J., Lu, D., Wang, W., and Lin, Y. (2011). Microfabricated Renewable Beads-Trapping/Releasing Flow Cell for Rapid Antigen–Antibody Reaction in Chemiluminescent Immunoassay. *Anal. Chem.* 83, 2685–2690.
- Gawad, S., Holmes, D., Benazzi, G., Renaud, P., and Morgan, H. (2010). Impedance Spectroscopy and Optical Analysis of Single Biological Cells and Organisms in Microsystems. In *Microengineering in Biotechnology*, (Humana Press, Totowa, NJ), pp. 149–182.
- Ghosh, A., and Fischer, P. (2009). Controlled Propulsion of Artificial Magnetic Nanostructured Propellers. *Nano Lett.* 9, 2243–2245.
- Gijs, M.A.M. (2004). Magnetic bead handling on-chip: new opportunities for analytical applications. *Microfluid. Nanofluidics* 1, 22–40.
- Grier, D.G. (2003). A revolution in optical manipulation.
- Guo, S.S., Zuo, C.C., Huang, W.H., Peroz, C., and Chen, Y. (2006). Response of super-paramagnetic beads in microfluidic devices with integrated magnetic micro-columns. *Microelectron. Eng.* 83, 1655–1659.
- Halpern, A.R., Wood, J.B., Wang, Y., and Corn, R.M. (2014). Single-Nanoparticle Near-Infrared Surface Plasmon Resonance Microscopy for Real-Time Measurements of DNA Hybridization Adsorption. *ACS Nano* 8, 1022–1030.
- Han, S.W., Jang, E., and Koh, W.-G. (2015). Microfluidic-based multiplex immunoassay system integrated with an array of QD-encoded microbeads. *Sens. Actuators B Chem.* 209, 242–251.
- Hansen, F.K., Ofstad, E.B., and Ugelstad, J. (1976). 1 - Emulsification of Styrene with Mixtures of Anionic Emulsifier and Long-Chain Fatty Alcohols. *Emulsion Polymerization with*

Initiation in Monomer Droplets. In *Theory and Practice of Emulsion Technology*, A.L. Smith, ed. (Academic Press), pp. 13–21.

Haukanes, B.-I., and Kvam, C. (1993). Application of Magnetic Beads in Bioassays. *Nat. Biotechnol.* *11*, 60–63.

Horák, D., Babič, M., Macková, H., and Beneš, M.J. (2007). Preparation and properties of magnetic nano- and microsized particles for biological and environmental separations. *J. Sep. Sci.* *30*, 1751–1772.

Huang, Y., Yang, J.M., Hopkins, P.J., Kassegne, S., Tirado, M., Forster, A.H., and Reese, H. (2003). Separation of Simulants of Biological Warfare Agents from Blood by a Miniaturized Dielectrophoresis Device. *Biomed. Microdevices* *5*, 217–225.

Jung, and Kwak, H.-Y. (2007). Separation of Microparticles and Biological Cells Inside an Evaporating Droplet Using Dielectrophoresis. *Anal. Chem.* *79*, 5087–5092.

Kim, Y.-J., Kim, S.H., Fujii, T., and Matsunaga, Y.T. (2016). Dual stimuli-responsive smart beads that allow “on-off” manipulation of cancer cells. *Biomater. Sci.* *4*, 953–957.

Koh, Y., Yang, J.-K., Oh, M.-H., Kang, H., Lee, Y.-S., and Kim, Y.-K. (2017). Nanoslit-concentration-chip integrated microbead-based protein assay system for sensitive and quantitative detection. *RSC Adv.* *7*, 29679–29685.

Krause, C.E., Otieno, B.A., Bishop, G.W., Phadke, G., Choquette, L., Lalla, R.V., Peterson, D.E., and Rusling, J.F. (2015). Ultrasensitive microfluidic array for serum pro-inflammatory cytokines and C-reactive protein to assess oral mucositis risk in cancer patients. *Anal. Bioanal. Chem.* *407*, 7239–7243.

Lata, J.P., Guo, F., Guo, J., Huang, P.-H., Yang, J., and Huang, T.J. (2016). Surface Acoustic Waves Grant Superior Spatial Control of Cells Embedded in Hydrogel Fibers. *Adv. Mater.* *28*, 8632–8638.

Laurell, T., and Lenshof, A. (2014). *Microscale Acoustofluidics*.

Laurell, T., Petersson, F., and Nilsson, A. (2007). Chip integrated strategies for acoustic separation and manipulation of cells and particles. *Chem. Soc. Rev.* *36*, 492–506.

Laurent, V.M., Hénon, S., Planus, E., Fodil, R., Balland, M., Isabey, D., and Gallet, F. (2002). Assessment of Mechanical Properties of Adherent Living Cells by Bead Micromanipulation: Comparison of Magnetic Twisting Cytometry vs Optical Tweezers. *J. Biomech. Eng.* *124*, 408–421.

Lee, J., Kim, O., Jung, J., Na, K., Heo, P., and Hyun, J. (2009). Simple fabrication of a smart microarray of polystyrene microbeads for immunoassay. *Colloids Surf. B Biointerfaces* *72*, 173–180.

Li, Y.-H., Su, T.-Y., Chang, T.-L., and Lee, Y.-W. (2016). Manipulating mimicked magnetosome chains produced Using superparamagnetic microbeads in a confined space. *Microelectron. Eng.* *153*, 37–42.

Lin, H.-C., Li, Y.-H., and Chen, C.-Y. (2014). Structural instability of an oscillating superparamagnetic micro-bead chain. *Microfluid. Nanofluidics* *17*, 73–84.

Malaquin, L., Kraus, T., Schmid, H., Delamarche, E., and Wolf, H. (2007). Controlled Particle Placement through Convective and Capillary Assembly. *Langmuir* 23, 11513–11521.

Manz, A., Harrison, D.J., Verpoorte, E., and Widmer, H.M. (1993). Planar chips technology for miniaturization of separation systems: a developing perspective in chemical monitoring. *Adv. Chromatogr.* 33, 1–66.

Martinez-Pedrero, F., and Tierno, P. (2015). Magnetic Propulsion of Self-Assembled Colloidal Carpets: Efficient Cargo Transport via a Conveyor-Belt Effect. *Phys. Rev. Appl.* 3, 051003.

Matijević, E., and Borkovec, M. (2004). *Surface and Colloid Science* (Boston, MA: Springer US).

Mazutis, L., Gilbert, J., Ung, W.L., Weitz, D.A., Griffiths, A.D., and Heyman, J.A. (2013). Single-cell analysis and sorting using droplet-based microfluidics. *Nat. Protoc.* 8, 870–891.

Megens, M., and Prins, M. (2005). Magnetic biochips: a new option for sensitive diagnostics. *J. Magn. Mater.* 293, 702–708.

Menad, S., Franqueville, L., Haddour, N., Buret, F., and Frenea-Robin, M. (2015). nDEP-driven cell patterning and bottom-up construction of cell aggregates using a new bioelectronic chip. *Acta Biomater.* 17, 107–114.

Morimoto, Y., Abe, M., Hatakayama, M., Handa, H., and Sandhu, A. (2009). Detection of Magnetic Nanobeads by Self-Assembly of Superparamagnetic Microbeads for Biosensing. *IEEE Trans. Magn.* 45, 2871–2874.

Neuman, K.C., and Nagy, A. (2008). Single-molecule force spectroscopy: optical tweezers, magnetic tweezers and atomic force microscopy. *Nat. Methods* 5, 491–505.

Nilsson, A., Petersson, F., Jönsson, H., and Laurell, T. (2004). Acoustic control of suspended particles in micro fluidic chips. *Lab. Chip* 4, 131–135.

Nilsson, J., Evander, M., Hammarström, B., and Laurell, T. (2009). Review of cell and particle trapping in microfluidic systems. *Anal. Chim. Acta* 649, 141–157.

Olsvik, O., Popovic, T., Skjerve, E., Cudjoe, K.S., Hornes, E., Ugelstad, J., and Uhlén, M. (1994). Magnetic separation techniques in diagnostic microbiology. *Clin. Microbiol. Rev.* 7, 43–54.

Osman, O., Toru, S., Dumas-Bouchiat, F., Dempsey, N.M., Haddour, N., Zanini, L.-F., Buret, F., Reyne, G., and Frénéa-Robin, M. (2013). Microfluidic immunomagnetic cell separation using integrated permanent micromagnets. *Biomicrofluidics* 7, 054115.

Ozaki, M. (2004). Magnetic Particles: Preparation, Properties, and Applications. In *Surface and Colloid Science*, (Springer, Boston, MA), pp. 1–26.

Pamme, N. (2006a). Magnetism and microfluidics. *Lab. Chip* 6, 24–38.

Pamme, N. (2006b). Magnetism and microfluidics. *Lab. Chip* 6, 24–38.

Pekin, D., Skhiri, Y., Baret, J.-C., Le Corre, D., Mazutis, L., Salem, C.B., Millot, F., El Harrak, A., Hutchison, J.B., and Larson, J.W. (2011). Quantitative and sensitive detection of rare mutations using droplet-based microfluidics. *Lab. Chip* 11, 2156–2166.

Pereiro, I., Bendali, A., Tabnaoui, S., Alexandre, L., Srbova, J., Bilkova, Z., Deegan, S., Joshi, L., Viovy, J.-L., Malaquin, L., et al. (2017). A new microfluidic approach for the one-step capture, amplification and label-free quantification of bacteria from raw samples. *Chem. Sci.* *8*, 1329–1336.

Petersson, F., Åberg, L., Swärd-Nilsson, A.-M., and Laurell, T. (2007). Free Flow Acoustophoresis: Microfluidic-Based Mode of Particle and Cell Separation. *Anal. Chem.* *79*, 5117–5123.

Pethig, R., and Markx, G.H. (1997). Applications of dielectrophoresis in biotechnology. *Trends Biotechnol.* *15*, 426–432.

Peyman, S.A., Iles, A., and Pamme, N. (2009). Mobile magnetic particles as solid-supports for rapid surface-based bioanalysis in continuous flow. *Lab. Chip* *9*, 3110–3117.

Rodrigo, P.J., Eriksen, R.L., Daria, V.R., and Glückstad, J. (2002). Interactive light-driven and parallel manipulation of inhomogeneous particles. *Opt. Express* *10*, 1550–1556.

Ruffert, C. (2016). Magnetic Bead—Magic Bullet. *Micromachines* *7*, 21.

Sæthre, B., Mørk, P.C., and Ugelstad, J. (1995). Preparation of poly(vinyl chloride) latexes by polymerization of stabilized monomer droplets. *J. Polym. Sci. Part Polym. Chem.* *33*, 2951–2959.

Sasso, L.A., Johnston, I.H., Zheng, M., Gupte, R.K., Ündar, A., and Zahn, J.D. (2012). Automated microfluidic processing platform for multiplexed magnetic bead immunoassays. *Microfluid. Nanofluidics* *13*, 603–612.

Sato, K., Tokeshi, M., Odake, T., Kimura, H., Ooi, T., Nakao, M., and Kitamori, T. (2000). Integration of an Immunosorbent Assay System: Analysis of Secretory Human Immunoglobulin A on Polystyrene Beads in a Microchip. *Anal. Chem.* *72*, 1144–1147.

Schnelle, T., Müller, T., Fiedler, S., Shirley, S.G., Ludwig, K., Herrmann, A., Fuhr, G., Wagner, B., and Zimmermann, U. (1996). Trapping of viruses in high-frequency electric field cages. *Naturwissenschaften* *83*, 172–176.

Serra, M., Ferraro, D., Pereiro, I., Viovy, J.-L., and Descroix, S. (2017). The power of solid supports in multiphase and droplet-based microfluidics: towards clinical applications. *Lab. Chip* *17*, 3979–3999.

Shim, J., Ranasinghe, R.T., Smith, C.A., Ibrahim, S.M., Hollfelder, F., Huck, W.T.S., Klenerman, D., and Abell, C. (2013). Ultrarapid Generation of Femtoliter Microfluidic Droplets for Single-Molecule-Counting Immunoassays. *ACS Nano* *7*, 5955–5964.

Singh, H., Laibinis, P.E., and Hatton, T.A. (2005). Rigid, Superparamagnetic Chains of Permanently Linked Beads Coated with Magnetic Nanoparticles. Synthesis and Rotational Dynamics under Applied Magnetic Fields. *Langmuir* *21*, 11500–11509.

Sista, R., Hua, Z., Thwar, P., Sudarsan, A., Srinivasan, V., Eckhardt, A., Pollack, M., and Pamula, V. (2008). Development of a digital microfluidic platform for point of care testing. *Lab. Chip* *8*, 2091–2104.

Smith, S.B., Cui, Y., and Bustamante, C. (1996). Overstretching B-DNA: The Elastic Response of Individual Double-Stranded and Single-Stranded DNA Molecules. *Science* 271, 795–799.

Squires, T.M., Messinger, R.J., and Manalis, S.R. (2008). Making it stick: convection, reaction and diffusion in surface-based biosensors. *Nat. Biotechnol.* 26, 417–426.

Stephanie G. Grancharov, †, Hao Zeng, †, Shouheng Sun, †, Shan X. Wang, §, Stephen O'Brien, ‡, C. B. Murray, †, J. R. Kirtley, † and, and G. A. Held\*, † (2005). Bio-functionalization of Monodisperse Magnetic Nanoparticles and Their Use as Biomolecular Labels in a Magnetic Tunnel Junction Based Sensor.

Stone, H.A., Stroock, A.D., and Ajdari, A. (2004). Engineering Flows in Small Devices: Microfluidics Toward a Lab-on-a-Chip. *Annu. Rev. Fluid Mech.* 36, 381–411.

Svec, F. (2006). Less common applications of monoliths: Preconcentration and solid-phase extraction. *J. Chromatogr. B* 841, 52–64.

Tabeling, P. (2005). *Introduction to Microfluidics* (OUP Oxford).

Tabnaoui, S. (2012). Magnetic fluidized bed for sample preconcentration and immunoextraction in microfluidic systems (Paris 6).

Taly, V., Pekin, D., Benhaim, L., Kotsopoulos, S.K., Le Corre, D., Li, X., Atochin, I., Link, D.R., Griffiths, A.D., and Pallier, K. (2013). Multiplex picodroplet digital PCR to detect KRAS mutations in circulating DNA from the plasma of colorectal cancer patients. *Clin. Chem. clinchem*–2013.

Tartaj, P., Morales, M. del P., Veintemillas-Verdaguer, S., González-Carreño, T., and Serna, C.J. (2003). The preparation of magnetic nanoparticles for applications in biomedicine. *J. Phys. Appl. Phys.* 36, R182.

Terry, S.C. (1975). A gas chromatography system fabricated on a silicon wafer using integrated circuit technology. PhD Thesis.

Teste, B., Kanoufi, F., Descroix, S., Poncet, P., Georgelin, T., Siaugue, J.-M., Petr, J., Varenne, A., and Hennion, M.-C. (2011a). Kinetic analyses and performance of a colloidal magnetic nanoparticle based immunoassay dedicated to allergy diagnosis. *Anal. Bioanal. Chem.* 400, 3395–3407.

Teste, B., Malloggi, F., Siaugue, J.-M., Varenne, A., Kanoufi, F., and Descroix, S. (2011b). Microchip integrating magnetic nanoparticles for allergy diagnosis. *Lab. Chip* 11, 4207–4213.

Thompson, J.A., and Bau, H.H. (2010). Microfluidic, bead-based assay: Theory and experiments. *J. Chromatogr. B* 878, 228–236.

Tirapu-Azpiroz, J., Temiz, Y., and Delamarque, E. (2015). Arraying single microbeads in microchannels using dielectrophoresis-assisted mechanical traps. *Appl. Phys. Lett.* 107, 204102.

Treleaven, J.G., Ugelstad, J., Philip, T., Gibson, F.M., Rembaum, A., Caine, G.D., and Kemshead, J.T. (1984). REMOVAL OF NEUROBLASTOMA CELLS FROM BONE MARROW WITH

MONOCLONAL ANTIBODIES CONJUGATED TO MAGNETIC MICROSPHERES. *The Lancet* *323*, 70–73.

Tsuboi, Y. (2016). Plasmonic optical tweezers: A long arm and a tight grip. *Nat. Nanotechnol.* *11*, 5–6.

Ugelstad, J., Söderberg, L., Berge, A., and Bergström, J. (1983). Monodisperse polymer particles — a step forward for chromatography.

Walt, D.R. (2013). Optical Methods for Single Molecule Detection and Analysis. *Anal. Chem.* *85*, 1258–1263.

Wang, X.-B., Huang, Y., Burt, J.P.H., Markx, G.H., and Pethig, R. (1993). Selective dielectrophoretic confinement of bioparticles in potential energy wells. *J. Phys. Appl. Phys.* *26*, 1278.

Wang, Y., Gao, Y., Wyss, H., Anderson, P., and den Toonder, J. (2013). Out of the cleanroom, self-assembled magnetic artificial cilia. *Lab. Chip* *13*, 3360.

Weddemann, A., Wittbracht, F., Auge, A., and Hütten, A. (2011). Particle flow control by induced dipolar interaction of superparamagnetic microbeads. *Microfluid. Nanofluidics* *10*, 459–463.

Wexler, J.S., Trinh, P.H., Berthet, H., Quennouz, N., Roure, O. du, Huppert, H.E., Lindner, A., and Stone, H.A. (2013). Bending of elastic fibres in viscous flows: the influence of confinement ‡. *J. Fluid Mech.* *720*, 517–544.

Yang, J., Huang, Y., Wang, X.-B., Becker, F.F., and Gascoyne, P.R.C. (1999a). Cell Separation on Microfabricated Electrodes Using Dielectrophoretic/Gravitational Field-Flow Fractionation. *Anal. Chem.* *71*, 911–918.

Yang, J., Huang, Y., Wang, X., Wang, X.-B., Becker, F.F., and Gascoyne, P.R.C. (1999b). Dielectric Properties of Human Leukocyte Subpopulations Determined by Electrorotation as a Cell Separation Criterion. *Biophys. J.* *76*, 3307–3314.

Yu, P., and Kornelsen, K. (2003). Bead trapping device.

Yu, C., Davey, M.H., Svec, F., and Fréchet, J.M.J. (2001). Monolithic Porous Polymer for On-Chip Solid-Phase Extraction and Preconcentration Prepared by Photoinitiated in Situ Polymerization within a Microfluidic Device. *Anal. Chem.* *73*, 5088–5096.

Zanini, L.F., Osman, O., Frenea-Robin, M., Haddour, N., Dempsey, N.M., Reyne, G., and Dumas-Bouchiat, F. (2012). Micromagnet structures for magnetic positioning and alignment. *J. Appl. Phys.* *111*, 07B312.

Zhang, C., Khoshmanesh, K., Mitchell, A., and Kalantar-zadeh, K. (2010). Dielectrophoresis for manipulation of micro/nano particles in microfluidic systems. *Anal. Bioanal. Chem.* *396*, 401–420.

Zhang, H., Fu, X., Liu, L., Zhu, Z., and Yang, K. (2012). Microfluidic bead-based enzymatic primer extension for single-nucleotide discrimination using quantum dots as labels. *Anal. Biochem.* *426*, 30–39.

Zhang, Y., Wei, F., Poh, Y.-C., Jia, Q., Chen, J., Chen, J., Luo, J., Yao, W., Zhou, W., Huang, W., et al. (2017). Interfacing 3D magnetic twisting cytometry with confocal fluorescence microscopy to image force responses in living cells. *Nat. Protoc.* *12*, 1437–1450.

Zhao, Y., Shum, H.C., Chen, H., Adams, L.L.A., Gu, Z., and Weitz, D.A. (2011). Microfluidic Generation of Multifunctional Quantum Dot Barcode Particles. *J. Am. Chem. Soc.* *133*, 8790–8793.

Zhuo, Y., Hu, H., Chen, W., Lu, M., Tian, L., Yu, H., Long, K.D., Chow, E., King, W.P., Singamaneni, S., et al. (2014). Single nanoparticle detection using photonic crystal enhanced microscopy. *Analyst* *139*, 1007–1015.

## Chapter 1

### The fluidized bed concept: from basic system to the new generation

#### 1. Fluidized bed: working principle

Fluidized beds are made of a moving fluid phase in a dense array of micro or macro particles in motion. The motivation of this structure is to enhance the interactions between the fluid and the solid phase to favor throughput as well as reaction kinetics. Fluidized bed systems are already widely used in industry. They are generally involved in processes requiring high exchange rates between a solid phase and a liquid or gas phase. Fluidized bed reactors are used in different fields such as biology or chemistry; they can be used for different applications: fluid catalytic cracking in petroleum refineries, combustion (Lyngfelt et al., 2001), heat or mass transfer, interface modification. For example, those systems are used as grain dryer in the agro-food industry, where the surface of contact is particularly important to favor efficient and fast treatments (Bayrock and Ingledew, 1997). Fluidized beds can also be used as bio or chemical reactors, developing interesting properties of mass or heat transfer (Wang et al., 2002). Among many other examples, the system of fluidized bed introduced in Figure 21 is used for layer-by-layer assembly of polymers, and creation of microcapsules (Richardson et al., 2014).

A fluidized bed is composed of a solid phase, made of particles, and a liquid or gas phase. The particles are dropped inside a large chamber. Because of gravity force, particles sediment in the chamber forming a dense and closely packed array also referred as compact bed. As shown in Figure 21, transition from the compacted regime to a fluidized regime is obtained with the liquid/gaseous phase flowing through the solid phase from the bottom,



dispersing the particles inside the chamber. Particles are subjected to a drag force and a buoyancy force created by the liquid/gas passing through. Equilibrium occurs between drag/buoyancy forces and gravity forces that tend to keep the particles inside the chamber. At low flow rate, the drag force applied is lower than the gravity, and the particles do not move. When this flow rate reaches a critical value named  $U_{MF}$ , particles are lifted by the flow and generate an area of granular phase in suspension. This area has a fixed volume and a surface that remains perpendicular to the gravity. It follows the same rules than a fluidic phase. When the flowrate increases, it hits a limit  $U_T$  where the drag force is higher than the gravity on particles, the phenomenon of fluidization become violent and the solid phase is drifted away. Those two critical values of flowrate can be evaluated theoretically using usual fluidic equations (Richardson and Zaki, 1954; Richardson et al., 2014).

Fluidization can thus be described as a steady state dynamic regime, where the mobile solid particles behave as a liquid phase.

The starting point to describe a pressure drop on a porous medium is the Darcy's law:

$$\frac{\Delta P}{L} = \frac{\mu}{k A} \frac{dU}{dt}$$

Equation 11

With  $\Delta P$  the pressure drop inside a chamber,  $L$  the length of the chamber,  $\mu$  the viscosity of the fluid,  $k$  the permeability of the fluidized bed,  $A$  the cross section of the chamber and  $\frac{dU}{dt}$  the flow velocity.

To describe particles assembly, Kozeny introduced a new way to write the permeability  $k$ . He introduced the notion of porosity  $\varepsilon$  and a constant  $K$  known as the Kozeny constant. The Kozeny-Carman equation is valid only for low Reynolds numbers.

$$\frac{\Delta P}{L} = \frac{\mu}{A} \frac{K (1 - \varepsilon)^2 S_V^2}{\varepsilon^2} \frac{dU}{dt} \text{ and } \varepsilon + C = 1$$

Equation 12

With  $C$  the volume fraction occupied by particles in the bed,  $S_V$  the specific surface area, defined as the specific area divided by the volume occupied. In case of spherical particles  $S_V = \frac{6}{d}$  with  $d$  the diameter of the sphere which leads to:

$$\frac{\Delta P}{L} = \frac{\mu}{A} \frac{36 K (1 - \varepsilon)^2}{\varepsilon^2 d^2} \frac{dU}{dt}$$

Equation 13

Those equations were written in case of laminar flow. A more complete description of the problem has been published by Ergun in 1952 (Ergun, 1952)

$$\frac{\Delta P}{L} = \frac{150 \mu (1 - \varepsilon)^2}{d^2 \varepsilon^2} \frac{dU}{dt} + \frac{1,75 \rho (1 - \varepsilon)}{d \varepsilon^2} |U| \frac{dU}{dt}$$

Equation 14

With  $\rho$  the density of the fluid. In case of laminar flow, the first term of the second part of the equation is dominant and leads back to the Kozeny-Carman equation.

To evaluate the minimal flow rate of fluidization  $U_{MF}$ , a balance has to be obtained between the pressure of the flow, the gravity forces and the buoyancy forces. This equilibrium can be described as follows:

$$A \Delta P = -g \rho_{fluid} V + g \rho_{part} V$$

Equation 15

With  $\rho_{fluid}$  the fluid density,  $\rho_{part}$  the density of particles and  $V$  the volume of particles. This volume can be calculated using the porosity  $V = (1 - \varepsilon)A L$  which leads to

$$\Delta P = g (\rho_{part} - \rho_{fluid})(1 - \varepsilon)L$$

Equation 16

Going back to Equation 13, the minimal flow rate of fluidization can be written:

$$U_{MF} = \frac{g}{\mu} \frac{\varepsilon^2}{(1 - \varepsilon)} \frac{d^2 A}{36 K} (\rho_{part} - \rho_{fluid})$$

Equation 17

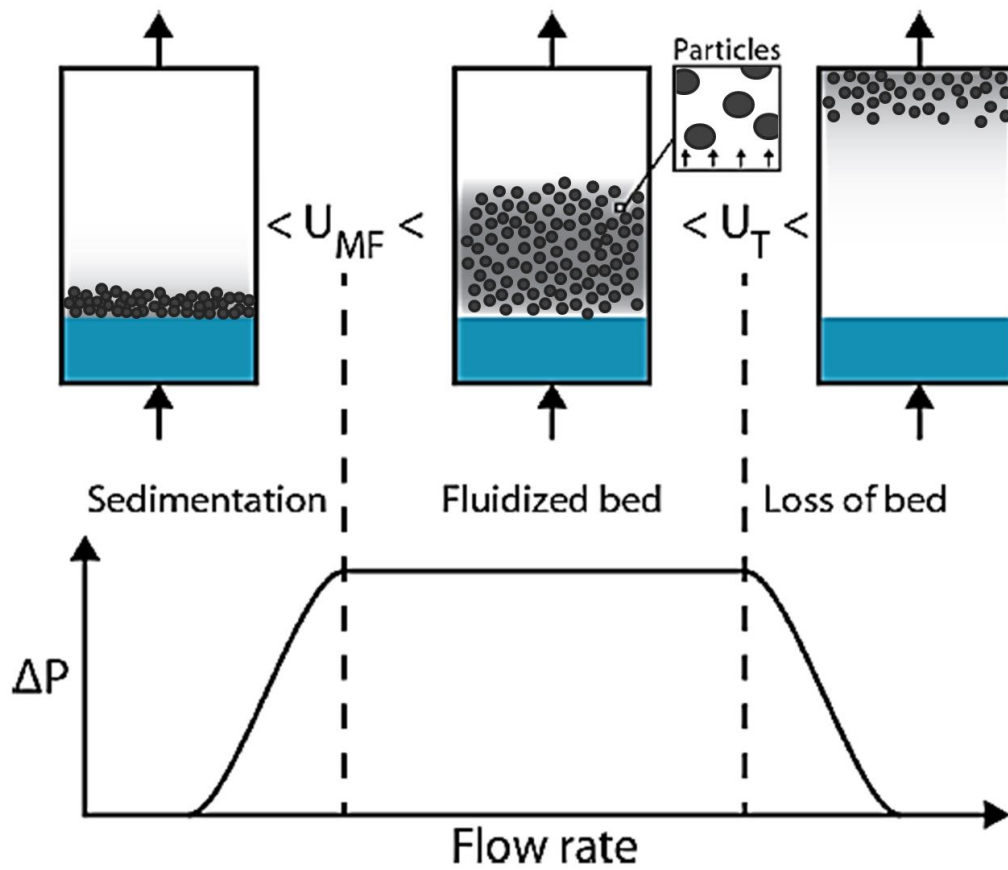


Figure 21 Illustration of different ranges of fluidization in a fluidized bed depending on the minimum fluidizing velocity ( $U_{MF}$ ) and the maximum velocity of a particle following Stokes equation ( $U_T$ ) (Richardson et al., 2014)

The maximum flowrate of fluidization  $U_T$  has been calculated for low Reynolds number by Kunii and al. (Kunii and Levenspiel, 2013)

$$U_T = \frac{g (\rho_{part} - \rho_{fluid}) d^2}{18 \mu}$$

Equation 18

Below  $U_{MF}$ , the bed is in the compact regime, meaning that the drag force is not enough to overcome gravity forces. In the contrary, above the  $U_T$  value, gravity forces are not enough to compensate the drag forces induced by the flow and a loss of particle is observed, leading to an instable regime. In between those two values of flow rate, the bed of particles reaches an intermediate steady state regime (fluidized regime) with an equilibrium between gravity and the drag/buoyancy forces.

The difference of density found in Equation 17 and Equation 18 and the mean particle size are two parameters used to classify different types of fluidization patterns. This classification is called the Geldart classification (Geldart, 1973). It aimed to divide fluidized beds in four groups with different particle density and recirculation patterns (tendencies to bubble, slugging, turbulences, channeling, spouting or stable fluidization as in Figure 22) (Siedlecki et al., 2011).

The configuration of fluidized beds allows to reach a high contact between the surface of the solid phase and the volume of the liquid/gaseous phase. This advantage is particularly useful to enhance reactions or interaction at the fluid/solid phase interface.

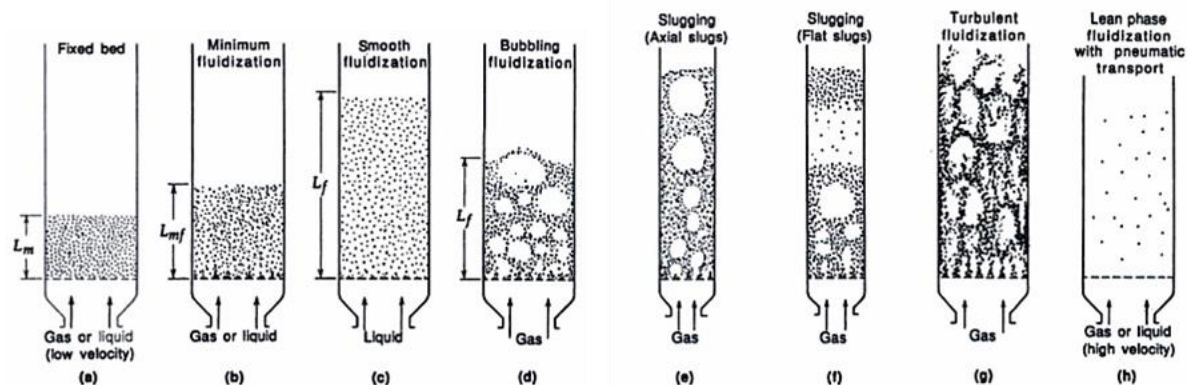


**Figure 22 A) Various forms of contacting of a batch of solids by fluid (Siedlecki et al., 2011) B) C. Geldart classification (Geldart, 1973)**

The system of fluidized bed has numerous other advantages. It provides a continuous mixing of the beads due to the recirculation of particles. Moreover, contrary to a compact bed, a fluidized bed offers a low back pressure and thus the possibility to work at high flow rates. Finally, it is compatible with complex matrices: the fluidized bed can deform itself to let bigger particles pass through, there is no clogging issue.

Development of the theory of the fluidized beds behavior has progressed over the years, and was adapted to different particles, different geometries of chambers. Therefore two different descriptions of fluidized bed have been developed (Gungor and Eskin, 2007):

- i. Eurlian models which rely on a continuous interpretation of phases and Navier Stokes equations

- ii. Lagrangian models are discrete particles modelisation. Newtonian equations of motion are solved for each particle on their interactions with gas

Both methods have led to several simulations of effects of particles in a fluidized state. But those situations are complex and difficult to model. Moreover, interactions between particles increase the complexity of the system (Rhodes et al., 2001). In this manuscript, we have preferred to develop an experimental approach to fluidization of particles related to the number of beads ( $10^6$ ) per chip and to the complexity of the evaluation of the forces. However, Comsol® simulations are used to support our assumptions.

Combining the concept of fluidized bed with microfluidics is a challenging question. The first question raising is the importance of surface forces at this scale (Zivkovic and Biggs, 2015; Zivkovic et al., 2013) and some attempts have been presented (surface coating) without any real solution, Moreover, working at small scale also changes the balance of forces applied on the particles and thus the fluidization regimes. The latter concern is addressed in the following section.

## **2. First generation of microfluidic magnetic fluidized bed**

### **a) Development of a fluidized bed at micro scale**

A first attempt to develop a miniaturized fluidized bed with glass beads inside a dry air was published in 2004 (Räsänen et al., 2004) with particles below 100  $\mu\text{m}$  diameter into a multi-chamber microscale fluid bed device. Those chambers had inner diameter from 20 mm to 100 mm. However, for the smallest particles, fluidization was difficult to reach. And even if this state was easier to reach in humid air, the fluidization was turbulent. This behavior is linked to strong interactions creating agglomerations between particles. They also demonstrated that computational methods are quite limited for fluidized beds at small scale, due to those inter-particles forces, along with particles size distributions, shape distributions and process conditions.

A newer paper published in 2013 reports on the development of a fluidized bed (Zivkovic et al., 2013) to enhance the importance of surface transfer. In this study, they compare two fluidized beds made either in polydimethylsiloxane (PDMS) or glass. The first one has a channel of 400 x 175  $\mu\text{m}$  with a computational fluid dynamics designed distributor. The second was a capillary of 200  $\mu\text{m}^2$  cross section. First observations showed that there are

strong interactions between glass particles and PDMS for experiments conducted in water. This problem disappeared in ethanol that could provide a stable fluidization regime. The parameter of this fluidization state were in good agreement with the results obtained by computation with Ergun equation and Richardson and Zaki law that link the velocity to the maximum velocity  $U_T$  (Richardson and Zaki, 1954).

$$U = C U_T \varepsilon^n$$

Equation 19

With C an empirical parameter and n an exponent determined at a value of 4.65 in their original work. These results showed that the set of equation established at the macro scale remains applicable in miniaturized devices.

Despite these first demonstrations and attempts to integrate fluidized bed in microfluidic devices none of these works could establish the conditions of stable fluidization in an aqueous liquid phase using particles below 10  $\mu\text{m}$  in diameter.

#### b) Miniaturization of the fluidized bed concept

The advantages to work with a fluidized bed (high contact, no clogging, low back pressure, continuous mixing) are quite interesting for a system at a smaller scale. MMBM team focused on the adaptation of the fluidized bed concept and mechanisms at the microscale. One of the biggest issues is related to the balance of forces that needs to be achieved to guarantee the bed stability for particles with diameters typically below 10 $\mu\text{m}$ .

The force due to the flow is the drag force. Using Stokes equation, this force can be formulated as following:

$$\vec{F}_d = 6 \pi \eta r \vec{v}$$

Equation 20

For beads with diameter of 1  $\mu\text{m}$  and a velocity of 1mm/s the drag force has an order of magnitude of  $10^{-11}$  N. In a usual fluidized bed, the drag force is balanced by the gravity. For a circular particle, the gravity force can be written:

$$\vec{F}_g = \frac{4}{3} \pi \rho r^3 \vec{g}$$

The order of magnitude of the gravitational force is  $10^{-15}$  N, which is found to be much lower than the corresponding drag force. Even if the equations describing the fluidized bed behavior remain applicable, gravity depends on the geometry with an order of magnitude of 3 whereas the drag force is linked to it with an order of 1. The stability of the fluidized bed is no longer ensured at the sub-millimeter scale with micrometric particles. At low scale, gravity is not enough to balance drag forces. In order to bypass this issue, superparamagnetic micro-particles have been used.

The team focused its attention to magnetic forces that were found to efficiently balance the drag force applied on the particles. As a matter of fact, magnetic forces applied on micrometric microbeads are evaluated at an order of magnitude of dozen of pN for a usual permanent magnet. In our case, the exact calculation is given in the paragraph e).

### c) Geometry of the chip

The first generation of fluidized bed has been developed by the two previous PhD candidates working on the subject. Sanae Tabnaoui elaborated a system of microbeads fluidized in a liquid. Her work was focused on the equilibrium of forces that could generate a suspension of beads inside a liquid. She relied on a previous work of magnetic beads trapped inside a straight channel. She designed the first chip of fluidized bed, and optimized the design (Tabnaoui, 2012). Iago Pereiro developed the design to promote the stability to the system and performed a careful characterization of the fluidized bed phase flow and operating conditions. He did and published (Pereiro et al., 2017) a full characterization of the system.

The microfluidic magnetic fluidized bed is made up of a large chamber of  $0.650 \mu\text{L}$  with diamond shape as shown in Figure 23. The height of the chamber is  $50 \mu\text{m}$ . A side of this chamber is connected to the input, and the diametrically opposed side is connected to the output. At the entrance an elbow channel of  $100 \mu\text{m}$  width has been designed to keep the beads inside the chamber when there is no flow. At the output, a channel of same width has been added to analyze the content of the sample. The particles in suspension inside the chamber are magnetic beads with typical diameter of  $2.8 \mu\text{m}$ . A NdFeB12 permanent magnet of 1.47 Tesla is positioned at 1.5 mm of the elbow entrance channel.

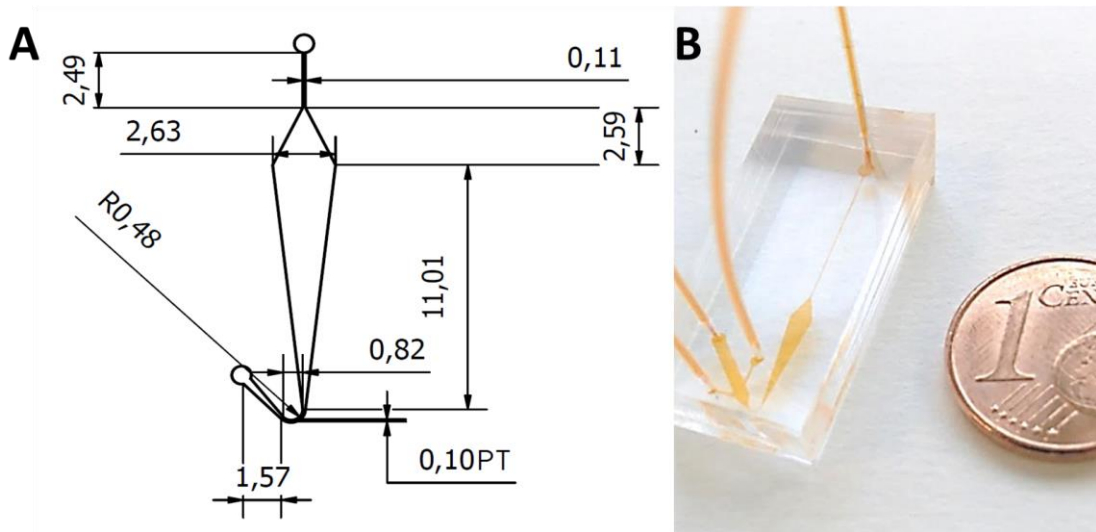


**Figure 23** A) *Blueprint of the fluidized bed chip* and B) *picture of the PDMS chip filled with an orange dye*

The flow of liquid crosses the chamber. The magnetic beads are then subjected to two forces: the drag force due to the liquid flowing through the chip and the magnetic force applied by the gradient of magnetic field. As the flow is oriented along the magnetic field direction, the enlargement of the bed chamber follows and compensates for the decay of the magnetic force occurring when particles get away from the bed inlet. At a certain distance from the inlet, the two forces applied on the magnetic beads balance themselves and promote the stability of the bed.



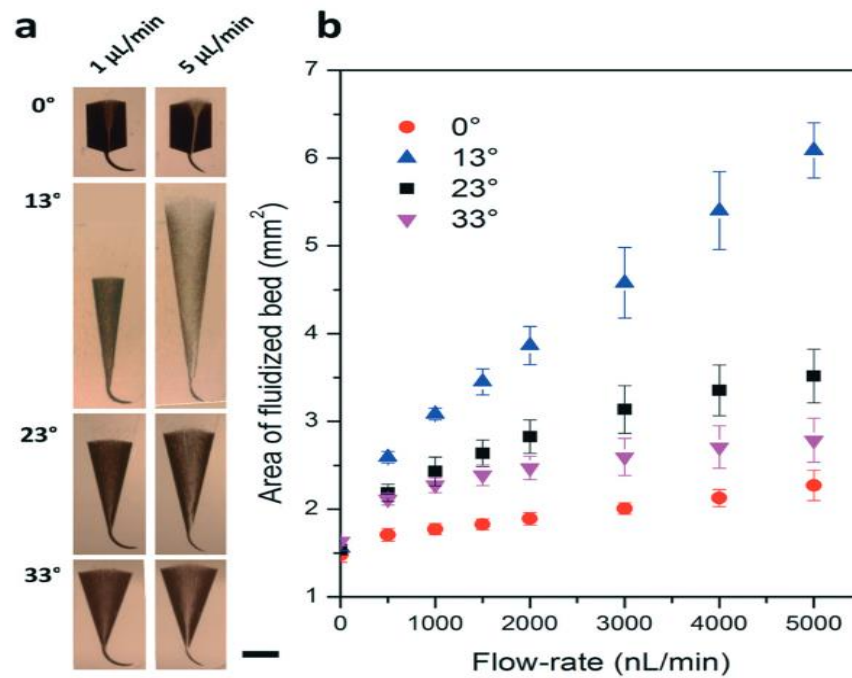


**Figure 24 ((a) Influence of chamber angle on fluidization behavior and (b) expansion as a function of imposed flow rate ( $n=3$ ). A chamber angle of  $13^\circ$  was seen to be optimal for the fluidization of a maximum of solid phase fraction (scale bar = 1 mm) (Pereiro et al., 2017)**

Moreover, the homogeneity of the spatial distribution of the beads figures prominently in the characteristics to optimize in the system. This aspect depends on both the magnetic field and the geometry of the chamber. An angle of  $13^\circ$  on the opening of the chamber has been experimentally optimized to avoid the creation of preferential pathways in the matrix of beads (Figure 24).

#### d) Operating regimes

When there is no flow, beads are only submitted to the magnetic force and are pulled back towards the chamber entrance. An elbow channel prevents them to go back to the inlet tubing. When the liquid pressure increases at the chamber entrance, the liquid is pushed through the packed bed. When the pressure is sufficiently high, the drag force exerted by the liquid flowing through the bed is enough to cause an expansion of the bed followed by a transition towards a fluidized regime. As we already described for macro scale systems, we can distinguish two working regimes: the packed bed and the fluidized bed.

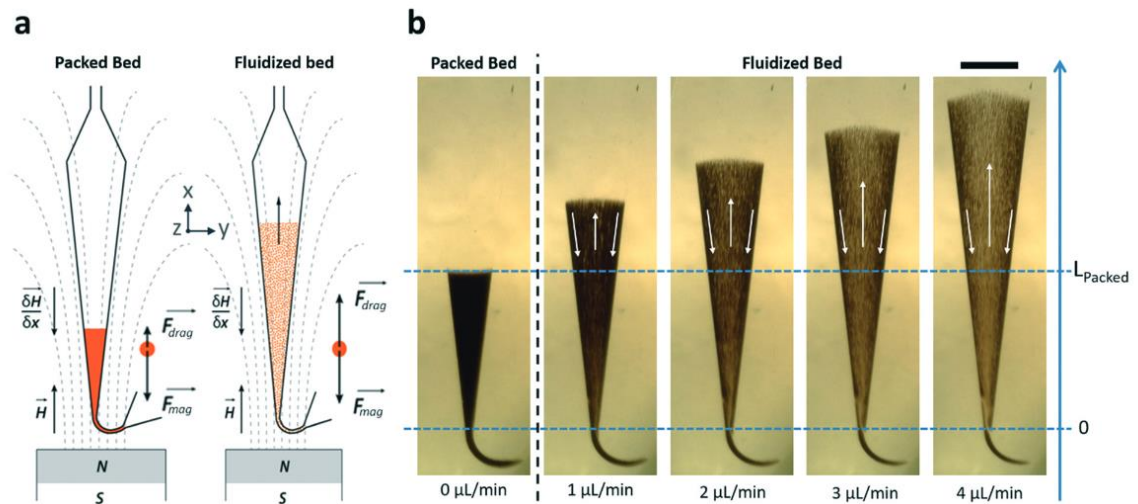


**Figure 25 (a) Schematic illustrations of the microfluidic fluidized bed for two working regimes: at low imposed pressure, particles are organized in a packed bed. Fluidization occurs when the pressure is sufficient to induce a fluid flow associated with drag forces that compensates for magnetic forces. Expansion of the bed volume occurs to maintain the equilibrium between drag and magnetic forces. (b) Images of the fluidized bed in the packed regime and fluidized for a series of flow rates (scale bar = 1mm) (Pereiro et al., 2017)**

The transition between the packed bed and the fluidized bed follows an hysteresis (Figure 26) as interactions between beads have to be broken before of complete fluidization of the matrix can appear. On this configuration, the packed bed shows a high hydrodynamic resistance, as an increase pressure of 10 mbar has to be applied to fluidize the bed. This point gives the pressure needed to reach the minimum velocity of fluidization  $U_{MF}$ , as shown on Figure 26 (Pereiro et al., 2017).

Once the interactions between particles are broken, and the bed works on a fluidized way. The back pressure of the system is defined as the difference of pressure needed to reach a fix flow rate between an empty system and a system with beads. This difference is quite low (around 10 mbar) as shown on Figure 26 a.

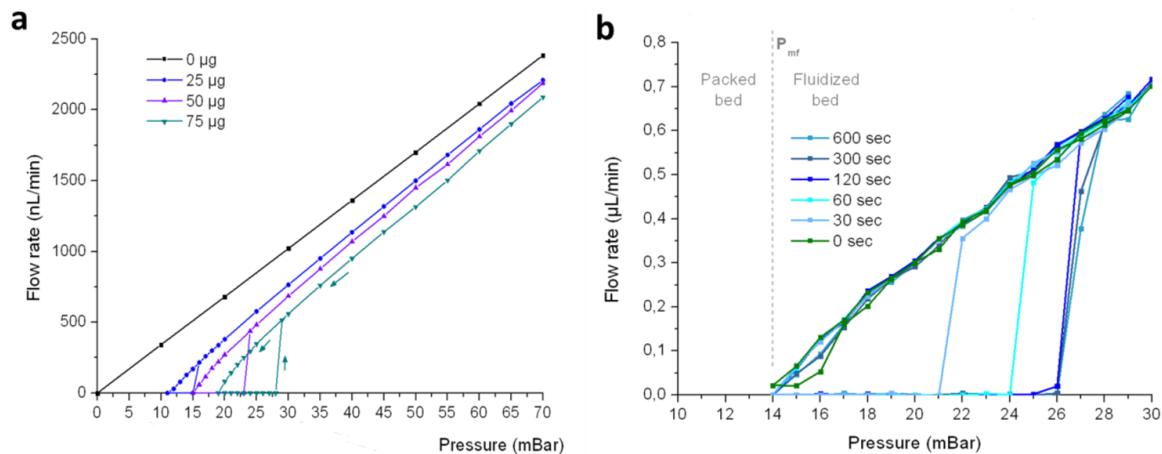


**Figure 26 a) Hydrodynamic pressure-flow-rate behavior of microfluidic magnetic fluidized bed for three different amounts of beads and for an empty chip. (b) Hysteresis observed for the effective fluidization pressure after different packing times (Pereiro et al., 2017)**

#### e) Magnetic interactions in the fluidized bed

In the fluidized bed experiments, superparamagnetic microbeads (Dynabeads, Thermofisher) were used. Experiments devoted to biological capture and analysis were usually done with Streptavidin coated Dynabeads M-280 with a diameter of 2.8 µm. Our calculations of the bead magnetization are based on the data provided by published results (Fonnum et al., 2005).

At magnetic fields higher than 0.15 Tesla, the magnetization of Dynabeads can be considered as constant. The magnetic moment applied on a superparamagnetic micro-particle is

$$\vec{m}_{part} = V_{part} \vec{M}_{part} = \frac{V_{part} \Delta\chi}{\mu_0} \vec{B}_{part}$$

Equation 22

Where  $\vec{m}_{part}$  is the magnetization of the particle,  $V_{part}$  the volume of the particle,  $\vec{M}_{part}$  the volumic magnetization,  $\Delta\chi$  the difference in magnetic susceptibilities between the particles and the media around,  $\mu_0$  the magnetic permeability in vacuum and  $\vec{B}_{part}$  the magnetic field of the particle.

As described in the introduction, the magnetization of the particle is saturated when placed in a sufficiently large magnetic field, so not varying in space ( $\nabla \vec{m}_{part} = 0$ ).

To create a force high enough to balance the drag force due to the flow of liquid passing through the particles, a permanent magnet (1.2 Tesla magnetic flux density) was positioned at 1.5 mm of the entrance channel. The magnetic force applied on the particles is given by:

$$\vec{F}_{mag} = \nabla(\vec{m}_{part} \cdot \vec{B}_{magnet}) = (\vec{m}_{part} \cdot \nabla) \vec{B}_{magnet}$$

Equation 23

Where  $\vec{m}_{part}$  is the magnetization of the particle and  $\vec{B}_{magnet}$  is the magnetic field applied by the magnet.

$$\vec{F}_{mag} = \frac{V_{part} \Delta\chi}{\mu_0} (\vec{B}_{magnet} \cdot \nabla) \vec{B}_{magnet}$$

Equation 24

The force created by the magnet is proportional to the gradient of the magnetic field. That's why it's important to know how is distributed the magnetic field in the microfluidic chamber. Simulations with Comsol Multiphysics© have given an idea of the repartition of magnetic field inside the chamber, and the magnetic force applied on the beads (Figure 27). In our case, the magnet is large enough to consider the magnetic field as only dependent on the main chamber axis (named x). It allowed us to compute the equation 14:

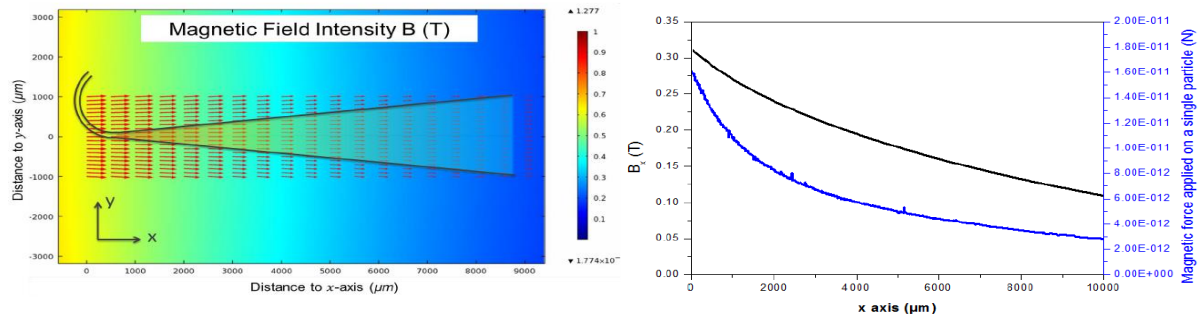


**Figure 27 A) Top view of the channel intensity and orientation of the magnetic field B) Spatial variation of the magnetic force exerted on a Dynabeads along the x axis (Pereiro et al., 2017)**

As shown in Figure 27 the decrease along the x axis is nonlinear for the global intensity of the magnetic field and the magnetic force applied on the beads. Following the x axis, the chamber widens, so the flow decreases. It counterbalances the decrease of the magnetic force due to the distance to the magnet.

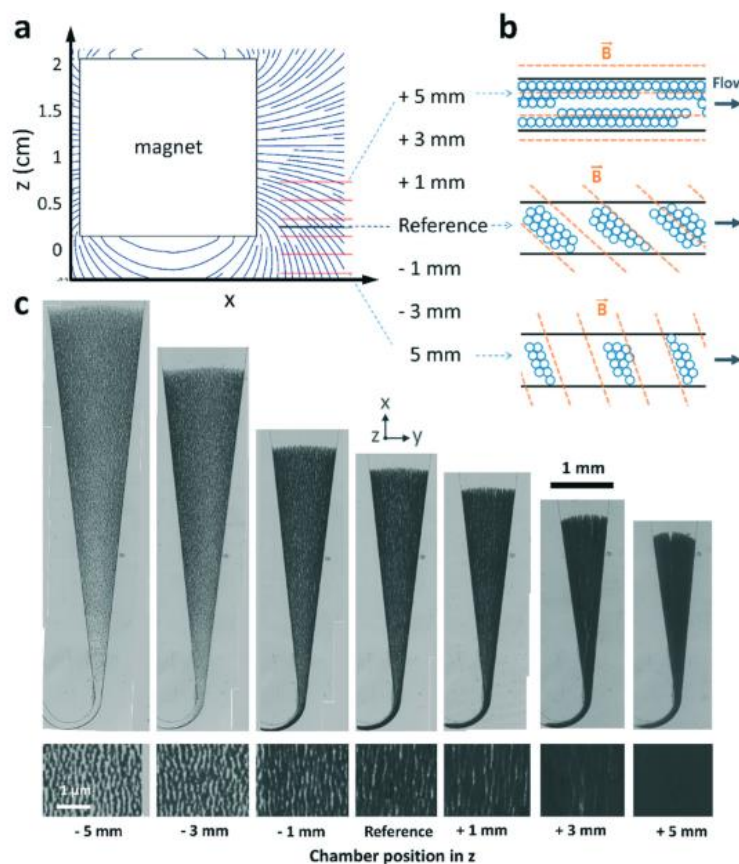


**Figure 28** Effect of magnetic streamline angle and field gradients in the fluidization of the magnetic beads. (a and b) Higher angles lead to smaller clusters and higher porosity. Small angles result in channeling effects and no fluidization (1  $\mu\text{L}/\text{min}$  flow rate for all images). (c) Lower zoomed images taken equidistant from the entrance and the upper bed border. (Pereiro et al., 2017)

The distance between the magnet and the device is also influencing the porosity in the bed (at short distances the magnetic force is stronger and the bed is more compact whereas at higher distances the porosity of the matrix is higher). At low porosity, the recirculation can be less efficient, while at high porosity, the beds density decreases affecting the capture efficiency. The magnet position in x and y is constant as it has to be aligned with the axis of the chamber. The usual distance between the magnet and the elbow channel at the entrance of the chip was settled at 1.5 mm. The z position of the magnet has been optimized (Figure 28). As magnetic beads align themselves along the magnetic field lines, they form columns of beads that can be called clusters. The z magnet position affects the orientation of the columns of beads. Those clusters limit the interaction between the solid surface of the beads and the liquid volume of the sample as it will be explained in the following chapters. A

compromise had been found by positioning the magnet 1 mm higher than the chip (Figure 28).

#### f) Recirculation and mixing of particles within the fluidized bed

The previous subsection introduced the question of the homogeneity of the beads distribution in the system. Additional studies were performed to investigate the motion of beads inside the matrix.

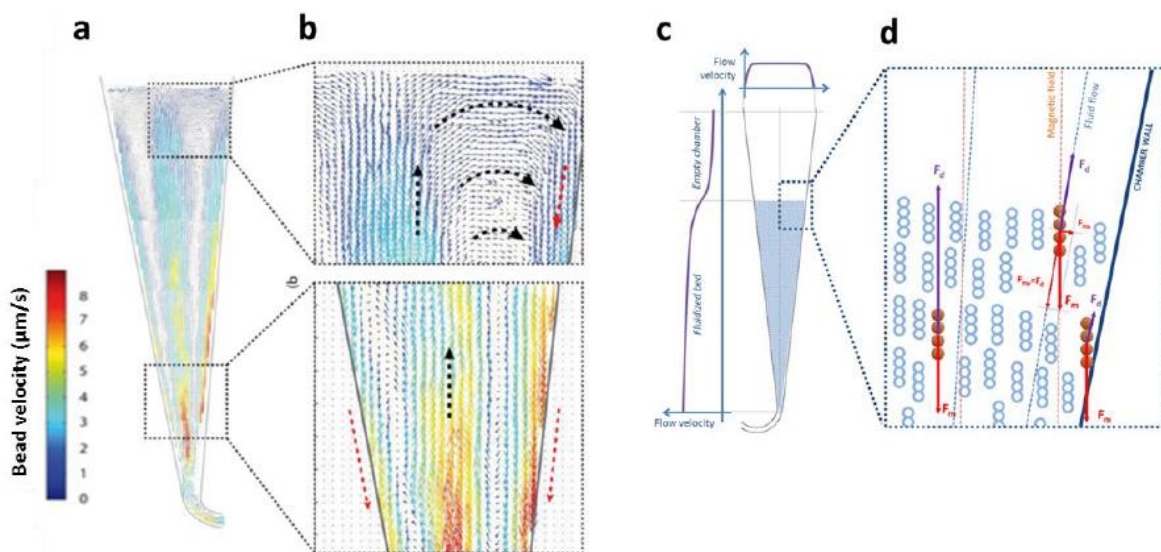


**Figure 29** A) Particle tracking cartography of the fluidized bed for a flow rate of 1.5  $\mu\text{L}/\text{min}$ ; B) detail of the sideward recirculation in the downstream limit of the bed, and of the opposite flow regions near the entrance; C) flow velocity distribution in the longitudinal and transversal axis of the system and D) scheme of equilibrium of forces for the three main steps in bead recirculation (Pereiro et al., 2017)

A particle tracking was performed with 50  $\mu\text{g}$  of 2.8  $\mu\text{m}$  magnetic beads at 1.5  $\mu\text{L}/\text{min}$  in the fluidized bed chamber in order to have a better understanding of the flow distribution and particle motion. As shown in Figure 29 A) and B), particle tracking highlights area of high beads velocity in the center of the chamber and close the chip edges. In between, beads don't seem to move. However, at the output, a movement from the center to the side of the chamber appears clearly. One possible explanation is given on the C and D panels of the Figure 29. On the center of the matrix of beads, the drag force and the magnetic force are collinear. The drag force is stronger than the magnetic one as the flow follows a Poiseuille's configuration. Beads are pushed towards the output. Along the way, as the chamber opens up, the flow slows down, and the y component of the drag force pushes the beads near the walls. Near the border of the chamber, there is a no-slipping boundary cancelling the drag



force. The magnetic force brings back the beads at the entrance of the chamber. In this fluidized bed configuration, we can thus obtain a continuous recirculation of the magnetic particles.

### **g) Application of fluidized bed to biological analysis**

Several bio-applications have been developed during the thesis of S. Tabanaoui and I. Pereiro.

- a) The fluidized bed has been first optimized for the capture of beta-amyloid peptides ( $A\beta$ ), a major biomarker in Alzheimer disease (Humpel, 2011). This observation led to the development of analytical techniques to detect  $A\beta$  in blood, and quantify its concentration. The magnetic fluidized bed previously described was validated as an efficient module for the extraction and pre-concentration of different  $A\beta$  peptides (Mai et al., 2015).
- b) The microfluidic magnetic fluidized bed has also been applied to the detection and amplification of DNA. I. Pereiro has implemented a complex bioassay called C2CA for circle to circle amplification. In particular, he has developed a two chambers chip. The first one was dedicated to DNA capture by hybridization and to the first amplification. The second one was a polymer microarray for integration of a single-molecule digital read-out (Hernández-Neuta et al., 2018).

Moreover the principle of microfluidic magnetic fluidized bed was also developed by Murphy et al. (Murphy et al., 2018) for analysis of histone modifications. Their system can be compared to the one presented in this work, at the exception of continuous injection of liquid inside the beads. Moreover, they completely developed the automation of the system with parallel assays performed simultaneously.

## **3. Evolution of the fluidized concept for high throughput analysis**

Fluidized beds have shown their efficiency in several field of biophysics. However, new promising projects have been initiated where larger volumes of sample needed to be analyzed. As an example, the search of new biomarkers (circulating tumor DNA, proteins...) emerged as new diagnosis challenges. Their low concentrations in complex real matrices can be an issue, and microfluidics is considered a technology that can take up this challenge. To tackle the challenges of trace analysis, we need to lower the limit of detection of current

systems. To this end, my PhD work focused on the development and characterization of approaches to be able to extract and pre-concentrate target analytes at high throughput.

The first generation of microfluidic fluidized bed developed in our team has demonstrated huge potential regarding its application for bioanalysis and in particular for extraction and preconcentration of biomolecules. However, this first generation of fluidized bed was adapted for flow rates in the range of 1 to 3  $\mu\text{L}/\text{min}$ . Careful analysis showed that at flow rate above 3  $\mu\text{L}/\text{min}$ , a fraction of the magnetic beads were taken away by the flow. At flow rates higher than 5  $\mu\text{L}/\text{min}$ , the full content of the magnetic bed is dragged away to the outlet by the device. This limit on the flow rate leads to a time of analysis quite long or to a severe limitation regarding the maximum volume to be analyzed (typically above 50  $\mu\text{L}$ ).

In order to reach the sensitivity required for different biomarkers especially in the field of cancer diagnosis, we have investigated how to tackle the challenge of processing larger volumes and consequently on the possibility to apply higher flow rates without affecting the bed performances. An easy and intuitive way to move toward higher volumes of sample consists in an enlargement of the chip's geometry. Preliminary experiments have shown that the geometry of the chip is critical and an angle of  $13^\circ$  at the entrance of the chip allows a homogenous distribution of the magnetic beads inside the chamber. The only geometrical parameter that could be changed was the height of the chamber. We have thus performed preliminary experiments with a chamber five times higher (250  $\mu\text{m}$ ), without any other modification of geometrical parameters.

#### a) Fluidized bed characterization as function of the chamber height

Increasing the chamber height by 5 implies that the volume of the chamber is also five times larger. To keep a system comparable to the previous one, the quantity of beads was set at 250  $\mu\text{g}$  (5 times more than in the first generation) increasing the total specific surface of capture. This configuration should allow us to increase the flow rate (by 5 times) and consequently the volume of sample analyzed in a given analysis time.



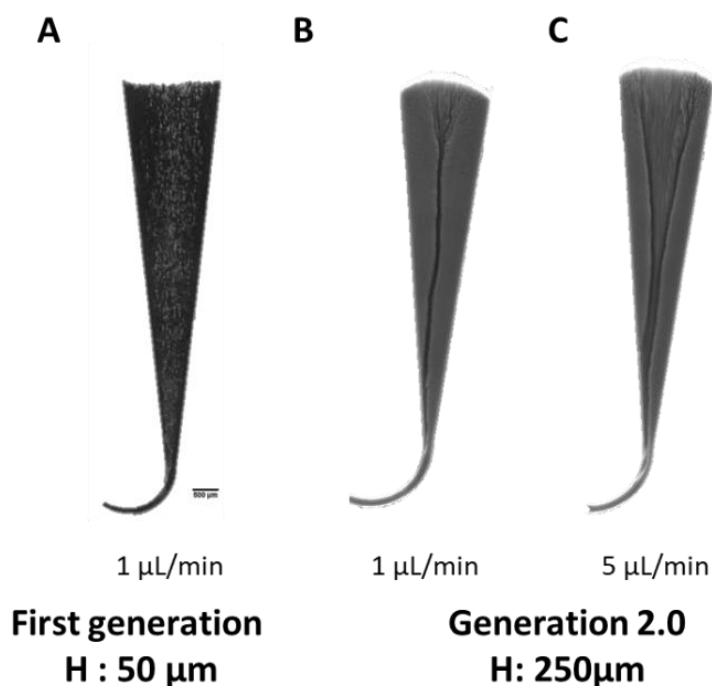


**Figure 30** Pictures of the beads bed at 1  $\mu\text{L}/\text{min}$  in a chip of A) 50  $\mu\text{m}$  and B) 250  $\mu\text{m}$  height and C) at 5  $\mu\text{L}/\text{min}$  in a 250  $\mu\text{m}$  height chip where a channeling effect can be observed on the second generation chip

First observations were centered on the beads re-circulation. This particular movement of beads could be observed in the 250  $\mu\text{m}$  chip, as well as in the 50  $\mu\text{m}$  chip. This first observation was a reassuring sign of the feasibility of the system scale-up.

However, these first observations also showed that the two generations do not present a similar behavior even at low flow rate (Figure 30). Indeed, with the second generation of fluidized bed, we observed the formation of preferential pathways inside the matrix of magnetic beads. In particular, a line of fracture appeared distinctly. Indeed, at 1  $\mu\text{L}/\text{min}$  we can observe the formation of a narrow fracture that can be identified as a zone where the beads concentration is lower (evidenced by the difference of grey level). This phenomenon is amplified at 5  $\mu\text{L}/\text{min}$  as a larger fracture is observed. Such bed morphology would certainly negatively affect the bed performances regarding solid phase extraction. Indeed, generating areas with a lower amount of beads will generate differential flow pathways, as most of the liquid will flow in this region of lower hydrodynamic resistance. We thus expect deteriorated capture efficiency in presence of such fractures.

## b) Capture efficiency as function of the chamber height

To verify our expectation, we used a streptavidin/biotin capture model to investigate the influence of the chamber height on the capture efficiency achieved in the bed. We used Streptavidin Dynabeads® M-280 and a fluorescently labeled DNA\_biotin at 100 nM (see Materials and method). We selected this model as it is characterized with high affinity ( $K_d = 10^{-15}$  M) (Lee et al., 1994; Weber et al., 1989)

This model of capture of biotin on the surface of magnetic beads allows us to compare the different configurations of the fluidized bed. Here we measured the percentage of capture on the beads. The comparison was directly made at a flow rate of 1 (as shown on Figure 30) and 3  $\mu\text{L}/\text{min}$ . This choice provides us conditions of work compatible with both systems. At higher flow rate, the 50  $\mu\text{m}$  chip loses beads and lower flow rates are not relevant for this study of high throughput sampling.

As shown on Figure 31, the fluidized bed first generation (50  $\mu\text{m}$  height) can work at 3  $\mu\text{L}/\text{min}$ . At this flow rate, the efficiency of capture is reduced to 31% of capture. It justifies our choice to develop a second generation of chip with a height of 250  $\mu\text{m}$ . As this new chip is filled with 250  $\mu\text{g}$  of beads (against 50  $\mu\text{g}$  for the first generation) we expected the capture to increase. We could observe a capture efficiency of 76% in this second chip with 13.6 pmol captured over the 18 pmol injected. This validates our approach with an increase of the size of the chip.

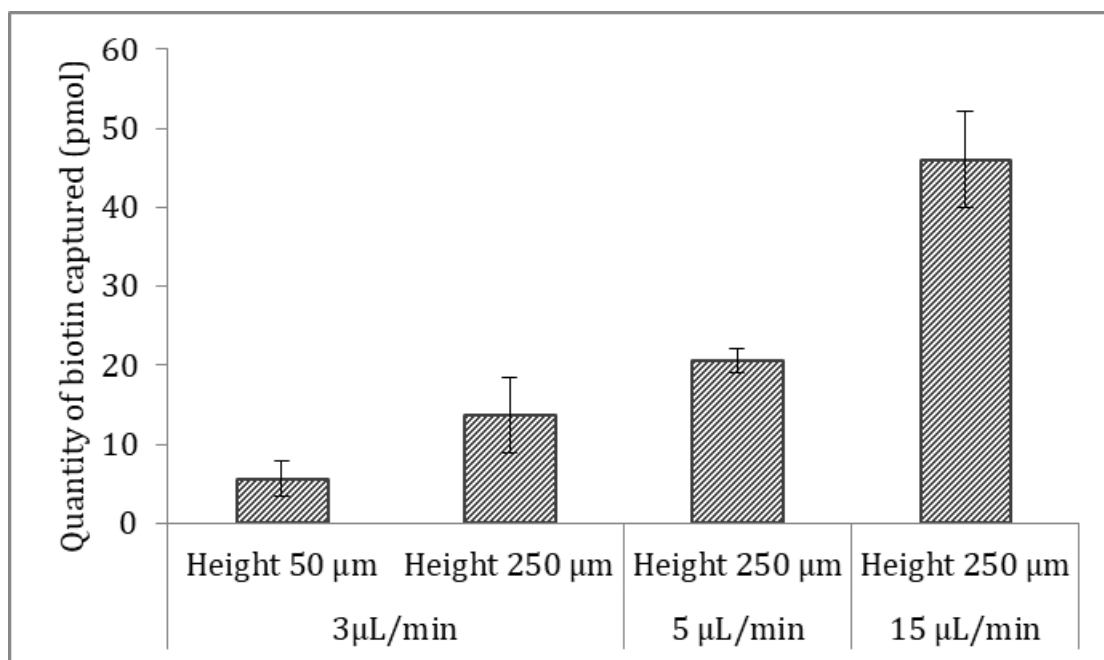


**Figure 31 Influence of the size of the chip on the quantity of biotin captured at three flowrates: 3, 5 and 15  $\mu\text{L}/\text{min}$  for a one hour experiment for a solution of DNA at 100 nM in PBS + 1% BSA**

However, the first generation (50 $\mu\text{m}$ ) could reach efficiency of 90% at 1  $\mu\text{L}/\text{min}$ . We expected such efficiency of capture to appear at 5  $\mu\text{L}/\text{min}$  in the second generation, as it is the perfect conditions of the scale-up. However, at 5 $\mu\text{L}/\text{min}$ , only 68% of capture was observed during the first hour of experiment. We related this decrease of efficiency with the formation of preferential pathways observed in the matrix of beads. The flow of liquid could not interact with all the beads of the bed, but only with the beads in suspension inside the low density area, moving inside the flow. The rest of the beads are packed and no more involved in the capture.

This effect could also be observed at 15  $\mu\text{L}/\text{min}$ , where 90 pmol were injected in one hour and only 46 pmol are captured, so the efficiency is around 51%. At 15  $\mu\text{L}/\text{min}$ , the area of low density was reduced. We then decided to investigate methods to homogeneously disperse beads inside the 250  $\mu\text{m}$  height chamber.

#### 4. Conclusion and perspectives

This initial work proves the conception of a fluidized bed at the microscopic scale based on magnetic forces. Superparamagnetic beads are in suspension between the drag force created by the flow of liquid injected in the matrix and a magnetic force created by a permanent magnet added to the system. Optimization of the geometry was performed in order to work with a homogeneous repartition of the beads inside the microfluidic chamber.

In order to tackle new challenges of trace analysis, we developed a new generation of chip based on the same geometry but with a height of 250  $\mu\text{m}$ . The lack of z-confinement of this new chip exposed new issues, such as the formation of area of low density. We showed that those areas could be problematic for the capture on the magnetic beads.

The first part of this manuscript will focus on new solutions to restore the homogeneity of the bed of beads. We will first begin with an approach based on either passive or active mixing solutions proposed in the literature. Those solutions are usually relying on molecular interactions, and will be translate to agitation of particles. Our second approach will rely on breaking the interaction between the beads by changing the beads composition. A full characterization will be performed with a model biotin/streptavidin and hybridization of DNA. Finally, we will also investigate how an active control of the flow could also be implemented on the bimodal matrix.

## 5. Materials and methods

Microfluidic chips were fabricated by mold casting on micro-milled molds. These molds were machined in brass piece of 5cm x 5cm by micromilling (Minitech Machinery). The designs were a positive replica of the chip. The chips were fabricated by pouring polydimethylsiloxane (PDMS, Sylgard184, Dow Corning) on the molds, and were bonded by oxygen plasma. A surface treatment of PDMA-AGE 0.5% was incubated inside the chip chamber for 2 hours then rinsed with distilled water and dried with compressed air.

The buffer was Phosphate-buffered saline "PBS" (Sigma Aldrich) with Bovine Serum Albumine "BSA" (1%, Sigma Aldrich).

The liquid flow was produced by a pressurization of the sample reservoir by a pressure controller (MFCS™, Fluigent). The outlet of the chip was connected to a flowrate controller (Flowunit S, Fluigent), which allowed precise flow rate measurement and feedback control on the pressure based on the Maesflo software (Fluigent). Peek tubing (Tube Peek 1/32"x0.25mm, Cil Cluzeau Info Labo) were used to connect the microfluidic chip to the other elements of the experimental set up. The resistance (12 cm peek tubing of 0.063 mm diameter) was positioned at the entrance of the chip. A NdFeB 1.47T permanent magnet was aligned with the chamber axis at a 1.5mm distance from the chip inlet.

Streptavidin Dynabeads® M-280 (2.8µm in diameter, Dynabeads®, Thermofisher) were used for characterization experiments. First generation chips contained 50 µg of beads, second generation chips 250 µg. All beads were washed three times in buffer solution before use following the data sheet protocol.

Biotinylated DNA conjugated to a biotin and a fluorophore Alexa488 was buy from IDT©. DNA was then diluted in ddwater, and the concentration was adjusted with PBS (Sigma Aldrich). The sequence ordered with HPLC purification was:

/5BiosG/CTCTCTCTCTCTCTCTCTCT/3AlexF488N/

## Bibliography

- Bayrock, D., and Ingledew, W.M. (1997). Fluidized bed drying of baker's yeast: moisture levels, drying rates, and viability changes during drying. *Food Res. Int.* *30*, 407–415.
- Ergun, S. (1952). Fluid flow through packed columns. *Chem Eng Prog* *48*, 89–94.
- Fonnum, G., Johansson, C., Molteberg, A., Mørup, S., and Aksnes, E. (2005). Characterisation of Dynabeads® by magnetization measurements and Mössbauer spectroscopy. *J. Magn. Magn. Mater.* *293*, 41–47.
- Geldart, D. (1973). Types of gas fluidization. *Powder Technol.* *7*, 285–292.
- Gungor, A., and Eskin, N. (2007). Hydrodynamic modeling of a circulating fluidized bed. *Powder Technol.* *172*, 1–13.
- Hernández-Neuta, I., Pereiro, I., Ahlford, A., Ferraro, D., Zhang, Q., Viovy, J.-L., Descroix, S., and Nilsson, M. (2018). Microfluidic magnetic fluidized bed for DNA analysis in continuous flow mode. *Biosens. Bioelectron.* *102*, 531–539.
- Humpel, C. (2011). Identifying and validating biomarkers for Alzheimer's disease. *Trends Biotechnol.* *29*, 26–32.
- Kunii, D., and Levenspiel, O. (2013). *Fluidization Engineering* (Elsevier).
- Lee, G.U., Kidwell, D.A., and Colton, R.J. (1994). Sensing Discrete Streptavidin-Biotin Interactions with Atomic Force Microscopy. *Langmuir* *10*, 354–357.
- Lyngfelt, A., Leckner, B., and Mattisson, T. (2001). A fluidized-bed combustion process with inherent CO<sub>2</sub> separation; application of chemical-looping combustion. *Chem. Eng. Sci.* *56*, 3101–3113.
- Mai, T.D., Pereiro, I., Hiraoui, M., Viovy, J.-L., Descroix, S., Taverna, M., and Smadja, C. (2015). Magneto-immunocapture with on-bead fluorescent labeling of amyloid- $\beta$  peptides: towards a microfluidized-bed-based operation. *Analyst* *140*, 5891–5900.
- Murphy, T.W., Hsieh, Y.-P., Ma, S., Zhu, Y., and Lu, C. (2018). Microfluidic Low-Input Fluidized-Bed Enabled ChIP-seq Device for Automated and Parallel Analysis of Histone Modifications. *Anal. Chem.* *90*, 7666–7674.
- Pereiro, I., Tabnaoui, S., Fermigier, M., Roure, O. du, Descroix, S., Viovy, J.-L., and Malaquin, L. (2017). Magnetic fluidized bed for solid phase extraction in microfluidic systems. *Lab. Chip* *17*, 1603–1615.
- Räsänen, E., Rantanen, J., Mannermaa, J.-P., and Yliruusi, J. (2004). The Characterization of Fluidization Behavior Using a Novel Multichamber Microscale Fluid Bed. *J. Pharm. Sci.* *93*, 780–791.
- Rhodes, M.J., Wang, X.S., Nguyen, M., Stewart, P., and Liffman, K. (2001). Use of discrete element method simulation in studying fluidization characteristics: influence of interparticle force. *Chem. Eng. Sci.* *56*, 69–76.

Richardson, J.F., and Zaki, W.N. (1954). The sedimentation of a suspension of uniform spheres under conditions of viscous flow. *Chem. Eng. Sci.* *3*, 65–73.

Richardson, J.J., Teng, D., Björnmalm, M., Gunawan, S.T., Guo, J., Cui, J., Franks, G.V., and Caruso, F. (2014). Fluidized Bed Layer-by-Layer Microcapsule Formation. *Langmuir* *30*, 10028–10034.

Siedlecki, M., De Jong, W., and Verkooijen, A.H.M. (2011). Fluidized Bed Gasification as a Mature And Reliable Technology for the Production of Bio-Syngas and Applied in the Production of Liquid Transportation Fuels—A Review. *Energies* *4*, 389–434.

Wang, Y., Wei, F., Luo, G., Yu, H., and Gu, G. (2002). The large-scale production of carbon nanotubes in a nano-agglomerate fluidized-bed reactor. *Chem. Phys. Lett.* *364*, 568–572.

Weber, P.C., Ohlendorf, D.H., Wendoloski, J.J., and Salemme, F.R. (1989). Structural origins of high-affinity biotin binding to streptavidin. *Science* *243*, 85–88.

Zivkovic, V., and Biggs, M.J. (2015). On importance of surface forces in a microfluidic fluidized bed. *Chem. Eng. Sci.* *126*, 143–149.

Zivkovic, V., Kashani, M.N., and Biggs, M.J. (2013). Experimental and theoretical study of a micro-fluidized bed. pp. 93–96.

## Note on the vocabulary

### **Area of low density – preferential pathways**

In the fluidized bed, beads in suspension are submitted to two main forces: the drag force and the magnetic force. When parameters are fully optimized (as it is for the first generation chip) beads fan out homogeneously in the micro-chamber. However, while working with the second generation of chip, we observed areas of low density inside the matrix of beads due to the formation of preferential pathways for the fluid passing through. These areas of low density of beads were recognized by transmission microscopy as the areas of higher transparency and thus lower grey level (due to a local decrease on beads concentration) whereas areas of high beads density were optically more opaque.

An analogy can be made between this phenomenon and the fracturing of a solid matrix when a fluid is injected inside. Nevertheless, this comparison has to be made carefully as areas of low density in the fluidized bed still contain beads, which interact with the fluid passing through. They should not be considered as liquid fracture causing a leak of liquid in the fluidized bed.

### **Mixing – Agitation of particles**

We are working with a matrix of particles of micrometric size. Our goal is to obtain a homogeneous spatial distribution of those particles inside a microfluidic chamber to promote a uniform injection of the sample through the bed and enhance capture efficiency. To do so, we tried to increase the mobility of the particles in suspension or to modify the flow distribution in the device. The latter approach is often involved in the mixing of molecular species where the reduction of the diffusion time is critical. It is important to notice that homogenization by agitation of micro particles and mixing by diffusion of molecular scale are two different phenomena that can complement each other.





**Part A**

**Development and physical characterization of  
a new generation of fluidized bed**



## Chapter 2

### Passive mixing in a fluidized matrix of beads based on Herringbones design

#### 1. Introduction

Microfluidics is “the science and technology of systems that process or manipulate small ( $10^{-9}$  to  $10^{-18}$  liters) amounts of fluids, using channels with dimensions of tens to hundreds of micrometers” (Whitesides, 2006). It presents numerous advantages such as manipulation of small volumes of samples and reagents, low costs, short analysis times, integration.... Hydrodynamic mechanisms involved in microfluidics are associated with small Reynolds number ( $Re < 1$ ). This means that friction forces prevail over inertial ones. This can be both an advantage and a disadvantage for analytical applications. On one hand, it provides very reproducible and predictable flow distributions and the possibility to exploit diffusion to create gradients. On the other hand, disadvantages are mainly related to difficulties in fast flow mixing and limits due to no slip boundary conditions. Mixing is indeed important for numerous fields of application such as chemical reactions, biochemical interactions or mass transfers. Mixing can be achieved either by advection or diffusion. Advection refers to the transport of a material through bulk motion. In case of a fluid, the main characteristic of advection is the flow velocity ( $U$ ). Diffusion refers to the spreading of molecules through thermal motion. This time dependent process is described by a diffusion coefficient  $D$  that can be written using the Stokes-Einstein formula:

$$D = \frac{k_B T}{6 \pi \eta R}$$

*equation 1*

$k_B$  is the Boltzmann constant,  $T$  the temperature,  $\eta$  the viscosity and  $R$  the particle radius.

Transport of molecules or particles through diffusion and advection processes can be described with the usual advection-diffusion equation for a unidirectional flow with quantity conservation:

$$\frac{\partial C}{\partial t} + U \nabla C = D \Delta C$$

*equation 2*

where  $C$  is the variable of interest,  $t$  the time,  $U$  the flow velocity (incompressible flow).

The second term of the equation reflects the advection of the system, the third one the diffusion. To analyze the importance of each term, we need a way to evaluate their effects. A usual way to compare two processes is to introduce a dimensionless number. In this case it is named the Peclet number, after the French physicist Jean Claude Eugène Péclet (1793 – 1857):

$$Pe = \frac{\text{diffusion time}}{\text{advection time}} \sim \frac{U \nabla C}{D \Delta C} \text{ or } Pe = \frac{U l}{D}$$

*equation 3*

The Peclet number assesses whether diffusion or advection is dominant in the phenomena investigated. For laminar flow, the mixing is purely diffusive; the minimal needed length to observe full mixing grows linearly with the Peclet number.

Proposed solutions to induce mixing in microfluidics can be either active or passive (Nguyen and Wu, 2005a). Active mixing introduces external forces to increase interactions between two fluids, usually by stirring and stretching the surface of contact. Passive mixing is based on an optimization of the channel configuration or structure to increase the contact time/area between two liquid phases. In the last case, the mixing element is directly incorporated inside the system during fabrication.

Both active and passive mixing approaches can be broken down in several domains of physics. This chapter focuses only on passive micromixers. Active mixers will be described in the chapter 4.

As previously mentioned, our goal here is to reach a homogeneous distribution of the beads inside the bed. To achieve this, we tried to increase the motion of particles inside the main

chamber. To do so, we first studied the different approaches described in the literature to increase the mixing in microfluidic devices.

### a) Passive mixing

Passive mixers have the huge advantage of simplicity. Those mixers rely on an increase of advection and bypass the diffusion time. Most of the methods rely on molecular mixing. Their application to mixing of micro-objects will be considered, as well as the use of the movement of the flows to increase the mobility of the beads.

#### A. T- and Y- shaped micro-mixers

The basic geometry to mix two liquids in continuous flow relies on T- or Y- mixers as illustrated in Figure 32 (Capretto et al., 2011; Kamholz et al., 1999). By fluorescence measurement (solution with a diffusion coefficient of  $4.55 \cdot 10^{-7} \text{ cm}^2/\text{s}$ ) Kamholz et al. visualized the area of diffusion in the mixing channel ( $w=550\mu\text{m}$  and  $h=25\mu\text{m}$ ) at 5 mm of the entrance at different flow rates (Figure 32). In this kind of design, the mixing is performed by diffusion on the molecular level at the interface between the two liquids. At steady state, the width of the inter-diffusion region, perpendicular to the flow, increases with the distance to the junction of the liquids and the velocity of the flow at a power of one third (Ismagilov et al., 2000).

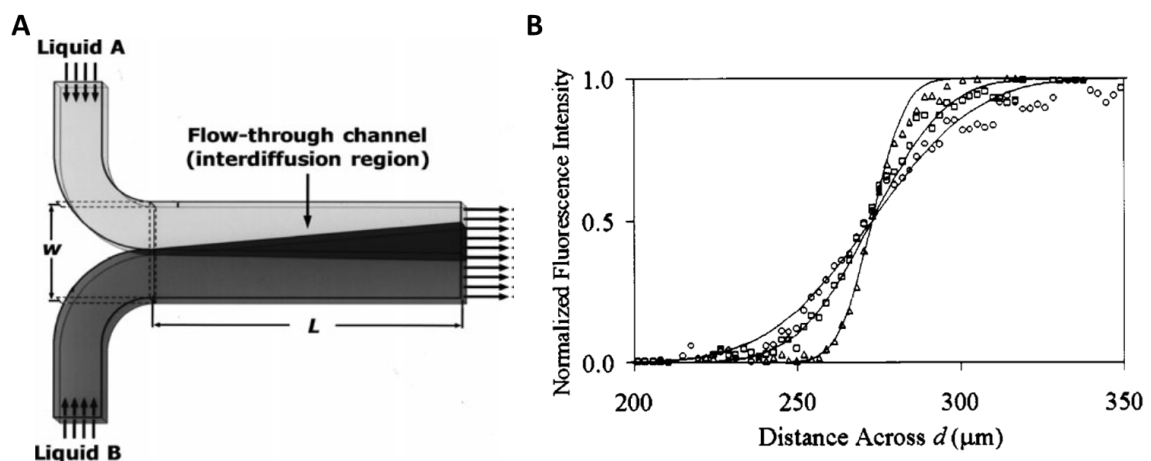


**Figure 32** A T-shaped micro-mixer with two entrance to inject liquids with diffusing molecules in the central mixing channel of length  $L$  and width  $w$ . The black area is the inter-diffusion region (Capretto et al., 2011) B Graphic representation of the intensity at 5 mm from the junction point across a  $550 \mu\text{m}$  width channel for three flowrates: 5 (round) 25 (square) and 50 (triangle)  $\mu\text{L}/\text{min}$  (Kamholz et al., 1999)

In a Y or T design, the average time for a molecule to diffuse over a distance  $x$  is:

$$t = \frac{x^2}{2D}$$

*equation 4*

where  $D$  is the coefficient of diffusion.

For example, in the case of a Y-shape channel of 100  $\mu\text{m}$  width and two entrance of 50  $\mu\text{m}$ , the diffusion of fluorescein ( $D \sim 2.6 \cdot 10^{-6} \text{ cm}^2/\text{s}$ ) across the channel takes 4.8 s to diffuse on half of the channel. This method cannot be applied to micro-objects confined in a chamber, as long distances are needed for the diffusion process.

#### B. Multi-lamination micro-mixers

To improve the mixing by molecular diffusion, the easiest way is to increase the surface of contact between the two liquids. In order to increase the area of diffusion, a simple way is to split the flow in  $n$  sub-streams and then gather them inside a main channel. These structures provide a bigger surface of interaction (multiply by the factor  $n$ ) and then decrease the time needed to reach a complete mixed flow.

Different geometries have already proved their efficiency. Cha et al. introduced a microfluidic mixer named 'chessboard mixing' based on parallel interleaving channels in PDMS as presented in Figure 33 A (Cha et al., 2006). Complete mixing could be reached at a distance of 1.4 mm at a flow rate of 12.7  $\mu\text{L}/\text{min}$  in a channel of 50  $\mu\text{m}$  width, and with 8 sub-flows. Floyd et al. presented a circular micro-mixer with a typical mixing time of 25 ms to reach 99% mixing at 4 mL/min and a Reynolds number of 40 (Figure 33 B, Tamara M. Floyd et al., 2004). This idea was developed further by Löb et al. up to 138 channels of 360  $\mu\text{m}$  width and 5 mm height, separated by 250  $\mu\text{m}$  walls (Figure 33 C, Löb et al., 2004). They obtained a mixing of 95% in 4 ms at the end of the channel.

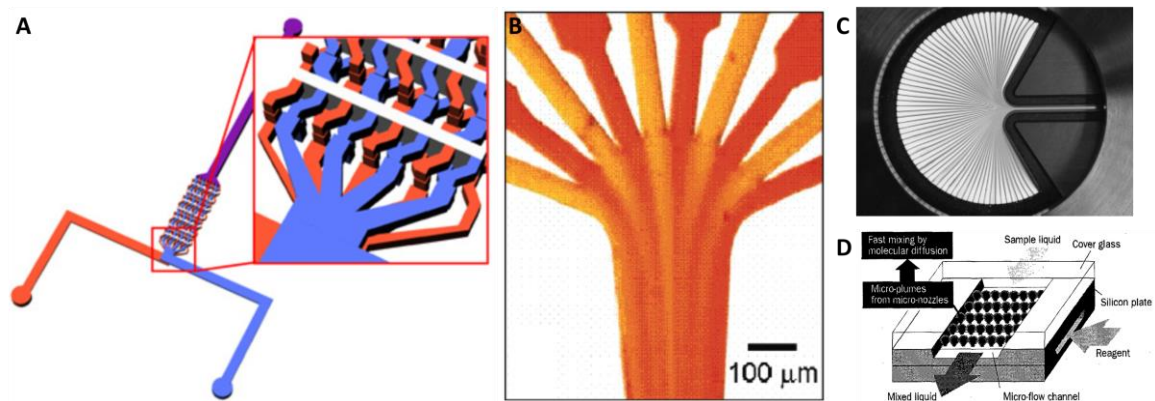


**Figure 33** A Schematic diagram of the full system of 'chessboard mixer' (Cha et al., 2006) B Hydrodynamic focusing of 10 streams of alternating acid (yellow) and base (orange) solutions (Tamara M. Floyd et al., 2004) C (Löb et al., 2004) D Principle of a micro-mixer by multiple injection (Miyake et al., 1997)

Multi-lamination micro-mixers decrease the average time described in equation 4. Erbacher et al. shown that the time  $t$  is therefore divided by  $n^2$  :

$$t = \frac{nL}{2u} + \frac{x^2}{2n^2D}$$

equation 5

where  $L$  is the length to reach the branching,  $u$  is the flow rate and  $n$  is the number of parallel flows as described on Figure 34 (Erbacher et al., 1999)

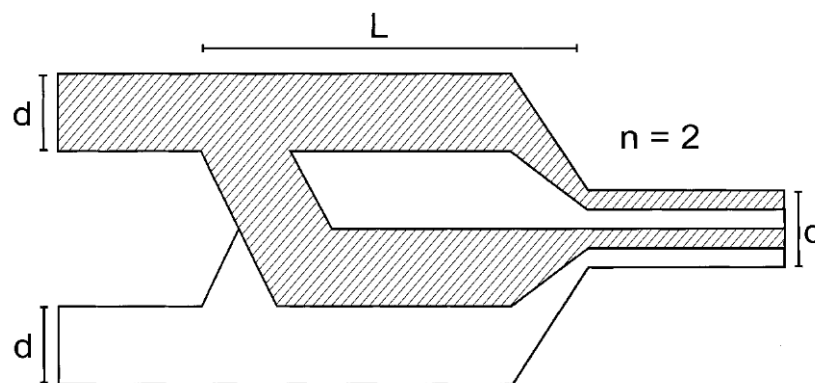


**Figure 34** Schematic representation of a parallel lamination (Erbacher et al., 1999)

The same idea can be developed in sequential lamination, where flows are split and recombined. The surface of interaction is then increased on an exponential way. For example, Lim et al. introduced a 3D built-in micro-mixer in a site controlled manner called 'crossing manifold micromixer' (Woo Lim et al., 2011). They were able to demonstrate a



complete mixing at 225  $\mu\text{m}$  from the beginning of the main channel at a flow rate of 3  $\mu\text{L}/\text{min}$ . Starting from a T-shape mixer, some configurations can be imagined, as the one introduced in Figure 35 A. Geometries can be compared using the time after which any point across a surface perpendicular to the main channel direction is at the same concentration  $\pm 5\%$  when the flow is stopped. This value is dependent on the diffusion coefficient of the liquids and on the distance of the surface to the inlet. In the case of the geometry presented on Figure 35 A, efficient mixing was obtained after 100 ms for a distance of 1 mm. As a counter part, this kind of geometry is usually complex to realize (spin coating, photo patterning and alignment). The efficiency of mixing was evaluated in stop flow mode (Hinsmann et al., 2001).

The surface of contact between fluids can also be increased by addition of supplementary channels such as the solution illustrated on Figure 35 B. Using this geometry, He et al. demonstrated an efficient mixing in less than 1 second in a total volume of 100 pL (He et al., 2001)

Very similar to the geometrical mixers, injection mixers are based on multiple inlets to inject a liquid into another one. For example (Miyake et al., 1997) reported a system with 400 injections into the main channel as presented on Figure 33 D. However, those systems are more difficult to fabricate due to the multiple inlets.

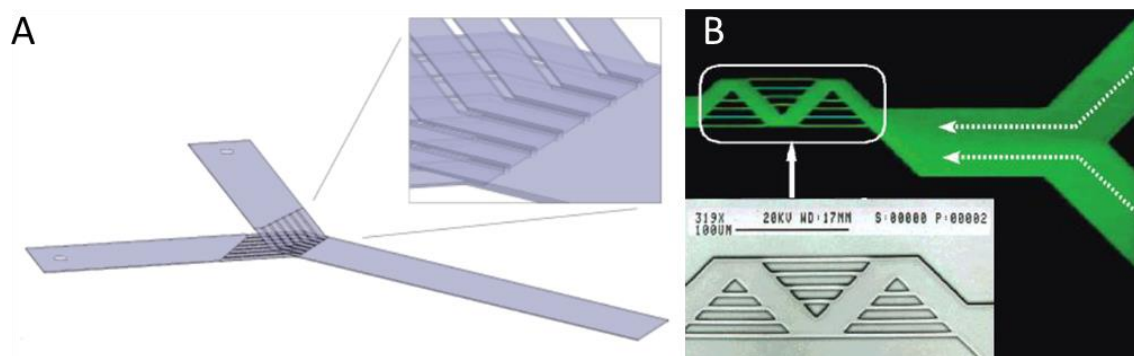


**Figure 35** *Passive micromixers based on geometry modification: A) drawing of a parallel micromixer allowing to multiply the surface of interaction of two liquid by multiplexing the entrance channels (Hinsmann et al., 2001) and B) picture of a serial micromixer where smaller channels are added at 45° in the main channel, the flow is coming from the right and indicated by the white arrows. On the bottom left corner is a picture of the device taken by scanning electron microscopy (He et al., 2001)*

### C. Serpentine structures

To create advection inside a microchannel, it is possible to use alternatively curved, serpentine or zigzag design. Those geometries have been developed in 2 dimensions (Mengeaud et al., 2002; P. Sudarsan and M. Ugaz, 2006) and 3 dimensions (Hong et al., 2004; Kim et al., 2005; Vijayendran et al., 2003). Those systems were able to reach high efficiency of mixing at high flow rate (dozens to hundreds mL/h), far from usual condition of most micro-fluidics systems. Unfortunately, these conditions are not compatible with our geometry, so we won't discuss them in details.

### D. Addition of obstacles

To disturb the flow and improve molecular mixing, another solution is to add geometrical obstacles. Wong et al. described a cross mixer with a mixing channel of 185  $\mu\text{m}$  length, 40  $\mu\text{m}$  width and 40  $\mu\text{m}$  depth (Wong et al., 2003). They showed a complete mixing after 500  $\mu\text{s}$  at the end of the mixing channel due to the asymmetrical position of the obstacles in the channel (Figure 36). Wu et al. introduced cylindrical obstacles inside the main channel and were able to reach complete mixing in 0.08 s at a flowrate of 1200  $\mu\text{L}/\text{min}$  (Wu et al., 2014). Moreover, The et al. presented a micro-mixer based on shifted trapezoidal blade as described on Figure 36 c where vortices, transversal flows and chaotic advection allowed to reach high efficiency (Le The et al., 2015).

These geometries are usually described as efficient at Reynolds numbers higher than 1, where vortex can be created, and advection increases the mixing efficiency

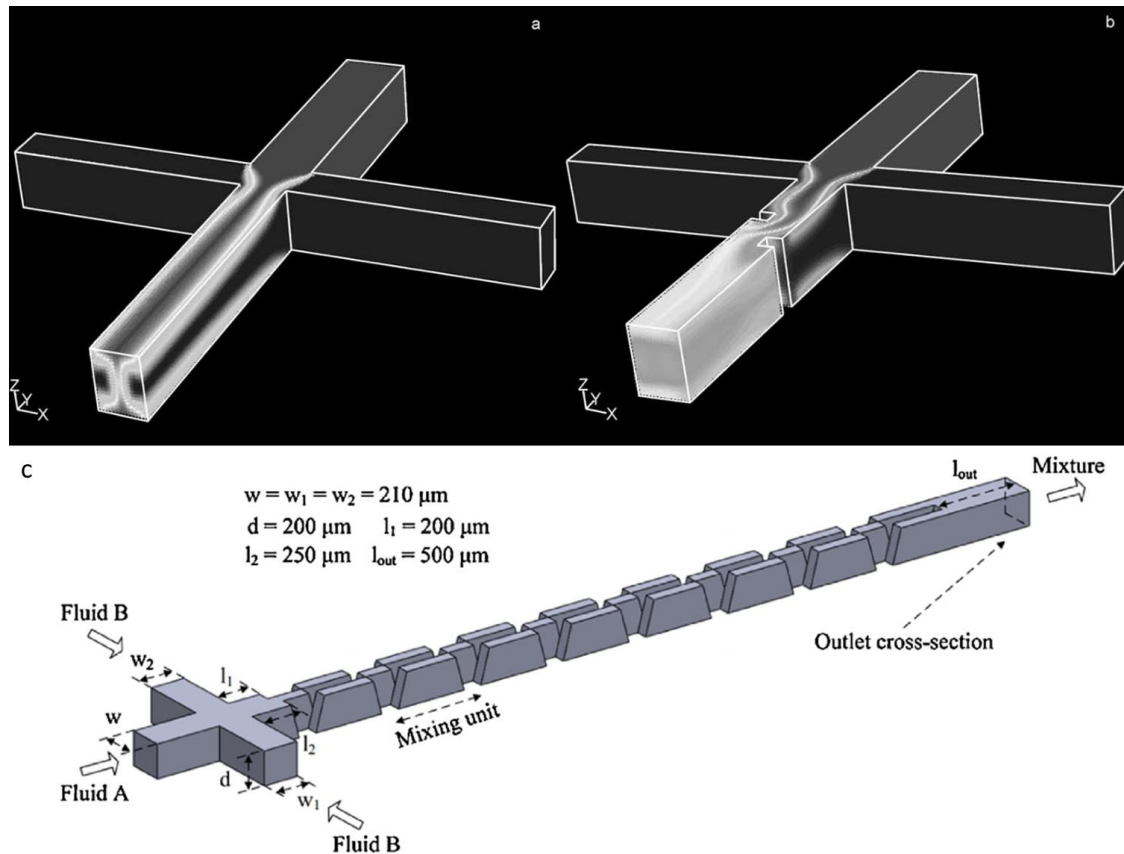


**Figure 36.** Simulation of mixing in a cross channel without (a) and with (b) addition of obstacles (Wong et al., 2003) and geometry of the shifted trapezoidal blades micromixer (Le The et al., 2015)

### b) Operating conditions

In order to choose which micro-mixer should be used for our system, it is possible to compare Reynolds and Peclet numbers to those described in the literature as summarized in Figure 37 (Kumar et al., 2011). However, it is important to keep in mind that those systems of passive mixing try to increase and support the molecular mixing process based on diffusion. In the case of presence of colloids, mixing should induce agitation to increase the mobility of the suspended objects. In our case, we focus on particles of low dimension ( $\mu\text{m}$ ). Their mass is not enough to use inertial effect; this is the reason why we need methods of mixing solutions to boost their dispersion in the liquid.

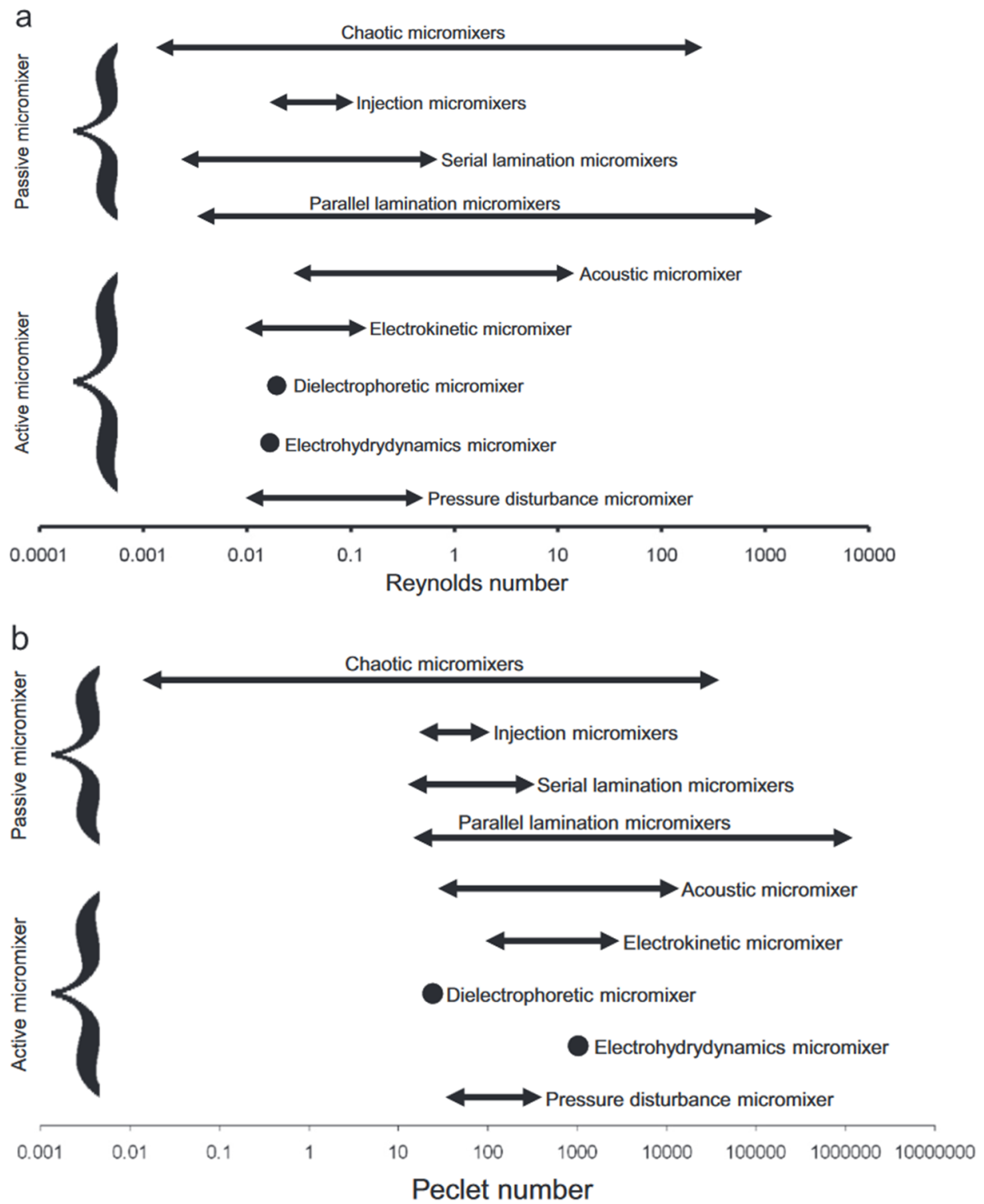


**Figure 37** A Typical operation range of micro-mixer and B Peclet number ( $Pe$ ) - Reynolds number ( $Re$ ) diagram showing the passive micro-mixers work at low  $Pe$  and low  $Re$  or at high  $Pe$  and high  $Re$  (Kumar et al., 2011)

### c) Herringbones design to create mixing

As previously shown, mixing in microfluidic channels requires ingenious approaches. Active mixing implies the integration of moving components or pumps, which increases the size and the complexity of the setup. This is why, in a first approach, we investigated passive methods that would allow to work with reduced modifications of the microfluidic devices. Their simplicity makes them more suitable for applications in analytical chemistry (Nguyen and Wu, 2005b).

An intriguing approach for passive mixing is to change the geometry of the channel by adding ribs or grooves to induce movement of the liquid inside the PDMS chip. Such an idea has been developed by Johnson et al. (Johnson et al., 2002) then by Stroock et al. (Stroock et al., 2002). Starting from a simple T-shape channel, they demonstrate a new way to mix two different liquid solutions. In the usual T-geometry, mixing is only driven by diffusion and appears after a long distance  $d$  that can be estimate at high Peclet number by  $d \sim Pe \times l$  where  $l$  is the dimension of the channel. They modified the geometry by adding periodic grooves on the floor of the main channel as shown on Figure 38. The design of the grooves has been improved from A to B to enhance mixing by fluid advection by adding another vortex. The centers of rotation are moving between each half-cycle of grooves in order to reach an efficient mixing.

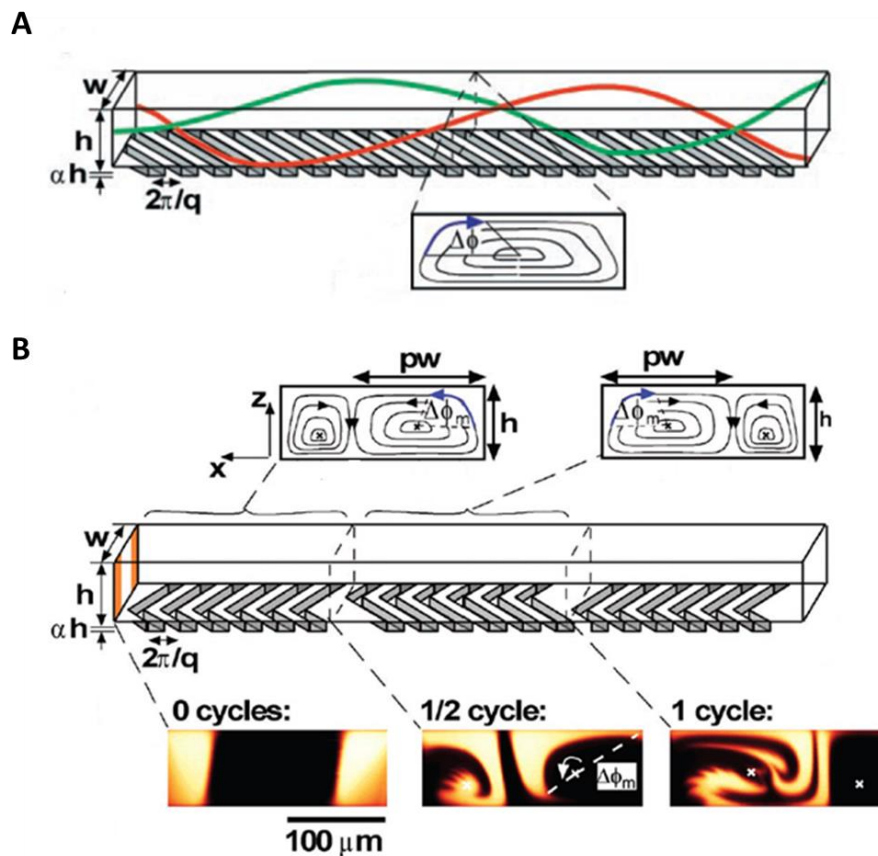


**Figure 38** Presentation of two systems integrating groove patterns into a straight channel with either A) obliquely oriented grooves or B) staggered herringbone mixer (SHM) with schematic representation of regions of ridges  $p$  is the fraction of the width occupied by the wide arms,  $\phi$  is the angular displacement of the fluid,  $h$  and  $w$  are the dimensions of the channel,  $\alpha$  and  $q$  are geometrical parameters to describe the grooves and confocal micrographs of vertical cross sections of the channel

This method offers an appealing solution easy to fabricate, and producing an efficient mixing. The mixing length to achieve 90 % of mixing is less than a centimeter for a Peclet number (Pe) of 2 000 and increases linearly with  $\ln(\text{Pe})$  for large Pe at a speed of 2 cm/s.

#### d) Fluidized bed and Herringbone design

Our goal was to investigate the possibility to modify the flow distribution in the fluidized bed using a herringbone structure and thus to improve particle mobility during capture. In particular, the generation of cross-courant flows could disrupt the formation of fractures and improve the homogeneity of the bed. This would be particularly interesting when

increasing the height of the main chamber of the fluidized bed chip that favors the creation of preferential pathways in the particle assembly.

We decided to add a passive mixer to the optimized geometry of our experiment. However, working with multiple streams is difficult for the fluidized bed. It creates different hydraulic paths, and reduce the homogeny repartition of the particles in the flow (Tabnaoui, 2012). We decided to implement the herringbone staggered mixer (SHM) as it can be easily integrated in our system. The geometry from Stroock can be adapted on the wall of the microfluidic magnetic fluidized bed. Its integration has been easy, without any major modification of the geometry.

For the fluidized bed, the Peclet number can be evaluated at:

$$Pe = \frac{U l}{D} = \frac{3.3 * 10^{-3} * 5 * 10^{-5}}{10^{-9}} \sim 1.5 * 10^2$$

Where  $U = 1 \mu\text{L}/\text{min} = 3.3 * 10^{-3} \text{ m/s}$ ,  $l = 50 \mu\text{m}$  and the diffusion coefficient is  $D = 10^{-9} \text{ m}^2/\text{s}$  for water. In case of a mix between water and glycerol,  $D = 10^{-10} \text{ m}^2/\text{s}$  and the Peclet number would be  $1.5 * 10^3$  (D'Errico et al., 2004)

Moreover the Reynolds number can be calculated as:

$$Re = \frac{U l}{\nu} = \frac{3.3 * 10^{-3} * 5 * 10^{-5}}{10^{-6}} \sim 1.5 * 10^{-1}$$

Where  $\nu$  is the kinematic viscosity ( $\nu \approx 10^{-6} \text{ m}^2/\text{s}$ )

As shown on Figure 37, almost all the passive solutions could be investigated for the fluidized bed. With our system we work at a Reynolds number around  $10^{-1}$  and a Peclet number around  $10^3$  for a mixture with glycerol (used for confocal imaging). These values are close to the ones reported in Stroock's paper, we thus expect the herringbones mixer to modify flow streamlines inside the beads matrix.

However, the integration of the SHM concept in our system is challenging regarding two aspects:

- a) The main chamber presents a widening angle of  $13^\circ$ , whereas all applications of SHM have been done in a straight channel
- b) The modification of the flow pattern have to be sufficient to compensate for the cohesive forces within the bed and increase the mobility of the particles.

To evaluate the efficiency of the SHM in our geometry, simulations have been run using the Comsol® software. Those simulations only dealt with a flow of liquid inside a triangular channel without any particles inside. The results were also used to optimize the parameters of the grooves geometry such as spacing and size.

## 2. Description of the adaption of the Herringbone design to the fluidized bed chip

### a) Numerical Simulations

The goal of the Comsol® simulations is to evaluate the influence of grooves on the fluid flow in a flared shape. Comsol® simulations use a finite element method to approximate solutions of partial differential equations. Numerical simulations were based on Stokes equation considering a laminar and incompressible flow at low Reynolds number and at steady state.

In such conditions, Stokes equation is defined as:

$$\eta \Delta \vec{u} - \vec{\nabla} p = 0$$

where  $\eta$  is the dynamic viscosity of the fluid,  $\Delta \vec{u}$  the Laplacian of the velocity vector and  $\vec{\nabla} p$  the gradient of the pressure. The boundary conditions are:

- a) The flow is laminar at the entrance and set to 3  $\mu\text{L}/\text{min}$
- b) The flow is laminar at the output and set to 3  $\mu\text{L}/\text{min}$
- c) No slip boundary conditions
- d) Fluid conditions were set to mimic water (dynamic viscosity  $\eta = 1\text{mPa}\cdot\text{s}$ )
- e) No conditions of pressure were imposed

Comsol® offers the possibility to simulate flows at very low Reynolds number using the Creeping Flow interface. To mimic flow patterns at  $\text{Re} \ll 1$ , this interface neglected the inertial forces in front of the viscous terms in the Navier-Stokes equations (isothermal flows). The mesh was automatically evaluated by the software between 700 000 and 800 000 elements giving rise to a converging solution in less than 20 minutes. The independence of the results to the mesh was verified by a study of the convergence.

To enlighten the mixing in a liquid, an easy way is to separate it in two parts and look at the mixing between those two. To differentiate the two parts, colors have been attributed to



each of them: red for the top part, and blue for the bottom one. To reduce the analysis time, we decided to work with tracers in the flow instead of concentration using the additional module “Particle Tracing for Fluid Flow interfaces” (3 minutes of computation against 20 in a standard case). Those tracers can be considered as spheres with a diameter of  $0 \mu\text{m}$  and have no mass. They are just used for visualization of the lines of flow, without any material existence.

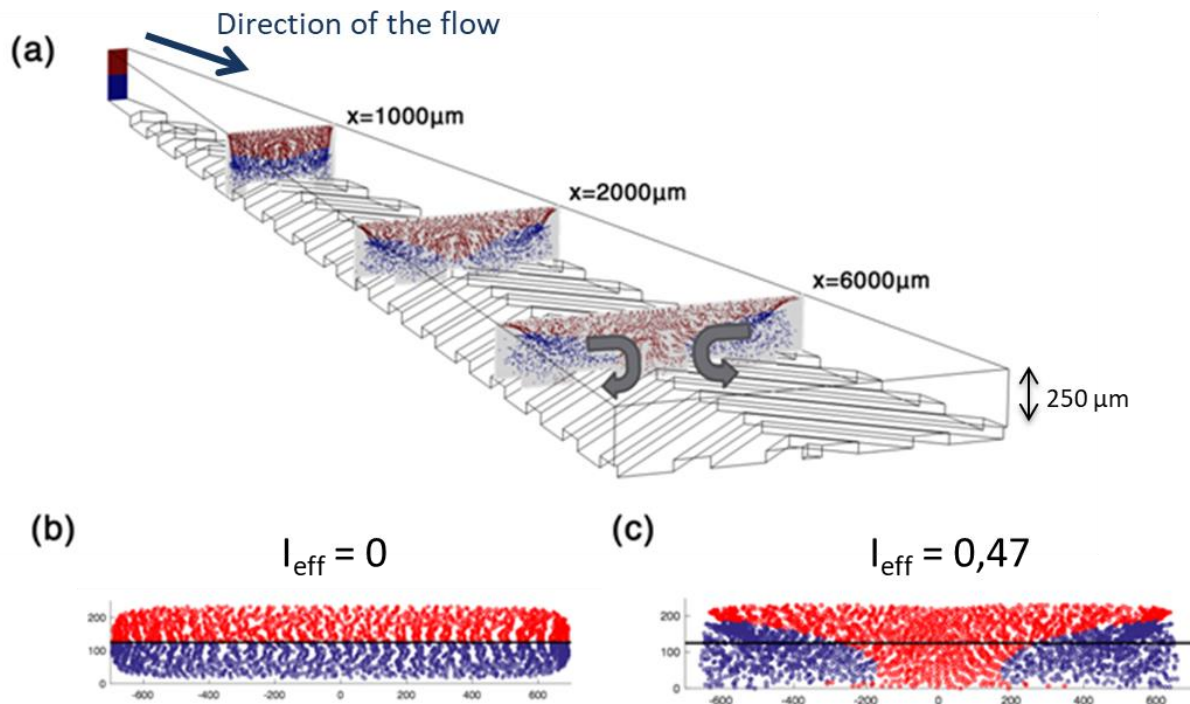


**Figure 39** Simulations of particle tracking in a  $250 \mu\text{m}$  chip with  $50 \mu\text{m}$  grooves A) in the full geometry of the chamber. 4 000 particles are introduced at the entrance of the chip (upper part, on the left) with red particles on the upper part and blue particle on the bottom part. Other cross-sections show the repartition of particles at different distances  $x$  to the entrance. Grey arrows indicate the movement induced by the flow. B) Schematic representation of the particles organization at 6 mm of the entrance for a geometry without groove C) Same representation with grooves of  $180 \mu\text{m}$  length and spaced by  $120 \mu\text{m}$ .  $I_{\text{eff}}$  is the efficiency of capture, calculated for each situation

Figure 39 (a) reports on the effect of  $50 \mu\text{m}$  grooves on the tracer distribution in cross section located at 1, 2 and 6 mm from the entrance. Simulations were performed using a flow rate of  $3 \mu\text{L}/\text{min}$  in a  $250 \mu\text{m}$  high chip. As shown by the two grey arrows, two opposite rotating movements can be distinguished in the cross sections.

To compare results of simulations in a quantitative manner, a mixing efficiency factor  $I_{eff}$  was defined as:

$$I_{eff} = \frac{\frac{\phi_{bottom}^{red}}{\phi_{up}^{red}} + \frac{\phi_{up}^{blue}}{\phi_{bottom}^{blue}}}{2}$$

With  $\phi_B^A$  the fraction of particles of the color A in the B half of the channel.

A complete mixing would be associated to an efficiency of  $I_{eff} = 1$ , whereas the absence of mixing would give a  $I_{eff}$  value of 0 (Figure 39 b).

The normal size of the fluidized bed is around 5.5 mm at 5  $\mu\text{L}/\text{min}$  and 6 mm at 10  $\mu\text{L}/\text{min}$ . Considering the differences between the b) and c) in Figure 39, we can expect to observe a high mixing inside the matrix of beads, particularly at the end of the bed. We decided to use the value of  $I_{eff}$  at 6mm of the entrance to compare different geometries.

### *b) Optimization of the parameters of the grooves*

The first optimization was performed on the central angle of the grooves, the angle between the central axis of the channel and the direction of the grooves, as defined on Figure 40 a. It has been shown that the mixing is maximal for an angle of  $45^\circ$  (Stroock et al., 2002), which is also confirmed by our simulations. We chose to follow the data given by (Stroock et al., 2002) for the depth of the grooves. They introduced a factor  $\alpha$  of 0.2 as the ratio between the depth of the grooves and the depth of the main channel. For a 250  $\mu\text{m}$  deep channel, the grooves had to be 50  $\mu\text{m}$  deep to respect the proportions. This factor hasn't been increased more at first to minimize the number of beads trapped inside the grooves.

The length of the grooves (a), and the space between each (b), were the two parameters that have been optimized through simulations (Figure 40 a). Lynn and Dandy already demonstrated that both parameters can be optimized to increase the mixing (Lynn and Dandy, 2007). Simulations have been performed and showed that mixing is maximum for  $a < b$ . This result is in good agreement with conclusions of the work of Lynn and Dandy.

Higher efficiency of mixing  $I_{eff}$  was obtained for  $a < b$ , with  $a=4b$  (green line). This first result was leading to really small values of a, whereas this value is limited by the possibility of the micro-milling process. Efficiency of mixing was also investigated for  $a=1.5b$ , with an optimum at  $a=180 \mu\text{m}$  and  $b=120\mu\text{m}$ . Another condition was considered:  $a=b$ , and had an optimum at  $a=b=175 \mu\text{m}$ . Those two last options were reachable by micro-milling.

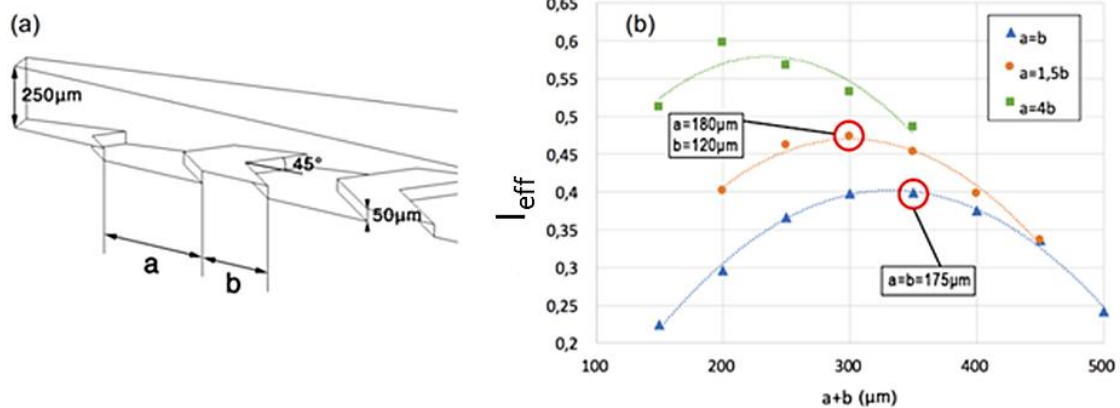


**Figure 40 (a) blueprint of the main chamber of the chip with grooves and annotations of the main characteristics and (b) graphic representation of the efficiency  $I_{eff}$  at 6 mm of the entrance evaluated as previously described as function of the geometrical parameters  $a$  and  $b$  as introduced by (Lynn and Dandy, 2007)**

Simulations showed that the flow advection induced by the patterns led to a partial rotation of the liquid flow. The best obtained results were a deformation of the flow. The geometry where  $a=4b$  was too difficult to micro-mill, so we chose to work with the two maximum represented on Figure 40 b:

$$a = b = 175 \mu m$$

$$a = 180 \mu m \text{ and } b = 120 \mu m$$

### 3. Efficiency of mixing using Herringbones design in the microfluidic magnetic fluidized bead

#### a) Visualization of flow path deformation

Molds were micro-milled in brass and chips were made of PDMS, following the conditions previously chosen:  $[a = b = 175\mu m]$  and  $[a = 180 \mu m \text{ and } b = 120 \mu m]$ . To visualize the effect of mixing, we decided to work with two different phases, one of them including a fluorophore. We investigated the mixing of two aqueous phase solutions, the first one, called S1, being composed of 50% water and 50% glycerol, the second one, called S2, was also being composed of 50% water and 50% glycerol with addition of fluorescein. The viscosity of the mixture with glycerol ( $6.88 \cdot 10^{-3} \text{ N.s/m}^2$ ) was used to limit the diffusion of the fluorophore and to make the imaging easier. S1 and S2 were simultaneously injected at  $2.5\mu\text{L}/\text{min}$  in two separate entrances leading to the same channel at the same controlled

flow rate. Parameters were adjusted to center the interface between the two phases at the center of the channel. Imaging of the flow mixing was performed by confocal microscopy (Leica DMI8, 10-fold magnification), as presented in Figure 41. Each picture is the reconstruction of a z-stack of 108 pictures spaced by  $4.27\ \mu\text{m}$ , for a total height of  $461\ \mu\text{m}$ , allowing to image the whole chip cross section.

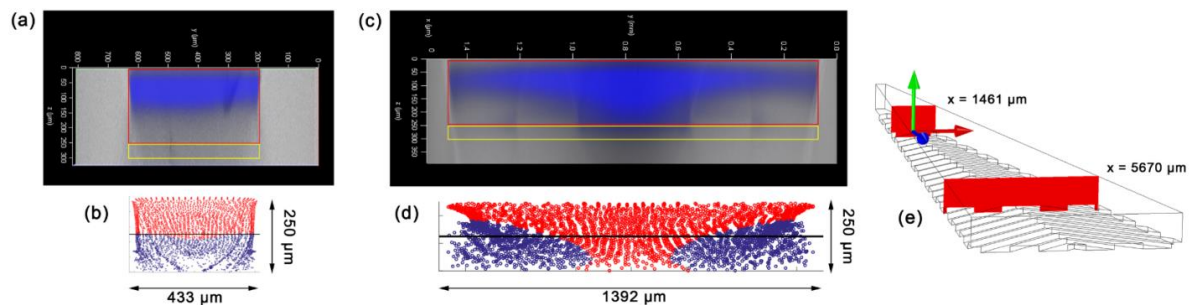


**Figure 41** Influence of the presence of grooves on the fluidized bed geometry at a flowrate of  $5\ \mu\text{L}/\text{min}$ . *a* and *c* are two pictures obtained by confocal microscopy with the corresponding prints of simulation on *b* and *d*. Confocal images are the superposition of the UV and white light scans. The red frame define the chamber and the yellow one the grooves. Pictures were taken at  $1.461$  and  $5,670\ \text{mm}$  from the entrance in a chip where  $a=180\ \mu\text{m}$  and  $b=120\ \mu\text{m}$  as illustrated on the part *e*

A very good agreement was observed between the confocal imaging and the simulations (Figure 41). A deformation of the flow could be visualized, which validated our approach with simulations. It is important to notice that these measures are qualitative and only refer to the characterization of the flow profile. At this stage, we cannot anticipate if the behavior of micro-particles inside the chamber will be similar.

### b) Effect on the bead mobility

The behavior of the beads has been observed and compared to the chip with and without herringbones grooves. As explained in the previous chapter, a channeling effect was observed in the matrix of beads once the height of the fluidized bed was increased up to  $250\ \mu\text{m}$ . To investigate the influence of the grooves on the magnetic beads motion, the area of the preferential pathway, recognized as area of low density of beads, was investigated based on grey value of the pictures (Figure 42 a and b). This area was measured and compared for the two herringbones geometries [ $a=180\ \mu\text{m}$   $b=120\ \mu\text{m}$ ] and [ $a=b=175\ \mu\text{m}$ ].

In the case of the second geometry [ $a=b=175\ \mu\text{m}$ ] with a flow rate of  $3\ \mu\text{L}/\text{min}$ , a significant difference of the area of low density in beads could be observed with a repeatability on 5 experiments (Figure 42 c). But this difference was not found with other parameters of flow ( $5$  and  $15\ \mu\text{L}/\text{min}$ ), where error bars were more important, and no significant difference was noticed.

To conclude on those observations, the area of the preferential pathway seems to expand at low flow rate in presence of herringbones structure. We were also able to notice the formation of smaller fractures that create sub-flows and increase the interactions between the fluid and the solid surface of the beads. At higher flow rate, the measure of the low density area and the observation of sub-flows could not be done, as the matrix of beads was moving faster.

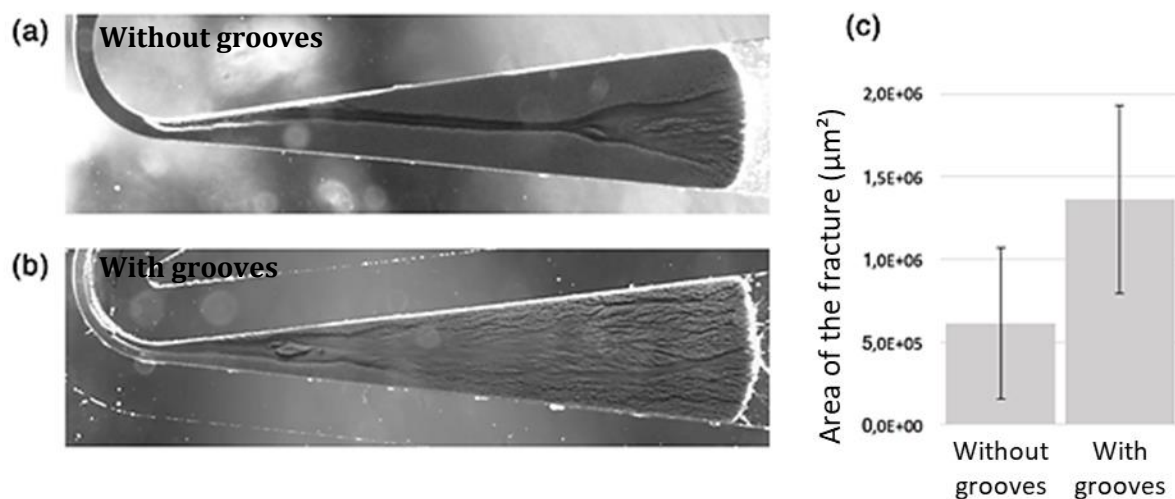


**Figure 42** a and b are pictures of the matrix of magnetic beads inside the main chamber with (b) or without (a) grooves at  $3\ \mu\text{L}/\text{min}$  in a geometry where  $a=b=175\ \mu\text{m}$ . c is a graphic representation of the area of the fracture for a chip with or without grooves at  $3\ \mu\text{L}/\text{min}$  for the geometry represented on b.

### c) Quantification of the mixing through biotin capture

In view of those first results, we investigated the potential gain provided by herringbone structures on the fluidized bed capture efficiency. The same method as presented in the previous chapter was used.  $2.8\ \mu\text{m}$  diameter Dynabeads© with streptavidin grafted on the beads surface were introduced in the chip. A solution of biotinylated fluorescent DNA at  $100\ \text{nM}$  was flowed through the matrix of beads to evaluate the efficiency of capture.

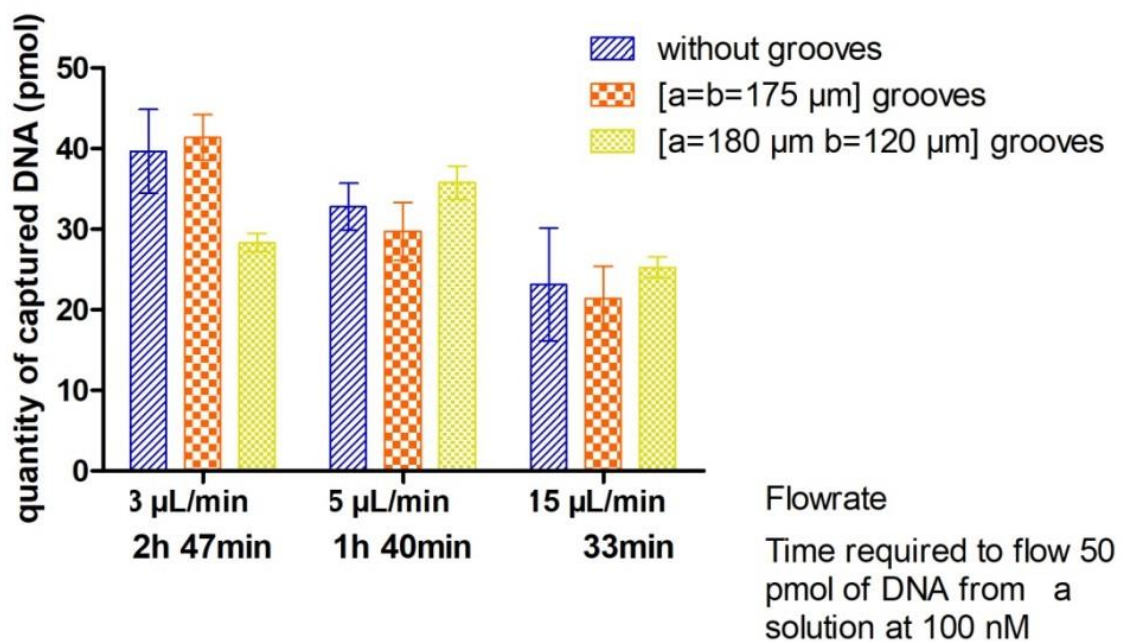


**Figure 43** Quantity of DNA captured at flowrates of 3, 5 and 15  $\mu\text{L}/\text{min}$  after flowing through the beads 50 pmol of the initial solution at 100 nM (a volume of sample of 500  $\mu\text{L}$ ) in a geometry without grooves (blue) with [a=b=175  $\mu\text{m}$ ] grooves (orange) and with [a=180  $\mu\text{m}$  b=120  $\mu\text{m}$ ] grooves (yellow). The number of experiments averaged to get those results was minimum 3

As shown in Figure 43, the flow rate of work has a significant influence on the efficiency of capture: the higher the flow rate the lower the capture efficiency. Indeed decreasing the flow rate increases the residence time of each molecule inside the matrix of beads, while decreasing the bed porosity. Unfortunately, no significant improvement has been obtained using the Herringbones geometries, as shown in Figure 43. However, another representation of this data could also show the interest to work at high flow rate. Indeed, we can compare the quantity of DNA captured at different flow rates for a given analysis time (here 1 hour), and we showed that, despite the decrease of capture efficiency, working at higher flow rate is still a better option to get a higher amount of DNA captured (if there is no limitation on the volume of the sample).



**d) Influence of the design of the grooves**

Despite these preliminary results, we decided to study new design of internal structures. Among the possibilities are side grooves (Yang et al., 2008), disorganized patterns (Camesasca et al., 2006; Reátegui et al., 2018), expanded design (Stott et al., 2010), arrow shape grooves (Jung et al., 2017), or double-sided herringbones (Wang et al., 2017). The multiple bio-applications using Herringbones mixing have encouraged the flourishing of new designs. Building on these new ideas, we decided to draw new designs for the herringbones grooves. As shown in Figure 44, six other designs have been developed and tested (Figure 44). The geometries are described on the Table 2. For each geometry, simulations have been run and capture tests using fluorescent DNA have been performed.

**Table 2 Name and description of the geometries tested**

<b>Name</b>	<b>Fig 10</b>	<b>Description</b>
<b>Geometry 1</b>	A - F	Inversion of the angle of incidence between the flow and the grooves
<b>Geometry 2</b>	B - G	Alternation of the asymmetry of the grooves
<b>Geometry 3</b>	C - H	Restriction of the grooves to the area under the fracture
<b>Geometry 4</b>	D - I	Restriction of the grooves to the area where the matrix of beads has less movement
<b>Geometry 5</b>	E - J	Disorganized patterns

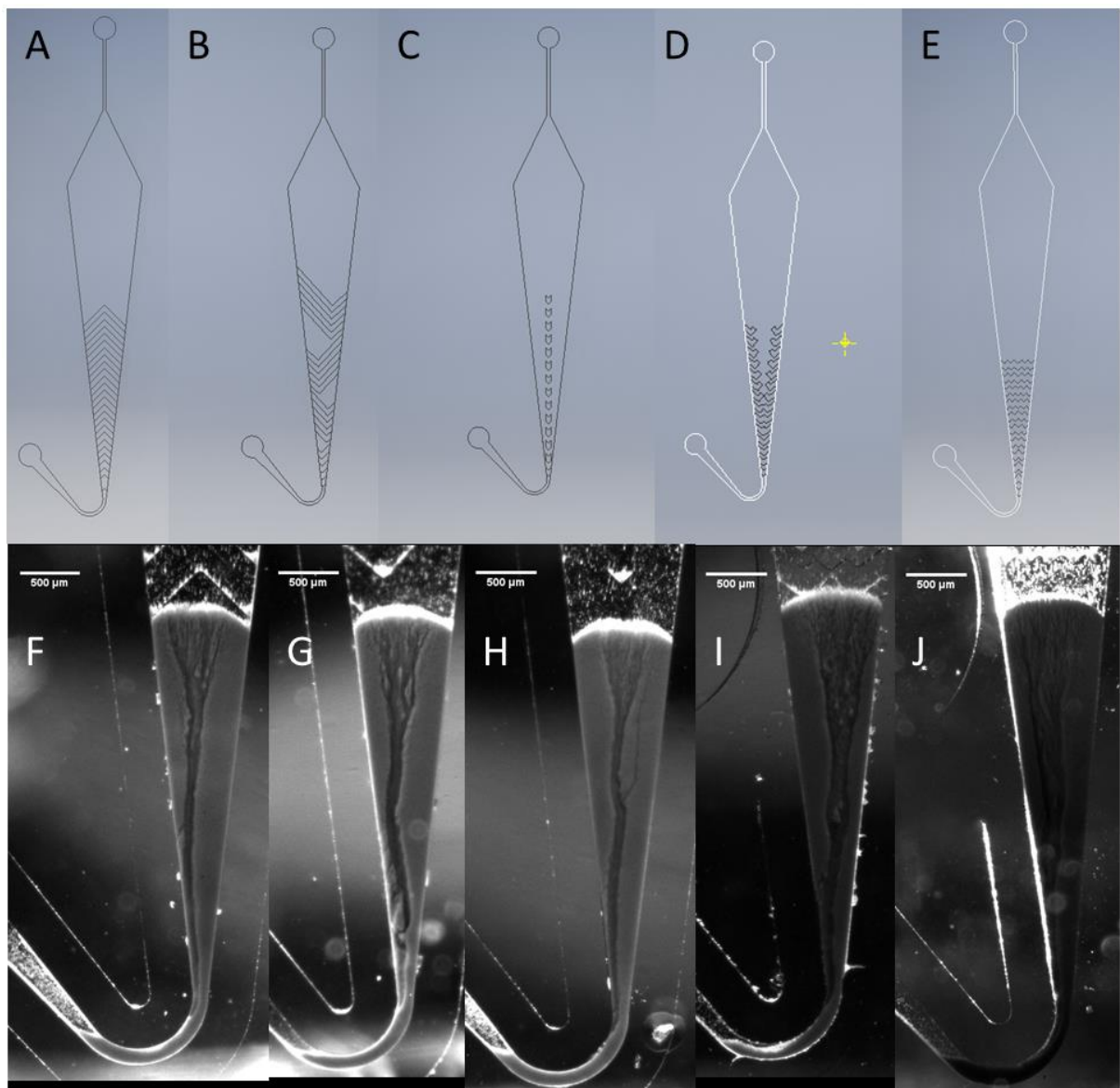


**Figure 44** Drawing and picture of the design of tested Herringbones grooves. Designs (A B C D E) were realized on Catia software©. The corresponding pictures (F G H I J) were taken in transmission mode in a devices loaded with 50  $\mu\text{g}$  of magnetic beads. The flow rate was set to 5  $\mu\text{L}/\text{min}$



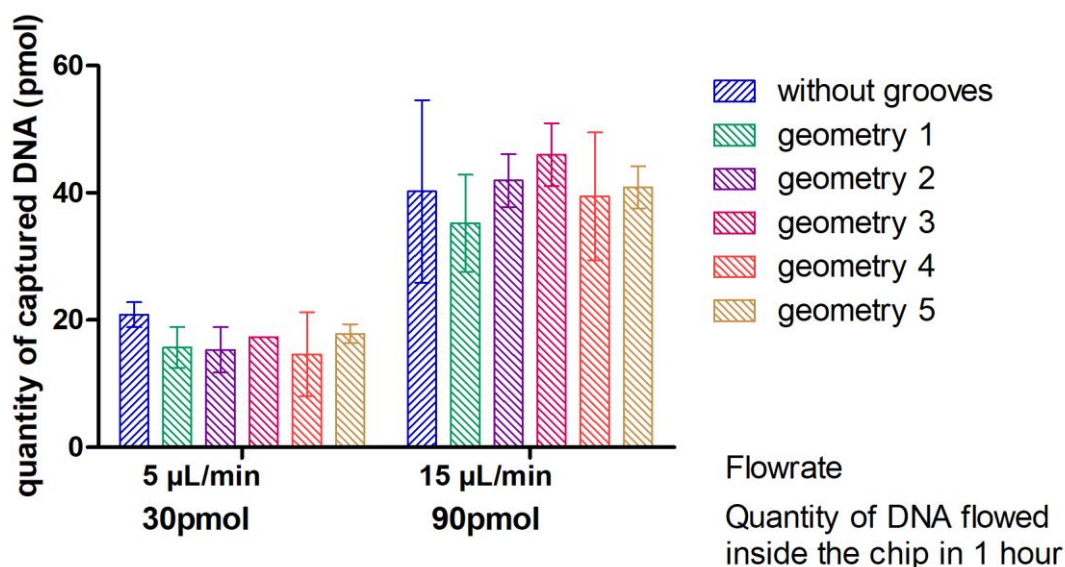
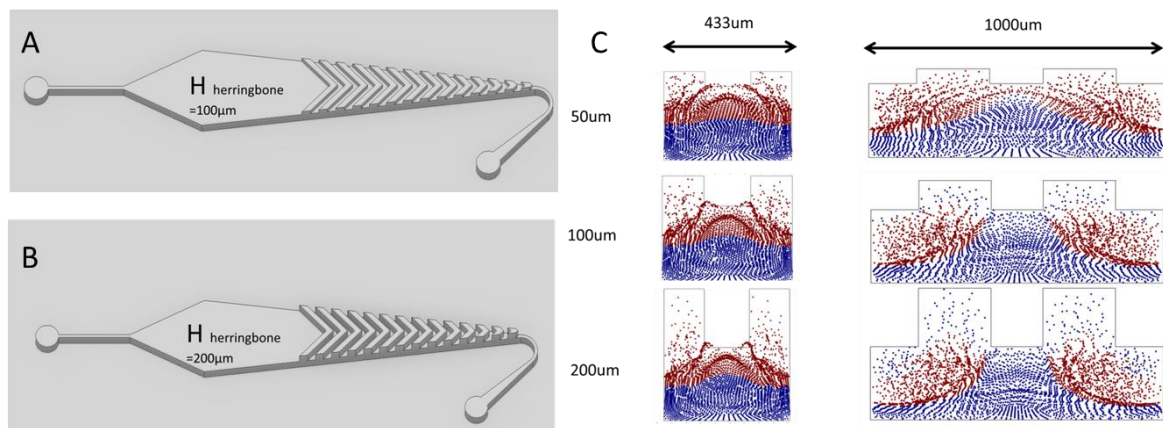


Figure 45 Quantity of DNA captured at flowrates of 5 and 15 µL/min after one hour of experiment in a geometry without grooves (blue) compared to all the geometries of Table 1.

However, none of those designs showed an increase of DNA capture efficiency as illustrated in Figure 45. No major modification of the morphology of the bed of beads was observed either. If an improvement of the design of the herringbones grooves cannot increase the capture, maybe some geometrical parameters have to be optimized for the fluidized bed experiment.

#### e) Influence of the depth of the grooves

Based on different papers (Aubin et al., 2005, Cantu-Perez et al., 2010), we investigated the importance of the depth of the grooves on the bed capture efficiency. Indeed, we suspected the height of the structure to significantly influence the flow distribution. We were assuming that the depth of the herringbones grooves was too low to induce significant advection movements. The first experiments have been performed with grooves of 50 µm deep. Here, we investigated 100 and 200 µm deep grooves (Figure 46).



**Figure 46** A and B are drawing of design realised on Catia software© for herringbones of 100 and 200  $\mu\text{m}$  and C summarize simulations with an increase of the depth of the grooves in a geometry [ $a=b=175 \mu\text{m}$ ]

Simulations with those new parameters showed an increase of the movement created inside the chamber (Figure 46 C). Unfortunately, no improvement of the capture rate was observed as only  $21.0\text{pmol} \pm 4.7\text{pmol}$  were captured at  $5\text{pmol}/\text{min}$  with grooves of  $200 \mu\text{m}$  against  $20.9\text{pmol} \pm 1.7\text{pmol}$  in standard conditions. At  $15\mu\text{L}/\text{min}$ , the capture decreased from  $40.2\text{pmol} \pm 12\text{pmol}$  in standard conditions to  $27.5\text{pmol} \pm 2.0\text{pmol}$  with  $200 \mu\text{m}$  grooves.

#### f) Inversion of the place of Herringbones to avoid anchoring

One hypothesis that would explain the limited impact of the herringbone structures on the fluid flow is the anchoring effect. The structures in the chamber may immobilize the fluidized bed particles.

Indeed, because of the orientation of the magnetic field, beads organized themselves as clusters with a column shape. Those columns of beads are inclined to follow the magnetic field lines (Figure 47 a) (Pereiro, 2016). There is thus a possibility that the grooves induces an anchoring of the clusters and prevent them from moving. Without re-circulation, the matrix of beads can not be homogenized and a fracture appears.

The grooves structures have been first implemented in the top part of the chip, for simplicity of fabrication. We expect the anchoring effect to be stronger with structure at the top due to the asymmetry in the magnet position. To test this hypothesis, chips with grooves at the bottom were fabricated. The behavior of beads was different on this line of view, as

the recirculation was observed from below. The central part seemed motionless, and movement was observed only on the border of the chamber (Figure 47 b).

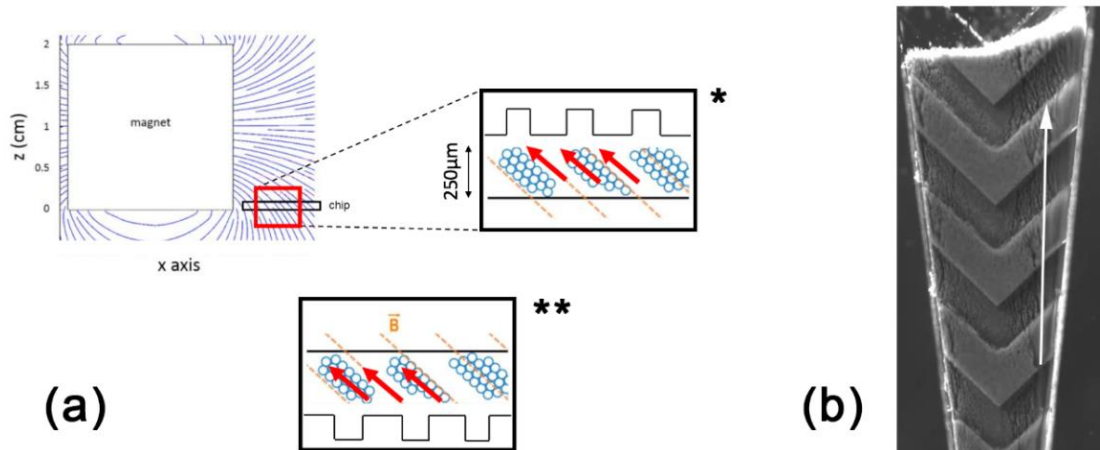


**Figure 47** Schematic representation of the clusters formation inside a chip with grooves (a). If grooves are on the top, columns of beads are drifted to the grooves (\*) whereas with grooves on the bottom art, clusters are drifted out (\*\*)(Pereiro, 2016). (b) Picture of the magnetic beads inside a chip with grooves on the bottom.

Capture efficiency was tested as previously described (Figure 48). However, the efficiency of capture seemed to be reduced in this new geometry. So there was no clear improvement of the capacity of capture. In a similar manner, chips with grooves on both the top and the bottom of the chip have been evaluated, without any significant improvement of the capture rate (Figure 48).

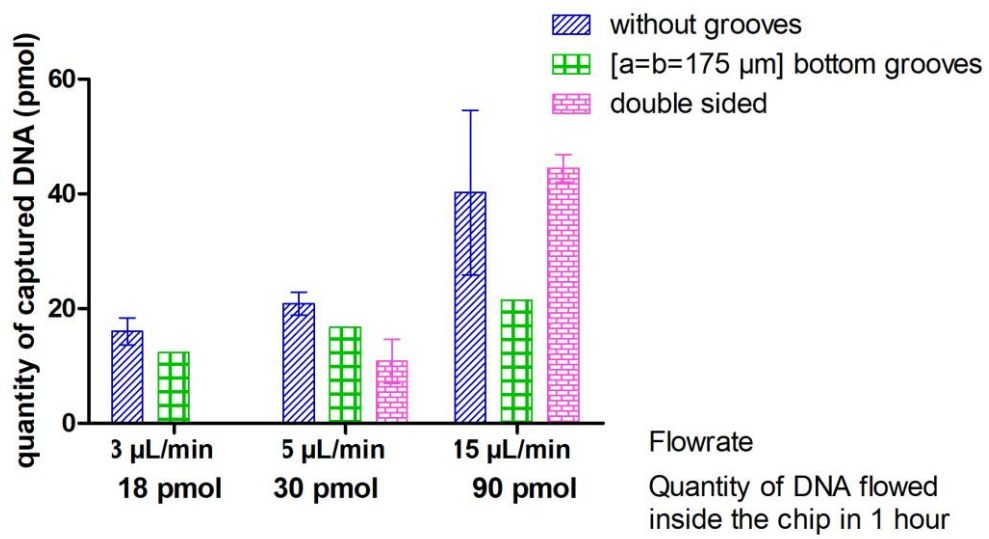


**Figure 48** Graphic representation of the quantity of DNA captured at flowrates of 5 and 15  $\mu\text{L}/\text{min}$  after one hour of experiment in a geometry without grooves (blue) compare to bottom grooves (green) and to double sided (top and bottom) grooves (magenta)

#### 4. Perspectives

This chapter showed that passive mixers are difficult to adapt to the system of fluidized bed. Herringbones grooves could be added to the chip and a significant influence on the fluid distribution could be observed. We tried to improve:

- The design of the grooves
- The depth of the grooves
- The anchoring of clusters of beads

However, we were not able to observe a significant influence on the movement inside the matrix of beads and on the capture efficiency. There are several possible explanations for this result. The most likely is that the movement induced on the flow was not high enough to modify the initial organization and motion the magnetic beads.

Comsol® simulations have shown that speeds perpendicular to the flow are ten times smaller than the ones in the direction of the flow. Then a factor ten can also be found between the drag force due to the herringbones grooves and the drag force generated by the flow from the inlet to the outlet. As the magnetic force is of the same order of magnitude as the second drag force, it could explain the difficulty to see an effect on the beads.

That's the reason why we decided to test new way to improve the mixing either directly on the matrix of beads, or with addition of active mixers.

## 5. Material and method

Chips were realized by pouring polydimethylsiloxane (PDMS) on brass micro-milled mold. Micro-milling was realized on a Mini-Mill by Minitech Machinery Corp. with drills of 0.2 X 0.4  $\mu\text{m}$ , 0.3 X 0.6  $\mu\text{m}$  and 1 X1  $\mu\text{m}$ . The bonding was performed through oxygen plasma. Surface treatment was performed using PDMA-AGE 0.5%, with one hour incubation.

Confocal images were acquired on a Leica DM18 microscope with a 10-fold objective. Solutions were prepared using glycerol (Sigma Aldrich,  $\geq 99.5\%$ ).

Streptavidin modified Dynabeads® M-280 (2.8 $\mu\text{m}$  in diameter, Dynabeads®, Thermofisher) were used for specific capture experiments. 250  $\mu\text{m}$  chips were filled with 250  $\mu\text{g}$  of beads. All beads were washed three times in buffer solution before use following the data sheet protocol.

Biotinylated DNA conjugated to a biotin and a fluorophore Alexa488 was buy from IDT®. DNA was then diluted in a Tris-EDTA buffer, and the concentration was adjusted with PBS (Sigma Aldrich). The sequence ordered with HPLC purification was:

/5BiosG/CTCTCTCTCTCTCTCTCT/3AlexF488N/

## Bibliography

- Aubin, J., Fletcher, D.F., and Xuereb, C. (2005). Design of micromixers using CFD modelling. *Chem. Eng. Sci.* *60*, 2503–2516.
- Camesasca, M., Kaufman, M., and Manas-Zloczower, I. (2006). Staggered passive micromixers with fractal surface patterning. *J. Micromechanics Microengineering* *16*, 2298.
- Cantu-Perez, A., Barrass, S., and Gavriilidis, A. (2010). Residence time distributions in microchannels: Comparison between channels with herringbone structures and a rectangular channel. *Chem. Eng. J.* *160*, 834–844.
- Capretto, L., Cheng, W., Hill, M., and Zhang, X. (2011). Micromixing Within Microfluidic Devices. In *Microfluidics*, (Springer, Berlin, Heidelberg), pp. 27–68.
- Cha, J., Kim, J., Ryu, S.-K., Park, J., Jeong, Y., Park, S., Park, S., Kim, H.C., and Chun, K. (2006). A highly efficient 3D micromixer using soft PDMS bonding. *J. Micromechanics Microengineering* *16*, 1778.
- D'Errico, G., Ortona, O., Capuano, F., and Vitagliano, V. (2004). Diffusion Coefficients for the Binary System Glycerol + Water at 25 °C. A Velocity Correlation Study. *J. Chem. Eng. Data* *49*, 1665–1670.
- Erbacher, C., Bessoth, F.G., Busch, M., Verpoorte, E., and Manz, A. (1999). Towards Integrated Continuous-Flow Chemical Reactors. *Microchim. Acta* *131*, 19–24.
- He, B., Burke, B.J., Zhang, X., Zhang, R., and Regnier, F.E. (2001). A Picoliter-Volume Mixer for Microfluidic Analytical Systems. *Anal. Chem.* *73*, 1942–1947.
- Hinsmann, P., Frank, J., Svasek, P., Harasek, M., and Lendl, B. (2001). Design, simulation and application of a new micromixing device for time resolved infrared spectroscopy of chemical reactions in solution. *Lab. Chip* *1*, 16.
- Hong, C.-C., Choi, J.-W., and Ahn, C.H. (2004). A novel in-plane passive microfluidic mixer with modified Tesla structures. *Lab. Chip* *4*, 109–113.
- Ismagilov, R.F., Stroock, A.D., Kenis, P.J.A., Whitesides, G., and Stone, H.A. (2000). Experimental and theoretical scaling laws for transverse diffusive broadening in two-phase laminar flows in microchannels. *Appl. Phys. Lett.* *76*, 2376–2378.

- Johnson, T.J., Ross, D., and Locascio, L.E. (2002). Rapid Microfluidic Mixing. *Anal. Chem.* 74, 45–51.
- Jung, Y., Hyun, J., Choi, J., Atajanov, A., and Yang, S. (2017). Manipulation of cells' position across a microfluidic channel using a series of continuously varying herringbone structures. *Micro Nano Syst. Lett.* 5, 6.
- Kamholz, A.E., Weigl, B.H., Finlayson, B.A., and Yager, P. (1999). Quantitative Analysis of Molecular Interaction in a Microfluidic Channel: The T-Sensor. *Anal. Chem.* 71, 5340–5347.
- Kim, D.S., Lee, S.H., Kwon, T.H., and Ahn, C.H. (2005). A serpentine laminating micromixer combining splitting/recombination and advection. *Lab. Chip* 5, 739–747.
- Kumar, V., Paraschivoiu, M., and Nigam, K.D.P. (2011). Single-phase fluid flow and mixing in microchannels. *Chem. Eng. Sci.* 66, 1329–1373.
- Le The, H., Le Than, H., Dong, T., Quoc Ta, B., Tran-Minhb, N., and Frank, K. (2015). An effective passive micromixer with shifted trapezoidal blades using wide Reynolds number range.
- Löb, P., Drese, K.S., Hessel, V., Hardt, S., Hofmann, C., Löwe, H., Schenk, R., Schönfeld, F., and Werner, B. (2004). Steering of Liquid Mixing Speed in Interdigital Micro Mixers – From Very Fast to Deliberately Slow Mixing. *Chem. Eng. Technol.* 27, 340–345.
- Lynn, N.S., and Dandy, D.S. (2007). Geometrical optimization of helical flow in grooved micromixers. *Lab. Chip* 7, 580–587.
- Mengeaud, V., Josserand, J., and Girault, H.H. (2002). Mixing Processes in a Zigzag Microchannel: Finite Element Simulations and Optical Study. *Anal. Chem.* 74, 4279–4286.
- Miyake, R., Tsuzuki, K., Takagi, T., and Imai, K. (1997). A highly sensitive and small flow-type chemical analysis system with integrated absorptiometric micro-flowcell. In *Proceedings IEEE The Tenth Annual International Workshop on Micro Electro Mechanical Systems. An Investigation of Micro Structures, Sensors, Actuators, Machines and Robots*, pp. 102–107.
- Nguyen, N.-T., and Wu, Z. (2005a). Micromixers—a review. *J. Micromechanics Microengineering* 15, R1–R16.



Nguyen, N.-T., and Wu, Z. (2005b). Micromixers—a review. *J. Micromechanics Microengineering* 15, R1.

Pereiro, I. (2016). Microfluidic magnetic fluidized bed for bioanalytical applications. phdthesis. Université Pierre et Marie Curie - Paris VI.

P. Sudarsan, A., and M. Ugaz, V. (2006). Fluid mixing in planar spiral microchannels. *Lab. Chip* 6, 74–82.

Reátegui, E., Vos, K.E., Lai, C.P., Zeinali, M., Atai, N.A., Aldikacti, B., Floyd, F.P., Khankhel, A., Thapar, V., Hochberg, F.H., et al. (2018). Engineered nanointerfaces for microfluidic isolation and molecular profiling of tumor-specific extracellular vesicles. *Nat. Commun.* 9, 175.

Stott, S.L., Hsu, C.-H., Tsukrov, D.I., Yu, M., Miyamoto, D.T., Waltman, B.A., Rothenberg, S.M., Shah, A.M., Smas, M.E., Korir, G.K., et al. (2010). Isolation of circulating tumor cells using a microvortex-generating herringbone-chip. *Proc. Natl. Acad. Sci.* 107, 18392–18397.

Stroock, A.D., Dertinger, S.K.W., Ajdari, A., Mezić, I., Stone, H.A., and Whitesides, G.M. (2002). Chaotic Mixer for Microchannels. *Science* 295, 647–651.

Tabnaoui, S. (2012). Magnetic fluidized bed for sample preconcentration and immunoextraction in microfluidic systems (Paris 6).

Tamara M. Floyd, †, Martin A. Schmidt, § and, and Klavs F. Jensen\*, † (2004). Silicon Micromixers with Infrared Detection for Studies of Liquid-Phase Reactions.

Vijayendran, R.A., Motsegood, K.M., Beebe, D.J., and Leckband, D.E. (2003). Evaluation of a Three-Dimensional Micromixer in a Surface-Based Biosensor. *Langmuir* 19, 1824–1828.

Wang, M., Wang, Z., Zhang, M., Guo, W., Li, N., Deng, Y., and Shi, Q. (2017). A microfluidic chip with double-sided herringbone microstructures for enhanced capture of rare tumor cells. *J. Mater. Chem. B* 5, 9114–9120.

Whitesides, G.M. (2006). The origins and the future of microfluidics. *Nature* 442, 368–373.

Wong, S.H., Bryant, P., Ward, M., and Wharton, C. (2003). Investigation of mixing in a cross-shaped micromixer with static mixing elements for reaction kinetics studies. *Sens. Actuators B Chem.* 95, 414–424.

---

Woo Lim, T., Son, Y., Jin Jeong, Y., Yang, D.-Y., Kong, H.-J., Lee, K.-S., and Kim, D.-P. (2011). Three-dimensionally crossing manifold micro-mixer for fast mixing in a short channel length. *Lab. Chip* 11, 100–103.

Wu, S.-J., Hsu, H.-C., and Feng, W.-J. (2014). Novel design and fabrication of a geometrical obstacle-embedded micromixer with notched wall. *Jpn. J. Appl. Phys.* 53, 097201.

Yang, J.-T., Fang, W.-F., and Tung, K.-Y. (2008). Fluids mixing in devices with connected-groove channels. *Chem. Eng. Sci.* 63, 1871–1881.



## Chapter 3

### Active mixing in microfluidic fluidized bed

#### 1. Introduction

As reported in the previous chapter, the passive mixers implemented in the fluidized bed have not been able to significantly improve the particle mobility in the bed. We thus considered that an active approach could be an interesting alternative to increase the movement of particles inside the fluidized bed. Contrary to passive approaches, active mixing gathers technologies requiring addition of an external energy input to initiate perturbations. It usually implies the integration of power sources and actuators, and may result in more complex fabrication processes. Even if, from a certain point of view, they can be considered as less convenient than passive mixers, active mixers are usually able to reach higher mixing efficiency and provide some additional flexibility such as the possibility to be turned on or off.

In this chapter, we will report on the use of active mixing approaches to enhance the mobility of particles in the fluidized bed. A special care will be taken regarding the compatibility of these approaches to trigger acoustic, electrokinetic or thermal effects that could be detrimental for the biomolecular species or markers to be detected.

### Pressure field fluctuations

The simplest way to induce mixing during the injection of liquid in microdevice is to create a modulation on the pressurization of the flow. This type of mixers appeared in 2000, in a paper from Deshmukh et al who introduced the notion of pulsatile micro-pumps (Deshmukh et al., 2000). In order to mix two liquids, the researchers published a system of bubbles acting like pistons in the liquid and going through the main channel one after the other (Figure 49). Bubbles were created by an increase of temperature, and could close valves on the fluidic way. Figure 49 B shows the mixing efficiency of this approach at 3.5mm/s and 3 Hz.

The use of segmented flow mixing has been further developed with addition of external micro-pumps (Fujii et al., 2003; Glasgow and Aubry, 2003; Niu and Lee, 2003) or integration of internal micro-pumps (Deshmukh et al., 2001; Lei and Li, 2008). Fujii and al. evaluated the efficiency of mixing using the bioluminescence of an enzymatic reaction: luciferin (solution A) and adenosine triphosphate (ATP) (solution B). Measuring the fluorescent signal along the channel allowed an optimization of the frequency of pumping, with an optimum between 40 and 100 Hz. Performances were strongly dependent on the frequency of alternation of the pressure disturbance (switch frequencies between 1 to 1 000 Hz have been explored).

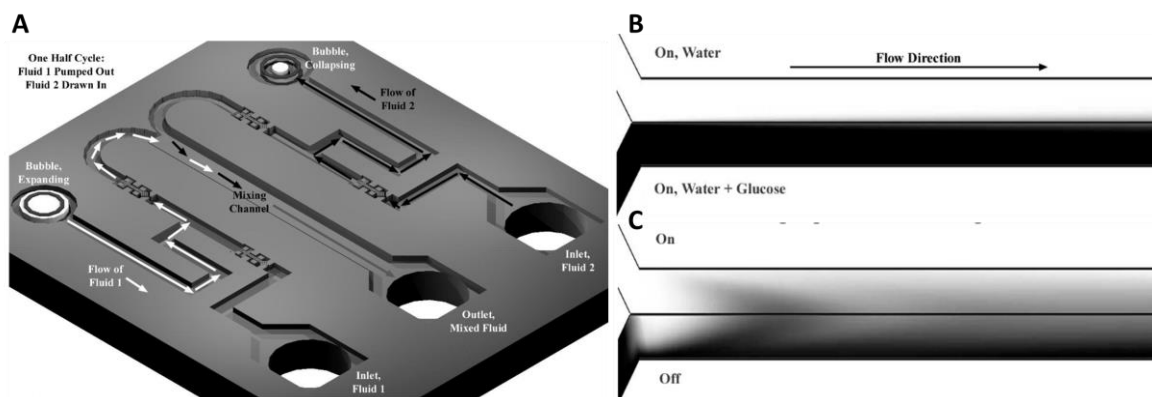


**Figure 49 A Schematic representation of the micromixer design and mixing of water and water with glucose in a 400  $\mu\text{m}$  wide channel at 6 mm/s ( $Re = 2.4$ ) with only diffusion (B) or with pulsatile micro-pumps system at a frequency of 3 Hz (Deshmukh et al., 2000)**

Pressure field fluctuations systems have the advantage of accurate control of the agitation induced, and high degree of flexibility and reproducibility at low Reynolds number. However, they require complex micro-fabrication processes to integrate all systems of pumps.

### Electrokinetic mixing

Mixing can also be induced by the fluctuation of an electric field passing through a microfluidic channel or chamber (Glasgow et al., 2004; Posner and Santiago, 2006; Qian and Bau, 2002; Tang et al., 2002). A fluctuating electric field can be used to create instabilities inside a flow by addition of electrodes perpendicular to the main channel of the fluidic path. Electrokinetics is a broad field that includes electroosmosis (mostly discussed here), electrophoresis, electrowetting and dielectrophoresis. In this paragraph, we will focus on the three first ones. Dielectrophoretic movement will be detailed in the next paragraph.

Electric field applied by electrodes through the flow directly acts on the buffer where ions are dissolved. It creates a Coulomb force on mobile electric charges at the interface between the electrodes and the solutions and moves the ions. The interface between the two fluids to mix will be stretched and folded, thus it reduces diffusion distance in the fluid and induces a stirring effect.

Oddy and al. introduced two micromixers based on electrokinetic flow instabilities, both able to work at Reynolds number around 1 (Oddy et al., 2001). The first one was used for a proof of concept of stirring by electrokinetic instabilities: 10 Hz and 1kV were enough to see the apparition of transversal flows. The second one, presented in Figure 50 A, was designed to continuously or intermittently work with small volumes and mixing was confined in a small chamber (0.1 $\mu$ L). Experiments were performed with an alternating current, at 4kV and 5 Hz, and could demonstrate at 0.5  $\mu$ L/min a mixing effect 100 times faster than in a usual Y-shape channel. Figure 50 B showed two fluids, one with and one without dye, moved from left to right inside the central chamber. AC field was applied between the second and the third picture and the intermediate surface is immediately deformed, up to a repartition almost uniform of the dye. This system could be adapted to PDMS, PMMA and glass materials, using buffers such as deionized water, borate or HEPES.

By an optimization of the position of the electrodes (introduction of an angle between them) Fang Yang and al. demonstrated an efficiency of mixing  $10^3$  times faster than the molecular diffusion process (Yang et al., 2017). Experiments were performed at 5 $\mu$ L/min, using two liquids with a conductivity ratio of 100, an AC voltage of 16 V and a frequency of 10 kHz.

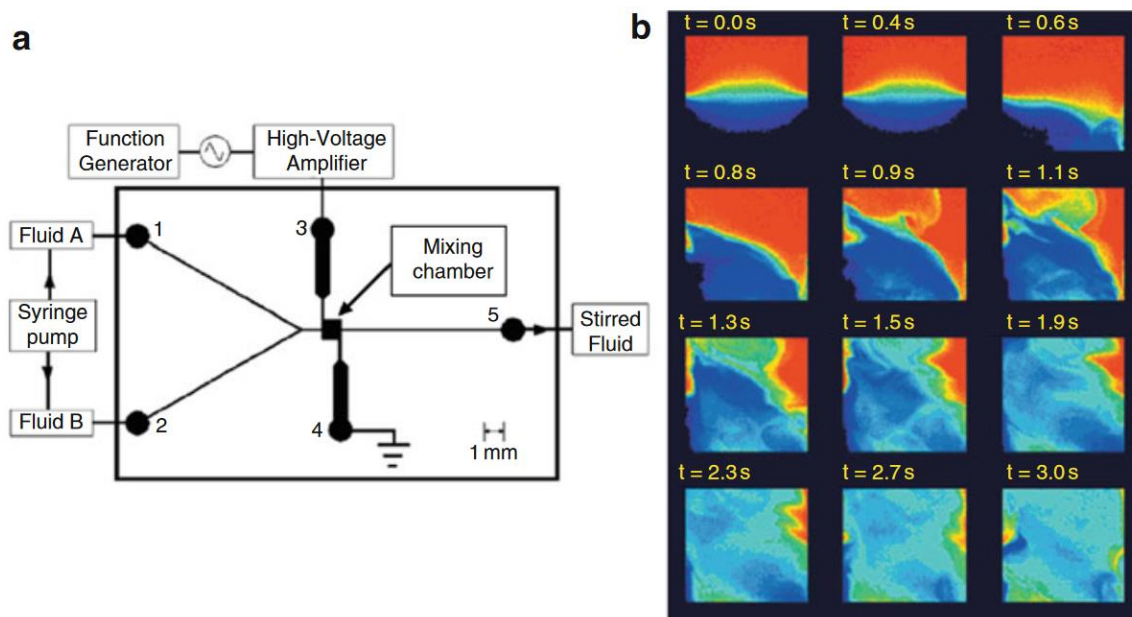


**Figure 50** A Design of the electrokinetic micromixer and B pictures of motion of two fluids, one with red dye and one with blue dye inside the mixing chamber after application of an AC field (Oddy et al., 2001)

Electrokinetic systems are advantageous as they can be fabricated at low cost using soft lithography. They also provide an accurate control of the mixing mechanisms. However, one of the drawbacks of those systems is that the transversal movement created inside the flow does not increase with the flow rate of the main flow, limiting the range of accessible flow rate (Campisi et al., 2009). Moreover, those systems are usually working at high voltages; they are prone to increase the temperature due to Joule effect. This can be minimized by choosing an appropriate buffer. However, it could be a limitation when working with fragile biological samples.

#### Dielectrophoretic mixing

Dielectrophoretic mixing is based on the movement of particles or biological elements polarized in a non-uniform electrical field (Deval et al., 2002; Lee and Voldman, 2007). Electrophoresis relies on the charge-to-size ratio whereas dielectrophoresis uses dielectric properties of the materials. Those elements move to or from an electrode, responding to positive and negative dielectrophoretic forces as shown on Figure 51 (Khoshmanesh et al., 2011). Movements are guided by the form and the configuration of the electrodes.

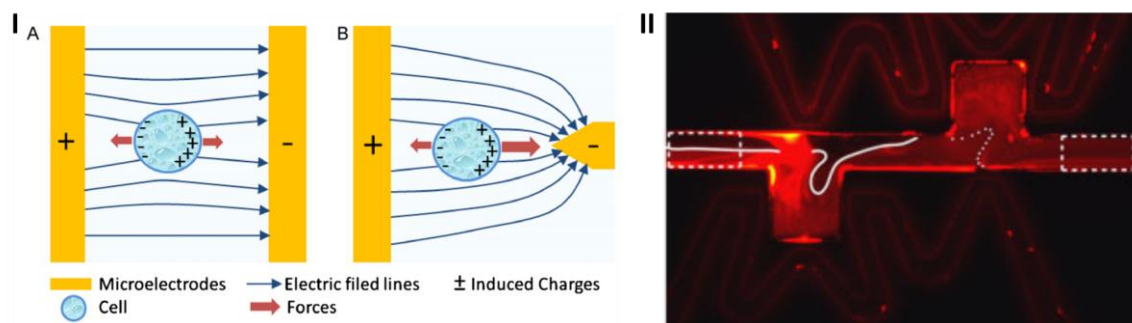


**Figure 51** I Basic diagram of the polarization of a bio-particle in a (A) uniform or (B) non uniform electric field (Khoshmanesh et al., 2011) II Pictures of the flow at 0.005 mL/h (300  $\mu$ L/min) after application of an electric field of 300 V and 600 kHz for a flow from left to right visualization is performed using a Rhodamine B solution (Salmanzadeh et al., 2011)

The movement of the charged particles in the solution can generate chaotic advection that causes mixing mechanism inside the chamber filled by ions. Salmanzadeh et al. presented a device based on dielectrophoresis to induce mixing without contact between the electrodes and the liquid (Salmanzadeh et al., 2011). Stretching and folding of the interface was visualized using fluorescent micro-beads in one half of the channel (Figure 51 II). For an electric field of 300 V and 600 kHz (optimized conditions), they reached a mixing index of 80% at 0.005 mL/h.

This type of micro-mixers does not require a complexification of the fluidic path, which makes its application easier. Moreover, this approach is very interesting in our configuration since dielectrophoretic forces are directly applied on particles and not on the liquid flow. It would allow a direct control of the particles motion in the fluidized bed. However, as previously discussed, temperatures increase due to electrical current established in the channels can be an issue for biomolecular species. Integration of electrodes to the design may require specific equipment, heavy and unwieldy.

#### Magneto-hydrodynamics

Magnetic forces can be used to force mixing inside micro-channels (Bau et al., 2001; Oh et al., 2007; West et al., 2002). In the approach proposed by Cao et al, micro-magnets are patterned around the fluidic channel to create potential difference and are supported by an external alternative magnetic field (Cao et al., 2015). The magnetic force depends on the gradient and on the direction of the applied magnetic field. Magnetic nano-particles (15 nm of diameter) are then used to improve the mixing inside a solution with addition of a fluctuating magnetic actuation, up to chaotic advection. As shown in Figure 52 A, B and C,



addition of magnetic components can create forces able to deform and stretch interfaces, to enhance mixing compared with a standard configuration based on diffusion (Figure 52 A a). It is possible to reach a mixing of more than 90% after 6s of flow at 600  $\mu\text{m}$  of the inlet (Figure 52 B) in the case of an external magnetic field  $B = 0.05\text{T}$  added to the magnetic actuation with a frequency of 10 Hz and a speed of fluid of 150  $\mu\text{m/s}$ .

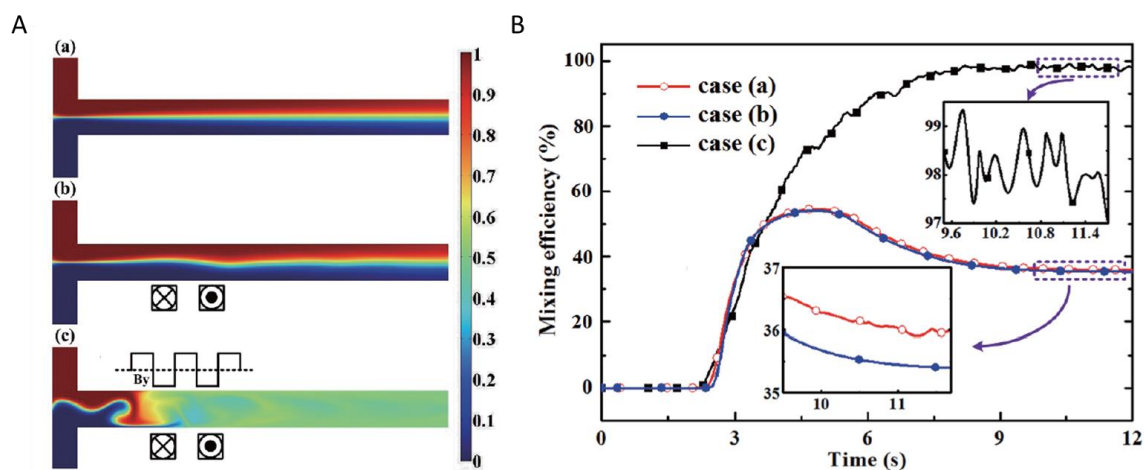


**Figure 52 A Concentration field of two streams (ferro-fluid and DI water) in a T-shape geometry (a) without magnetic actuation (b) with magnetic actuation but without external magnetic field (c) with magnetic actuation and external magnetic field and B Mixing efficiency in the main channel for each strategies (Cao et al., 2015)**

This approach bypasses the problems linked to Joule effect and complex micro-fabrication. It needs a magnetic support to mix. The example presented here relies on mixing of two fluids. Handling of magnetic particles has been introduced in the first part of this manuscript. Moreover, this technique is well adapted to fluidic mixing; however, it is still less easily adjustable to micro-particles agitation, its adaptation to a matrix of micrometric particles remains a challenge.

As previously discussed, magnetic particles organize themselves into columns. This property has been used to create actuators such as pumps or valves. Thus, beads were used to geometrically close the access to a channel (Terray et al., 2002). They could also enhance the flow of liquid up to 200 fL/s (200  $\mu\text{m}^3/\text{s}$ ) by their rotation induced by optical tweezers (frequency of rotation up to 10 Hz using the transfer of a spin angular momentum from a circularly polarized laser beam) (Leach et al., 2006). Those columns can be stabilized by addition of smaller beads or polymers to form magnetically driven cylinders. By addition of an external rotating magnetic field (created by two perpendicular pairs of Helmholtz coils), Biswal et al. induced rotation of the cylinders inside the “Y” junction. They demonstrated the

apparition of secondary flows that could enhance the mixing (Biswal and Gast, 2004). They were able to show that the mixing efficiency is dependent to the flexibility of the chains and to the frequency of the rotating magnetic field. If the chains are too rigid and the frequency too high, structures broke under the pressure of the flow, and the mixing became less efficient. The issue could be bypassed using more flexible chains that will bend. The advantage of this technic is that magnetic cylinders can be created directly inside a micro-channel, or easily added to the solutions before injection. However, the construction of a fully controlled magnetic field is more difficult but simple stir plate can produce an efficient mixing too.

Magnetic fields can be coupled to electric field to create Lorentz forces in the fluid and induce mixing. Such systems are called magneto hydrodynamic (MHD) stirrers. They are based on deposition of electrodes around a microfluidic channel. When an electrolyte solution is injected inside the chip, alternating potential is applied on the electrodes inducing a current in various directions in the solution. When a magnetic field is added, the coupling induces Lorentz forces formation in the fluid, perpendicular the both fields. MHD systems have been used to create micro-pumps (Jang and Lee, 2000). By changing the orientation of the electrodes (transversal direction against the channel) Bau et al. shown the possibility to create flows in different directions (Bau et al., 2001). As shown on Figure 53, the activation of electrodes could create a deformation of the lines of separation between the two liquids. The deformation could almost be resorbed as the polarity of the electrodes was inverted because diffusion process was slower (Figure 53 A a-b). This method has been applied in different situations, such as circulatory fluid motion. MHD stirrer has been used to increase the interfacial area between two liquids in this particular geometry (West et al., 2003). As presented on Figure 53 B, the initial mixing was clearly induced by the MHD stirrer, once the interfacial area between the two liquids was increased, diffusion dominated.

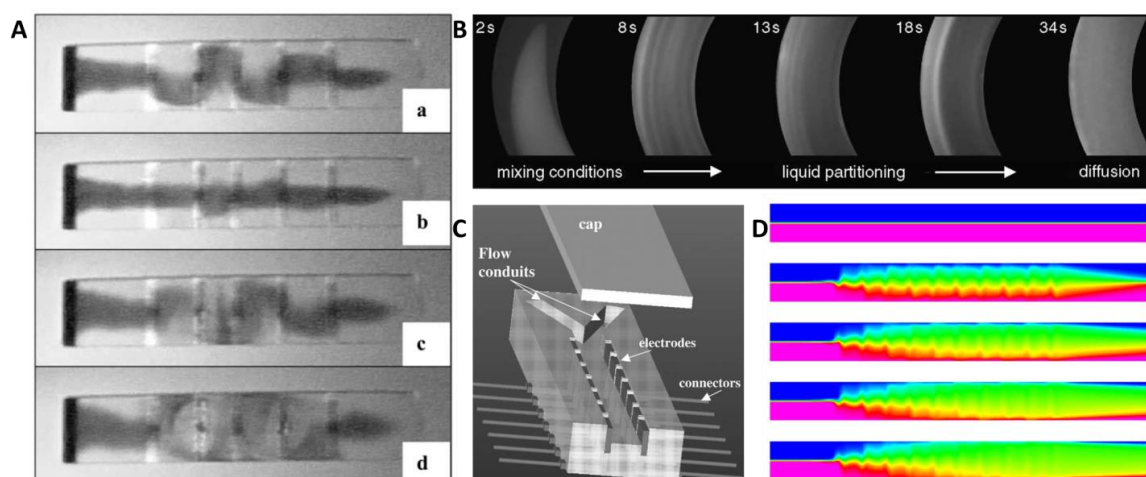


**Figure 53** *A Pictures of the deformation of a dye line in a transparent liquid with activation of the electrodes (a) inversion of the polarity of the electrodes (b) deformation due to the Lorentz forces (c) up to the formation of eddies (d) (Bau et al., 2001) B Pictures of the evolution of mixing in a circular channel at an average velocity of 7.6 mm/s (West et al., 2003). C schematic representation of the MHD stirrer D Schematic representation of the evolution over time of the special distribution of two initially separated fluids at a flowrate of 5 mm/s (Qian and Bau, 2005)*

This kind of mixer does not need the addition of any moving part as shown on Figure 53 C. It can easily be implemented on a system in flow (Figure 53 D Qian and Bau, 2005) even at high flow rates (up to tens of mm/s). However, the creation and geometry of the electrodes can be complex. And as the magnitude of the magnetic forces is proportional to the fluid volume in question, this system has difficulties with the scale down.

#### Ultrasound and acoustic disruptions

Ultrasounds and acoustic waves can also be used to modify a flow pattern. For instance, ultrasounds can be produced by addition of piezoelectric ceramic transducers to the chip (Yang et al., 2001; Yaralioglu et al., 2004). Martin Bengtsson and Thomas Laurell described a system to create vortex flow inside any geometry by introduction of lateral acoustic flow, or Rayleigh flow (Bengtsson and Laurell, 2004). High frequency (around 5 MHz) ultrasounds were used to produce acoustic standing waves of the same dimension than the geometry chosen, a Y-shape channel (30 mm long 300  $\mu\text{m}$  deep and 75  $\mu\text{m}$  wide). As mixing became less efficient when the flow rate increases, complete mixing was observed for flow rates lower than 4  $\mu\text{L}/\text{min}$  while efficient (meaning more efficient than diffusion) mixing is achieved for flows rates lower than 20  $\mu\text{L}/\text{min}$ . One of the main issues of those systems still is the temperature increase induced by the transducers. This effect can be controlled either

by implementation of cooling systems or be advantageously used by using this heat generated to enhance temperature sensitive reactions.

This acoustic based mixing can be applied to objects inside the flow, such as small particles or air bubbles (Ahmed et al., 2009; Liu et al., 2003; Yang et al., 2001). In the latter cases, the interface with the fluid acted like a vibrating membrane under the action of the sound field, creating a bulk fluid movement. Moreover, cavitation bubbles vortices can appear in channels creating mixing as exposed in Figure 54 (Dong et al., 2016). The results of their work showed a significant reduction of the time required for mixing, approximately 20 times lower than diffusion only. This system can work at wide range of Reynolds number (3 to 100), even if the cavitation activity is reduced with confinement, and ultrasound performances decrease with the size of the channel.

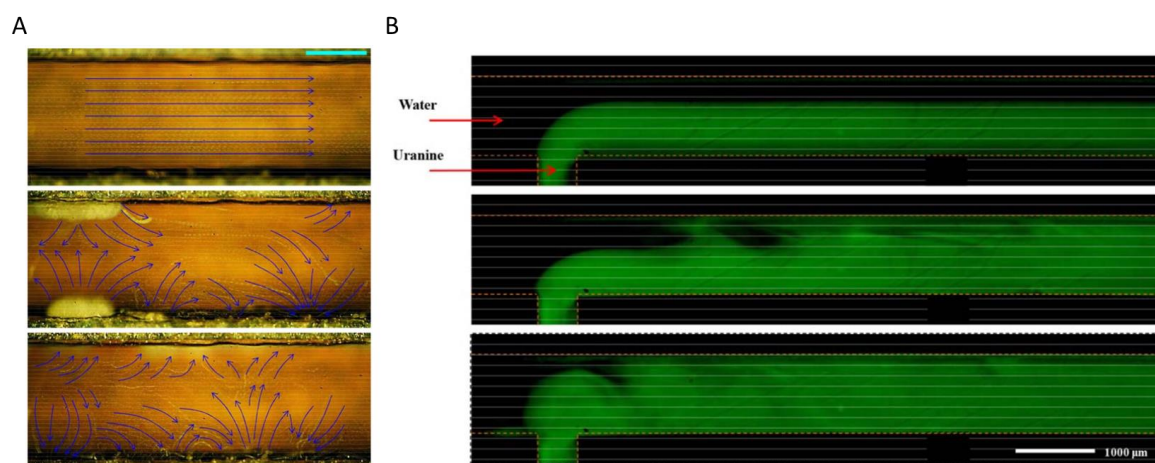


**Figure 54** A Photographs of the channel with addition of streak lines of the flow field (blue arrows) for a flowrate of 200  $\mu\text{L}/\text{min}$  using a Langevin-type transducer of 100 W and a frequency of 20 kHz at different ultrasound power (0, 20 and 30) [blue scale bar on the top right is 500  $\mu\text{m}$ ] and B images of mixing between water and uranine solution at a flowrate of 500  $\mu\text{L}/\text{min}$  at different ultrasound power (0, 10, 30) [scale bar on the bottom right is 1 mm] (Dong et al., 2016)

Ultrasound and acoustic mixing allows increasing diffusion process remotely. However, this technique has a higher efficiency in large channels, as cavitation activity is reduced in small channels, and temperature increased is still difficult to regulate.

#### Centrifugal and Coriolis forces based mixing

Centrifugal micromixer can induce mixing by rotating movements (Haeberle et al.; Shih et al., 2009; Tang et al., 2016). Ducrée and al. introduced a planar rotating disk as a fully

integrated and automated platform for fluidic handling (Ducrée et al., 2007). One of the features developed on this platform was mixing by moving particles or folding interfaces between two liquids as shown in Figure 55. Quite interestingly, most of the systems of pressure driven mixing can be adapted to centrifugally driven flows. The first method presented in Figure 55 was working in stopped-flow in a mixing round chamber of 25  $\mu\text{L}$  (diameter 6 mm), with large magnetic beads ( $r=68\mu\text{m}$ ,  $\chi=0.95$ ) with an external magnetic field  $B=125\text{ mT}$  (Grumann et al., 2005). In constant spinning mode, mixing was optimum for frequencies of rotation between 5 and 7 Hz, where forces on beads were balanced: the centrifugal force  $F_E$ , the magnetic force  $F_B$  and the drag force  $F_d$ . In alternate spinning mode, the optimum frequency was 8 Hz. Mixing was characterized by the standard deviation  $\sigma$  of the repartition of the ink introduced on one side, through the channel and the time  $\tau$  such as  $\sigma \sim e^\tau$ . Compared to diffusion with  $\tau_d = 7\text{ min}$ , constant spinning reduced the mixing time to  $\tau_c = 1.3\text{ s}$  and alternate spinning to  $\tau_a = 0.5\text{ s}$ . The loading of the beads was a delicate step that needed to be performed upstream.

Moreover, the Coriolis force generated by the rotation could be used to create transversal flow components, as pictured on the right part of Figure 55, where two solutions of water and ink were mixed under the action of the centrifugal force  $f_\omega$  and the Coriolis one  $f_c$  (Ducrée et al., 2006a). The mixing can be improved by addition of multi-lamination techniques that can be easily scaled up (Ducrée et al., 2006b). Coriolis force was more efficient at higher frequency of rotation (150 Hz) for which mixing could be performed at high flow rate up to 1mL/s (300 rad/s). Coriolis force based methods have the huge advantage of portability. This mixing technique is efficient both at molecular scale and in large magnetic beads suspension. However, such systems are not compatible with continuous flow over large injection time and large volumes. In addition, the format Lab on a Disc can be constraining for continuous flow, fabrication and coupling with an external magnetic field.

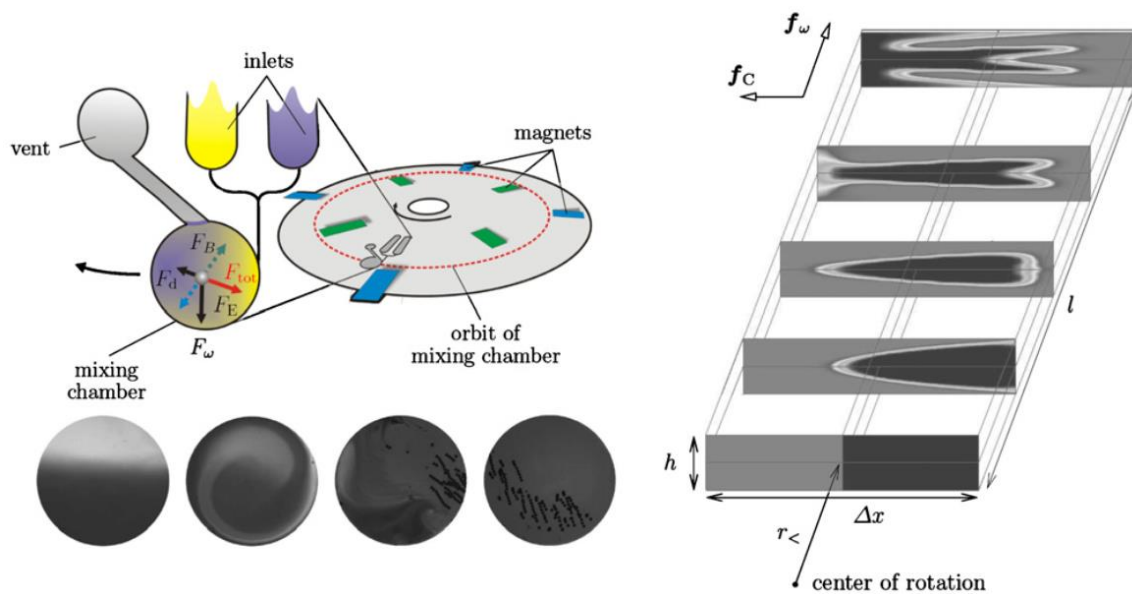


**Figure 55** Schematic representation of the rotating microfluidic disk, with picture of the movement induced on paramagnetic beads (bottom right) or on flow patterns (left) for an angular frequency of 300 rad/s in a radial channel of 2.1 cm, with a height of 65  $\mu\text{m}$  and a width of 320  $\mu\text{m}$  and at an orbit at 3 cm from the center (Ducrée et al., 2007)

### Thermal mixing

Two effects related to thermal activation can be used for mixing purposes. First the temperature gradient across a channel can generate mixing by playing with gel-to-liquid phase transition temperature as presented by Vreeland and Locascio. The team used thermally triggered liposomes for reagent delivery (Vreeland and Locascio, 2003) and showed a rapid mixing within 200  $\mu\text{m}$  channel with an average mixing time of 110 ms (flowrate of 100  $\mu\text{L/h}$ ). The same approach was presented by Kim et al. as part of a PCR process (Kim et al., 2009) or by Mao et al. to rapidly obtain activation energies from catalytic reactions, melting point transitions from lipid membranes, and fluorescence quantum yield curves from semiconductor nanocrystal probes (Mao et al., 2002)

Thermal mixing can also be induced by the movement of a bubble trapped in a microchannel. Tsai and Lin introduced this concept in a channel of 10.5 mm length, 200  $\mu\text{m}$  width and 50  $\mu\text{m}$  depth at a flow rate of 6.5  $\mu\text{L/min}$  (Tsai and Lin, 2002). A frequency of 200 Hz of pulse frequencies was used to create a bubble oscillation. Tsai and Lin have shown that dense fluidic waves increased the mixing.

Thermal mixing systems are often poorly adapted to bio-applications due to the temperature control required by many biologic protocols. Moreover, the complex

fabrication process and selection of the thermo-resistant materials for the chip can be a disadvantage.

## 2. Alternation of regimes of fluidization

The main limitations that have been observed so far in the fluidized bed are the formation of fractures that behave as a leak inside the fluidized bed and the lack of particle mobility in certain regions of the bed. We believe and showed that both mechanisms impede the global capture efficiency. To increase the beads homogeneity in the fluidized bed, we investigated different approaches to induce more favorable behaviors. The previous chapter introduced different passive strategies to generate mixing between two species diluted inside two liquids coming from two distinct channels. With this new approach, we aimed at increasing beads mobility by modifying the flow streamlines in order to increase the exchange rate between the volume of the fluid and the surface of the beads.

We previously showed that the fluidized bed behavior was strongly influenced by the inlet pressure. As described above in the case of dual channels, modulation of the input pressure is a feature relatively easy to implement in microfluidic devices. In our case, modulating the entrance pressure used to inject fluids inside the chip could result in mechanisms comparable to the mechanisms occurring while initiating or stopping fluidization. Working in a configuration where the bed can be continuously opened/closed would allow to create a new opening and a new formation of preferential pathways, to avoid the establishment of long-term preferential pathways and thus to improve the bead homogeneity.

### a) Observations of the movement induced on the matrix of beads

We worked with a 250  $\mu\text{m}$  high chamber, filled with 2.8  $\mu\text{m}$  diameter beads (250  $\mu\text{g}$ ). The experimental set-up was the same as presented in chapter 1: a PDMS chip filled with Dynabeads, injection of the liquid through a peek tubing (diameter 65  $\mu\text{m}$ ), feedback control of the pressure through flow rate controllers (Fluigent). The injection of the liquid was performed by pressurization of the initial reservoir.

We created a program to temporarily stop the flow at a given frequency, labeled as 'on/off'. The interruption was generated by switching the inlet pressure down to 0 Pa for  $t_{\text{OFF}} = 100$  ms thus stopping the flow in the device and further switching the flow rate back to the value of work. Our aim was to induce relatively short switching times to keep the dynamic aspect



of our system. As described below, the frequency of interruptions and opening times had been optimized to increase the efficiency of the method.

First observations confirmed the full closing of the fluidized bed with an interruption time  $t_{OFF}$  of 100ms. We were able to observe for all the frequencies investigated a packed bed configuration during the interruption and the formation of a new pathway when the flow rate was set back to the value of work (experimental validation). Shorter  $t_{OFF}$  values did not present a complete closing of the bed.

The creation of the preferential pathways simultaneously occurred with the transition from packed bed regime to fluidized regime. The time needed to initiate the bed fluidization mainly depends on the interaction between beads and on the time the bed stayed closed (Pereiro et al., 2017). The opening time, i.e. the time needed at working pressure to reach a fluidized bed in a stationary state, is about 10 s so our frequency of work  $f_{ALT}$  was always set below 0.1 Hz.

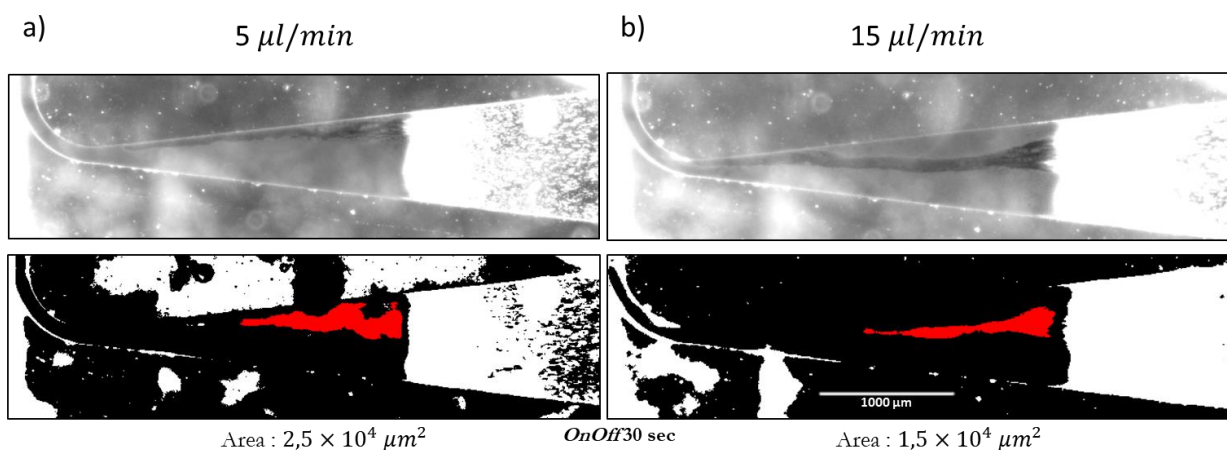


**Figure 56** Pictures of the fractures formation at 5  $\mu\text{L}/\text{min}$  (a) and 15  $\mu\text{L}/\text{min}$  (b) with superposition of the area explored by the fracture over seven closing/reopening of the bed (250  $\mu\text{m}$  chip, 250  $\mu\text{g}$  of COOH Dynabeads) for  $t_{OFF} = 100\text{ms}$  and  $f_{ALT} = 0.03\text{ Hz}$  (corresponding to an alternation period of 30 seconds)

For each cycle of opening/closing, a picture of the fluidized bed was taken once the fluidization regime was established. The preferential pathway of liquid percolation was clearly identified by the decreased density of magnetic beads (also observed as a local decrease of the grey level). Pictures were processed using a thresholding algorithm to discriminate and identify high density regions (homogeneous bed) from low density ones (fracture) using grey levels of the picture. The thresholding was then arbitrary based on the porosity of the bed. Figure 56 represents the sum of seven pictures already analyzed. The



red area is the sum of all the low density of magnetic beads area. As shown on Figure 56, we noticed that closing and re-opening the bed allowed to modify the flow pattern and the fracture position and thus to explore, during cycles, an area of  $2.5 \cdot 10^4 \mu\text{m}^2$  at  $5 \mu\text{L}/\text{min}$  and  $1.5 \cdot 10^4 \mu\text{m}^2$  at  $15 \mu\text{L}/\text{min}$ .

Interestingly, we observed that the area of the preferential pathway decreased when increasing the flow rate in on/off mode. It could be explained by the shape of the low density area, larger at high flowrates, so needing more time to really pack. Area of low density of beads would not have enough time to homogenize the hydraulic resistance, which would suggest an opening of the preferential pathway always at the same place. Another hypothesis was on the pressure used to re-open the bed. At higher flow rate the pressure used was higher and could impact the formation of the area of low density. The overall mobility of particles was also affected and tended to decrease with an increase in the flow rate. It was rather difficult to explain this behavior: both the higher pressure used at high flow rates and the higher shear stress imposed by the flow may affect the organization and the mobility of the particles in the bed.

As a result of these considerations, we expected this method to have a significant effect at low flow rates, where the preferential pathways explored higher area inside the matrix of beads.

#### **b) Quantification using a streptavidin-biotin capture model**

To evaluate the potential of this method, we first investigated the capture efficiency achieved with a biotin streptavidin capture model, as previously described. As shown on Figure 57, a first comparison between the continuous injection and the on/off mode showed a difference of capture at  $5 \mu\text{L}/\text{min}$ . For  $100 \text{ pmol}$  of biotin injected only  $40 \text{ pmol}$  were captured on continuous mode against  $59 \text{ pmol}$  with a closing of the bed every  $30 \text{ s}$ . At  $15 \mu\text{L}/\text{min}$  the difference between the two modes could not be observed due to smaller differences and high error bars.

Even if first observations and optimizations were carried out on the base of morphological studies, the parameters would needed to be optimized in the case of a real capture experiment. The closing time was set to  $t_{\text{OFF}} = 100 \text{ ms}$  as defined on Figure 57 C. Control of the flow was always performed based on flow rate measurement. We explored three frequencies of work ( $f_{\text{ALT}}$ ):  $0.03 \text{ Hz}$  (on/off every  $30 \text{ sec}$ ),  $0.008 \text{ Hz}$  (on/off every  $2 \text{ min}$ ) and  $0.003 \text{ Hz}$  (on/off every  $5 \text{ min}$ ). As shown on Figure 57 A, the capture can be improved at a

flowrate of 5  $\mu\text{L}/\text{min}$  by increasing the on/off frequency: working at 0.03 Hz (on/off every 30 sec) allowed to capture around 60% when 100 pmol of target are injected in the fluidized bed at 5  $\mu\text{L}/\text{min}$ , whereas less than 50 % are captured at a frequency of 0.003 Hz (on/off every 5 min). At 15  $\mu\text{L}/\text{min}$ , scale bars were too large to conclude on the effect. We decided to work with 30 seconds between each closing of the bed (including the time of closing of the bed).

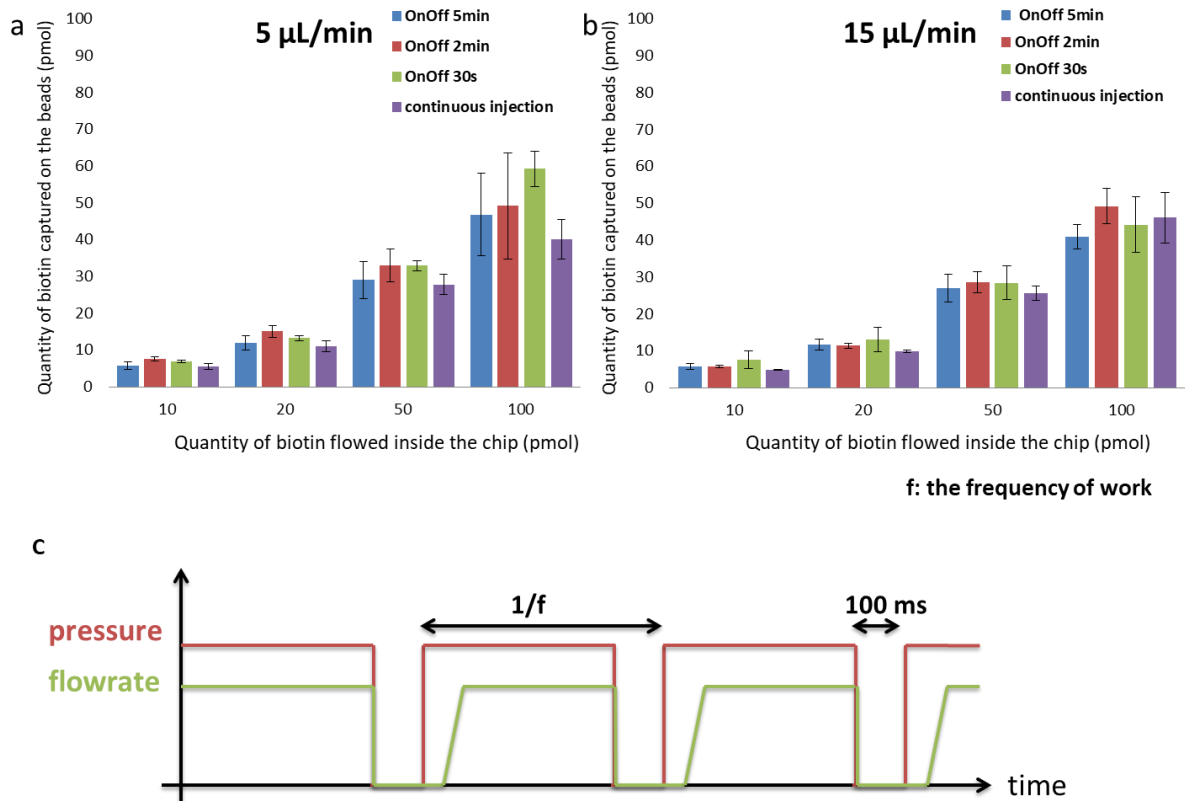


**Figure 57** Graphic representation of the quantity of DNA captured (pmol) as function of the quantity of DNA injected in the beads (pmol) at 5  $\mu\text{L}/\text{min}$  (A) and 15  $\mu\text{L}/\text{min}$  (B) for different frequencies of 'on/off'. Evolution of both inlet pressure and flow rate (ON/OFF mode) in the device during the process (C)

Figure 57 B shows that no improvement has been obtained at 15  $\mu\text{L}/\text{min}$  whatever the open/close frequency applied. At high flowrate, the area of low density explored less surface of the matrix of beads. A smaller area means that fewer beads are involved in the capture, so the ratio of interaction surface/volume is decreased.

Experimentally a burst effect at the opening of the bed was observed. This effect is characterized by a transient regime with a sudden expansion of the particle bed with a total area higher than the bed value observed in continuous operation conditions The algorithm

inducing regulation in the MFCS may play a role in this burst of pressure: to reach fluidization the regulator imposes a pressure higher than the normal operating pressure. This mechanism affects the spatial repartition of the beads in the matrix before reaching the pressure stabilization value and encourages the creation of preferential pathways.

The on/off approach allowed to increase the capture efficiency compared to the standard 250  $\mu\text{m}$  chip. The effect was more striking at 5  $\mu\text{L}/\text{min}$  than at 15  $\mu\text{L}/\text{min}$  as we expected. We showed that higher frequencies increased the effect on the capture.

The effect of the on/off method was particularly interesting and we decided to investigate this aspect even more, by the use of a more robust experimental approach where frequency, amplitude, and duty cycle can be better controlled. That's the reason why we implemented a vibration system in the fluidized bed in order to reproduce the mechanical stimulation that we could induce manually and further increase the mixing inside the bed to reach higher capture efficiencies.

### **3. Increase of the mobility of the beads at high frequencies**

#### **a) How to create movement of beads on a microfluidic chamber?**

The vibration approach is complementary to the one previously described. Both methods were settled on a precise control of the pressure and flow rate of injection, with addition of fluctuations in pressure and flow rate to induce mobility inside the matrix of beads. The "on/off" method worked at low frequencies and produced interesting and reproducible results. The control of pressure by MFCS system was limited by its reaction time. One question still remained regarding the influence of higher actuation frequencies on the capture efficiency.

We tried to work with pinched valves to pinch the entrance tubing and stop the flow in order to turn on and off the fluidization process such as in the work of (Ferraro et al., 2018). However, a first limit of frequency appeared as the maximum frequency of such micro-valves was dependent of the length (2.2 mm) the plunger had to travel. To cover this distance quickly, the solenoid system that control the movement of the pinching system was reaching important temperatures, not easily controllable. Moreover, the electronic system needed to control the valve and the scaffold to hold it at high frequencies were restrictive

due to their size and difficulty to make it portable. Another alternative was to periodically induce a compression on the injection tubing in order to generate a periodic fluctuation of pressure and flow rate in the system. This approach was performed using a motorized translation stage applying a force on a deformable tubing (silicone) inserted before the injection channel. Unfortunately, the speed of the stage ( $v_{\max}$ : 10mm/s) and the period of actuation (min 500 ms) were not enough to generate significant fluctuations in the device and to work at frequencies higher than 10Hz.

Another alternative has been investigated: the integration, on the injection channel, of a device inducing a fluctuation of pressure/flow rate with amplitudes and frequency sufficient to increase the particle mobility in the bed and affect the fracture position. To realize it, we added a vibration system similar to the one of cell phones on the entrance tubing of the PDMS chip.

#### **b) Characterization of the vibration motor and observations of the movement induced on the matrix of beads**

We investigated a vibration system, very close to the systems implemented in mobile phones. It is composed of a miniature electric motors coupled to mass partially off-balanced. When the motor rotates, the irregular weight causes the system to vibrate. The vibration system was added on the inlet PEEK tubing, just at the entrance of the chip. However, we noticed that the setting up of the vibration system was critical to achieve reproducible data, and that a more precise procedure was established using a 3D printed holder. The system was set at a voltage of 2.4 V and a current of 0.04 A. The vibration amplitude reached was around 11g, the vibration frequency just less than 200Hz and the acceleration efficiency 12g/W (Figure 58).

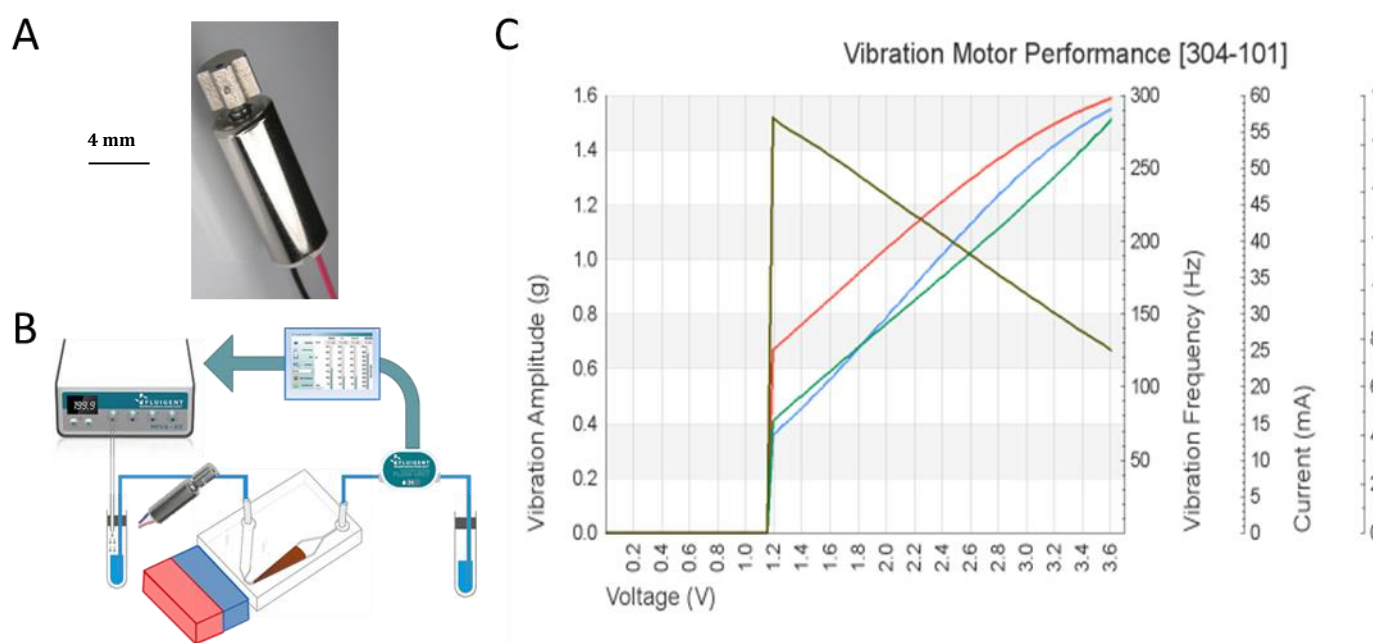


**Figure 58** A Picture of the vibration motor, B Position of the vibration system in the set-up and C characterisation of the system used (Precision Microdrives, reference 304-101)

The effects of the vibration have been directly observed within the fluidized bed, with an increase of the bed size, and more movement of the beads inside the matrix. The shape of the preferential pathway was also modified. It will be described in the next paragraph.

This approach seems, at least qualitatively, to enhance the mobility of the particles in the bed. However, the origin of the fluctuations induced in the device and the coupling mechanism between the vibrating device and the particle in the fluidized bed have still to be better understood. We believe that the oscillations induced by the motor cause a periodic deformation (bending) of the inlet tubing. As shown in Figure 59 (Karamanos, 2002), an elastic tube submitted to an external force perpendicular to its axe causes a bending and consequently a modification of the cross section of the tube that tends to ovalize. This ovalization induces a decrease of the inner cross section area of the tube and thus a decrease of the internal volume. By this process, mechanical deformations generated by the vibrating device should generate periodic fluctuations of the flow rate around a mean value. This modulation of the flow rate occurs with a period matching the one of the vibrating system. It is difficult to accurately estimate the amplitude of these deformations and thus the resulting flow rate fluctuations. Nevertheless, this mechanism confirms the possibility, by tuning the frequency and amplitude of the oscillations, to induce a rapid modulation of the flow rate within the fluidized bed and consequently disturb the fluidization process (combination of shear stress and expansion/compaction mechanism of the bed).

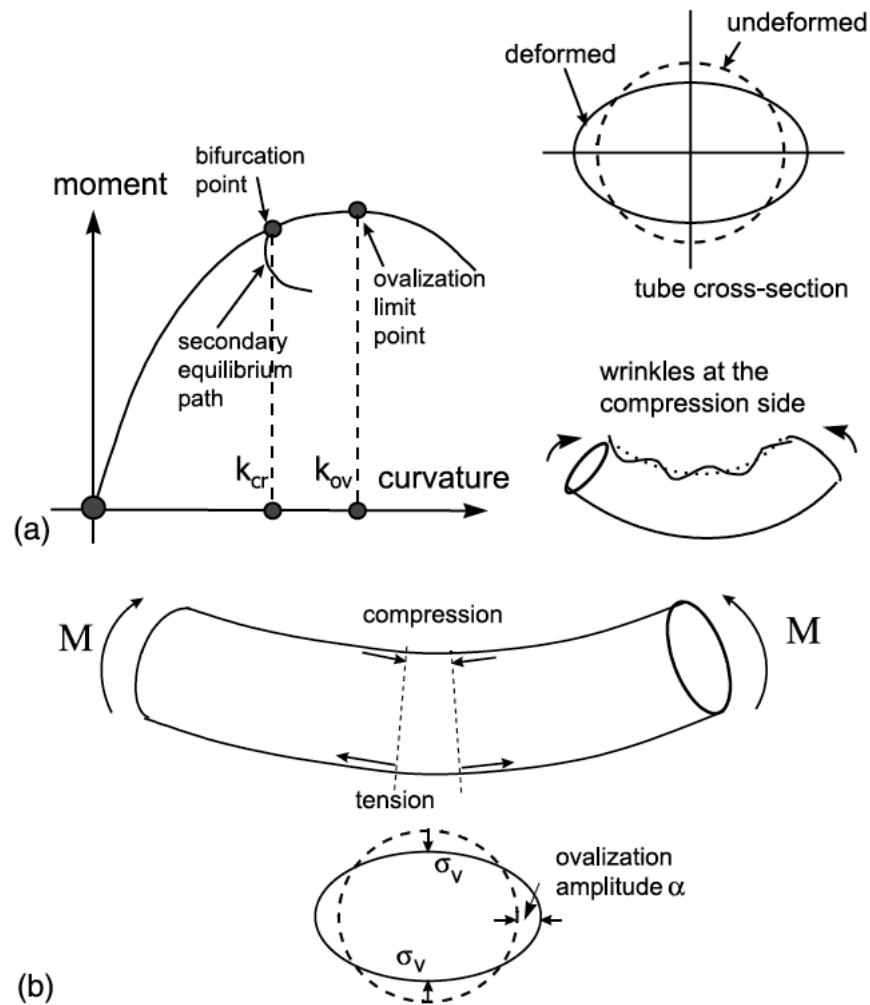


**Figure 59** Representation of the movement induced by the vibration motor on the tubing with (a) description of the moment that affects the tubing as function of its curvature and (b) drawing of the deformation of the tubing (Karamanos, 2002)

Observation of the low density areas showed the same behavior as the one observed with on/off method. The increase of those areas could be noticed with the naked eye. As shown on Figure 60, the area of low density could be evaluated without or with vibration added to the system. At  $5 \mu\text{L}/\text{min}$  the area of low density increased by a factor 2.5 compared to standard system when a system of vibration is added at the entrance of the system. At  $15 \mu\text{L}/\text{min}$  the area of low density is increased by a factor 1.6 (results not shown).

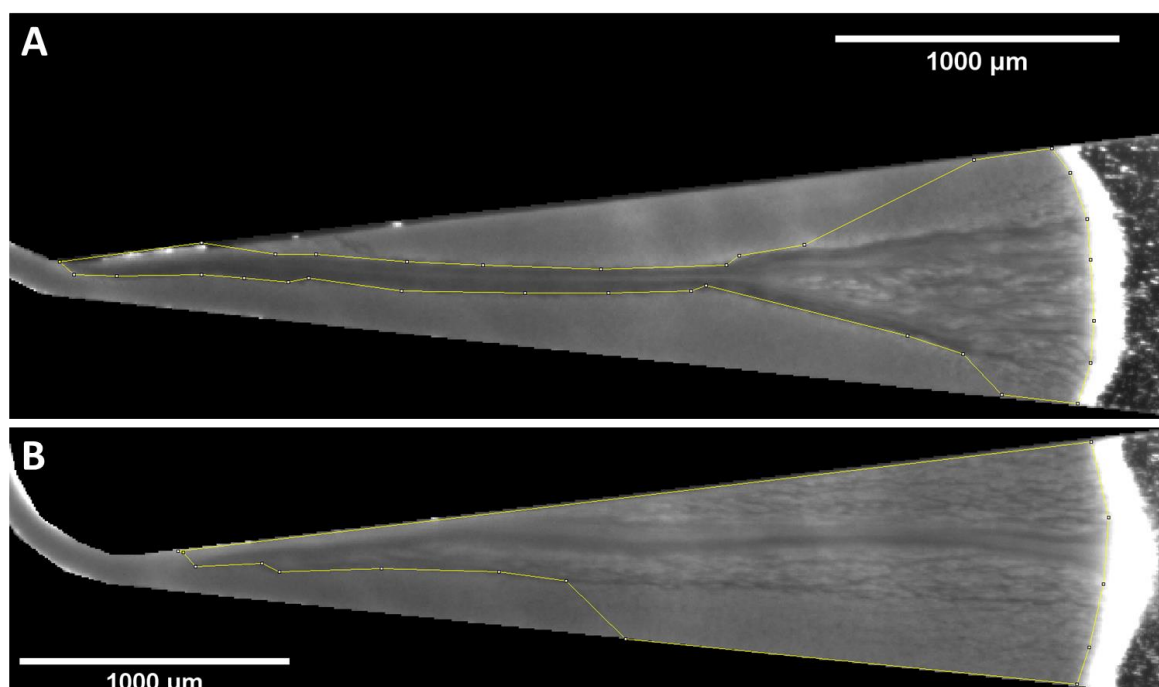


**Figure 60** Picture of a 250 µm chip with 250 µg of Streptavidin M-280 beads at 5 µL/min A) without and B) with vibration. The areas of low density are circled in yellow

### c) Quantification using a streptavidin-biotin model

To evaluate the potential of this approach, the bed capture efficiency has been measured with a biotin-streptavidin capture model. The results, presented in Figure 61, have been obtained with 50 pmol of biotinylated target injected (500 µL at 100 nM ). The injection lasted 2h45 for 3 µL/min, 1h40 for 5 µL/min and 33 min for 15 µL/min.

As shown in Figure 61, the addition of vibration has a positive effect on the capture efficiency at low flow rate. At 3 and 5 µL/min, the efficiency of capture was improved by about 8 % when vibrations were added to the system. However, due to the difficulties to fix the vibration system on the tubing obtained results were not perfectly reproducible. Moreover, at 15 µL/min, the vibrations did not affect significantly the capture efficiency. This phenomenon is not understood. Our hypothesis is that at such flow rate, kinetics effects (related to the affinity between the molecules involved in the capture process) may be important. However, more parameters such as the porosity in the capture area or mobility and grafting of the beads may affect the efficiency of capture too.

The system of vibration is able to increase the capture efficiency mainly at low flowrates.

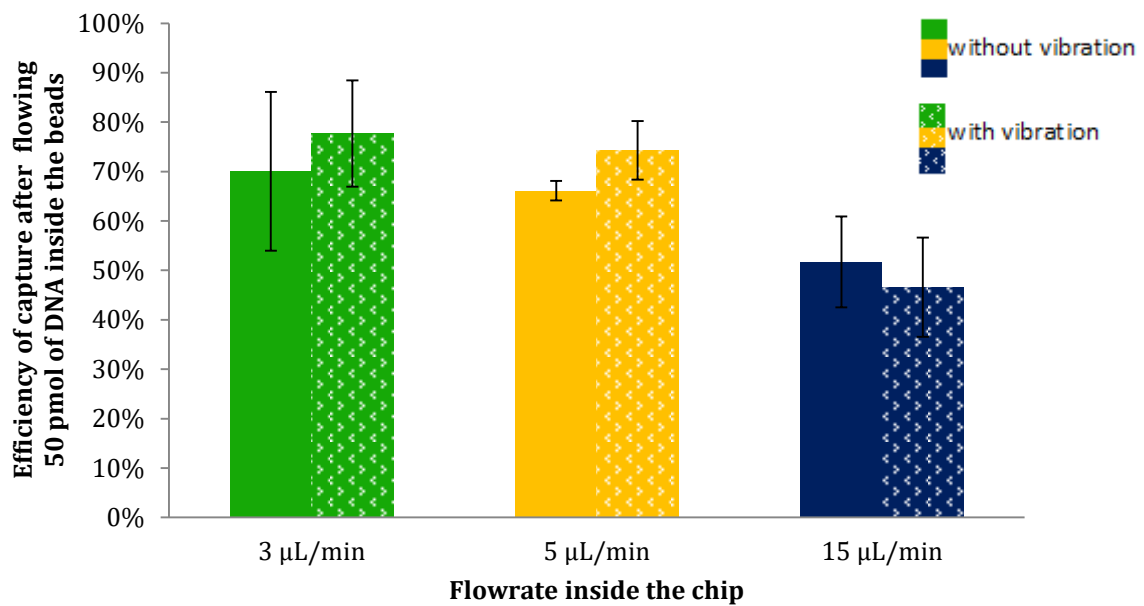


**Figure 61** Capture efficiency after flowing 50 pmol of biotin inside the matrix of beads at 3, 5 or 15  $\mu\text{L}/\text{min}$  with or without vibration in the 250  $\mu\text{m}$  chip in a PBS + 1% BSA buffer

#### d) Bio-application: influence on the capture of DNA

The different approaches described in this chapter have been tested on a biotin-streptavidin model to mimic the capture on a simple model. To go further, we decided to work with a model of hybridization of DNA. We worked with sequences of 80 base pairs. The target DNA was labeled with a fluorophore Alexa Fluor 488. The complementary sequence was attached on the surface of the beads. Hybridization was performed at 49°C on chip. As presented on Figure 62, standard capture was compared to manual tapping, 'on/off' with a frequency of 0.03 Hz and addition of the vibration motor.

The experiment was carried out at 5  $\mu\text{L}/\text{min}$  with a solution of DNA at 10 nM. We compared our approach with the standard capture in a 250  $\mu\text{m}$  chip as presented in the first chapter, but also with a manual process that we found to influence the bed stability. Manual tapping was realized by making manually vibrate the entrance resistance (frequency could be evaluated to 1 Hz). We used a solid object (lab clamp) to hit the entrance peek tubing. It provides a burst of pressure that induces a flow rate fluctuation in the device. Somehow, it is the same as on/off except that the burst is shorter in time with manual stimulation and not measurable. However, this action is clearly person dependent and not reproducible. For the vibration motor, the system was set at 2.4 V and 0.04 A.



We could show that the 'on/off' method was able to increase the efficiency of capture. However, it could not reach the efficiency of capture of the manual tapping. Switching on and off either by the use of pressure regulation or manual beating seems to improve the efficiency. This tends to suggest that increasing the mobility of beads and modifying the flow pattern in the bed helps improving the solid/liquid exchange.

One can notice that addition of a vibration system significantly improved the capture efficiency. A multiplicative factor of 8 was found between the standard capture and the capture with vibration. Same results were measured at 15  $\mu\text{L}/\text{min}$ : 10 % of capture in standard conditions and 81% in optimized conditions with vibration. It showed that our system can have the same efficiency at higher flow rates, so in smaller times of analysis. The effect on the capture was more than twice the improvement brought by the "on/off" method. Our hypothesis is based on the fact that hybridization is a more complex process than biotin/streptavidin capture. Kinetic, but also density of ligands on the surface, difference of affinity and porosity of the beads could explain why the improvements brought by those methods are more important in this situation.

The capacity of binding of the matrix of beads was 100 pmol of DNA. As we injected only 2.5 pmol of DNA inside the matrix (to stay close to real concentration), the risk of saturation was negligible. However, the efficiency of capture slightly decreased when the quantity of DNA percolated increased. This observation can be related to the decrease over the capture of the surface available for hybridization, but also to steric effects due to the presence of DNA already capture on the surface of some of the beads.

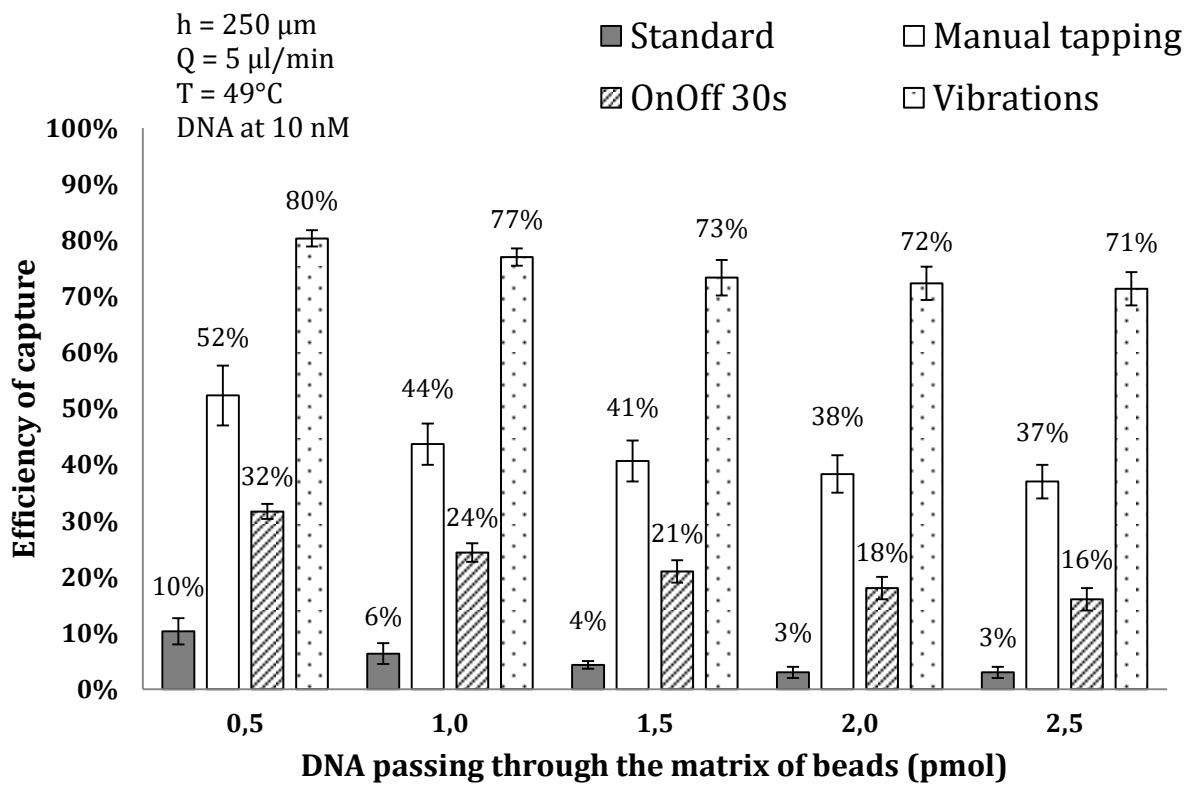


*Figure 62 Capture efficiency of DNA at a flowrate of 5  $\mu\text{L}/\text{min}$ , a temperature of 49°C and with a solution of DNA at 10 nM, comparing effect of manual tapping, 'on/off' method and vibrations to a standard capture.*

## 4. Conclusion and perspectives

We investigated the implementation of active mixers to the fluidized bed system. We have compared two flow configurations: a cyclic open/closed configuration and another one with a vibrating system inserted at the inlet of the chip. Both approaches improved the capture efficiency when capturing biotin on strepta-beads and DNA by hybridization on the beads. The integration of an automated vibration motor has shown the best efficiency to work with a controlled frequency of vibration. Indeed, working with a controlled vibration system should generate periodic fluctuations of the flow rate around a mean value is the best solution so far as the DNA capture efficiency was improved from 10% (in standard conditions) to 80% at both 5 and 15  $\mu\text{L}/\text{min}$ .

### a) Control of the frequency and the amplitude

In order to have a better control of the frequency and amplitude of the vibration applied on the system, we would like to work with sound-induced vibrations. Mak and al. described a system to apply and transmit small vibrations as the ones produced by sound (Mak et al., 2014). They used a loud speaker (SPA2210V, Philips), controlled by a Matlab program from a laptop, to produce vibrations. Then the vibrations were transmitted to the fluid through the inlet tubing. The membrane of the speaker was in direct contact with the tubing (Figure 63 a and b). They were able to show a linear correlation (slope of one) between the sound frequencies controlled (from 10 to  $2 \cdot 10^3$  Hz) and the frequency of the ripples produced (Figure 63 e). They were even able to go up to ultrasound (10 and 20 Hz). As shown on Figure 63 c and d, the vibrations are transmitted to the fluid.

In a next future, we would like to implement this vibration system in our system to be able to control the frequency and amplitude applied. We aim in particular to characterize more accurately the effects of vibrations on the beads. From a conceptual point of view, this solution is similar to the one presented in this chapter with rotating motors. However, we believe that this solution will offer a better control of the parameters influencing vibrations (amplitude, frequency, duty cycle) and thus a more accurate control of the particle mobility in the bed. Controlling these parameters is essential to understand the parameters influencing the bed efficiency and thus to establish a phase diagram that can be adapted to the working conditions (flow rate, type of beads volumes ...) of each application to be considered.

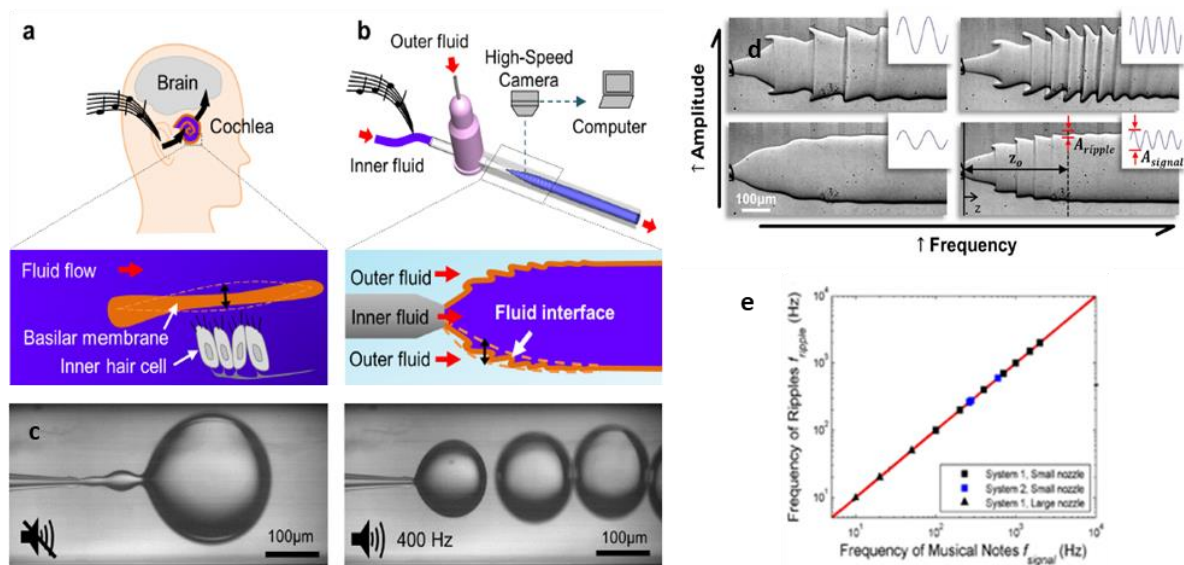


**Figure 63** Schematic representation of action of sound either by earing (a) or by application on a fluid tubing (b) and comparison between the human ear and the fluidic set-up (c) picture of a co-flow system and effect of a musical note of 400 Hz applied by loud speaker (d) Picture of the answer on an aqueous jet of a musical signal with a frequency between 100 and 200 Hz and an amplitude between 0.07 and 0.34 mm (e) log-log plot of the frequency of the ripples as function of the frequency of the musical notes

### b) Ultrasounds to move particles

In parallel, preliminary experiments have been performed using acoustic waves. We have studied their influence on the homogenization of the fluidized bed matrix of beads. The order of magnitude of the acoustic forces on usual particles is close to the drag and magnetic one ( $10^{-11}$  N). Those tests have been performed during a short stay in the team of Thomas Laurell and particularly with Andreas Lenshof.

In order to generate acoustic waves in the chip, we decided to first implement transducers directly inside the PDMS. Even if we were able to see an effect on polystyrene micro-particles (5 µm diameter) with a bead distribution following the pattern of acoustic waves, this was not enough to hold the particles in a flow of liquid. We reiterated the tests with Dynabeads® (2.8 µm diameter, Carboxylic acid on the surface). Similar mechanisms have been observed.

To avoid the dissipation inside the PDMS, we decided to work with transducer mounted on the glass slide below the PDMS chamber. This configuration (Figure 64 A) allowed us to

have higher impact on the beads. We could see depletion areas moving inside the matrix of particles (Figure 64 B and C). We supposed that those areas without beads matched the geometry of the acoustic waves traveling through the PDMS chip. However, we did not already fully investigate how both were related.

Unfortunately, the effect of acoustic waves was not enough to hold Dynabeads® in the flow without any magnetic force to balance the drag one. To balance the drag force induced by the flow passing through, we added a magnet to the system. The effect of acoustic waves was reduced, however, a pulsatile movement was observed on the beads near the preferential pathway. This study need to be deepened to fully understand how acoustic waves could homogenize the matrix of beads.

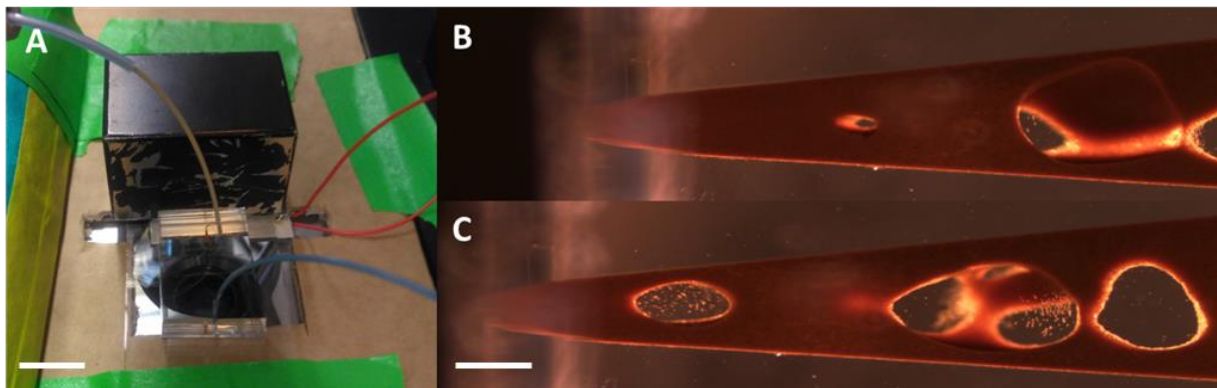


**Figure 64** *A* Picture of a chip with transducers below the glass slide (scale bar in white represent 1 cm) *B* and *C* are pictures of chips with a transducer below the entrance of the chip, function sweep between 2.03 and 2.05 MHz, no flow, no magnet (scale bar in white represent 300  $\mu\text{m}$ )

## 5. Material and method

Chips were realized by pouring polydimethylsiloxane (PDMS) on brass micro-milled mold. Micro-milling was realized on a Mini-Mill by Minitech Machinery Corp. with drills of 0.2 X 0.4  $\mu\text{m}$ , 0.3 X 0.6  $\mu\text{m}$  and 1 X1  $\mu\text{m}$ . The bonding was performed through oxygen plasma. Surface treatment was performed using PDMA-AGE 0.5%, with one hour incubation.

Streptavidin modified Dynabeads® M-280 (2.8 $\mu\text{m}$  in diameter, Dynabeads®, Thermofisher) were used for specific capture experiments. 250  $\mu\text{m}$  chips were filled with 250  $\mu\text{g}$  of beads. All beads were washed three times in buffer solution before use following the data sheet protocol.

Biotinylated DNA conjugated to a biotin and a fluorophore Alexa488 was buy from IDT®. DNA was then diluted in a Tris-EDTA buffer, and the concentration was adjusted with PBS (Sigma Aldrich). The sequence ordered with HPLC purification was:

/5BiosG/CTCTCTCTCTCTCTCTCT/3AlexF488N/

BRAF sequence was purchased from EUROFINs® or IDT®. The sequence capture was 5'TTCATGAAGACCTCACAGTAAAAATAGGTGATTTTGGTCTAGCTACAGAGAAATCTCGATGGAG TGGGTCCCATCAGTTTGAACAG3' conjugated to a fluorophore Alexa488. The reverse sequence

3'AAGTACTTCTGGAGTGTCATTTTTATCCACTAAAACCAGATCGATGTCTCTTTAGAGCTACCTC ACCCAGGGTAGTCAAACCTTGTC5' was also purchased, but combined to a biotin. The reverse sequence was grafted on the surface of M-280 Streptavidin beads following the protocol of the supplier (Dynabeads®, Thermofisher). The capture was performed in a TRIS HCl buffer (10mM pH 7.5), with EDTA (5mM), NaCl (1M) Tween 20 1% (w/v). The temperature was set at 49°C using an ITO plate.

## Bibliography

- Ahmed, D., Mao, X., Shi, J., Krishna Juluri, B., and Jun Huang, T. (2009). A millisecond micromixer via single-bubble-based acoustic streaming. *Lab. Chip* 9, 2738–2741.
- Bau, H.H., Zhong, J., and Yi, M. (2001). A minute magneto hydro dynamic (MHD) mixer. *Sens. Actuators B Chem.* 79, 207–215.
- Bengtsson, M., and Laurell, T. (2004). Ultrasonic agitation in microchannels. *Anal. Bioanal. Chem.* 378, 1716–1721.
- Biswal, S.L., and Gast, A.P. (2004). Micromixing with Linked Chains of Paramagnetic Particles. *Anal. Chem.* 76, 6448–6455.
- Campisi, M., Accoto, D., Damiani, F., and Dario, P. (2009). A soft-lithographed chaotic electrokinetic micromixer for efficient chemical reactions in lab-on-chips. *J. Micro-Nano Mechatron.* 5, 69–76.
- Cao, Q., Han, X., and Li, L. (2015). An active microfluidic mixer utilizing a hybrid gradient magnetic field. *Int. J. Appl. Electromagn. Mech.* 47, 583–592.
- Deshmukh, A.A., Liepmann, D., and Pisano, A.P. (2000). Continuous micromixer with pulsatile micropumps. 5.
- Deshmukh, A.A., Liepmann, D., and Pisano, A.P. (2001). Characterization of a Micro-Mixing, Pumping, and Valving System. In *Transducers '01 Eurosensors XV*, (Springer, Berlin, Heidelberg), pp. 922–925.
- Deval, J., Tabeling, P., and Ho, C.-M. (2002). A dielectrophoretic chaotic mixer. In *Technical Digest. MEMS 2002 IEEE International Conference. Fifteenth IEEE International Conference on Micro Electro Mechanical Systems (Cat. No.02CH37266)*, pp. 36–39.
- Dong, Z., Zhao, S., Zhang, Y., Yao, C., Yuan, Q., and Chen, G. (2016). Mixing and residence time distribution in ultrasonic microreactors. *AIChE J.* 63, 1404–1418.
- Ducrée, J., Haeberle, S., Brenner, T., Glatzel, T., and Zengerle, R. (2006a). Patterning of flow and mixing in rotating radial microchannels. *Microfluid. Nanofluidics* 2, 97–105.
- Ducrée, J., Brenner, T., Haeberle, S., Glatzel, T., and Zengerle, R. (2006b). Multilamination of flows in planar networks of rotating microchannels. *Microfluid. Nanofluidics* 2, 78–84.

Ducrée, J., Haeberle, S., Lutz, S., Pausch, S., Stetten, F. von, and Zengerle, R. (2007). The centrifugal microfluidic Bio-Disk platform. *J. Micromechanics Microengineering* 17, S103.

Ferraro, D., Serra, M., Ferrante, I., Viovy, J.-L., and Descroix, S. (2018). Microfluidic valve with zero dead volume and negligible back-flow for droplets handling. *Sens. Actuators B Chem.* 258, 1051–1059.

Fujii, T., Sando, Y., Higashino, K., and Fujii, Y. (2003). A plug and play microfluidic device. Electronic supplementary information (ESI) available: mpg files showing flow patterns. See <http://www.rsc.org/suppdata/lc/b3/b301410j/>. *Lab. Chip* 3, 193.

Glasgow, I., and Aubry, N. (2003). Enhancement of microfluidic mixing using time pulsing. *Lab. Chip* 3, 114–120.

Glasgow, I., Batton, J., and Aubry, N. (2004). Electroosmotic mixing in microchannels. *Lab. Chip* 4, 558–562.

Grumann, M., Geipel, A., Riegger, L., Zengerle, R., and Ducrée, J. (2005). Batch-mode mixing on centrifugal microfluidic platforms. *Lab. Chip* 5, 560–565.

Haeberle, S., Brenner, T., Schlosser, H.-P., Zengerle, R., and Ducrée, J. Centrifugal Micromixery. *Chem. Eng. Technol.* 28, 613–616.

Jang, J., and Lee, S.S. (2000). Theoretical and experimental study of MHD (magnetohydrodynamic) micropump. *Sens. Actuators Phys.* 80, 84–89.

Karamanos, S.A. (2002). Bending instabilities of elastic tubes. *Int. J. Solids Struct.* 39, 2059–2085.

Khoshmanesh, K., Nahavandi, S., Baratchi, S., Mitchell, A., and Kalantar-zadeh, K. (2011). Dielectrophoretic platforms for bio-microfluidic systems. *Biosens. Bioelectron.* 26, 1800–1814.

Kim, S.-J., Wang, F., Burns, M.A., and Kurabayashi, K. (2009). Temperature-Programmed Natural Convection for Micromixing and Biochemical Reaction in a Single Microfluidic Chamber. *Anal. Chem.* 81, 4510–4516.

Leach, J., Mushfique, H., Leonardo, R. di, Padgett, M., and Cooper, J. (2006). An optically driven pump for microfluidics. *Lab. Chip* 6, 735–739.



- Lee, H.-Y., and Voldman, J. (2007). Optimizing Micromixer Design for Enhancing Dielectrophoretic Microconcentrator Performance. *Anal. Chem.* *79*, 1833–1839.
- Lei, K.F., and Li, W.J. (2008). A Novel In-Plane Microfluidic Mixer Using Vortex Pumps for Fluidic Discretization, A Novel In-Plane Microfluidic Mixer Using Vortex Pumps for Fluidic Discretization. *JALA J. Assoc. Lab. Autom.* *13*, 227–236.
- Liu, R.H., Lenigk, R., Druyor-Sanchez, R.L., Yang, J., and Grodzinski, P. (2003). Hybridization Enhancement Using Cavitation Microstreaming. *Anal. Chem.* *75*, 1911–1917.
- Mak, S.Y., Li, Z., Frere, A., Chan, T.C., and Shum, H.C. (2014). Musical Interfaces: Visualization and Reconstruction of Music with a Microfluidic Two-Phase Flow. *Sci. Rep.* *4*, 6675.
- Mao, H., Yang, T., and Cremer, P.S. (2002). A Microfluidic Device with a Linear Temperature Gradient for Parallel and Combinatorial Measurements. *J. Am. Chem. Soc.* *124*, 4432–4435.
- Niu, X., and Lee, Y.-K. (2003). Efficient spatial-temporal chaotic mixing in microchannels. *J. Micromechanics Microengineering* *13*, 454.
- Oddy, M.H., Santiago, J.G., and Mikkelsen, J.C. (2001). Electrokinetic Instability Micromixing. *Anal. Chem.* *73*, 5822–5832.
- Oh, D.-W., Jin, J.S., Choi, J.H., Kim, H.-Y., and Lee, J.S. (2007). A microfluidic chaotic mixer using ferrofluid. *J. Micromechanics Microengineering* *17*, 2077.
- Pereiro, I., Tabnaoui, S., Fermigier, M., Roure, O. du, Descroix, S., Viovy, J.-L., and Malaquin, L. (2017). Magnetic fluidized bed for solid phase extraction in microfluidic systems. *Lab. Chip* *17*, 1603–1615.
- Posner, J.D., and Santiago, J.G. (2006). Convective instability of electrokinetic flows in a cross-shaped microchannel. *J. Fluid Mech.* *555*, 1–42.
- Qian, S., and Bau, H.H. (2002). A Chaotic Electroosmotic Stirrer. *Anal. Chem.* *74*, 3616–3625.
- Qian, S., and Bau, H.H. (2005). Magneto-hydrodynamic stirrer for stationary and moving fluids. *Sens. Actuators B Chem.* *106*, 859–870.
- Salmanzadeh, A., Shafiee, H., Davalos, R.V., and Stremmler, M.A. (2011). Microfluidic mixing using contactless dielectrophoresis. *ELECTROPHORESIS* *32*, 2569–2578.

Shih, C.H., Lu, C.H., Lin, C.H., and Wu, H.J. (2009). Design and Analysis of Micromixers on a Centrifugal Platform.

Tang, M., Wang, G., Kong, S.-K., and Ho, H.-P. (2016). A Review of Biomedical Centrifugal Microfluidic Platforms. *Micromachines* 7, 26.

Tang, Z., Hong, S., Djukic, D., Modi, V., West, A.C., Yardley, J., and Osgood, R.M. (2002). Electrokinetic flow control for composition modulation in a microchannel. *J. Micromechanics Microengineering* 12, 870.

Terray, A., Oakey, J., and Marr, D.W.M. (2002). Microfluidic Control Using Colloidal Devices. *Science* 296, 1841–1844.

Tsai, J.-H., and Lin, L. (2002). Active microfluidic mixer and gas bubble filter driven by thermal bubble micropump. 7.

Vreeland, W.N., and Locascio, L.E. (2003). Using Bioinspired Thermally Triggered Liposomes for High-Efficiency Mixing and Reagent Delivery in Microfluidic Devices. *Anal. Chem.* 75, 6906–6911.

West, J., Karamata, B., Lillis, B., P. Gleeson, J., Alderman, J., K. Collins, J., Lane, W., Mathewson, A., and Berney, H. (2002). Application of magnetohydrodynamic actuation to continuous flow chemistry. *Lab. Chip* 2, 224–230.

West, J., Gleeson, J.P., Alderman, J., Collins, J.K., and Berney, H. (2003). Structuring laminar flows using annular magnetohydrodynamic actuation. *Sens. Actuators B Chem.* 96, 190–199.

Yang, F., Kuang, C., Zhao, W., and Wang, G. (2017). AC Electrokinetic Fast Mixing in Non-Parallel Microchannels. *Chem. Eng. Commun.* 204, 190–197.

Yang, Z., Matsumoto, S., Goto, H., Matsumoto, M., and Maeda, R. (2001). Ultrasonic micromixer for microfluidic systems. *Sens. Actuators Phys.* 93, 266–272.

Yaralioglu, G.G., Wygant, I.O., Marentis, T.C., and Khuri-Yakub, B.T. (2004). Ultrasonic Mixing in Microfluidic Channels Using Integrated Transducers. *Anal. Chem.* 76, 3694–3698.



## Chapter 4

# Modulating the fluidized bed behavior by controlling magnetic particles properties and dimensions

### 1. Bimodal matrices to enhance mixing

#### a) Fluidized bed in industry

As previously discussed, the fluidized beds are technologies widely used in industry for their numerous advantages. In many applications such as coal combustors or in fluidized bed polymerization, the particles involved in the process can present different sizes. Indeed, chemical reaction, mass and heat transfer are dependent on the size distribution of the particles. The size of the particles is thus an important parameter that requires optimization.

The particle size distribution can play a significant role in properties of the fluidized bed. A phenomenon commonly observed in conventional fluidized bed based on gravity is that beads segregate within the bed as function of their size. For particles of same density, the larger ones stay preferentially at the bottom of the bed, whereas smaller ones have the tendency to go at the surface (Huilin et al., 2003).

Besides, it has been shown that the bed expansion observed in industrial applications may be increased by a factor of two compared to monodispersed distribution when a large particle size distribution (PSD) is involved (De Groot, 1967). Two approaches have been developed to study matrices of different sizes of particles:

- The use of large distribution of particles size
- Addition of very small particles inside a monodisperse matrix of large particles

To better characterize the behavior of poly-disperse particle size matrices reported in the literature, an M index has been defined. We introduce the mixing index M to compare abilities of fluidized beds to achieve an efficient mixing as:

$$M = \frac{S_0^2 - S^2}{S_0^2 - S_R^2}$$

Equation 25

Where  $S^2$  is the variance on the size of the particles in the system,  $S_0^2$  and  $S_R^2$  are the variances of the respectively completely unmixed and completely random states (Lacey, 1954).

This mixing index can quantify a complete segregation (M=0) or a perfect mixing (M=1). It will be used to compare mixing efficiency.

#### **b) Particles segregation in complex mixture**

As previously mentioned, a segregation of the particles of different sizes can be observed in conventional fluidized beds. This particularity has been used to model the sedimentation in rivers and streams. Sediments transport could be a key to a better understanding of natural hazard management by flow. Natural sediments are made of grains of wide size distribution interacting in a liquid. Zrostlík and Matousek have first investigated a fluidized bed model with spheres of 3.18 and 5.41 mm diameter respectively (Zrostlík and Matoušek, 2017). They observed the formation of an interfacial layer made by only smaller grains (M=0) related to vertical sorting, which size increases with shear stress intern of the bed.

Based on those observations, the fluidized beds have been used to separate particles by playing with their geometry, flow rate of percolation, or even with the polydispersity of size of the particles. Segregating systems rely on operating conditions, but also on the creation of preferential pathways (Naimer et al., 1982). They can be used to sort grains or pharmaceutical granulates (Wormsbecker et al., 2005). Segregation due to change of particles density can also be used to sort fruits and vegetables (Zaltzman et al., 1987). The quality, the maturity, the juice content or the mealiness of most fruits and vegetables is

correlated to their density, which can be used as a criterion for sorting. Zaltzman et al. demonstrated a sorting of pecan pieces from weevils larvae (both in the range between 150 and 300  $\mu\text{m}$  diameter) based on different densities and created by fluidization air at 0.24 m/s. Fluidized beds proved their efficiency to distinguish a difference of density of 0.025 g/cm<sup>3</sup> with 48% of the 448 pecan pieces on the top 8 mm (for a theoretical value of 53%) and only 5 (1.1%) of weevils.

These studies demonstrate that, besides their initial function, fluidized bed systems can also be used to sort particles of different sizes or densities.

### c) Increasing mixing by adding different size of particles

Contrary to segregation, working with different sizes of particles can also be used to improve the mixing inside the fluidized bed. As mentioned previously, adding small particles among a bed of large particles can change their distribution inside the chamber. Under certain conditions, it can thus lead to an improvement of particles mixing.

Addition of 'fines' has been known to improve the quality of fluidization for more than 40 years (Sun and Grace, 1990). Fines are small particles with a diameter smaller than 45  $\mu\text{m}$  or of a least one fifth of the usual particles size used in the bed. There are used in industry to improve fluidized bed performances. Sun and Grace proved that a wide size distribution of small particles (between 40 to 80  $\mu\text{m}$  diameter) in a gas fluidized bed reactor improved the performances at a velocity between 0.06 and 1.8 m/s. Optimization has to be done on the quality of the small particles added, but also on their density, their size and their nature. Those particles were able to increase the mass transfer between phases, change the properties of fluidization, improve the bed expansion and decrease the formation of clusters (Bruni et al., 2006; Lettieri and Macrì, 2016).

For example chemical looping combustion (CLC) is a technological process based on two bubbling fluidized beds that work together to perform the oxidation of hydrocarbon based fuels. One of them (fuel reactor) provides by metal oxidation the oxygen needed for the combustion. The second one called air reactor is used to reduce the metal by the fuel before injecting it again in the first fluidized bed. It has been shown that the redox reaction can be enhanced by using binary mixture of particles to carry oxygen (Moghtaderi and Song, 2010). The particles used had different sizes and different densities (small particles had a diameter of 116  $\mu\text{m}$  and a density between 939 and 8075 kg/m<sup>3</sup> and the bigger ones a diameter of 328  $\mu\text{m}$  and a density of 939 kg/m<sup>3</sup>). In those conditions, particles have tendencies to

segregate, and it was not the effect wanted. It has been shown (Figure 1 D) that an optimization of the density ratio ( $\rho_R$ ) of the particles could improve the mixing (up to  $M=0.83$ ). These conditions were found to provide conditions for comparable slip velocities (interstitial fluid velocity minus particle velocity) for both particles, and same forces acting on them. On the contrary, an increase of the diameter of the bigger particles induces the apparition of segregation. Figure 1A, B and C represent the aspect of a fluidized bed made of bimodal matrix with small 116  $\mu\text{m}$  particles and bigger ones in red of 234, 328 and 393  $\mu\text{m}$ . At low particle size ratio ( $d_r$ ) both particles are fluidized whereas at higher  $d_r$ , red particles tend to segregate. An increase of the particle size ratio decreases the mixing of those particles. The same study was made on particle density ratio as shown on Figure D and an optimum was found at  $\rho_R = 5.2$ . It was also found that the mixing increases with the velocity of the phase passing through the particles up to a certain velocity where mixing can't be improved (Peng et al., 2013).

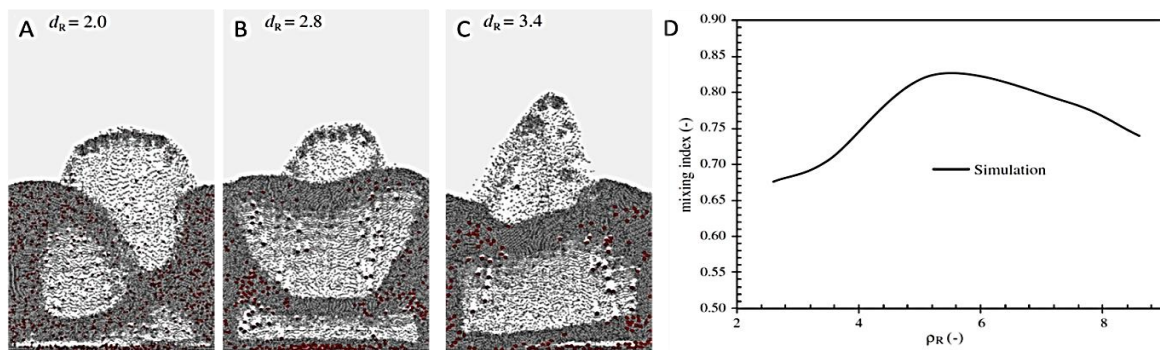


**Figure 65-A) -B)- C) Pictures of the repartition of particles for different particles size ratio  $d_R$  where bigger particles ( $d_{red}=328 \mu\text{m}$ ,  $\rho_{red}=939 \text{ kg/m}^3$ ) are represented in red inside a fluidized bed of smaller particles ( $d_{grey}=116 \mu\text{m}$ ,  $\rho_{grey}=2462 \text{ kg/m}^3$ ) at a speed of fluidization of  $U=0.04 \text{ m/s}$  -D) graphic representation of the mixing index as function of the particle density ratio  $\rho_R$  (Peng et al., 2013)**

A recent study focused on the mixing of nanoparticles from hydrophilic powders, such as the ones used in paint or pharmaceutical industries. Those particles, which had an initial size of 12 nm, ended to form clusters from 2 to 100  $\mu\text{m}$  (Ali et al., 2018). Syed Sadiq Ali and al. shown that addition of sand with a diameter around 50  $\mu\text{m}$  and at a volume percentage of less than 10 % could decrease the minimum fluidization velocity, improve the hydrodynamics of the bed and reduce the void fraction (contraction of the volume of particles). Moreover, a reduction up to 66% of the size of the agglomerates could be observed at high fractions of mixing. Addition of particle seemed to promote deagglomeration.

Several assumptions have been made (Gu et al., 2016) to understand the role of those fine particles in fluidized beds:

1. Fines act like a lubricant. It decreases the effective viscosity of the dense phase (no confirmation by experiment has been done) and splits the voids
2. Fines change the porosity and the density (not settle by experiments) and would lead to more expansion of the fluidized bed, so more contact between the gas and the solid phases
3. Velocity of the particles is increased inside the dilute phase (experimental measures), so is the number of particles in suspension. It would reduce the size of the bubbles created inside the matrix and help homogenization of the repartition of the particles and reduction of voids

It is important to notice that many of the experiments done at macroscale focused on a gas-solid fluidized bed. In this configuration bubble occurred and improved the mixing. However, those studies outline the dependency of the mixing on the size and the density of the smaller particles added.

At large scale, studies are based on rheological aspects in porous media, where interactions between particles are small. Going to micro-scale enhances surface interaction. As discussed in the introduction, interactions between beads are important in our configuration and beads tend to create columns due to dipole-dipole interactions. We need to consider those groups as entities. Moreover, going to microscale means working at low Reynolds number, where viscous effects overtake inertial ones, which is not always the case in previous described articles (air/liquid fluidized bed). At microscale, bimodal matrices can be fabricated and used as support in order to characterize separation systems (Dutz et al., 2012; Inglis, 2009). Only few articles really investigate the interactions between micro-beads. For example, Petousis et al. developed a model to understand the shape of clusters of beads in the case of bimodal matrices, their rotation, their ruptures (Petousis et al., 2007). They showed that fragility of columns of beads was increase when the columns were composed of beads of different magnetic susceptibilities. However, this polydispersity ensured a variation in the behavior of the columns, that they suggested to use for mixing.

#### **d) Theoretical model of bimodal matrices in fluidization**

Many observations of bimodal matrices in fluidized beds have been made experimentally. Both experiments and theoretical models confirm that multiple factors are involved in the



behavior of poly-disperse matrix of particles in a fluidized bed. That's the reason why theoretical models are so important in the understanding of fluidized beds. More particularly, they offer the possibility to scan different parameters to find an optimum for each of them. It can be for example the density of fines as shown on Figure 66 (Shire et al., 2016). Figure 66 represents different organizations of a bimodal matrix. Small beads fill the porosity of the bigger ones (a) (b) up to the point where they modify the morphology of the matrix and the interactions between the bigger beads (c). The number of smaller beads needed to reach this point is dependent to the size of the beads (d)

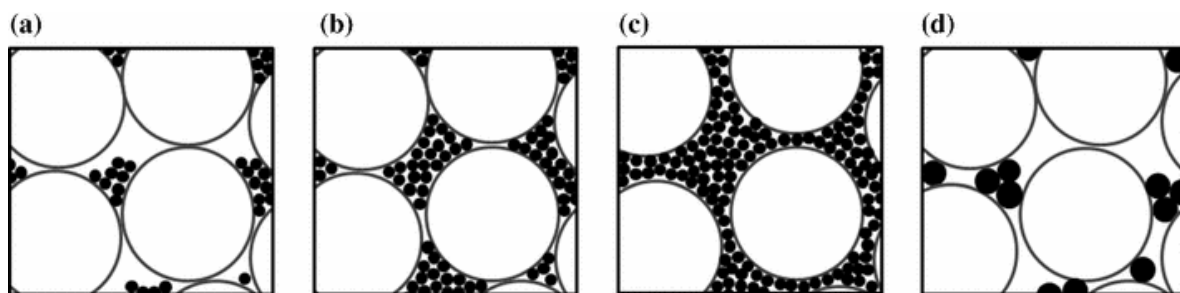


**Figure 66 Schematic representation of soil with fines content a : under filled with large size ratio b filled c overfilled d under filled with small size ratio (Shire et al., 2016)**

It is difficult to propose accurate models for dense arrays of particles with large size distribution: this is due to the large number of particles, to the global versus local vision, the high number of instabilities at a same time and to the difficulty to consider in an exhaustive manner the interactions between particles.

As described in the literature, working with a poly-disperse matrix of beads can either increase the segregation or encourage the mixing of particles. In order to improve the fluidization, the difference of size between the particles has to be optimized. This approach can be transfer to the microfluidic magnetic fluidized bed. We decided to use a bimodal support to improve the homogeneity of the repartition of the beads in the matrix.

## **2. Integration of bimodal matrix in magnetic micro fluidized beds**

### **a) Bimodal fluidized bed – qualitative approach**

Based on preliminary observations realized with small biologic spherical objects inserted in a monodisperse matrix of beads, the use of two types of beads with varying diameters was investigated further in order to improve the 250 $\mu$ m fluidized bed performances. To characterize their effect in the microfluidic fluidized bed, their influence on the bed

homogeneity has been first analyzed in a qualitative manner. Pictures were taken to compare the bed properties as function of the beads composition.

To begin with, we decided to keep the mass of beads constant in order to compare beads matrices. The mass is related to the hydraulic behavior of the fluidized bed, it regulates the pressure of opening and closing of the bed. We were usually working with beads with a diameter of 2.8  $\mu\text{m}$ . In order to investigate the influence of the polydispersity in size of the matrix of beads, percentages of 1 $\mu\text{m}$  2.8 $\mu\text{m}$  and 4.5 $\mu\text{m}$  diameter beads were adjusted in order to kept constant the total mass of the matrix of beads.

First, we observed that beads with a diameter of 4.5 $\mu\text{m}$  do not distribute homogeneously with smaller beads of 2.8  $\mu\text{m}$  diameter (in absence of 1 $\mu\text{m}$  beads). As pictured on Figure 68, smaller beads could be found close to the entrance of the fluidized bed, whereas most of the 4.5  $\mu\text{m}$  diameter beads were at the end of the bed of beads (Figure 67). This segregation appeared for any percentage of 4.5 $\mu\text{m}$  beads mix, without any possibility to provide a uniform spatial distribution of each bead population. This effect was not observed in the case of a mixing between 1 $\mu\text{m}$  and 2.8 $\mu\text{m}$  beads. These observations can be related to the segregation process at macroscale, the exact same behavior was noticed at the microscale.

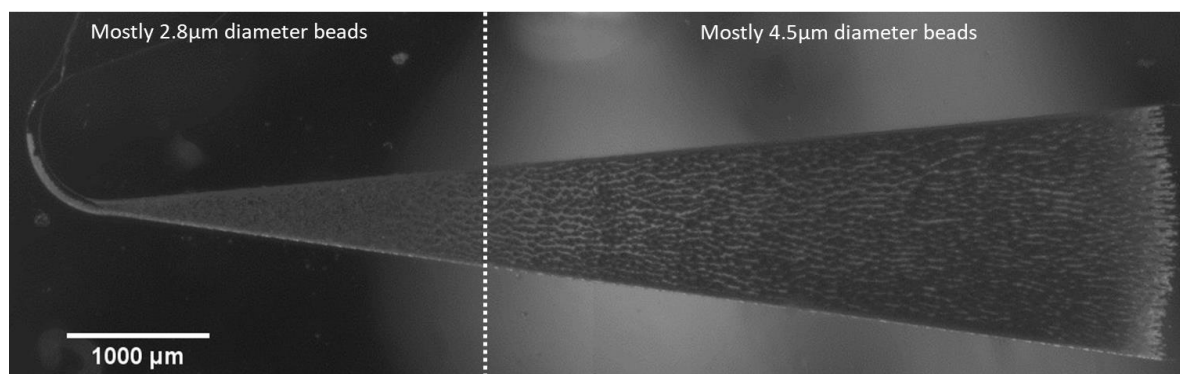


**Figure 67 Bimodal matrix of beads with segregation (75 % of M450 and 25 % of M270 Dynabeads COOH)**

To explain this phenomenon, it is necessary to go back to the equilibrium of forces applied on the beads i.e. the balance between the drag and the magnetic forces. An assumption to explain this observation is related to the fluid drag force proportional to the square of the radius of the particles. On the other hand, the magnetic force is proportional to the quantity of magnetite inside the beads if the magnetic field is small enough (chapter 1- Figure 7) to not reach the saturation of the beads. As seen before:

$$F_{mag} \sim \Delta\chi R^3 \text{ and } F_{drag} \sim R$$

So  $\Delta\chi R^2$  should be constant to have a balance between the drag force and the magnetic one.

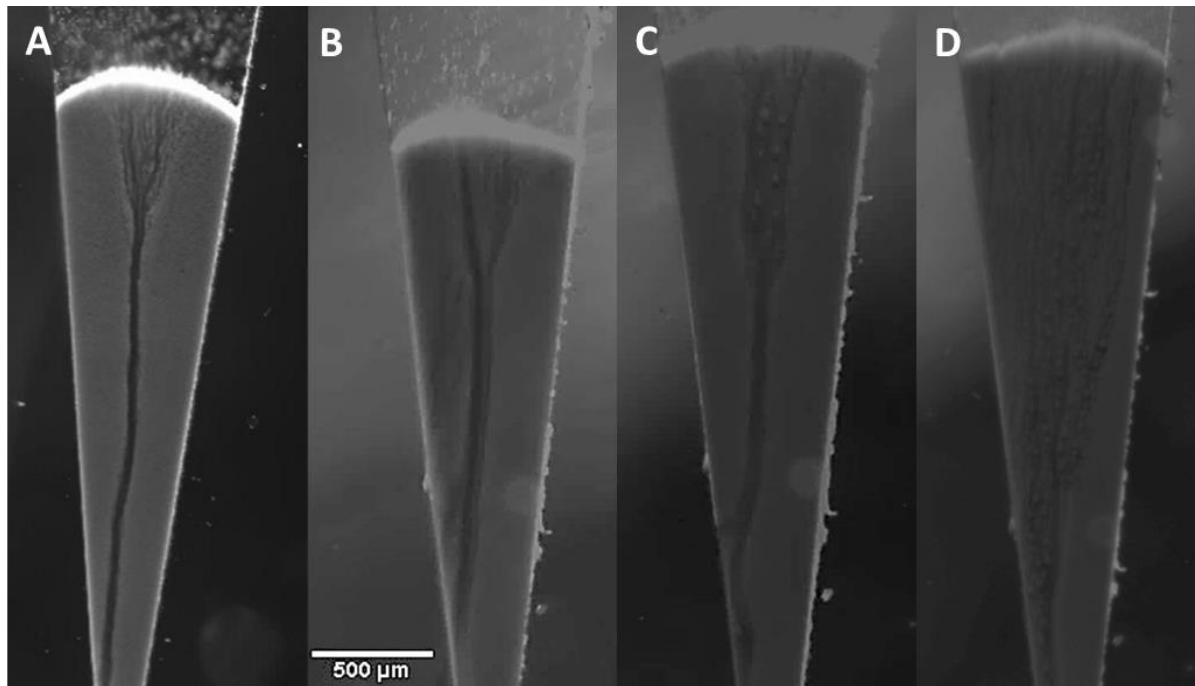
We supposed that a good homogenization can be correlated with  $\frac{\Delta\chi_1}{\Delta\chi_2} \approx \left(\frac{R_2}{R_1}\right)^2$ .

Table 3 Characterization of the magnetic beads used

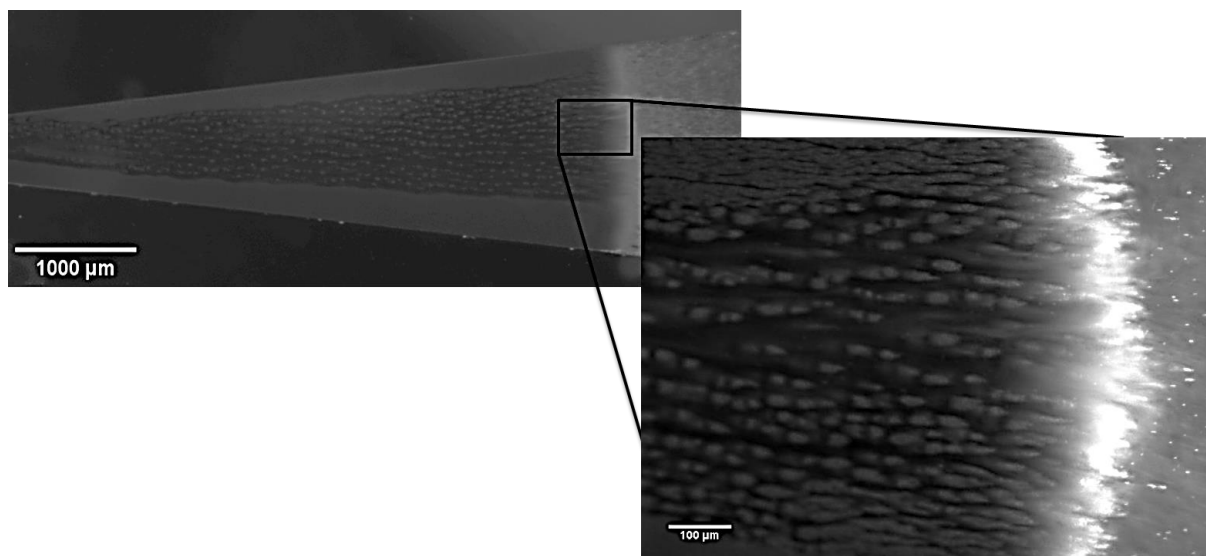
	Radius R ( $\mu\text{m}$ )	Magnetic suscepibility $\Delta\chi$ * $10^{-5}$ ( $\text{m}^3/\text{kg}$ )	$\Delta\chi R^2$ * $10^{-23}$ ( $\text{m}^6/\text{kg}$ )
MyOne	0.525	81	22
M-280	1.415	54	108
M-450	2.200	102	494

Table 3 gathers values of magnetization taken from (Fonnum et al., 2005). However, we are still unable to explain the observed segregation.

For a bed only made of  $2.8\mu\text{m}$  beads, one can notice the creation of preferential pathways inside the matrix of beads. As shown in Figure 68, increasing the quantity of  $1\mu\text{m}$  beads (ranging from 0 to 40 % w/w) present in the bed of  $2.8\mu\text{m}$  beads had a significant impact on the global morphology. The behavior of the bed is significantly affected. First of all, the area of low density of beads, where the liquid percolates, is more important with a bimodal matrix. This is an advantage as it is related to the beads in contact with the liquid passing through. The contrast is lower, which indicates a better homogeneity of the beads. Moreover, we observed the formation of bigger columns inside the line of percolation of the liquid; they appeared as whiter agglomerates of beads. Our hypothesis is that those columns are essentially made of smaller beads that homogenize and widen the fracture of the matrix. Figure 69 shows a clear enlargement of the area of low density for a bimodal matrix. It seems that beads still create the same aggregates but those columns move inside the fracture and widen it even more.



**Figure 68** Pictures of the bed of particles in a 250  $\mu\text{m}$  chip with different beads composition- M-270 COOH and A) + nothing B) + 4% of MyOne COOH, C) + 20% of MyOne COOH and D) + 40% of MyOne COOH. Beads were dispersed in PBS and BSA 1%. Pictures were taken with a flow rate of 5  $\mu\text{L}/\text{min}$



**Figure 69** Image of a matrix of 250  $\mu\text{g}$  Streptavidin Dynabeads M-280 and 250 g of MyOne Dynabeads COOH in a 250  $\mu\text{m}$  chip. Beads were dispersed in PBS and BSA 1%. Pictures were taken with a flow rate of 5  $\mu\text{L}/\text{min}$

Those first observations were quite encouraging, and bimodal matrices seemed to have higher impact at high number of smaller beads. As large beads ( $> 4 \mu\text{m}$  diameter) induced segregation and the smallest ones ( $< 700 \text{ nm}$  diameter) did not have enough intern magnetization to be confined in the bed, we have performed the following experiments with a composition of beads consisting in beads of 1 and  $2.8 \mu\text{m}$  in diameter

#### b) Influence of beads composition on the expansion of the micro-fluidized bed

As observed in Figure 68, the size of the fluidized bed varied in presence of smaller beads in the matrix. This phenomenon was not related to the addition of particles, as the total mass of the particles was kept constant.

We first measured the length of the bed (defined as the length between the entrance of the main chamber and the edge of the beads matrix) as a function of particle composition for different flow rates. First, as expected, the expansion of the bed was bigger at high flow rate. Figure 70 seemed to show that the expansion of the bed could be related to the quantity of  $1 \mu\text{m}$  beads added to the matrix of  $2.8 \mu\text{m}$  ones.

The expansion of the fluidized bed can be interpreted as an advantageous parameter as the volume of the suspension of the beads was increased. The time of residence of each molecule inside the matrix of beads was then increased too. However, a balance had to be found to keep a high local concentration of beads inside the main chamber to increase chances of contact between the sample and the beads.

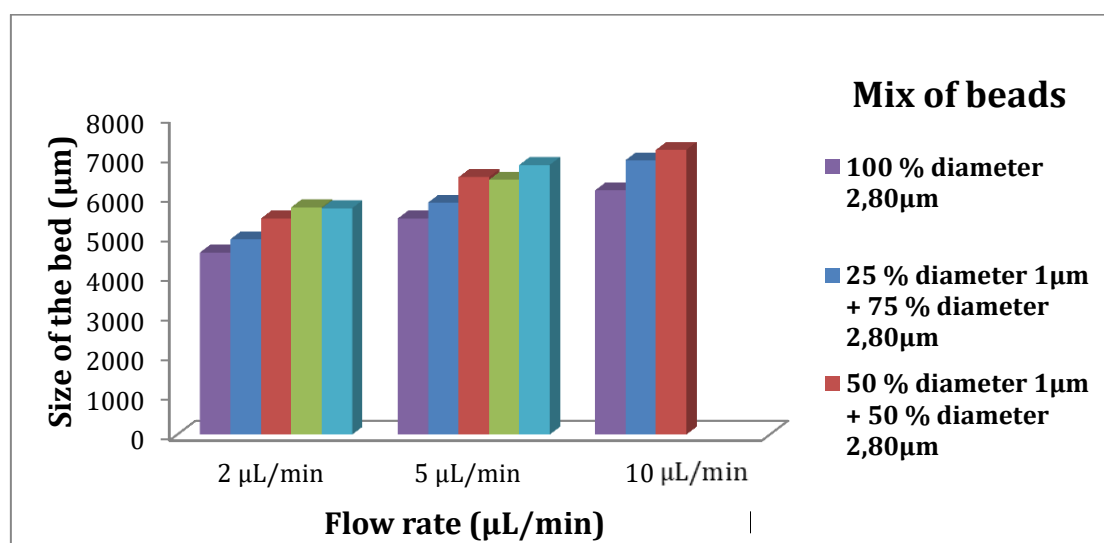


**Figure 70 : Influence of the beads compositions on size of the bed at different flow rate for different mix of beads (mass percentage)**

When working at higher flow rate (5  $\mu\text{L}/\text{min}$  up to 15  $\mu\text{L}/\text{min}$ ), the composition made of half small beads and half bigger ones gives the largest bed expansion, and a good spatial distribution of the beads, without any sign of segregation. Above 10 $\mu\text{L}/\text{min}$ , smaller beads were pushed by the flow and were lost for any composition of bimodal matrix (Figure 70). In order to keep all beads inside the fluidized bed and work at high flowrate, a balance was found.

The mix 50 % MyOne 50 % M280 was a good compromise to keep the particles inside the chamber while applying a high flowrate and increasing the length of the bed to fluidize the beads in a larger volume of sample.

It is intriguing to notice that increasing the fraction of 1 $\mu\text{m}$  bead increases the bed length. This can be explained by the fact that magnetic forces on small beads are lower (as explained previously) than in big particles, thus it increases the role of drag forces. As a consequence, magnetic confinement forces decreases which leads, for a given flow rate, to a higher bed length.

### c) Model of interaction

To explain the distribution of the bimodal matrix, and in particular the limitation of the surface occupied by the fracture, different mechanisms can be discussed:

- As suggested by the bed pictures, smaller beads could organize themselves and fill at least partially the void volume around the columns made of 2.8 $\mu\text{m}$  beads.
- The 1 $\mu\text{m}$  beads could also insert themselves inside the columns of 2.8 $\mu\text{m}$  beads and consequently decrease the columns stability

#### *Filling void volume*

The beads used here are superparamagnetic particles. In the absence of a magnetic field, their magnetization is in average null. However, if an external source of magnetization is added, superparamagnetic beads become dipoles with a high magnetization. Particles can thus interact with each other and organize on a preferential direction, aligned along the magnetic field lines. We have previously discussed the fact that the presence of preferential pathways (fracture observed in figure 3) can be due to the formation of these columns that induce an anisotropy in the internal organization of the bed.

The addition of smaller beads seems to increase the size of the area of lower density of beads in the bed and thus improves the homogeneity of the particle spatial distribution. One hypothesis is that smaller particles can fill the empty spaces in between large particles. Filling this empty volume would reduce the heterogeneity of the bed of beads. Those beads filling the porosity do organize themselves as columns too. These columns should be less stable due to lower interactions between the beads. Driven by the beads constantly circulating inside the fluidized bed and by the homogenization of the local hydrodynamic resistance, the flow splits into multiple ways to cross the bed instead of linear tight path.

#### **Modifying the particle assembly in the bed**

When beads are organized as columns they can be depicted as a train of polarized dipoles holding together by magnetic interactions. Even if the interaction forces between particles depend on the beads magnetization, we can reasonably assume that in the case of bimodal systems, small and large particles are interacting and create columns made of both types of particles. The morphology of these columns might be very complex and different for the ones previously observed with monodispersed population of beads. One can assume that the stability of these columns when submitted to a shear stress and flow recirculation is lower. It may result in a better homogeneity in the flow distribution. This explanation is supported by the work of Petousis et al (Petousis et al., 2007) where they showed that the insertion of beads of smaller magnetization in columns of normal beads increased the risks of rupture of the column.

Both mechanisms tend to decrease the local variation of the hydrodynamic resistance of the matrix of beads in presence of a bimodal support. They may contribute to improve the bed homogeneity. The use of a bimodal beads matrix would help to distribute the flow of liquid inside the beads. Based on these preliminary observations, we expect that the use of such bimodal matrix would improve the contact between the volume of sample and the surface of the beads and thus promote efficient solid phase extraction in this new generation of fluidized bed.

#### **d) Proof of concept with capture of biotinylated DNA on Streptavidin beads**

To investigate the effect of using a bimodal beads matrix, we first evaluated the capture efficiency of the new generation of fluidized bed with a model system of biotin-streptavidin. To be able to compare the approach with previous results of capture in the same conditions, we decided to perform the capture on the same specific surface for a normal and a bimodal

support. The smaller beads added did not interact with biotin. The mass of beads was not constant anymore; it varied with addition of smaller beads. The 2.8 $\mu\text{m}$  beads were grafted with a ligand (streptavidin beads) while the 1 $\mu\text{m}$  beads were not functionalized (COOH-beads).

The capture was performed with 250  $\mu\text{g}$  of M 280 Streptavidin beads. The specific capture surface was constant all along the experiment and it represented already more than 350  $\text{mm}^2$ .

**Table 4 Composition of the bimodal matrix of beads**

Name	chip	Mass of M270 Strepta	Mass of MyOne COOH ( $\mu\text{g}$ )	Mass of MyOne Strepa ( $\mu\text{g}$ )
Height 50 $\mu\text{m}$	50 $\mu\text{m}$	50 $\mu\text{g}$	0	0
Height 250 $\mu\text{m}$	250 $\mu\text{m}$	250 $\mu\text{g}$	0	0
4%	250 $\mu\text{m}$	250 $\mu\text{g}$	10	0
20 %	250 $\mu\text{m}$	250 $\mu\text{g}$	50	0
40 %	250 $\mu\text{m}$	250 $\mu\text{g}$	100	0
100%	250 $\mu\text{m}$	250 $\mu\text{g}$	250	0
Bimodal full Strepta	250 $\mu\text{m}$	250 $\mu\text{g}$	0	250

To create a bimodal support, we added different masses of carboxylic Dynabeads (Table 4). Those beads were 'inactive' for the capture; they did not interact with the biotin. A negative control was performed using only 'inactive' beads. We confirmed that inactive beads do not interact with the biotinylated DNA. Those experiments were conducted to achieve a better understanding of the role of the smaller beads in the physics of the fluidized bed, and not to increase the capture efficiency.



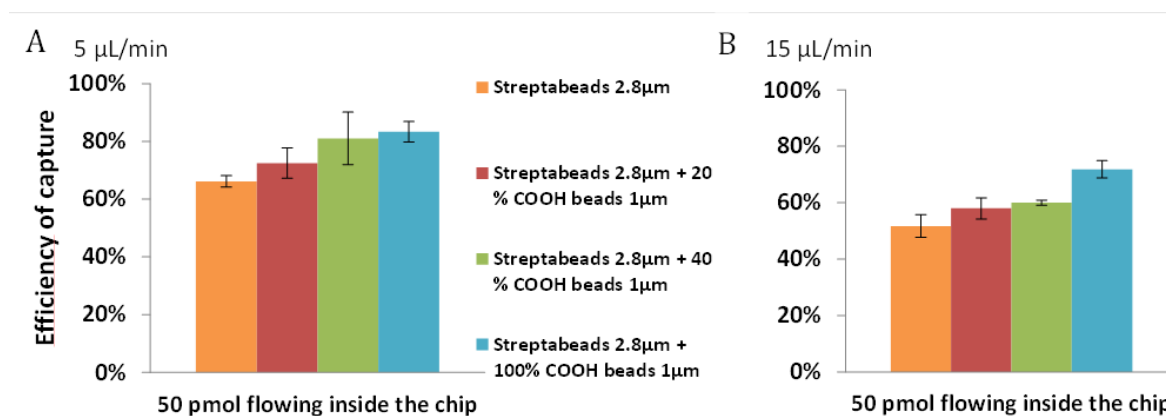


**Figure 71** Variation of the capture as a function of the beads composition. Injection of 50 pmol of biotinylated DNA (100 nM) at A) 5 µL/min or B) 15 µL/min

As shown on Figure 71 A, at 5 µL/min the capture efficiency increased when the percentage of 1 µm beads increased in the bed (from 66 to 83% for 0 and 50% of 1 µm beads respectively). In particular, with the beads matrix of 50% of 1 µm the best capture efficiency was achieved.

At 15 µL/min (Figure 71 B), the formation of preferential pathways was boosted by the strength of the flow. Overall, the capture efficiencies were reduced at higher flow rate. However, this effect was limited by the presence of a bimodal matrix that allowed to increase the capture efficiency at 15 µL/min from 52% to 72%.

To have a better understanding of the effect of beads matrix composition on the capture efficiency at different flowrates, it can be interesting to present results as a 'one hour' experiment to overtake the limitation of volume sample and focus on limitations in analysis time. We have thus tested and compared two different configurations with different particles compositions and flow rates. Measurements of captured biotin performed in 1 hour of experiment are reported in Figure 72. These results show that a high capture efficiency (around 90%) can be achieved with first generation of fluidized bed (chamber height of 50 µm) at usual flow rate of work of 1 µL/min. However this first generation of chip cannot capture as much as (in terms of quantity of the target) the second generation which has five times more beads. At higher flow rate (3 µL/min), the matrix of beads is too disturbed in the first generation chip, beads are lost in the flow, and the efficiency of capture goes down to 36%. An increase of the flowrate allows to analyze a higher volume of sample for a given analysis time (180 µL in one hour at 3 µL/min, 300 µL at 5 µL/min and 900 µL at

15  $\mu\text{L}/\text{min}$ ). It leads to a higher quantity of captured DNA: around 13 pmol at 3  $\mu\text{L}/\text{min}$ , more than 20 pmol at 5  $\mu\text{L}/\text{min}$  and up to 45 pmol at 15  $\mu\text{L}/\text{min}$ . Those results are summarized in Figure 72.

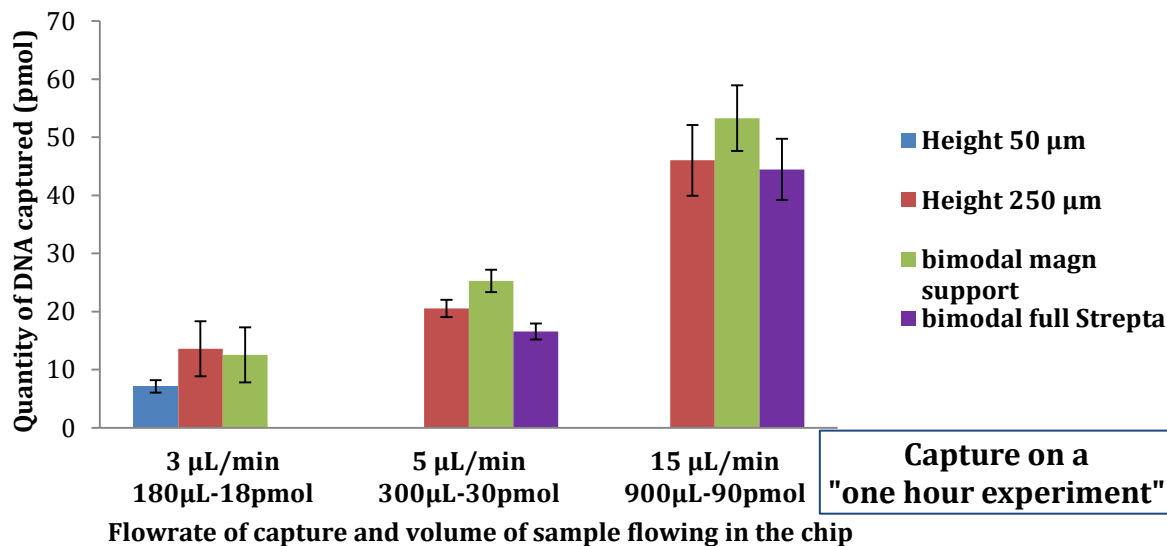


**Figure 72 Influence of the beads composition on the quantity of biotinylated DNA captured for two chip designs (50  $\mu\text{m}$  and 250  $\mu\text{m}$ ) and different flow rates and with different magnetic supports for a sample of DNA at 100 nM**

All bimodal results have been presented for now with the same active surface. The only beads used for the capture were the 2.8  $\mu\text{m}$  ones with a surface functionalized with streptavidin. We tried to combine both physical effects of the 1  $\mu\text{m}$  beads on the bed homogeneity with an increase of the specific surface, the 1  $\mu\text{m}$  beads being grafted with streptavidin. As the active surface was increased, we were expecting to further increase the efficiency of capture. However, as shown on Figure 72, the capture rate was not significantly increased when the entire bimodal matrix was grafted with capture ligand. It could be explained by the non-specific interactions between beads that were certainly stronger compared to the electrostatic repulsion that should occur between carboxylic beads. Indeed in these conditions, a fracture could be observed on the matrix of beads. Moreover, as shown on Figure 73 A, where the matrix is composed of 50% 2.8  $\mu\text{m}$  Streptavidin beads and 50% 1  $\mu\text{m}$  Streptavidin beads, areas of high density on the side of the main chamber were not involved in the capture process (they stayed black, which means that no fluorescent biotin has been captured in these regions) whereas Figure 73 B present uniform repartition of the DNA captured over the 50% 2.8  $\mu\text{m}$  Streptavidin beads and 50% 1  $\mu\text{m}$  COOH beads matrix of beads.

These results demonstrate that bimodal beads composition can improve the capture efficiency mainly by modifying the bed homogeneity. On the contrary, addition of beads grafted with the capture ligands decreases the efficiency of capture while the surface of interactions is increased. We also demonstrate that for a given analysis time, it is highly favorable to work with the second generation of fluidized bed (H: 250 $\mu$ m) integrating a bimodal matrix, as a flow rate of 15 $\mu$ L/min can be applied while preserving a quite good capture efficiency.

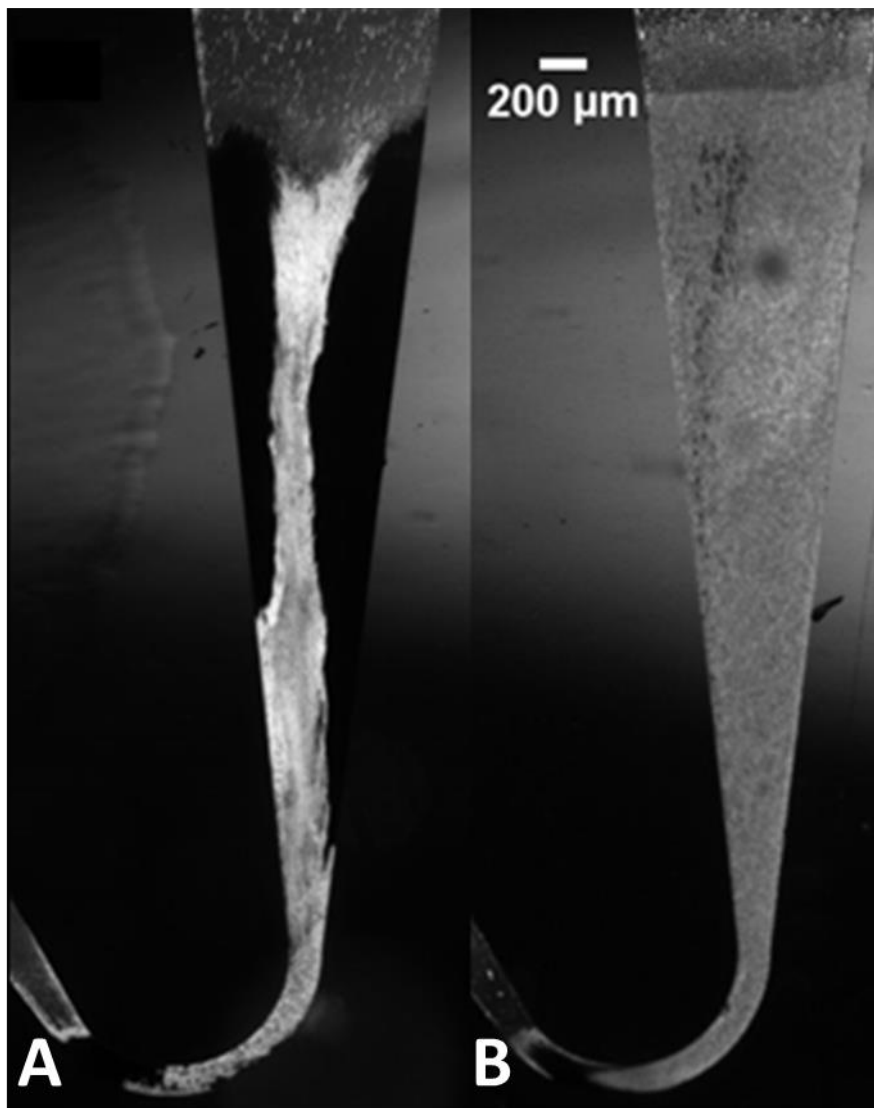


**Figure 73** Images in fluorescence of the packed matrices of beads after the capture of fluorescent biotin at 5  $\mu$ L/min (50 pmol) with A) a bimodal: 50% 2.8 $\mu$ m Streptavidin beads and 50% 1  $\mu$ m Streptavidin beads matrix and B) a bimodal: 50% 2.8 $\mu$ m Streptavidin beads and 50% 1  $\mu$ m COOH beads matrix

### 3. Evaluation of the 250 $\mu\text{m}$ chip with vibration and bimodal matrix

Changing the beads composition is therefore an interesting approach to improve the fluidized bed performances. In the previous chapter, an alternative option based on the addition of vibrations was also investigated to improve the capture rate of the fluidized bed. These two approaches have demonstrated their potential to improve the capture in the second generation of fluidized bed, so we investigated on how the combination of both approaches could further improve the bed performances.

#### a) Proof of concept with streptavidin/biotin model

As previously, the efficiency of our approach was first tested with a biotin-streptavidin model. Figure 74 shows that the amount of target captured was increased by almost a factor 2 using the second generation compared to the first one. However, at moderate flowrate (3  $\mu\text{L}/\text{min}$ ), both bimodal and vibration approaches did not appear to increase significantly the capture compared to the standard second generation of fluidized bed. Quantities of DNA captured in the 250  $\mu\text{m}$  chip are just below 15 pmol for 20 pmol of DNA injected in the chip, with means an efficiency of capture around 70%. In the 50  $\mu\text{m}$  chip, the efficiency of capture was around 90% during the first hour. So for precious samples where time is not an issue, it may be better to work with the 50  $\mu\text{m}$  chip. The 250  $\mu\text{m}$  chip allows more target to be extracted in a finite amount of time, but at lower efficiency.

However, at 5 and 15  $\mu\text{L}/\text{min}$  (flowrates that cannot be reached with the 50  $\mu\text{m}$  chip without losing the beads), both bimodal matrix and vibrations improve significantly the capture. At 5  $\mu\text{L}/\text{min}$ , 30 pmol are injected in the chip in one hour, and around 25 pmol are extracted using bimodal support, vibration or the combination of both. The efficiency of capture is around 85%.

At 15  $\mu\text{L}/\text{min}$ , when 90 pmol of DNA are injected in the bed, the combination of vibration and bimodal support impacts and improves significantly the capture efficiency. Bimodal matrix allows a capture of 55 pmol (60% of efficiency). Addition of vibrations allows to capture 43 pmol (48%). The combination of both reach a capture efficiency of 73% with 65 pmol captured. At high shear stress, the combined effect of vibration on the bimodal matrix seems to be important. It could be related to the instability of the bimodal matrix and its ability to be fractured during the sample percolation.

As previously mentioned, to tackle the challenge of trace analysis, we need to be able to analyze high sample volumes and if possible, as fast as possible. In order to face this challenge, we aimed at working at high flow rates, we thus focused on the approaches that improve the capture efficiency at high flow rate.

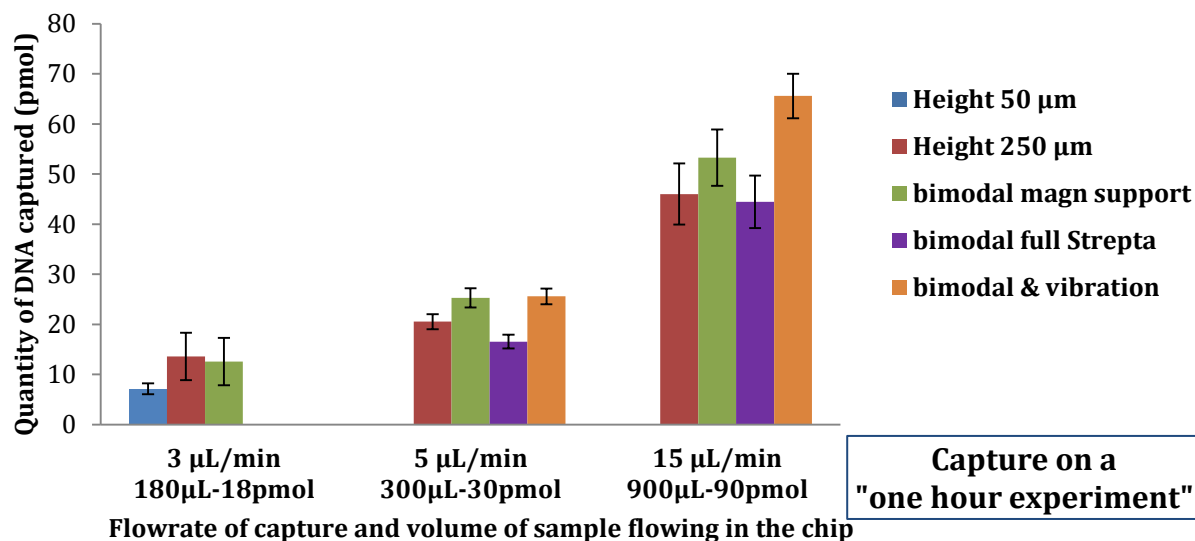


**Figure 74** Graphic representation of the quantity of DNA captured in chip during a ‘one hour’ experiment for a sample of DNA 100 nM

#### b) Validation of the model on DNA hybridization

To move one step further this first proof of concept, we applied these approaches to the extraction of DNA by hybridization on beads. This project is conducted in the framework of the European project Catch-U-DNA. This project aims to extract (from patient sample) and detect circulating tumor DNA (ctDNA) without PCR based amplification. This project gathers several teams to achieve this goal. Our team’s objective is mainly related to the extraction and pre-concentration of ctDNA from clinical samples. One of the challenges is that ctDNA is usually present at very low concentration in patient samples, it is thus necessary to extract DNA from large samples in order to reach the sensitivity required.

This project falls within the development of the new generation of the fluidized bed. To evaluate the potential of our homogenization approaches, we applied them to the ctDNA extraction. To do so, the magnetic beads have been functionalized with capture oligos of 80 base pairs complementary of the target DNA. We investigated the capture of the BRAF gene. It is located on the chromosome 7 and composed of 206 801 base pairs. Only 2 298 base

pairs are used to code for the protein BRAF from the family of Raf kinases and are involved in cellular signalization allowing control of the growth, differentiation and proliferation.

Somatic mutation can be found in more than 60% of the human skin malignant melanoma, but also in other types of cancer such as metastatic colorectal adenocarcinoma, ovarian cancer or sarcomas.

The mutated sequence used was a 80 base pair with the mutation underline in red:

TTCATGAAGACCTCACAGTAAAAATAGGTGATTTTGGTCTAGCTACAGAGAAATCTCGATGGAGTGGGTCCCATCAGTTT  
GAACAG

After a preliminary optimization of the hybridization conditions, we have investigated the potential of our approaches to capture DNA through hybridization in the fluidized bed at 5 or 15  $\mu\text{L}/\text{min}$ . First tests were made on 50  $\mu\text{L}$  of sample at a DNA concentration of 10 nM. The detection was performed optically, as the target DNA was conjugated with a fluorophore (Alexa Fluor 488).

As shown in Figure 75, the standard capture has a very low efficiency (less than 10 %) whereas we were able to drastically improve the capture efficiency by adding a vibration system and working with a bimodal support. The combination of the two approaches allows to reach capture efficiency around 80% both at 5 and 15  $\mu\text{L}/\text{min}$  against an efficiency of 10% with the standard method on the first 0.5 pmol injected. The gain of adding a vibration system and working with a bimodal support is higher than with the biotin-streptavidin system. Several assumptions could explain this behavior: the nature and kinetic of the ligation of the molecule of interest, the surface density of ligand on the surface of the beads, the size of the target...

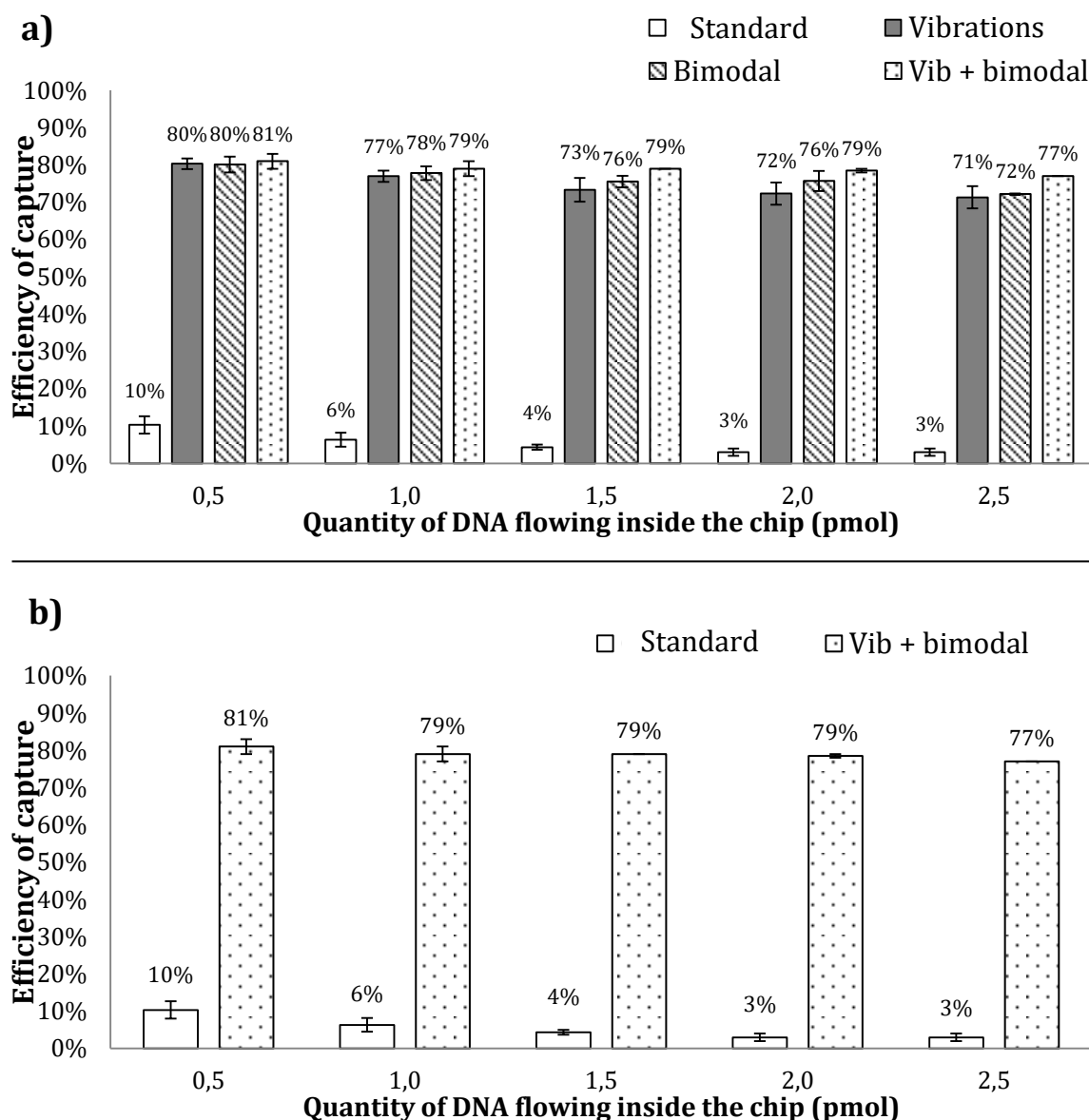


**Figure 75** Graphic representation of the efficiency of capture of the gene BRAV 600 E at 10 nM in a Tris buffer with beads coated with the complementary DNA. Capture is realized at 49° C in a 250 μm chip at 5 (a) and 15 (b) μL/min with different techniques to improve the efficiency such as addition of vibration, bimodal support, both and both with an shutdown of the bed every 30s

A bimodal matrix and an incorporated vibration system allow to work at high throughput (15 μL/min as presented, but higher flowrates can be explored) with a high efficiency of capture (80%). For now, our limit of detection is fixed by the optical detection. This project will be continued with new ways of quantification of DNA, including a ligase chain reaction and an acoustic detection.

## 4. Conclusion and Perspectives

### a) Conclusion

We introduced a new concept to improve the capture efficiency in the new generation of fluidized bed based on the use of a bimodal magnetic support. The optimal composition of the beads matrix is to use equally two sizes of beads (1  $\mu\text{m}$  and 2.8  $\mu\text{m}$  diameter).

The use of bimodal systems seems to modify significantly the morphology of the bed: we observe an increase of the bed volume as well as a better uniformity in both the particles and the flow distribution in the bed. We believe that the presence of two populations affects the way particles interact inside the bed, favors the mobility of particles by decreasing the stability of columns and fills gaps induced by the formation of columns.

To investigate how these physical improvements can affect the solid phase extraction performed in the bed, a first evaluation of the capture in the bed has been performed using biotin-streptavidin model. We demonstrated that the use of a bimodal matrix coupled with vibrations at the inlet of the chip strongly improved the capture, as capture efficiency of 65% was achieved at 15  $\mu\text{L}/\text{min}$  while only 46% of capture was obtained with a standard system. To further investigate the potential of this approach, a more realistic model has been used. We have investigated the capture of DNA target by hybridization on beads with a complementary strand of DNA. The effect of bimodal matrix and vibrations was even more striking than for the streptavidin/biotin model. 80% of capture was achieved while only 10% of capture was obtained with the standard method. In both situations, we were able to demonstrate an improvement of the capture efficiency by working with a bimodal support. We have also shown that the best configuration is the combination of the two approaches (bimodal matrix/vibrations). It leads to a system of extraction and pre-concentration working at high throughput while maintaining a high capture efficiency.

### b) Perspectives to further improve the bed homogeneity

To complete this approach, new experiments are in progress to modify not the dimension but the shape of the particles. Our hypothesis is that it could help to weaken the columns stability. Our goal is to destabilize more the organization of the columns of beads.



Two approaches have been conducted in parallel: addition of nano-needles inside the matrix of beads and use of particles of different shapes to create more instability inside the columns.

We did a first trial with nano-needles (Figure 76 A and B), kindly given by Gaelle Charron from Paris Diderot. Those needles had a length around  $5.69\ \mu\text{m}$  and were made of magnetic nano particles assembled by a polymer through a dialysis process (Lugagne et al., 2017). The ratio between the negative charges brought by the nanoparticles and the positive charges brought by the polymer was around 6. We could directly observe segregation between the beads and the needles (mass concentration of the nano-needles remained unknown). This may be due to the not well controlled length of the needles and to their adhesion to PDMS. However, beads seemed to make fewer columns (Figure 76 B) when they interacted with the needles.

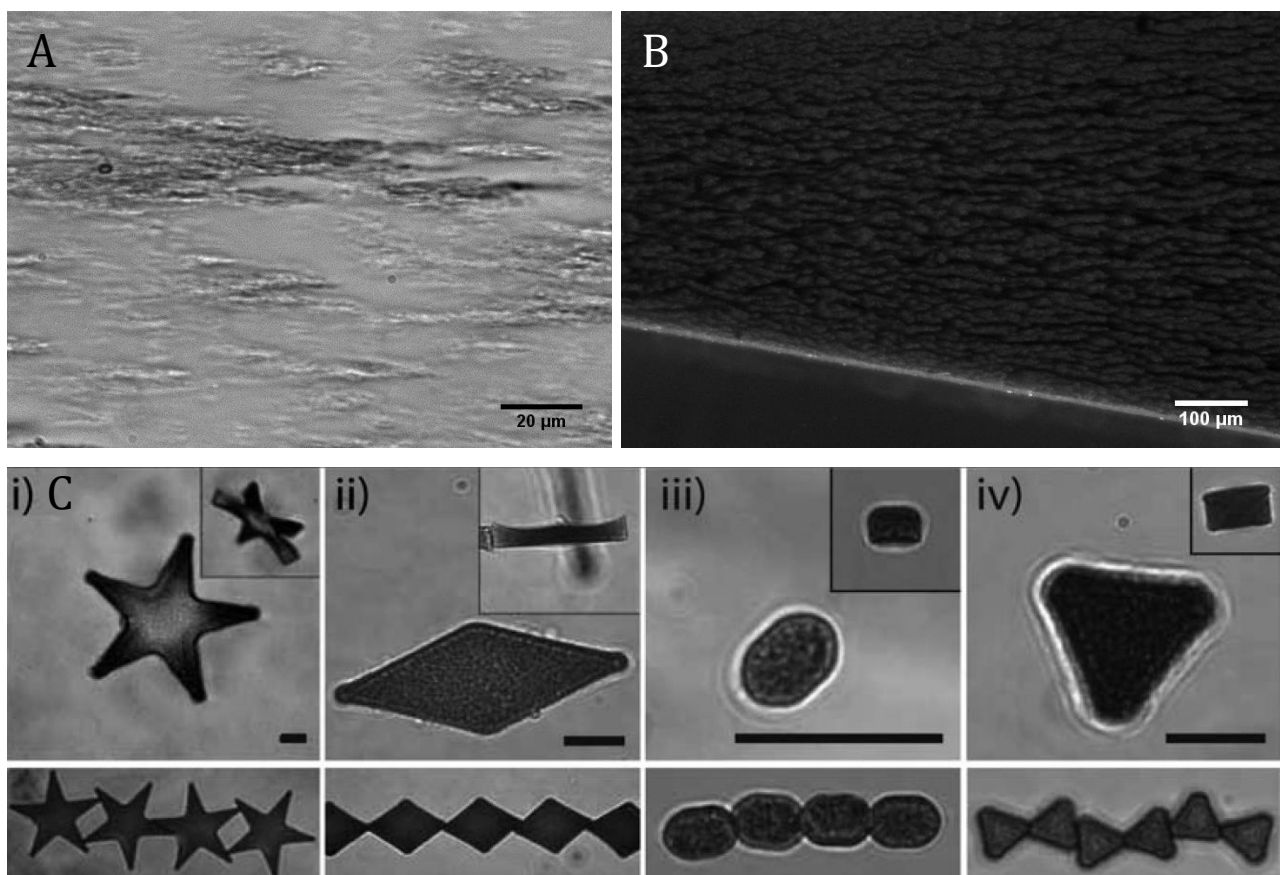


**Figure 76** Pictures of nano-needles inserted in the PDMS chip (A) and mixed with  $250\ \mu\text{g}$  of carboxylic Dynabeads of  $2.8\ \mu\text{m}$  diameter (B). (C) panels are superparamagnetic particles and their chaining under an homogeneous field (Tavacoli et al., 2013). Scale bars of the lower panel C are  $10\ \mu\text{m}$

Based on these preliminary observations, we initiated a collaboration with Olivia Du Roure team to introduce in the matrix of beads superparamagnetic particles of different shapes (Figure 76 C). Those particles are created by polymerization of an assembly of nano-magnetic particles (Tavacoli et al., 2013) and have superparamagnetic properties. We hope to disrupt the formation of columns and weaken the columns in order to homogenize the bed of beads.

This work is ongoing and will be completed with a full characterization. If we see an improvement of the re-circulation of the beads and their repartition in the bed, we could work with those particles and maybe even functionalize them.

## 5. Material and method

Chips were realized by pouring polydimethylsiloxane (PDMS) on brass micro-milled mold. Micro-milling was realized on a Mini-Mill by Minitech Machinery Corp. with drills of 0.2 X 0.4  $\mu\text{m}$ , 0.3 X 0.6  $\mu\text{m}$  and 1 X1  $\mu\text{m}$ . The bonding was performed through oxygen plasma. Surface treatment was performed using PDMA-AGE 0.5%, with one hour incubation.

MyOne™ and M-270 Carboxylic Acid Dynabeads® (1 and 2.8 $\mu\text{m}$  in diameter, Dynabeads®, Thermofisher, 6011, 14305D) were used as 'inactive' magnetic beads. Dynabeads® M-450 were used to see the impact of larger beads. Streptavidin modified Dynabeads® Myone T1 and M-280 (1 and 2.8 $\mu\text{m}$  in diameter, Dynabeads®, Thermofisher) were used as solid phase for capture experiments. Second generation chips were filled with 250  $\mu\text{g}$ . All beads were washed three times in buffer solution before use following the data sheet protocol.

Streptavidin modified Dynabeads® M-280 (2.8 $\mu\text{m}$  in diameter, Dynabeads®, Thermofisher) were used for specific capture experiments. 250  $\mu\text{m}$  chips were filled with 250  $\mu\text{g}$  of beads. All beads were washed three times in buffer solution before use following the data sheet protocol.

Biotinylated DNA conjugated to a biotin and a fluorophore Alexa488 was buy from IDT®. DNA was then diluted in a Tris-EDTA buffer, and the concentration was adjusted with PBS (Sigma Aldrich). The sequence ordered with HPLC purification was:

/5BiosG/CTCTCTCTCTCTCTCTCTCT/3AlexF488N/

BRAF sequence was purchased from EUROFINS® or IDT®. The sequence capture was 5'TTCATGAAGACCTCACAGTAAAAATAGGTGATTTTGGTCTAGCTACAGAGAAATCTCGATGGAG TGGGTCCCATCAGTTTGAACAG3' conjugated to a fluorophore Alexa488. The reverse sequence

3'AAGTACTTCTGGAGTGTCATTTTTATCCACTAAAACCAGATCGATGTCTCTTTAGAGCTACCTC ACCCAGGGTAGTCAAACCTTGTC5' was also purchased, but combined to a biotin. The reverse sequence was grafted on the surface of M-280 Streptavidin beads following the protocol of the supplier (Dynabeads®, Thermofisher). The capture was performed in a TRIS HCl buffer (10mM pH 7.5), with EDTA (5mM), NaCl (1M) Tween 20 1% (w/v). The temperature was set at 49°C using an ITO plate.

## Bibliography

- Ali, S.S., Al-Ghurabi, E.H., Ibrahim, A.A., and Asif, M. (2018). Effect of adding Geldart group A particles on the collapse of fluidized bed of hydrophilic nanoparticles. *Powder Technol.* *330*, 50–57.
- Bruni, G., Lettieri, P., Newton, D., and Yates, J. (2006). The influence of fines size distribution on the behaviour of gas fluidized beds at high temperature. *Powder Technol.* *163*, 88–97.
- De Groot, J.H. (1967). Scaling Up of Gas Fluidized Bed Reactors. *Proc. Int. Symp. Fluid. Eindh.* 348–361.
- Dutz, S., Hayden, M.E., Schaap, A., Stoeber, B., and Häfeli, U.O. (2012). A microfluidic spiral for size-dependent fractionation of magnetic microspheres. *J. Magn. Mater.* *324*, 3791–3798.
- Fonnum, G., Johansson, C., Molteberg, A., Mørup, S., and Aksnes, E. (2005). Characterisation of Dynabeads® by magnetization measurements and Mössbauer spectroscopy. *J. Magn. Mater.* *293*, 41–47.
- Grace, J.R., and Sun, G. (1991). Influence of particle size distribution on the performance of fluidized bed reactors. *Can. J. Chem. Eng.* *69*, 1126–1134.
- Gu, Y., Ozel, A., and Sundaresan, S. (2016). Numerical studies of the effects of fines on fluidization. *AIChE J.* *62*, 2271–2281.
- Huilin, L., Yurong, H., Gidaspow, D., Lidan, Y., and Yukun, Q. (2003). Size segregation of binary mixture of solids in bubbling fluidized beds. *Powder Technol.* *134*, 86–97.
- Inglis, D.W. (2009). Efficient microfluidic particle separation arrays. *Appl. Phys. Lett.* *94*, 013510.
- Lacey, P.M.C. (1954). Developments in the theory of particle mixing. *J. Appl. Chem.* *4*, 257–268.
- Lettieri, P., and Macrì, D. (2016). Effect of process conditions on fluidization. *KONA Powder Part. J.* *2016*, 86–108.

Lugagne, J.-B., Brackx, G., Seyrek, E., Nowak, S., Sivry, Y., Vitorazi, L., Berret, J.-F., Hersen, P., and Charron, G. (2017). Assembly and Characterizations of Bifunctional Fluorescent and Magnetic Microneedles With One Decade Length Tunability. *Adv. Funct. Mater.* *27*, 1700362.

Moghtaderi, B., and Song, H. (2010). Reduction Properties of Physically Mixed Metallic Oxide Oxygen Carriers in Chemical Looping Combustion. *Energy Fuels* *24*, 5359–5368.

Naimer, N.S., Chiba, T., and Nienow, A.W. (1982). Parameter estimation for a solids mixing|segregation model for gas fluidised beds. *Chem. Eng. Sci.* *37*, 1047–1057.

Peng, Z., Doroodchi, E., Alghamdi, Y., and Moghtaderi, B. (2013). Mixing and segregation of solid mixtures in bubbling fluidized beds under conditions pertinent to the fuel reactor of a chemical looping system. *Powder Technol.* *235*, 823–837.

Petousis, I., Homburg, E., Derks, R., and Dietzel, A. (2007). Transient behaviour of magnetic micro-bead chains rotating in a fluid by external fields. *Lab. Chip* *7*, 1746–1751.

Shire, T., O’Sullivan, C., and Hanley, K.J. (2016). The influence of fines content and size-ratio on the micro-scale properties of dense bimodal materials. *Granul. Matter* *18*, 52.

Sun, G., and Grace, J.R. (1990). The effect of particle size distribution on the performance of a catalytic fluidized bed reactor. *Chem. Eng. Sci.* *45*, 2187–2194.

Tavacoli, J.W., Bauër, P., Fermigier, M., Bartolo, D., Heuvingh, J., and du Roure, O. (2013). The fabrication and directed self-assembly of micron-sized superparamagnetic non-spherical particles. *Soft Matter* *9*, 9103.

Wormsbecker, M., Adams, A., Pugsley, T., and Winters, C. (2005). Segregation by size difference in a conical fluidized bed of pharmaceutical granulate. *Powder Technol.* *153*, 72–80.

Zaltzman, B. P. Verma, and Z. Schmilovitch (1987). Potential of Quality Sorting of Fruits and Vegetables Using Fluidized Bed Medium. *Trans. ASAE* *30*, 0823–0831.

Zrostlík, Š., and Matoušek, V. (2017). On the effect of segregation on intense bimodal bed load. *EPJ Web Conf.* *143*, 02148.

---

## Transition

The first part of this thesis was focused on the development of a new generation of fluidized bed to work at high throughput. We have overcome the difficulty related to the matrix of beads homogeneity. Our approach was based on disturbances of the flow streamlines by addition of a module of vibration and on a lower stability of the magnetic columns thanks to the use of a bimodal matrix of beads.

These improvements of the microfluidic magnetic fluidized bed have shown their efficiency on two models: the first one was a capture of biotin on streptavidin beads and the second one was extraction of DNA with beads functionalized with short complementary sequences of DNA.

The second part of this manuscript will focus on bio-applications of the microfluidic magnetic fluidized bed. As both part of my PhD have been conducted in parallel, these applications have been developed on the first generation of fluidized bed. First a demonstration of extraction, pre-concentration and detection of bacteria in chip will be presented. Then the fluidized bed will be used as a biomimetic platform to test specific ligands in order to relieve women with pre-eclampsia during pregnancy. Finally ELISA on chip will be directly performed within the fluidized bed. Those three projects demonstrate the versatility, adaptability and efficiency of the microfluidic magnetic fluidized bed for bio-applications. It offers a low cost, portable and accurate method to extract and pre-concentrate molecules of interest.



**Part B**

**Application of the first generation of fluidized bed to bio-analytical  
challenges**





## Chapter 5

# A microfluidic fluidized bed to capture, amplify and detect bacteria from raw samples

### 1. Introduction

#### a) Health standards in food poisoning

There are at least as many bacteria in the human body as there are human cells (Sender et al., 2016). The complex communities of bacteria hosted by the human body have different functionalities such as help to digestion or consolidation of the immune system (more than 500 species of bacteria inside a human body) (Dethlefsen et al., 2007). It has been recently demonstrated that immunotherapies efficiency is affected by antibio-therapy before or during the cancer treatment (Vétizou et al., 2015). Bacteria can be found in many different regions of the human body. Most of them are located in the colon ( $10^{14}$  bacteria), but there are also huge amount of bacteria in the mouth, the skin, the oesophagus and the stomach.

Most of the time, those microbial communities live in harmony with the human body but in some cases, bacteria are pathogens and can produce disease. Infection of a human body can spread through direct contact, such as nosocomial infections (4 000 deaths in 2012 in France declared (Institut de veille sanitaire, 2012)) or through alimentation, where bacteria have a prominent place. Among the different bacteria involved in such infections, Salmonella have been for quite a long time and still are the main cause of food toxi-infection in France (Brisabois et al., 1997). The number of food poisoning increases every year, and can lead to

severe implications. As shown on Figure 77, food poisoning is an issue that concerns all regions of France, getting more important every year (French Public Service, 2016). A recent scandal concerning baby milk powder has enlightened the importance of this issue (BBC, 2018; Le Maire, 2017), with 35 babies infected by salmonella after consuming Lactalis products.

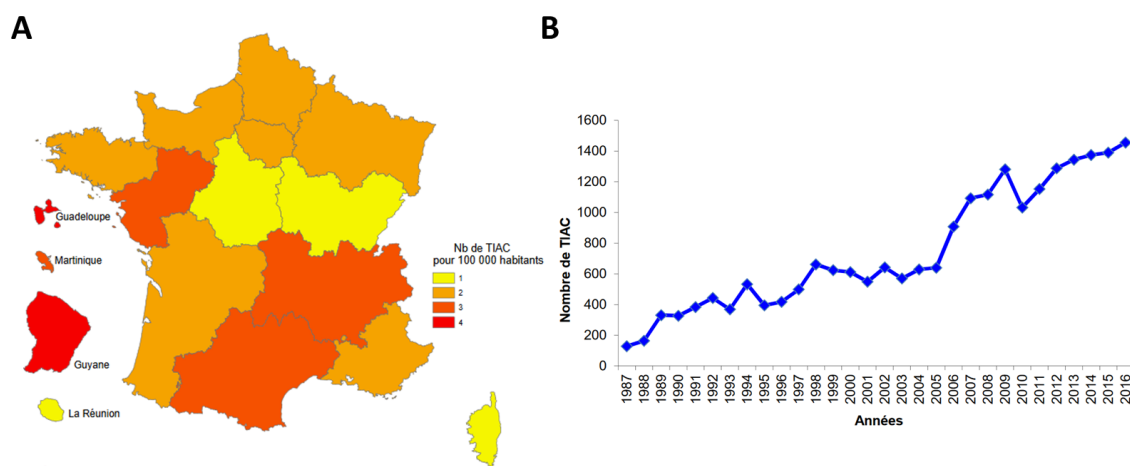


**Figure 77 : Distribution of Collective Food Toxi Infection (CFTI) declared in France for 100 000 inhabitants and evolution of the number of CFTI over the years (French Public Service, 2016)**

In industries, health standards are used to fix an upper limit (which can be null) of living bacteria in final products or at each step of their industrial process. Health and agri-food sectors are the most concerned by those standards. For both, it is important to detect and analyse the presence of bacteria at low costs, high throughput and with low volumes of samples. Matrices of those samples are usually complex and dense (milk, blood...). Of course, being able to detect the presence of pathogens in short period of time with a high confidence level is essential to prevent global contamination.

#### **b) Microfluidics for the capture and detection of bacteria**

Nowadays, the detection and quantification of bacteria are usually done by conventional plating. It consists in performing bacteria culture on selective media with manual count of colonies. The gold standard in clinics is still petri dish culture that provides a high sensitivity and selectivity. However, the time to result is still long, around 24 to 48 hours which is the time needed for bacteria development and pre-enrichment. Despite being highly efficient and sensitive, this approach remains long, tedious and labour-intensive with the need of specialized staff. This explains why numerous groups have developed alternatives strategies

to tackle these issues. One of the most famous is the GeneXpert –Cepheid system, used for detection of sepsis, with an average time of 60 minutes and based on PCR, nested PCR and RT-PCR in real time. The machine itself costs US\$17 000 and each tests costs approximately US\$17. More recently the MOBIDIAG company has launched a micro-fluidic based technology named Novodiag®. It is a fully automated platform for infectious disease based on PCR diagnostic, microarray technology and fluorescent detection. This platform has been supplemented by Amplidiag®, a molecular test for detection of resistance (Rintala et al., 2016). Results are accessible in 1 hour. The platform costs 40 000 euros and each chip is around 40 euros more.

Numerous analytical methods have been developed for bacteria detection. Usual protocols can be divided in two steps: capture and detection. These steps can be performed either with surface or whole cell recognition (immunoassay technics, mass or flow cytometry, molecule-specific probes), nucleic acid methods (hybridization, PCR, qPCR, microarray) or enzyme/substrate methods (chromogenic or fluorogenic substrates). Those developments fall within a perspective of high sensitivity technology, usually by means of pre-concentration or enrichment steps.

Microfluidic methods facilitate automation, increase the reproducibility and allow to work with small volumes of samples. A large numbers of microfluidic approaches have been developed to tackle the challenge of bacteria analysis. Some of them rely on integration of usual techniques as described in the previous section, while others are based on 1) physical properties of bacteria such as the size, 2) sorting by hydrodynamic effect, 3) electrophoresis. In the following section, we will essentially focus on the technology developed to capture and/or sort bacteria from complex samples.

Selection by size in a complex media is also a feature that microfluidic can execute. Bacteria have an average diameter of 1  $\mu\text{m}$ , which is 5 to 20 times smaller than eukaryote cells. Separation using physical criteria such as inertia in microchannel allows to work in continuous flow and at high flowrate (Wu et al., 2009). As shown on Figure 78, in inertia-based separation, the sample is pinched between two layers or flow streams, this effect organised the particles by size inside the matrix. This is amplified by the size dependency of the velocity in a straight channel. As shown in figure 2, using this approach, the group of Wu et al. was able to separate bacteria from red blood cells. This system could work at quite high flowrate, up to 18  $\mu\text{L}/\text{min}$ , which allowed to test higher volumes of samples and then to increase the sensibility of the device. The total cell survival rate was greater than 95%, which means that the sample isn't altered and the factor of concentration could reach 300.

However, this device needed a first step of dilution of the blood sample (1:5 to 1:10) and the red blood cell fraction collected at the end is not fully decontaminated.

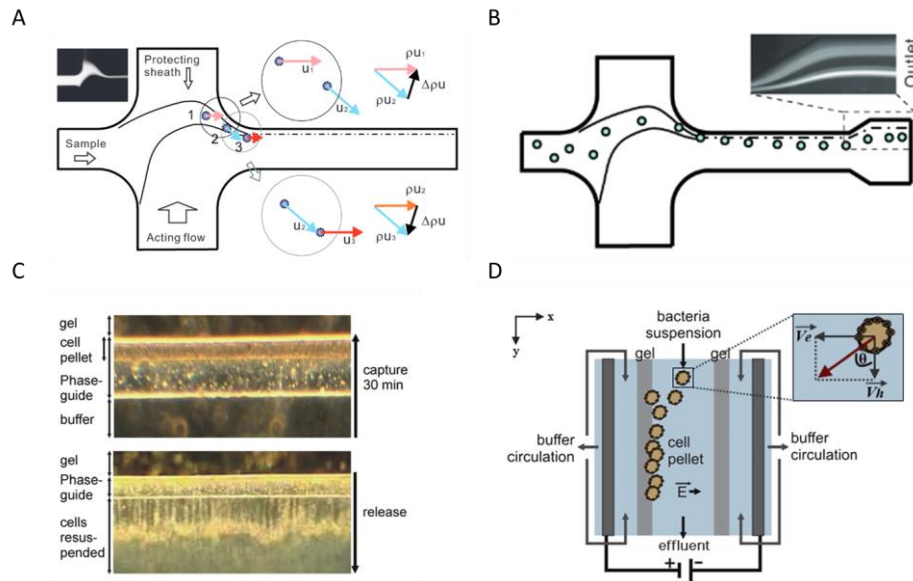


**Figure 78 : Capture of bacteria size selection by A) and B) (Wu et al., 2009) or C) and D) electrophoretic method (Podszun et al., 2012). A) and B) illustrate the principle of soft inertial separation using cross shape channel to separate smaller particles from bigger ones. As bacteria have a diameter 4 to 6 times smaller than red blood cells, they can be isolated from diluted blood. C) is a picture of the chip And D) is an illustration of and electrophoresis-based trapping principle: bacteria are continuously injected through the channel where they are deflected following the relation between the electrophoretic velocity  $V_e$  and the hydrodynamic velocity  $V_h$ . The gel creates a protective boundary between the electrodes and the sample (Podszun et al., 2012).**

Dielectrophoresis and free flow electrophoresis provide very intriguing approaches to perform specific sorting of bacteria. Dielectrophoresis methods are still complex to handle, require slow flowrate of work and low buffer conductivity, hardly compatible with biological matrices. Free flow electrophoresis is an interesting solution to bypass those issues. Electrophoretic mobility of a bacterium is a function of the charge to size ratio. As explained in Figure 78 (Podszun et al., 2012), the angle of deflection near electrodes can be written as  $\tan \theta = \frac{V_e}{V_h}$  with  $V_e$  the electrophoretic velocity and  $V_h$  the hydrodynamic velocity. This deflection is used to separate bacteria from a complex sample, as long as the viscosity is not a constraint (all experiments are realized in a Tris buffer). Enrichment efficiencies only reached 80%, and the concentration factor was around 20. The geometry of the chip was quite complex and the material needed to resist high temperatures due to the operation of the electrodes. However, this technique enables to work with high volumes of

sample ( $3\mu\text{L}/\text{min}$ , for an initial volume of  $100\ \mu\text{L}$ ) and low concentrations (down to 266 cells per mL). This system still needed its integration with analysis platforms, such as PCR detection.

More selectivity compared to the previously described system can be achieved with labelling methods usually based on capture antibodies. Microfluidic channels can be coated by specific antibodies using for example salinization to capture bacteria of interest. This capture needs to be coupled with a detection method that could be for example impedance based measurement that offers a limit of detection down to  $10^5$  colony forming unit (cfu)/mL (Boehm et al., 2007). Coupled with surface plasmon resonance imaging (Bouguelia et al., 2013), it also offers the possibility to perform real time analysis, and gets down the limit of detection to 3 cfu/mL. In both these works, specificity and selectivity are increased thanks to antibody capture. However, methods including grafting of the channel walls are usually limited by the diffusion of bacteria and they usually need a sedimentation/incubation step in small channel, which introduces limits in accessible flowrates. In such approach, it is also important to take care of aggregation processes and unspecific attachment to the channel walls that may impede the measurement specificity and accuracy.

Magnetic microbeads offer a simple solution to circumvent some of those limitations. They can be used as a solid support to improve the specific surface of bacteria capture but clogging and aggregation are still two major issues for magnetic beads manipulation. Magnetic beads have the advantage of being already commercially available with different functionalization processes. They can be used to isolate bacteria in complex matrices but also to manipulate them, from a fluid to another.

To compensate aggregation, a moving magnet can be used. For instance, a system of wheel containing magnets that rotate below a microfluidic channel was introduced by Verbarth et al. to induce continuous movement of particles (Verbarth et al., 2013). Beads can also be directly introduced inside the liquid, using the dynamic of the flow to mix and a magnet positioned at the end of the channel to extract them (Kang et al., 2014). The system introduced was a blood-cleaning device able to remove bacteria in whole blood at a flowrate up to  $1.25\ \text{L}/\text{h}$ . Analysis in continuous flow offered the opportunity to work with a system close to extra corporal circulation for animal samples. The authors demonstrated the possibility to implement the system to a living rat and showed an increase of survival after injection of a lethal dose from 13% to 89% on a 5h experiment ( $n=3$  for both groups).

We have described several approaches for bacteria capture. It is important to notice that the detection of bacteria requires the addition of a second module for detection and quantification (Gracias and McKillip, 2004; Mairhofer et al., 2009) such as micro flow cytometer (Krüger et al., 2002), PCR (Csordas et al., 2008), ELISA (Paula et al., 2002; Yeh et al., 2002), measure of impedance (Boehm et al., 2007; Wang et al., 2012) or surface plasmon resonance (Bouguelia et al., 2013). These techniques allow multiplexing with sandwich of antibodies or specific area for each bacterium.

## **2. New module of extraction and pre-concentration of bacteria using a moving magnetic matrix of beads**

During my PhD project, we introduced a new technology able to capture and detect bacteria that gathers at low cost the selectivity of the immunocapture and the possibility to work in flow without a dependence on diffusion of particles. This technique also takes advantages of capture with solid support on magnetic particles and involves the magnetic fluidized bed concept that we previously introduced.

### **a) Microfluidic magnetic fluidized bed as a platform of capture, extraction and detection of bacteria**

The microfluidic magnetic fluidized bed previously described offers the possibility to increase interactions between the solid surface of the beads and the liquid volume of the sample flowing through while presenting non-clogging features as it will be described in the following article in Chemical Science (Pereiro et al., 2017).

Extraction on magnetic beads has already shown its efficiency for molecule or cells capture. As we have seen before, the main disadvantage of this method is the complexity of handling due to numerous steps of washing. The fluidized bed offers an interesting solution to this issue in particular thanks to its stability and automation capabilities.

Moreover, by flowing nutritive medium inside the beads after the capture and washing steps, an expansion of the volume of the matrix of beads can be observed and quantified. The time of expansion is directly linked to the initial concentration of bacteria in the sample. This low cost method allows us to detect and quantify in chip the presence of bacteria in a sample, in a fast, selective and reliable way.

**b) Article**





Cite this: *Chem. Sci.*, 2017, 8, 1329

## A new microfluidic approach for the one-step capture, amplification and label-free quantification of bacteria from raw samples†

Iago Pereiro,<sup>abc</sup> Amel Bendali,<sup>‡abc</sup> Sanae Tabnaoui,<sup>‡ab</sup> Lucile Alexandre,<sup>‡abc</sup> Jana Srbova,<sup>d</sup> Zuzana Bilkova,<sup>d</sup> Shane Deegan,<sup>e</sup> Lokesh Joshi,<sup>f</sup> Jean-Louis Viovy,<sup>abc</sup> Laurent Malaquin,<sup>abc</sup> Bruno Dupuy<sup>\*g</sup> and Stéphanie Descroix<sup>\*abc</sup>

A microfluidic method to specifically capture and detect infectious bacteria based on immunorecognition and proliferative power is presented. It involves a microscale fluidized bed in which magnetic and drag forces are balanced to retain antibody-functionalized superparamagnetic beads in a chamber during sample perfusion. Captured cells are then cultivated *in situ* by infusing nutritionally-rich medium. The system was validated by the direct one-step detection of *Salmonella* Typhimurium in undiluted unskimmed milk, without pre-treatment. The growth of bacteria induces an expansion of the fluidized bed, mainly due to the volume occupied by the newly formed bacteria. This expansion can be observed with the naked eye, providing simple low-cost detection of only a few bacteria and in a few hours. The time to expansion can also be measured with a low-cost camera, allowing quantitative detection down to 4 cfu (colony forming unit), with a dynamic range of 100 to 10<sup>7</sup> cfu ml<sup>-1</sup> in 2 to 8 hours, depending on the initial concentration. This mode of operation is an equivalent of quantitative PCR, with which it shares a high dynamic range and outstanding sensitivity and specificity, operating at the live cell rather than DNA level. Specificity was demonstrated by controls performed in the presence of a 500× excess of non-pathogenic *Lactococcus lactis*. The system's versatility was demonstrated by its successful application to the detection and quantitation of *Escherichia coli* O157:H15 and *Enterobacter cloacae*. This new technology allows fast, low-cost, portable and automated bacteria detection for various applications in food, environment, security and clinics.

Received 30th August 2016  
Accepted 9th October 2016

DOI: 10.1039/c6sc03880h

www.rsc.org/chemicalscience

## Introduction

The dramatic decrease of mortality rates due to infectious diseases in the 20th century, following progress in hygiene and the discovery of antibiotics, raised the hope that they would become a minor health problem in the future of mankind.

However, the rate has been increasing again since the 80's, and infectious diseases have been identified in a recent World Health Organization (WHO) report as a global threat to human health.<sup>1</sup> Foodborne illnesses alone are responsible for 600 million infections and 400 000 deaths each year worldwide<sup>2</sup> (9.4 million infections and 1351 deaths in the US). Considering the slow progress in the discovery of new antibiotics, the main hopes of control lie in the development of prevention and of fast, convenient and low-cost technologies for early pathogen identification in clinics, environmental control and the food and beverages industry.

This is critically true in the food industry, for which, due to the long time required by existing detection methods, products carrying pathogenic bacteria can be widespread before alert, resulting in disease outbreaks with high risks for consumers and important economic costs. In the developing world, production and consumption mostly remain local, so testing should be able to accommodate non-centralized and low-technicity environments. The cost and technicity of current analysis techniques often make them unsuitable or unaffordable where analysis would be needed. The present paper focuses on

<sup>a</sup>Laboratoire Physico Chimie Curie, Institut Curie, PSL Research University, CNRS UMR168, 75005 Paris, France. E-mail: stephanie.descroix@curie.fr

<sup>b</sup>Sorbonne Universités, UPMC Univ Paris 06, 75005 Paris, France

<sup>c</sup>Institut Pierre-Gilles de Gennes, 75005 Paris, France

<sup>d</sup>Dept. of Biological and Biochemical Sciences, Faculty of Chemical Technology, University of Pardubice, 53210 Pardubice, Czech Republic

<sup>e</sup>Aquila Bioscience Limited, Business Innovation Centre, National University of Ireland Galway, Galway, Ireland

<sup>f</sup>Glycoscience Group, National Centre for Biomedical Engineering Science, National University of Ireland Galway, Galway, Ireland

<sup>g</sup>Laboratory Pathogenesis of Bacterial Anaerobes, Dept. Microbiology, Institut Pasteur, 75724 Paris, France. E-mail: bruno.dupuy@pasteur.fr

† Electronic supplementary information (ESI) available. See DOI: 10.1039/c6sc03880h

\* These authors contributed equally to this work: Amel Bendali, Sanae Tabnaoui, Lucile Alexandre.



foodborne pathogens, but of course the same issue exists for diagnostic issues.

Plating and colony-counting is still considered the “Gold Standard” for bacteria detection. The protocol starts with an overnight or even longer enrichment phase conducted in liquid broth in agitated flasks. Then, cultures are plated on Petri dishes containing agar-based growth medium and incubated for durations that may range from 12 hours to several days before counting. Finally, additional molecular or immunological typing methods may be needed, for specific strain identification. This protocol is highly sensitive and specific, but it typically requires several days, skilled personnel and large volumes of consumables. Hence, a great diversity of alternative analytical methods, based either on metabolic properties (biochemical identification techniques, chromogenic agar broth<sup>3</sup>), protein constitution (MALDI-TOF<sup>4</sup>), antibody targeting (ELISA,<sup>5</sup> flow cytometry,<sup>6</sup> immune-separation<sup>7</sup>), nucleic acid techniques (hybridization,<sup>8</sup> PCR,<sup>9</sup> microarrays<sup>10</sup>) or microfluidics,<sup>11</sup> has been developed. For the sole case of *Salmonella*, the first cause of non-diarrheal foodborne deaths in the world, several tens of kits are commercially available, the majority being based on immunorecognition.<sup>12,13</sup> The cost and complexity of current detection methods, either based on plating or on molecular assays, however, still strongly limit their extended use in routine practice.

Microfluidic-based technologies can offer platforms for faster and more automated detection systems, while reducing testing costs. A variety of microfluidic separation methods for bacteria can be found in the literature, based *e.g.* on size sorting through inertial microfluidics,<sup>11,14</sup> electrophoresis<sup>15</sup> or antibody capture.<sup>16</sup> For bacterial identification, these methods are often coupled with nucleic acid amplification techniques or further immuno-recognition protocols, increasing the complexity of the system. In addition, due to their low initial input volume, most microfluidic methods require a preliminary enrichment cultivation step to reach the sensitivity level required for most food pathogen detection standards. This is usually performed by conventional, non-microfluidic protocols, limiting the gain brought by the use of microfluidics. The specific challenges raised by clogging and need for pre-concentration were identified as early as 2007.<sup>17</sup> Recently, an interesting article reported a single-step detection of bacteria, using an integrated on-chip culture on antibody arrays and label-free detection.<sup>18</sup> This study was an important step towards global assay acceleration, achieving a sensitivity of around 140 cfu (colony forming units) ml<sup>-1</sup> in 10 hours for *Salmonella* spiked in raw milk, but it retained some limitations, such as baseline drift in the presence of real samples, a need for sample pre-treatment, and the cost of the surface plasmon resonance technology used for detection. Also, specificity *versus* other commensal bacteria in excess was not assessed. Kang *et al.* alternatively proposed a system combining DNazymes, microfluidic droplets and 3D optical detection, reaching sensitivities between 10 and 100 cfu ml<sup>-1</sup>, but this method is also prone to false positive results in the case of dead or lysed bacteria.<sup>19</sup>

Here, we present an original and compact microfluidic device allowing sensitive, fast and low-cost pathogen detection

directly from a complex raw liquid sample, down to a few cfu in a few hours. It relies on a new microfluidic technology: a microfluidic fluidized bed in which superparamagnetic beads bearing specific ligands of the pathogens of interest recirculate continuously while the raw sample is passed through. To our knowledge, this is the first time the concept of a magnetic fluidized bed has been transferred to the microfluidic scale.<sup>20–22</sup> This approach ensures a high density of beads and specific surface to improve target capture, combined with low working pressures and high resistance to clogging. Therefore, the system is ideal for analyte pre-concentration.

We apply it here for the efficient extraction of bacteria from raw milk, but go further by showing how the same system can be employed for their subsequent label-free detection with no added complexity. This is simply obtained by amplifying the bacteria *in situ* by flowing a nutritious medium through the fluidized bed. Importantly, the volume occupied by the newly formed bacteria leads to modifications of the physical properties of the fluidized magnetic bed (expansion phenomena) that can be directly monitored to perform a highly specific quantification of the initial number of microorganisms in the sample. This unique detection method presents no direct macroscopic equivalent and allows for very simple and low-cost detections. We applied and characterized it here with *Salmonella enterica* serovar Typhimurium, with a sensitivity down to bacteria numbers in the single digits, and with 5 orders of magnitude in dynamic range. The behavior was equivalent even in real application conditions of unskimmed milk and the presence of natural flora more concentrated by several orders of magnitude. We further expanded its use to the detection of *Escherichia coli*, the second most common cause of non-diarrheal foodborne deaths in the world after *Salmonella*.<sup>2</sup> The successful detection of *Enterobacter cloacae*, a major cause of nosocomial diseases, with a non-antibody ligand was also characterized to further demonstrate the versatility of the system. Regarding the latter, finally, we considered here only foodborne pathogens, but the technology also has strong potential for diagnosis at the point of care, notably thanks to its capacity for automation and reduction of contamination risk.

## Results

### Microfluidic fluidized bed operation

Macroscopic fluidized beds have been used for decades in industry. They typically comprise a cylindrical reservoir in which particles are kept in suspension by a balance between their weight and the drag force exerted by a fluid flowing upward. The flow velocity and consequently the drag force are reduced when inter-particle distance (*i.e.* porosity) increases, so that the equilibrium between drag and gravitational forces leads to a stable, steady-state and stirred suspension of particles behaving as a fluid. Some attempts at creating a microscale fluidized bed can be found in the literature,<sup>23</sup> but miniaturization is not favorable for gravitational fluidized beds, since the drag force scales with the particle radius  $r$ , whereas gravitational forces scale with  $r^3$ , limiting these devices to large particles, large chamber sizes, and low flow rates. To overcome



this limitation, we propose a new approach, replacing gravity with magnetic forces induced by a magnetic field gradient, and using superparamagnetic particles (1–4  $\mu\text{m}$  in diameter) as the solid phase. At this scale, magnetic field gradients easily achievable with permanent magnets typically exert forces 3 to 4 orders of magnitude larger than gravitational forces. This allows the use of high flow rates combined with low chamber volumes and high surface/volume ratios, thus combining fast capture kinetics and high capacity.

The microfluidic fluidized bed involves a microchamber, partially filled with micrometric magnetic particles, an external permanent magnet and a fluid flow controller (Fig. 1a). The triangular shape of the microfluidic chamber serves two purposes. First, in contrast to gravitational fluidized beds, here the force opposing drag is derived from a gradient, and it cannot be kept constant over large areas. We thus chose a monotonously decreasing magnetic force along the main axis of the chamber, compensated by a decrease of the drag force along the same axis thanks to the triangular shape of the chamber. The divergences of the field and of the flow were also

optimized to favor a stable and continuous recirculation of beads for optimal capture (Fig. 1b, Movie S1 & 2<sup>†</sup>). The obtained particle trajectory pattern is comparable to the spouting regimes sometimes employed in macroscopic fluidized beds.<sup>24</sup> We hypothesize that in the central part, drag forces are dominant over magnetic forces, resulting in particles being dragged towards the exit of the chamber. When reaching the front of the fluidized bed, a sudden drop in flow velocity, due to the end of the solid fraction, leads to the equilibrium of drag and magnetic forces. A lateral displacement of particles then takes place. This is the combined consequence of the particle inflow, which maintains the mass transfer balance, and of the no slip boundary condition near the walls: in this region, the fluid velocity decreases significantly, so that the magnetic forces dragging particles upstream become dominant. As a result, a flow of particles is formed back to the channel entrance. Thus, this new geometry avoids the formation of a narrow open pathway of the percolating liquid through the magnetic beads bed, or “bed fracture”, a phenomenon that usually occurs with magnetic packed beds at high flow rates.<sup>22</sup> We thus obtain a completely dynamic and almost homogeneous bed of magnetic microparticles. As visible in Movie S2<sup>†</sup> & Fig. 1d, beads are organized by dipole–dipole interactions into small columns oriented mostly along the flow, a feature also contributing to decreasing flow resistance. Upon flow rate increase, the effective friction coefficient of each bead decreases due to the increased spacing between the beads, so the system is intrinsically stable for a large range of flow rates (flow rates ranging from 0.5 to 5  $\mu\text{L min}^{-1}$  were used here). This flow rate can then be optimized for each given application, higher flow rates leading to a longer total length of the fluidized bed and consequently to a higher bed porosity (Fig. 1c).

#### Capture of *Salmonella enterica* serovar Typhimurium

The capture efficiency of this new approach regarding *Salmonella enterica* serovar Typhimurium (*S. Typhimurium*) was investigated, using commercial anti-*Salmonella* Dynabeads®.<sup>25</sup> Capture efficiency was first evaluated by flowing, at 1  $\mu\text{L min}^{-1}$ , a sample spiked with *S. Typhimurium* at initial bacteria concentrations ranging from  $10^2$  to  $10^4$  cfu  $\text{mL}^{-1}$  (corresponding to 5 to 500 cfu, respectively, in 50  $\mu\text{L}$ ; see ESI<sup>†</sup> Experimental). For bacteria spiked in phosphate buffer pH 7.4 (PBS), high capture rates of 84–93% ( $\pm 25\%$  at  $10^2$  cfu  $\text{mL}^{-1}$  and  $\pm 3\%$  at  $10^4$  cfu  $\text{mL}^{-1}$ ) were achieved. The extraction rate from raw milk samples was evaluated by spiking *S. Typhimurium* in 50  $\mu\text{L}$  of whole UHT milk, and directly flowing this mix, without pre-filtration or dilution, through the fluidized bed. The capture rate ( $71\% \pm 8$ ,  $n = 3$ ) was high, though slightly lower than in PBS. Thus, the presence of lipids and a high concentration of proteins in milk did not result in a dramatic loss of capture efficiency or clogging. In Movie S3,<sup>†</sup> a large number of fat droplets (visible as light grey dots) can be seen escaping the fluidized bed and flowing towards the outlet. The fluidized bed itself, however, behaves as without milk. The system is thus able to extract bacteria efficiently from a complex matrix. In addition, dairy products often contain mesophilic lactic bacteria (at

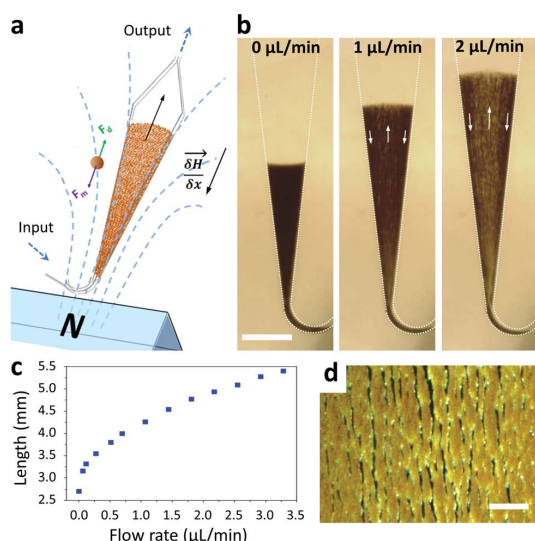


Fig. 1 Scheme of the microfluidic fluidized bed. An external permanent magnet creates a magnetic field gradient inside a triangle-shaped chamber, resulting in magnetic forces globally oriented towards the chamber inlet, applied on superparamagnetic beads (a). Fluids are passed into the chamber through the inlet located on the magnet side, using a pressure-based flow controller (MFCS Fluigent). If no pressure is applied, the beads remain in a packed-bed configuration due to magnetic forces (scale bar = 1 mm) (b); under flow, the beads are also subject to drag forces oriented upstream, and above a flow threshold a new, steady-state dynamic equilibrium, called the fluidized bed regime, is achieved, favoring high percolation rates and internal recirculation of the beads (indicated with arrows). The total length of the fluidized bed is directly dependent on the applied flow rate due to a change in the porosity of the bed (c). The bed in the fluidized state is shown in the micrograph (d) and in Movie S2,<sup>†</sup> showing the high bead density and the multiple percolation paths leading to efficient and uniform capture (scale bar = 200  $\mu\text{m}$ ).



View Article Online

Edge Article

Chemical Science

concentrations from  $10^1$  to  $10^4$  cfu ml<sup>-1</sup> (ref. 26)). Such non-pathogenic, naturally occurring bacteria could greatly outnumber the pathogenic ones and potentially negatively affect their immunocapture. Oppositely, in the case of non-specific capture, they could yield false positive results. To mimic such situations, we tested additional samples, in which *Lactococcus lactis* was spiked in UHT milk samples with a ratio of 500 *L. lactis* for 1 *S. Typhimurium*. This lactic bacterium is particularly relevant, since it is naturally occurring in healthy raw milk, and is also the primary organism used in the manufacturing of cheese, buttermilk or sour cream, being added to milk for the enzymatic production of lactic acid. As shown in Fig. 2, no significant difference in *S. Typhimurium* capture rate was found between samples with and without *L. lactis*, while the non-specific capture of *L. lactis* was below 0.15% for the three concentrations tested, corresponding to a selectivity of at least 500/1 (or >99.8%).

### Bacteria culture, detection and quantification by bed expansion

A key innovation to achieve high sensitivity using a full microfluidic process without pre-culture was the implementation of bacteria culture directly in the fluidized bed. Immediately after bacteria capture, nutritious medium (LB broth) was perfused through the chamber at  $0.15 \mu\text{L min}^{-1}$  and the chip temperature was set to  $37^\circ\text{C}$ . At this flow rate, the full content of the chamber is renewed in about 5 min, and the content of fluid in the fluidized bed itself (before bacteria expansion) is renewed in less than 2 min. On-chip bacteria growth was investigated by monitoring fluorescence in the chamber after the capture of *S. Typhimurium* expressing GFP (Fig. 3 & ESI† Experimental). From 0 to 120 min, the development of bacteria is evidenced by a multiplication of bright (green) dots attributed to individual bacteria or isolated colonies (Fig. 3a). Beyond this time, individual dots tend to merge into a bright background. Whereas individual dots become difficult to isolate (Fig. 3a), fluorescence

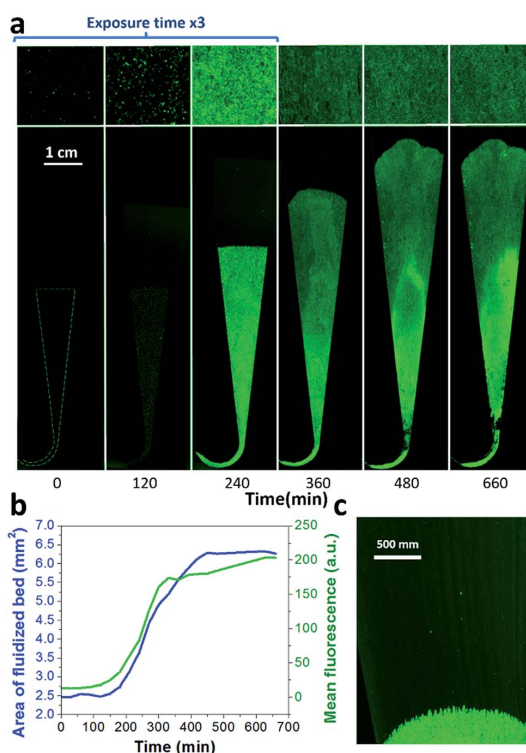


Fig. 3 On-chip culture of GFP-expressing *S. Typhimurium*. Bacteria were first captured from  $50 \mu\text{L}$  at  $10^5$  cfu ml<sup>-1</sup> (5000 total bacteria perfused in the chamber), and then cultured on chip, perfusing LB at a flow rate of  $0.15 \mu\text{L min}^{-1}$ . (a) Images of the whole bed (lower frame) and zoom (upper frame), taken every 120 min. (b) Fluorescence intensity (green) and fluidized bed area (blue). (c) Towards the end of the bed expansion (300 min), a flow of bacteria can be seen leaving the magnetic beads, dragged by the flow (at this low resolution, bacteria flow appears as faint streaks).

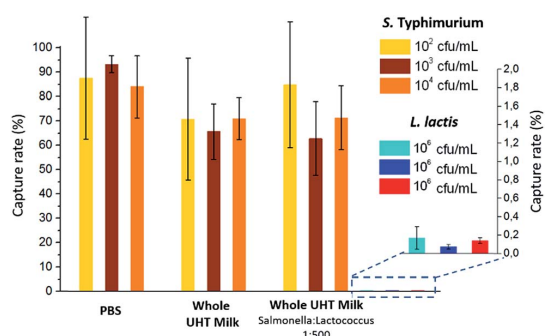


Fig. 2 Capture rates obtained for *S. Typhimurium* at two different initial concentrations and for different matrices: PBS, whole UHT milk and whole UHT milk with a proportion of *S. Typhimurium* to *L. lactis* of 1 : 500. The non-specific capture of *L. lactis* is given in expanded scale at the right of the histogram. Data are presented as mean  $\pm$  s.d. of at least three independent experiments.

intensity continues to increase (Fig. 3b, green curve) and finally reaches a plateau. These results evidence the possibility to keep bacteria alive after their capture and to multiply them within the microfluidic device. Even for initial amounts of bacteria in the single digits, the distribution of fluorescence tends to spread across the whole fluidized bed, suggesting that “daughter” bacteria distribute all over the bed. This feature, which we associate with the fluid nature of the bed, retains a main advantage of culture in liquid state (*i.e.* an optimal access to nutritious medium independently of bacteria generation), while keeping bacteria highly confined on a solid support for maximal sensitivity. Indeed, when on-chip culture is performed in a non-fluidized situation, no bed expansion is observed: we believe that in this latter case, the newly grown bacteria rapidly accumulate in clumps which block access to nutritious medium, and thus cannot develop optimally.

Interestingly, these experiments also showed a physical change in the fluidized bed during culture, revealed by an expansion of the bed, apparent as a progressive increase of area





(Fig. 3a and b and Movie S4†). The area increase roughly follows that of fluorescence, with an initial plateau, an exponential-looking growth, a linear zone and a saturation plateau. This behavior is typical of nonlinear reaction kinetics with reagent saturation. Towards the end of the bed expansion an important flow of bacteria leaves the fluidized bed, dragged by the flow of nutritious medium (Fig. 3c and Movie S5, ESI Fig. 5 and 6†). This is a consequence of the saturation of the fluidized bed capacity to capture all the newly produced bacteria, a fact that could also explain the observed final plateau in the total fluorescence intensity, and the limited extent of bed expansion. Overall, the device can be used for the direct processing and analysis of samples containing only a few bacteria and allows to obtain, in a few hours, amplification factors of typically  $10^6$ , thus avoiding the need of flask-based pre-enrichment. Further, the modification of the chip aspect, in the presence of living bacteria, is indeed large enough to be detected by the naked eye, opening the possibility to assess, with a high specificity, in a few hours and without any complex or expensive detection means, the presence of only a few infectious bacteria in a raw liquid sample (Fig. 4b). To evaluate the dynamic range of the assay, the expansion of the bed was measured (Fig. 4c and ESI† Experimental) as a function of time for different initial concentrations of bacteria. This yields a series of similar curves shifted along the horizontal axis, reminiscent of the DNA quantity plots obtained in PCR (Fig. 4c). We defined an expansion threshold at  $200\ \mu\text{m}$ , corresponding to the onset of the quasi-linear expansion phase. The intersection of growth curves with this threshold defines for each initial concentration an expansion time. When plotted against the logarithm of the initial bacteria number, this expansion time follows a linear behavior (Fig. 4d, blue), providing a calibration curve for the quantitation of the initial bacteria concentration with a wide dynamic range (from  $4$  to  $10^6$  cfu per  $50\ \mu\text{l}$ ). The time required to reach an observable expansion ranges from  $60$  min for  $60\ 000$  cfu per  $50\ \mu\text{l}$  ( $1.2 \times 10^6$  cfu  $\text{ml}^{-1}$ ) to approximately  $7$  hours for  $4$  cfu per  $50\ \mu\text{l}$  ( $80$  cfu  $\text{ml}^{-1}$ ). To confirm the method specificity regarding *S. Typhimurium* quantification, cultures with the same beads were performed after flowing *L. lactis* in the device; no expansion of the bed occurred for subsequent cultures. Similar experiments were performed, starting from whole UHT milk spiked with bacteria. The results (Fig. 4d) yield very similar outcomes, showing the applicability of the technology to complex, real-life food samples. Expansion times seem slightly shorter in milk than in PBS, maybe due to the fact that the bacteria were kept in milk for  $50$  minutes during the capture step, and could thus start to grow in this medium.

We assessed the ability of our device to detect and quantify other relevant foodborne pathogens, in particular *Enterobacter cloacae* and *Escherichia coli* O157:H7. Fig. 4d shows that both bacteria species can be, similarly to *S. Typhimurium*, cultured and quantitatively detected *in situ*, except with different expansion times. Expansion times specifically depend on bacteria type and strain, but also on culture conditions, leaving room for speeding up the process by the specific optimization of the culture broth and temperature.<sup>27</sup> Besides, these assays are also interesting regarding the versatility of the technology, since

the ligand used to capture *E. cloacae* is a lectin specific to *E. cloacae* (GSL-I-B4), recently identified by a lectin array screen (for *E. coli*, commercial anti-*E. coli* 0157 Dynabeads® were employed). These experiments suggest that the fluidized bed expansion approach for bacteria detection will be applicable to a wide range of problems beyond the specific application of detecting *Salmonella* in dairy products. Finally, to further demonstrate the specificity of the device, reciprocal negative controls (*S. Typhimurium* with anti-*E. coli* beads and *E. coli* with anti-*Salmonella* beads) were performed and in both cases, as expected, no expansion was observed in the time scale of the experiments (up to  $10$  h).

### Deciphering the mechanism of bed expansion

Bed expansion could be due to different causes, such as a direct steric effect, related to the volume occupied by the new bacteria, but also differences in the aggregation state of particles due to bacteria adhesion or the formation of a biofilm. In order to discriminate between these possibilities, additional series of experiments were performed, using a wider range of bacteria concentrations in the initial sample, and mutant bacteria with modified adhesion and/or biofilm formation capabilities (see ESI† for details). These experiments demonstrated that bed expansion could be obtained without culture, if a large number of bacteria was infused during the capture, and that in such a situation, bacteria growth immediately starts during the culture phase (ESI text and Fig. 2†). Finally, the bed expansion was similar for mutant bacteria deficient in adhesion and biofilm formation, indicating that at least for *S. Typhimurium*, the formation of biofilms does not play a significant role in the expansion phenomenon. Then, assuming in addition that all the bacteria produced during culture remain confined inside the fluidized bed, a very simple expression can be proposed for the volume of expansion ( $V_{\text{exp}}$ ) as a function of time, based on an exponential cell division:

$$V_{\text{exp}} = V_{\text{bac}} n_0 2^{\frac{t}{t_d}} \quad (1)$$

where  $n_0$ ,  $t_d$  and  $V_{\text{bac}}$  are the initial number of captured bacteria, the mean doubling time, and the effective volume occupied by a single bacterium, respectively. From this expression, it is possible to estimate the time needed for the front to reach the  $200\ \mu\text{m}$  threshold defined before, this occurring when the necessary volume of expansion ( $V_{200}$ ) is reached:

$$t_{200} = t_d \log_2 \left( \frac{V_{200}}{n_0 V_{\text{bac}}} \right) \quad (2)$$

Inserting into this equation the previously measured capture efficiency, and leaving division time and effective volume as free parameters, allowed fitting of the calibration data from Fig. 4d. The best fit doubling time,  $t_d = 23.7$  min, is very close to the  $24$  min measured in batch (Fig. S4†). The best fit bacteria volume is  $V_{\text{bac}} = 4.8 \times 10^{-9}$   $\mu\text{L}$ , also consistent with the geometrical features of *S. Typhimurium* (ESI†). Inserting these values into eqn (1) with the initial amounts of analyzed bacteria yields a series of expansion curves (Fig. 4c), which agree well



View Article Online

Edge Article

Chemical Science

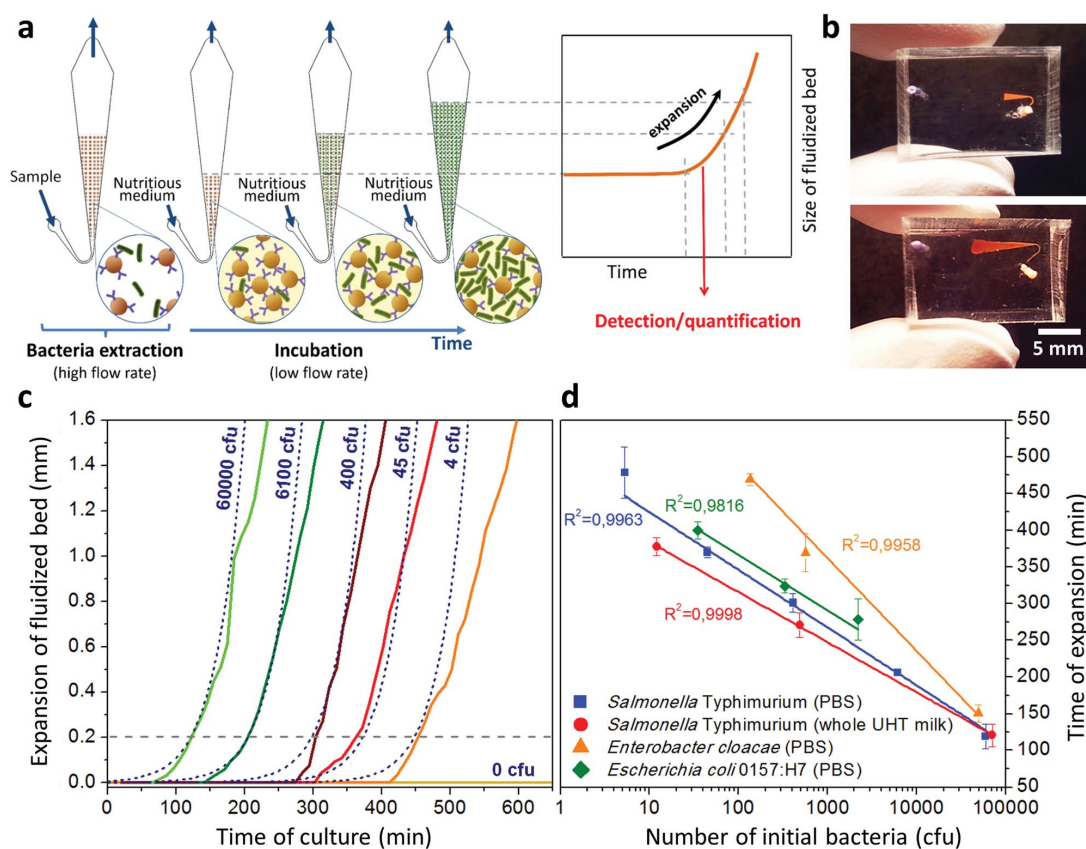


Fig. 4 Protocol and results for the direct detection of bacteria by bed expansion. (a) After sample capture and rinsing steps (at 1 and 1.5  $\mu\text{L min}^{-1}$ , respectively), measurements of the expansion of the fluidized bed (at a constant flow rate of 0.15  $\mu\text{L min}^{-1}$ ) were made along the chamber axis, with reference to the initial position of the front of the bed before expansion, resulting in expansion curves. (b) Image of a microfluidic chip at the beginning and end of a typical experiment, for a positive result. The expansion curves obtained with different initial concentrations of *S. Typhimurium* (indicated in the figure as cfu per 50  $\mu\text{L}$  of sample) are shifted with regards to each other (c), and are in good agreement with a model of expansion based on the volume of newly-formed bacteria (c, dashed lines). Defining an expansion threshold at 200  $\mu\text{m}$  (c, dotted line), a time of expansion can be measured for each initial concentration. A logarithmic plot of this expansion time versus initial bacterial load is shown in (d) for *S. Typhimurium* in PBS (blue squares) and *S. Typhimurium* in whole UHT milk (red circles), *Enterobacter cloacae* in PBS (orange triangles) and *Escherichia coli* O157:H7 in PBS (green diamonds).

with the experimental data, except for the latest part of the curves. Deviations from the model at high expansions are probably due to the saturation of the available immunocapture sites, preventing the recapture of newly generated bacteria (see ESI† for details). As a second conclusion, the quasi-identity of the doubling time, as measured in our device and in batch, demonstrates that the flow rate used for LB infusion is sufficient to nourish bacteria adequately, since any starvation would result in an increase in doubling time, or growth arrest in most severe situations.

## Discussion

This work demonstrates that the fluidized bed concept can be efficiently transposed to the microfluidic world, replacing

gravity by magnetic forces. Indeed, this transposition brings, in turn, new possibilities in fluidized bed technology, allowing for the first time stabilization in the normal gravity of a fluidized bed by purely magnetic forces, a feature that could so far only be achieved in microgravity.<sup>28</sup> As compared to previous systems based on packed or magnetically stabilized micro-columns, it brings numerous advantages. With a suitable design of micro-chamber and magnetic field, a constant recirculation of beads with close to uniform density can be achieved, maximizing capture efficiency while conferring non-clogging properties to the bed. As compared to the commonly used batch capture with magnetic particles, this mode (combining flow-through operation, recirculation and high bead density) allows an acceleration of kinetics and, importantly, the development of hands-free fully integrated detection processes. This is a major advantage



for applications in a non-technical environment (fast screening on production or consumption sites, point-of-care diagnosis), and for increased protection of operators. Also, flow-through operations can be performed with low backpressure, in order to capture analytes from relatively large volumes with a very limited mass of capture particles. The device was successfully applied to the capture of *S. Typhimurium* with capture efficiencies higher than 70% and specificity higher than 500/1 versus other bacteria. This was achieved for bacteria spiked in undiluted, unskimmed UHT milk. Then, the direct *in situ* culture of the captured bacteria was demonstrated. This cultivation yields a physical expansion of the fluidized bed, as a consequence of the volume occupied by the developing bacteria. The experimental results are in agreement with a simple analytical model associating the volume of expansion as a function of time to an exponential stochastic division of bacteria. In a first mode, this allows for a very simple method for “yes or no” specific detection of infectious bacteria with direct visual inspection. This mode, which does not require any electrical or optical detection method, nevertheless yields a sensitivity of 100 cfu ml<sup>-1</sup> in a few hours, as compared to the typical 1 or 2 days needed by conventional techniques. The versatility of the device was demonstrated by detecting other bacteria species (*E. coli* and *E. cloacae*). As an additional advantage, the microfluidic chip design is very simple and compact, and disposable chips can be easily fabricated at the industrial level by replication-based techniques. This can be a breakthrough in non-technical environments, e.g. for on-site investigation of food primary products. The technology is very generic, and we believe it will also find a wide range of applications, for instance, in early diagnosis or epidemic control. With addition of a low-cost visible light camera, the technique can be made quantitative, by measuring the time required to reach a threshold of bed expansion. In this mode, quantitative detection with a dynamic range of four to five orders of magnitude can be achieved in a total time from raw sample to result of 2 to 8 hours, depending on the initial concentration of *S. Typhimurium*, the longest time corresponding to a sensitivity of 100 cfu ml<sup>-1</sup>. This sensitivity is only limited by the volume of analyzed sample, since we demonstrated amplification from a few bacteria only in 50 µl. This is already a larger volume than accommodated by earlier microfluidic bacteria analysis devices, and is suitable for many applications.<sup>28,29</sup> Additional preliminary experiments showed that the device geometry could be scaled up to accommodate sample volumes in the mL range.

In order to reduce development costs and allow widespread development including wireless communication of results, the whole imaging and analysis process can be easily carried out on a smartphone, as suggested in ref. 30. The fluidized bed technology, however, achieves higher sensitivity and specificity, and is able to operate directly from raw samples. Due to the flat nature and small footprint of the device, one could also use ultra-low-cost detection concepts<sup>31,32</sup> (see e.g. cost analysis details in ESI†). The system can accommodate the direct infusion of complex samples such as unskimmed milk. This robustness against clogging or matrix effects, a definite advantage with regards to micro-columns, filter-based or paper-

based devices, is a consequence of the fluidized nature of the capture bed, which can be perfused by liquids containing debris or particles much bigger than the capture beads or targets, as long as these contaminating objects do not present at their surface antigens targeted by the beads. In comparison with methods based on PCR, this new approach is much simpler and thus less expensive to implement, and it detects only bacteria with a proliferative potential, whereas PCR-based methods, while very precise in terms of species identification, may yield false-positive results in the presence of dead bacteria or even residuals of lysed cells.

Live bacteria are released in important amounts during and after bed expansion, which is not the case with beads devoid of specific capture antibodies (ESI Fig. 6†). The fluidized bed could thus be used simultaneously as a first line rapid detection device, sensitive to proliferative bacteria only, and as a pre-amplification module, able to yield amplifications by typically 10<sup>3</sup> to 10<sup>5</sup> in one to two hours. Thanks to this spontaneous bacteria release, the enriched broth could be directly fed to a second microfluidic molecular characterization device, or collected and sterilized for storage or mailing to a central facility for molecular analysis, without requiring any additional elution step.

## Conclusions

Overall, the magnetic microfluidic fluidized bed approach offers the possibility to perform direct sample-to-result analyses all-in-chip, with a high flexibility regarding initial sample size and nature. It also combines a small footprint and low reagent consumption, with low-cost chip production and detection technologies. We thus believe that it will find applications in numerous bioanalytical, point-of-care and/or point-of-sampling applications.

## Experimental

Detailed descriptions of the microfluidic chip, pressure/flow controls and *in situ* capture and culture steps are provided in ESI† Experimental. Briefly, microfluidic chips were fabricated in PDMS by standard casting. They comprise a triangle-shaped chamber connected to the inlet by a 100 µm-wide bent channel. After bead insertion, an NdFeB 1.47 T permanent magnet was positioned at a distance of 2 mm from this channel and aligned with the main microfluidic chamber. A pressure controller (MFCS™, Fluigent) and a flow meter (Flowell, Fluigent) allowed flow at predefined rates. The system was initially filled with PBS with 1% bovine serum albumin (BSA). Anti-*Salmonella* Dynabeads® (50 µg) were used to form the fluidized bed for bacteria experiments, passing 50 µL of the sample solution at 1 µL min<sup>-1</sup> followed by a PBS/BSA wash (at 1.5 µL min<sup>-1</sup>). Colonies were counted the following day after plating of the initial reservoir, the flushed beads and the collected passed-through liquid (in a Tygon® tube connected at the outlet, Fig. S8†), and the capture rate was estimated as the ratio between captured bacteria and the sum of both captured and non-captured bacteria. For on-chip culture, after the washing step the



View Article Online

Edge Article

Chemical Science

temperature was set at 37 °C with an indium tin oxide glass slide connected to a voltage controller (Eurotherm 3508) and LB broth was passed through the system. Images were obtained by real-time recording of the bed using a low-cost camera (AM4013MZTL, Dino-Lite).

## Acknowledgements

This work was supported by a PhD grant from the Institut Pierre-Gilles de Gennes IPGG to IP, by ANR "Investissements d'Avenir" for Labex and Equipex IPGG, and by European FP7 programs (LOVEFOOD FP7-ICT-2011-317742, NAPES FP7-NMP-2013-604241, Nadine NMP-2009-4.0-3-246513). We thank A. Hamiot (Institut Pasteur, IP) for OD measurements, S. Dogniaux (Institut Curie) for kindly sharing L2 facilities and F Norel (IP) and MC Martel (INRA-Aurillac) for providing *S. Typhimurium* and *L. lactis*.

## Notes and references

- W. H. Organization, *Antimicrobial resistance: global report on surveillance*, World Health Organization, 2014.
- F. disease burden epidemiology reference group 2007–2015*, WHO estimates of the global burden of foodborne diseases, 2015.
- R. Cassar and P. Cuschieri, *J. Clin. Microbiol.*, 2003, **41**, 3229–3232.
- Y. Zhu, L. Qiao, M. Prudent, A. Bondarenko, N. Gasilova, S. B. Möller, N. Lion, H. Pick, T. Gong, Z. Chen, P. Yang, L. T. Lovey and H. H. Girault, *Chem. Sci.*, 2016, **7**, 2987–2995.
- R. Gutiérrez, I. González, T. García, E. Carrera, B. Sanz, P. E. Hernández and R. Martín, *J. Food Prot.*, 1997, **60**, 23–27.
- O. Karo, A. Wahl, S. B. Nicol, J. Brachert, B. Lambrecht, H. P. Spengler, F. Nauwelaers, M. Schmidt, C. K. Schneider, T. H. Müller and T. Montag, *Clin. Chem. Lab. Med.*, 2008, **46**, 947–953.
- C. Y. Wen, J. Hu, Z. L. Zhang, Z. Q. Tian, G. P. Ou, Y. L. Liao, Y. Li, M. Xie, Z. Y. Sun and D. W. Pang, *Anal. Chem.*, 2013, **85**, 1223–1230.
- C. H. Kang, Y. Do Nam, W. H. Chung, Z. X. Quan, Y. H. Park, S. J. Park, R. Desmone, X. F. Wan and S. K. Rhee, *J. Microbiol. Biotechnol.*, 2007, **17**, 945–951.
- S. G. Pathmanathan, N. Cardona-Castro, M. M. Sánchez-Jiménez, M. M. Correa-Ochoa, S. D. Puthuchery and K. L. Thong, *J. Med. Microbiol.*, 2003, **52**, 773–776.
- G. Mitterer, M. Huber, E. Leidinger, C. Kirisits, W. Lubitz, M. W. Mueller and W. M. Schmidt, *J. Clin. Microbiol.*, 2004, **42**, 1048–1057.
- Z. Wu, B. Willing, J. Bjerketorp, J. K. Jansson and K. Hjort, *Lab Chip*, 2009, **9**, 1193–1199.
- K. M. Lee, M. Runyon, T. J. Herrman, R. Phillips and J. Hsieh, *Food Control*, 2015, **47**, 264–276.
- H. P. Dwivedi, G. Devulder and V. K. Juneja, in *Encyclopedia of Food Microbiology*, 2014, vol. 2, pp. 339–342.
- H. W. Hou, R. P. Bhattacharyya, D. T. Hung and J. Han, *Lab Chip*, 2015, **15**, 2297–2307.
- S. Podszun, P. Vulto, H. Heinz, S. Hakenberg, C. Hermann, T. Hankemeier and G. A. Urban, *Lab Chip*, 2012, **12**, 451.
- D. A. Boehm, P. A. Gottlieb and S. Z. Hua, *Sens. Actuators, B*, 2007, **126**, 508–514.
- C. A. Batt, *Science*, 2007, **316**, 1579–1580.
- S. Bouguelia, Y. Roupioz, S. Slimani, L. Mondani, M. G. Casabona, C. Durmort, T. Vernet, R. Calemczuk and T. Livache, *Lab Chip*, 2013, **13**, 4024–4032.
- D.-K. Kang, M. M. Ali, K. Zhang, S. S. Huang, E. Peterson, M. A. Digman, E. Gratton and W. Zhao, *Nat. Commun.*, 2014, **5**, 5427.
- B. Potic, S. R. A. Kersten, M. Ye, M. A. Van Der Hoef, J. A. M. Kuipers and W. P. M. Van Swaaij, in *Chemical Engineering Science*, 2005, vol. 60, pp. 5982–5990.
- V. Zivkovic, M. J. Biggs and Z. T. Alwahabi, *AIChE J.*, 2013, **59**, 361–364.
- E. Doroodchi, Z. Peng, M. Sathe, E. Abbasi-Shavazi and G. M. Evans, *Powder Technol.*, 2012, **223**, 131–136.
- T. Vilknér, A. Shivji and A. Manz, *Lab Chip*, 2005, **5**, 140–145.
- R. G. Holdich, online B, [http://www.Part.org.uk/particle\\_technology\\_book/particle\\_book.htm](http://www.Part.org.uk/particle_technology_book/particle_book.htm), Loughbrgh. Univ., 2003.
- S. J. Shaw, B. W. Blais and D. C. Nundy, *J. Food Prot.*, 1998, **61**, 1507–1510.
- M. C. Montel, S. Buchin, A. Mallet, C. Delbes-Paus, D. A. Vuitton, N. Desmases and F. Berthier, *Int. J. Food Microbiol.*, 2014, **177**, 136–154.
- A. Bevilacqua, M. Cannarsi, M. Gallo, M. Sinigaglia and M. R. Corbo, *J. Food Sci.*, 2010, **75**, M53–M60.
- T. Sornchamni, G. N. Jovanovic, B. P. Reed, J. E. Atwater, J. R. Akse and R. R. Wheeler, *Adv. Space Res.*, 2004, **34**, 1494–1498.
- C. J. Easley, J. M. Karlinsey, J. M. Bienvenue, L. A. Legendre, M. G. Roper, S. H. Feldman, M. A. Hughes, E. L. Hewlett, T. J. Merkel, J. P. Ferrance and J. P. Landers, *Proc. Natl. Acad. Sci. U. S. A.*, 2006, **103**, 19272–19277.
- T. S. Park, W. Li, K. E. K. McCracken and J. J.-Y. Yoon, *Lab Chip*, 2013, **22**, 256–258.
- A. Greenbaum, W. Luo, T.-W. Su, Z. Göröcs, L. Xue, S. O. Isikman, A. F. Coskun, O. Mudanyali and A. Ozcan, *Nat. Methods*, 2012, **9**, 889–895.
- K. K. Ghosh, L. D. Burns, E. D. Cocker, A. Nimmerjahn, Y. Ziv, A. El Gamal and M. J. Schnitzer, *Nat. Methods*, 2011, **8**, 871–878.





### c) Versatility of the system toward bacteria strain

The versatility of the system has been tested with several bacteria. As shown in the article, our approach can be adapted to other bacteria such as *Enterobacter cloacae* or *Escherichia coli*. One can notice the same ability of the system of fluidized bed to correlate the expansion time of the matrix of beads to the initial concentration of the sample for both strains tested.

Capture on the microfluidic magnetic fluidized bed is highly dependent on the antigen/antibody interactions. It means that the development of magnetic beads functionalization has to be done in priority, before evaluation of the efficiency of the microfluidic device.

A larger panel of bacteria strain has also been tested to further challenge the adaptability of the system. For example, *Bacillus Cereus* and *Listeria* have been considered as potential target. A limit due to the efficiency of capture specific to the beads themselves was enlightened with the following results of capture on magnetic beads in batch presented on Figure 79. Batch experiments were realized as close as possible of the on-chip experiments: same quantity of beads, same volume of sample and same incubation time. Mixing is performed by rotation during the incubation time with temperature fixed at 37°C.

As shown on Figure 79 A, anti-bacillus beads are specific to the *Bacillus Cereus* bacteria. However, the anti-*Listeria* Dynabeads® (ThermoFisher, 71006) are able to capture *enterobacter*, *salmonella* and *Bacillus Cereus* but not *listeria* (Figure 79 B). It means that *bacillus cereus* bacteria could be a possible candidate for extraction and detection on fluidized bed, whereas new selective beads had to be found in order to investigate *Listeria* capture. These experiments illustrate how the specificity of the ligand on the beads (antibody or lectin) is essential for the extraction in fluidized bed, and has to be controlled prior to the experiments.

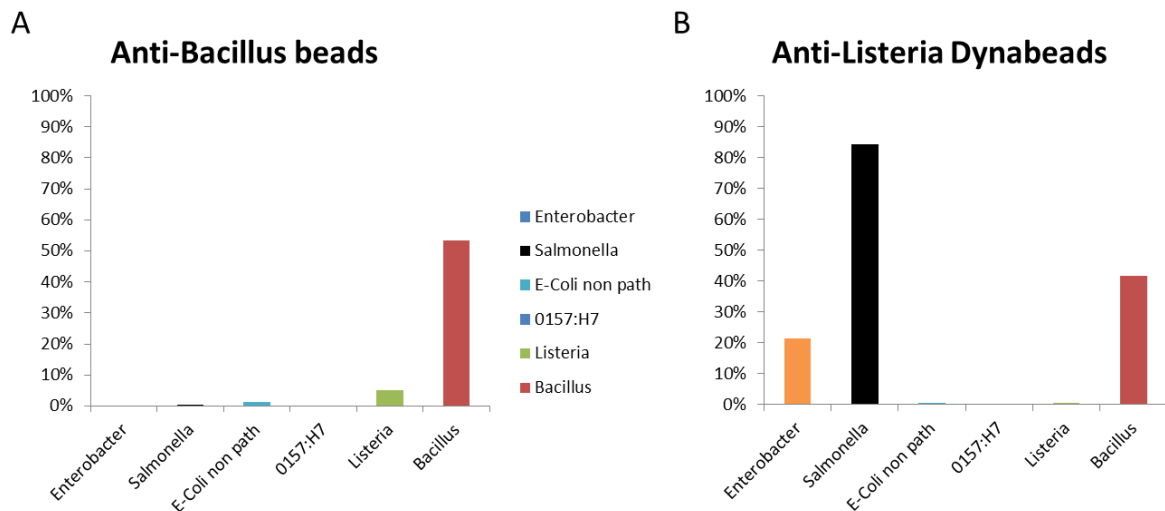


**Figure 79** Evaluation of the capture rate of two types of beads selective to either *Bacillus Cereus* or *Listeria*.

Regarding the versatility of our approach, further experiments have also shown that the formation of biofilm may also add some complexity to the device, mainly for the amplification step. The increase in size of the matrix of beads is normally directly linked to the division of bacteria following the rule that each bacteria divides in two in a known time, as it was modelled in the Chemical Sciences paper. This model of expansion does not take into account the formation of filaments or biofilm that may induce a deformation of the matrix of beads. The measure of the expansion could thus be distorted in these conditions.



**Figure 80** Formation of biofilm by *Bacillus Cereus* in the matrix of magnetic beads after one night of medium percolation at 37 °C

To verify this assumption, capture and growth experiments have been performed with *Bacillus Cereus*. As shown in Figure 80, beads inside the channel gathered and formed clumps whatever the initial concentration of *Bacillus Cereus*. The homogeneity of beads inside the flow is thus completely lost. It affected the measure of the expansion of the fluidized bed, used for detection. A new model must be developed to work with this type of bacteria.

**d) A further development of the fluidized bed platform towards antibiotic susceptibility investigation**

Antimicrobial resistance has become a major issue of our century. 700 000 people die of resistant infections every year. It is estimated that by 2050, 10 million lives a year and a cumulative 100 trillion USD of economic output are at risk due to the rise of drug-resistant infections if adapted solutions are not found (O'Neill, 2016). Among the steps to reduce demand of antimicrobials are the global surveillance of drug resistance and the promotion of new, rapid diagnostics to cut unnecessary use of antibiotics.

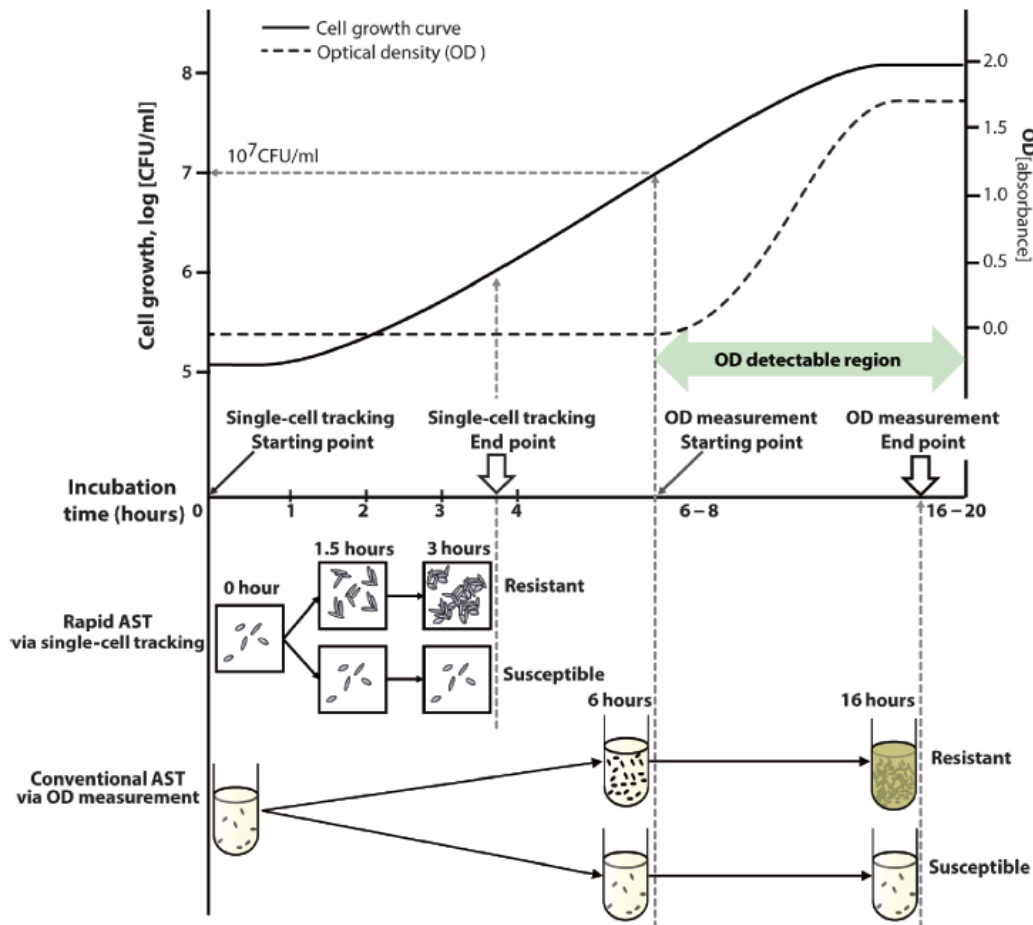


**Figure 81** Comparison of an AST based on single-cell morphological analysis (SCMA) with the conventional method using OD measurements. The OD value does not change until the bacterial concentration reaches  $10^7/\text{ml}$ , so OD measurement cannot be performed for 6 to 8 hours. However, in single-cell tracking using a microscope, changes in bacterial cells can be detected as soon as cells divide, so antibiotic susceptibility can be determined in 3 to 4 hours (Choi et al., 2014).

First, the commonly used method for antibiotic susceptibility test (AST) is cell culture that involves long incubations. It has been measured that in case of septic shock, administration of an antimicrobial within the first hour of hypotension was associated with a survival rate of 79.9% (for ethical reasons, this number cannot be compared to patients without any treatment). Then, each hour of delay in antimicrobial administration after the ensuing 6 hours implies a decrease in survival of 7.6% (Kumar et al., 2006). As shown on Figure 81 (Choi et al., 2014), Choi et al demonstrated that going to microscale allows to reduce time of

diagnosis, by detection of single cell division, which is a motivation for scaling down the analysis. Single cell morphological (filamentary formation, swelling formation, dividing, no change...) analysis also gives access to minimal inhibitory concentrations (MIC) of relevant antibiotics needed to neutralize the bacteria

This type of detection has to be supported by a good data processor to analyse for each image the morphological pattern of each bacteria. It can also help to differentiate between bacteria growth and formation of biofilms or filaments.

Different systems to tests antimicrobial action have been developed. Microfluidic is a powerful tool to increase knowledge in this field, and test strategies quickly, at low cost and at high throughput.

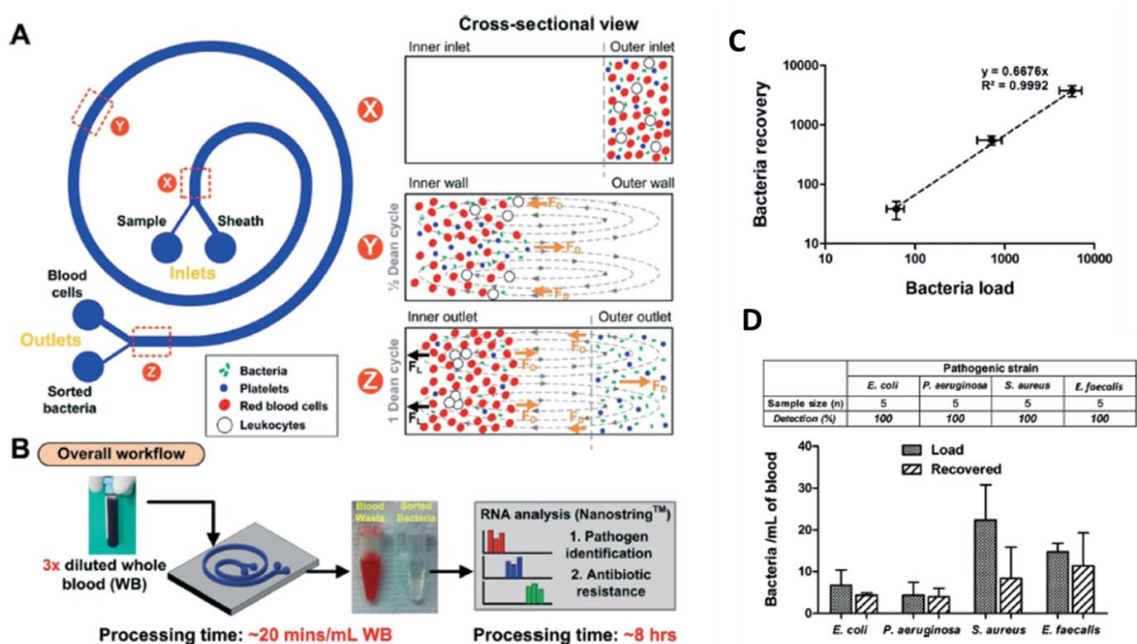


**Figure 82** A) Schematic representation of a spiral microchannel device for pathogen isolation using Dean Flow Fractionation (DFF). This system is usually exploited for CTCs separation from blood B) Overall workflow for clinical diagnostic from a whole blood sample C) Recovery of *E. coli* for bacteria spotted in 1 mL of blood D) Histogram of bacteria load and recovery for different pathogen strains (Hou et al., 2015)

Moreover, microfluidics allows to analyse the antibiotic susceptibility even in complex samples, such as whole blood (Hou et al., 2015). Separation of bacteria from the blood components is a first mandatory step in this case. Microfluidic characteristics of flow can be

used for this purpose (75% of bacterial recovery) as explained in Figure 82. By coupling this system with lysis and ribosomal RNA detection, Hou et al. showed that the level of expression of a set of mRNAs can determine antibiotic susceptibility of bacteria. This technology allows to reduce the time scale of analysis (around 8 hours) and to work at low concentration of pathogens, around 100 per mL (cfu/mL undercount the value of microbial numbers as counting by cfu assumes that colonies are necessarily separated and founded by only one single bacteria)

Digital microfluidic also allows to screen high level of combinatorial drug tests using compartmentalization in droplets. Libraries of mutant phenotypes may help to enlighten resistance mechanisms. As generation of antimicrobial resistance (AMR) mutant is statistically rare, digital microfluidic can allow the manipulation of a complex genome at high frequency. For example, flow focusing can be used to create droplets of bacteria encapsulated with antibiotics as in Figure 83. Optical detection of proliferation of bacteria may be coupled with microfluidic sorting to isolate drug resistant bacteria (Liu et al., 2016). Sorting (~240 droplets per second) was performed on the intensity of scattered light with application of high voltages pulses to direct the droplets. This label-free high throughput method of detection allows to work with high number of bacteria ( $10^9$  bacteria for AMR in water-in-oil picolitre-volume droplets). However, this method requires long incubation time (5 hours for  $10^6$  cfu mL<sup>-1</sup> bacterial suspension up to overnight incubation for high concentration of antibiotic) at 37°C to reach detectable density and complex designs for sorting.

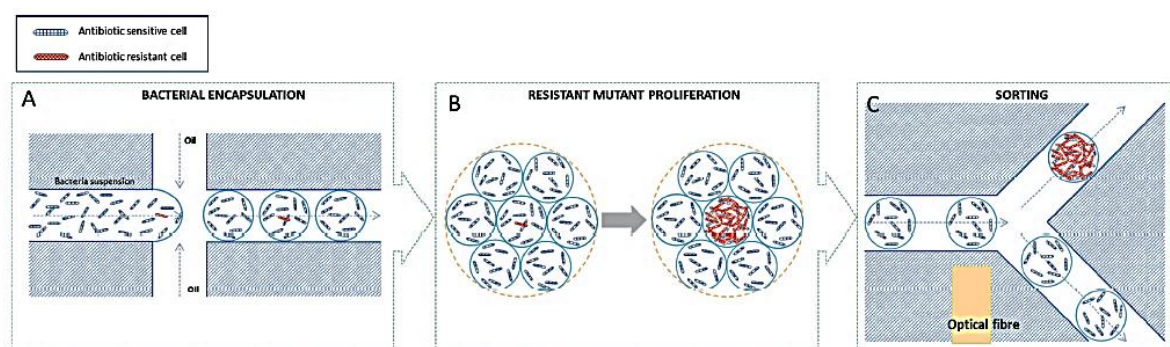


**Figure 83** Schematics of picodroplet based workflow for resistant mutant screening. (A) Bacteria, culture media and antibiotics were injected into a flow focusing microfluidic device. Multiple bacteria were encapsulated into picodroplets (B) Only antibiotic resistant mutant cells will proliferate in presence of antibiotics. After incubation, the picodroplets with mutants will contain more cells. (C) The cell number differences among the picodroplets could be

**differentiated based on their light-scattering properties. Picodroplets containing proliferating bacteria were sorted out in a Y shaped microfluidic channel (Liu et al., 2016)**

The system of fluidized bed has already shown its efficiency as a module of extraction and detection of bacteria. A development toward drug resistance tests could be envisioned directly with bacteria captured on the beads. As demonstrated by Chung et al., an antibiotic susceptibility test (AST) could be developed after capture of bacteria on the beads (Chung et al., 2016). News challenges are the time of analyse and the reliability. We have also demonstrated that during the detection step previously described (Pereiro et al., 2017) the nutritive medium can be mixed with antibiotic at controlled concentration to see its influence on the development of bacteria in chip.

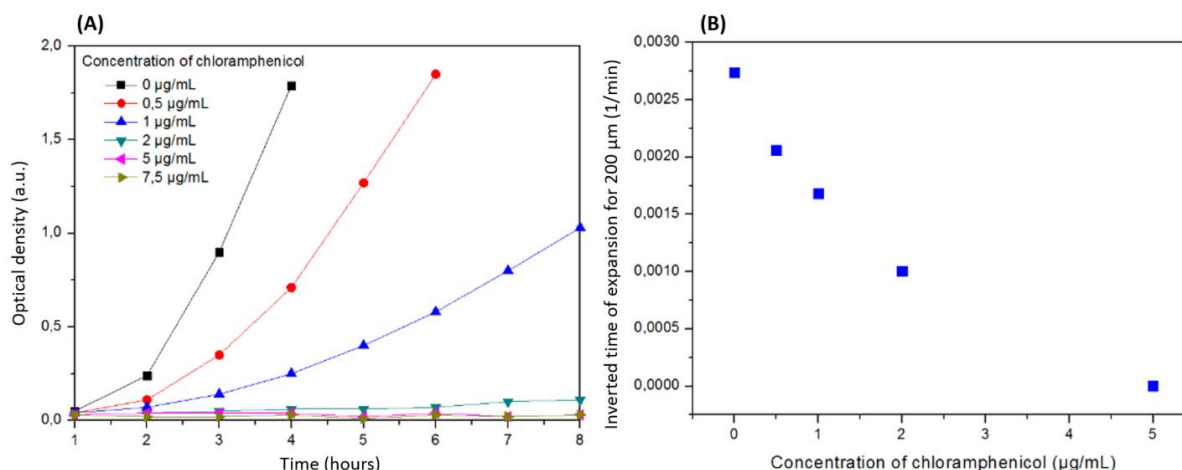


**Figure 84 (A) Exponential growth of *Salmonella Typhimurium* in the presence of LB-broth and an antibiotic (chloramphenicol) measured by optical density as function of time. The concentration of this antibiotic in the nutritive medium injected during the incubation step also affects the time of expansion of the microfluidic magnetic fluidized bed (B).**

For example, Figure 84 reports the results obtained with the fluidized bed approach regarding the expansion of the bed with *Salmonella Typhimurium* in presence of an antibiotic (chloramphenicol) at various concentrations within the nutritive medium. As expected, Chloramphenicol affects the multiplication of bacteria inside the matrix of beads during the detection step (A). The expansion of the fluidized bed is delayed or cancelled by the presence of antibiotics (B) and the inverse of the time of expansion (as the time of expansion can be infinite for high concentration of antibiotics) is correlated with the concentration of chloramphenicol.



### 3. Perspectives

The microfluidic magnetic fluidized bed can be used to extract, pre-concentrate and detect bacteria in complex matrix such as milk. It can detect down to 10 bacteria in 1 mL of sample in less than 8 hours. This performance is comparable to new strategies developed to improve the gold standard of plating in nutritive media. Moreover, it provides an opportunity to access new information on antibiotic effect such as resistance or modification of the division time.

An automation of the system of micro fluidized bed would lead to the creation of a portable module of detection and quantification of bacteria in complex matrices. This system where only the chips are experiments dependant would be low cost, user independent and faster than usual methods that need long incubation. Moreover, this system can adapt to different bacteria, and could be used to test antimicrobial resistance.

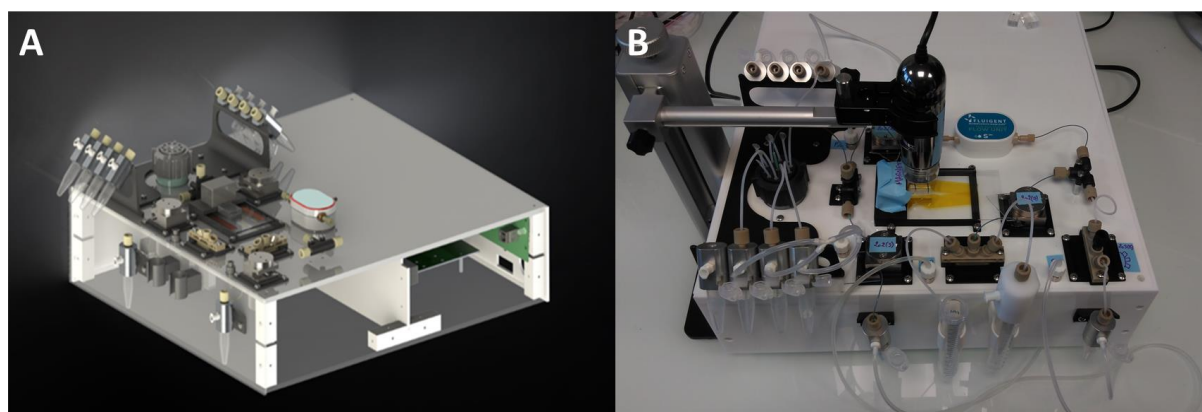


**Figure 85 A and B Mobile platform developed by Fluigent and MMBM team for a fully automated platform for microfluidic magnetic fluidized bed experiments made up of a pump, a flowmeter and several valves to control the fluidic pathway**

A first mobile platform has been developed with Fluigent company in our laboratory as shown on Figure 85. This instrument can lead the way to automatic, easy to manipulate, low cost and mobile experimentations. This platform will be included in new development and new projects.



## Bibliography

BBC (2018). Salmonella baby milk “affects 83 countries.” BBC News.

Boehm, D.A., Gottlieb, P.A., and Hua, S.Z. (2007). On-chip microfluidic biosensor for bacterial detection and identification. *Sens. Actuators B Chem.* *126*, 508–514.

Bouguelia, S., Roupioz, Y., Slimani, S., Mondani, L., Casabona, M.G., Durmort, C., Vernet, T., Calemczuk, R., and Livache, T. (2013). On-chip microbial culture for the specific detection of very low levels of bacteria. *Lab. Chip* *13*, 4024.

Brisabois, A., Lafarge, V., Brouillaud, A., De Buyser, M.L., Collette, C., Garin-Bastuji, B., and Thorel, M.F. (1997). Les germes pathogènes dans le lait et les produits laitiers : situation en France et en Europe: -EN- -FR- -ES-. *Rev. Sci. Tech. OIE* *16*, 452–471.

Choi, J., Yoo, J., Lee, M., Kim, E.-G., Lee, J.S., Lee, S., Joo, S., Song, S.H., Kim, E.-C., Lee, J.C., et al. (2014). A rapid antimicrobial susceptibility test based on single-cell morphological analysis. *Sci. Transl. Med.* *6*, 267ra174-267ra174.

Chung, C.-Y., Wang, J.-C., and Chuang, H.-S. (2016). Rapid Bead-Based Antimicrobial Susceptibility Testing by Optical Diffusometry. *PLOS ONE* *11*, e0148864.

Csordas, A.T., Delwiche, M.J., and Barak, J.D. (2008). Nucleic acid sensor and fluid handling for detection of bacterial pathogens. *Sens. Actuators B Chem.* *134*, 1–8.

Dethlefsen, L., McFall-Ngai, M., and Relman, D.A. (2007). An ecological and evolutionary perspective on human-microbe mutualism and disease. *Nature* *449*, 811–818.

French Public Service, T. (2016). Données épidémiologiques / Toxi-infections alimentaires collectives / Maladies à déclaration obligatoire / Maladies infectieuses / Dossiers thématiques / Accueil.

Gracias, K.S., and McKillip, J.L. (2004). A review of conventional detection and enumeration methods for pathogenic bacteria in food. *Can. J. Microbiol.* *50*, 883–890.

Hou, H.W., Bhattacharyya, R.P., Hung, D.T., and Han, J. (2015). Direct detection and drug-resistance profiling of bacteremias using inertial microfluidics. *Lab. Chip* *15*, 2297–2307.

Institut de veille sanitaire (2012). Enquête nationale de prévalence des infections nosocomiales et des traitements anti-infectieux en établissements de santé, France, mai-juin

2012 / 2013 / Maladies infectieuses / Rapports et synthèses / Publications et outils / Accueil.

Kang, J.H., Super, M., Yung, C.W., Cooper, R.M., Domansky, K., Graveline, A.R., Mammoto, T., Berthet, J.B., Tobin, H., Cartwright, M.J., et al. (2014). An extracorporeal blood-cleansing device for sepsis therapy. *Nat. Med.* *20*, 1211–1216.

Krüger, J., Singh, K., O'Neill, A., Jackson, C., Morrison, A., and O'Brien, P. (2002). Development of a microfluidic device for fluorescence activated cell sorting. *J. Micromechanics Microengineering* *12*, 486.

Kumar, A., Roberts, D., Wood, K.E., Light, B., Parrillo, J.E., Sharma, S., Suppes, R., Feinstein, D., Zanotti, S., Taiberg, L., et al. (2006). Duration of hypotension before initiation of effective antimicrobial therapy is the critical determinant of survival in human septic shock\*: *Crit. Care Med.* *34*, 1589–1596.

Le Maire, B. (2017). Contamination à Salmonella Agona de jeunes enfants: extension des mesures de retrait-rappel de produits de nutrition infantile. 23.

Liu, X., Painter, R.E., Enesa, K., Holmes, D., Whyte, G., Garlisi, C.G., Monsma, F.J., Rehak, M., Craig, F.F., and Smith, C.A. (2016). High-throughput screening of antibiotic-resistant bacteria in picodroplets. *Lab. Chip* *16*, 1636–1643.

Mairhofer, J., Roppert, K., and Ertl, P. (2009). Microfluidic Systems for Pathogen Sensing: A Review. *Sensors* *9*, 4804–4823.

O'Neill, J. (2016). TACKLING DRUG-RESISTANT INFECTIONS GLOBALLY: FINAL REPORT AND RECOMMENDATIONS Home | AMR Review.

Paula, A.M., Gelli, D.S., Landgraf, M., Destro, M.T., and Franco, B.D. (2002). Detection of Salmonella in foods using Tecra Salmonella VIA and Tecra Salmonella UNIQUE rapid immunoassays and a cultural procedure. *J. Food Prot.* *65*, 552–555.

Pereiro, I., Bendali, A., Tabnaoui, S., Alexandre, L., Srbova, J., Bilkova, Z., Deegan, S., Joshi, L., Viovy, J.-L., Malaquin, L., et al. (2017). A new microfluidic approach for the one-step capture, amplification and label-free quantification of bacteria from raw samples. *Chem. Sci.* *8*, 1329–1336.

Podszun, S., Vulto, P., Heinz, H., Hakenberg, S., Hermann, C., Hankemeier, T., and Urban, G.A. (2012). Enrichment of viable bacteria in a micro-volume by free-flow electrophoresis. *Lab. Chip* 12, 451–457.

Rintala, A., Munukka, E., Weintraub, A., Ullberg, M., and Eerola, E. (2016). Evaluation of a multiplex real-time PCR kit Amplidiag® Bacterial GE in the detection of bacterial pathogens from stool samples. *J. Microbiol. Methods* 128, 61–65.

Sender, R., Fuchs, S., and Milo, R. (2016). Revised Estimates for the Number of Human and Bacteria Cells in the Body. *PLoS Biol.* 14.

Verbarg, J., Plath, W.D., Shriver-Lake, L.C., Howell, P.B., Erickson, J.S., Golden, J.P., and Ligler, F.S. (2013). Catch and Release: Integrated system for multiplexed detection of bacteria. *Anal. Chem.* 85, 4944–4950.

Vétizou, M., Pitt, J.M., Daillère, R., Lepage, P., Waldschmitt, N., Flament, C., Rusakiewicz, S., Routy, B., Roberti, M.P., Duong, C.P.M., et al. (2015). Anticancer immunotherapy by CTLA-4 blockade relies on the gut microbiota. *Science* aad1329.

Wang, Y., Ye, Z., and Ying, Y. (2012). New Trends in Impedimetric Biosensors for the Detection of Foodborne Pathogenic Bacteria. *Sensors* 12, 3449–3471.

Wu, Z., Willing, B., Bjerketorp, J., K. Jansson, J., and Hjort, K. (2009). Soft inertial microfluidics for high throughput separation of bacteria from human blood cells. *Lab. Chip* 9, 1193–1199.

Yeh, K.-S., Tsai, C.-E., Chen, S.-P., and Liao, C.-W. (2002). Comparison between VIDAS Automatic Enzyme-Linked Fluorescent Immunoassay and Culture Method for Salmonella Recovery from Pork Carcass Sponge Samples. *J. Food Prot.* 65, 1656–1659.

## Chapter 6

### The fluidized bed as a miniaturized extra-corporeal platform - New therapeutic strategy against preeclampsia

#### 1. Introduction

##### a) Epidemiology of pre-eclampsia

Preeclampsia is a hypertensive disorder of pregnancy associated to placenta insufficiency and extreme prematurity. It affects 5-10 % of pregnant women in the world (Brazdova et al., 2014). Pre-eclampsia is connected to significant mortality for both mother and child. Worldwide, it affects about 18% of maternal deaths, 62 000 to 77 000 deaths per year (Khan et al., 2006) among the 140 million births identified. The risks are due to hypertensive disorders and depend on the patient geographic area as shown in Figure 86.

Causative factors have not been identified yet. It could be related to an abnormal development of the placenta, immunologic factors, a pre-existing maternal pathology, dietary factors and/or environmental ones.

For normal pregnancy, the placenta connects the mother (by the uterine wall) to the fetus, allowing exchange of water, nutrients, gas... At the first stage of development of the pathology, placenta insufficiency can be observed: defective remodeling of the uterine vascularization during the first trimester, placenta hypoperfusion and trophoblast dysfunction, increased release of trophoblastic factors into the maternal circulation. The second stage of pre-eclampsia syndrome is the maternal reaction with an excessive inflammatory response and endothelial dysfunction (Brazdova et al., 2014).

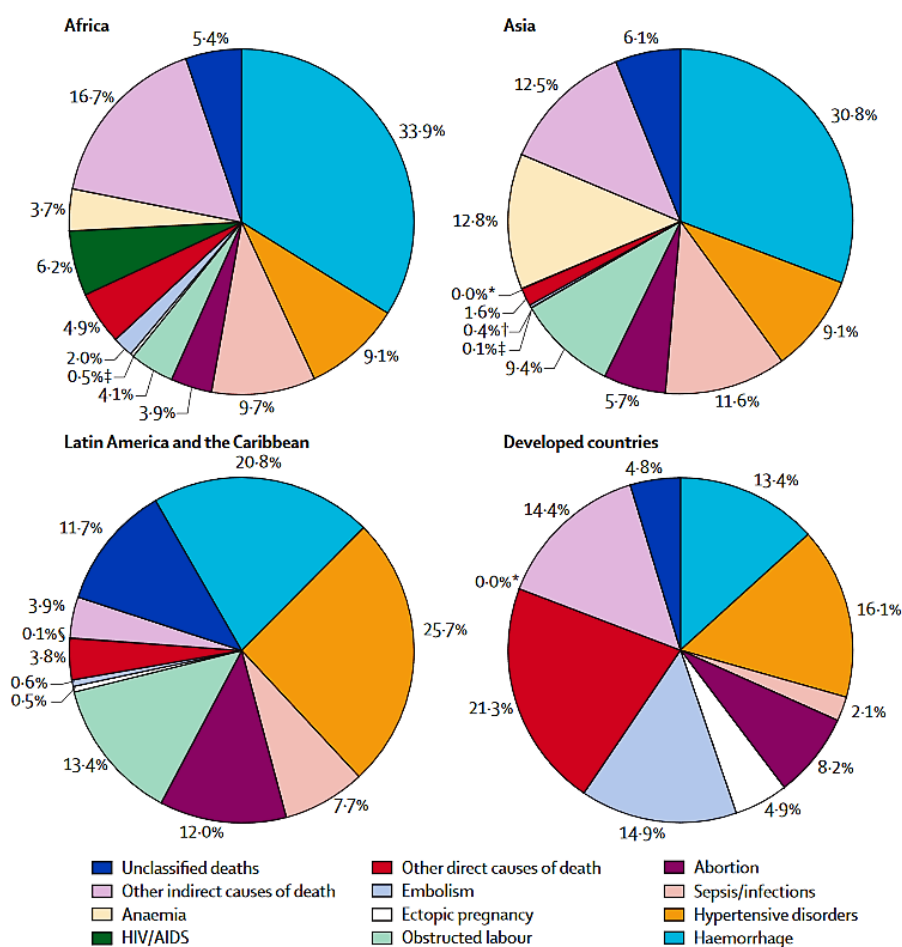


**Figure 86 Geographical variation of the distribution of causes of maternal deaths in Africa, Asia Latin America and Caribbean and developed countries (Khan et al., 2006) Data were produced by combination of all dataset with precedence for national ones in case of conflict.**

The placenta triggers pre-eclampsia: maladaptation of the vessels that supply the fetus can lead to abnormal villous development and placenta insufficiency. The maternal response is due to vascular disorder and strong inflammatory response (Walker, 2000). The blood pressure increases and the renal function is generally altered. It is important to notice that this disease is specific to pregnancy as it disappears as soon as birth is given.

Pre-eclampsia seems to have some hereditary factors, followed through men and women (Arngrimsson et al., 1990). This hypothesis is supported by its occurrence through history; from Ancient Egypt (Kahun papyrus 3000 years ago) to nowadays (Roberts and Cooper, 2001). Nevertheless, no gene has been specifically identified so far for pre-eclampsia. The idea of one single gene is unlikely, and further studies are currently investigating the multi-gene assumption (Khvorova et al., 2018; Nafee et al., 2008).

For now, no treatment has been successfully developed for preeclampsia, and drug developments are poor. The only solution is to induce delivery of the fetus and the placenta long before the due date to relieve the mother and prevent her from serious complications. In case of severe preeclampsia, this decision must be taken at 24-26 weeks of gestation.

#### **b) Diagnostic of preeclampsia based on growth factors balance**

Different definitions of the symptoms of pre-eclampsia do exist; it leads to diagnostic uncertainty.

A commonly used method to diagnose pre-eclampsia is a measure of the blood pressure. However, high diastolic blood pressure ( $> 90$  mm Hg) is frequent during pregnancy (40%), particularly for young pregnant women carrying their first child (Plouin et al., 1982). The diagnostic of persistent hypertension relies on two high measures at least 4 hours apart. All pregnant women with high blood pressure are monitored in clinical facilities. The diagnostic is associated to a measure of proteinuria ( $> 300$  mg/24h) after 20 weeks gestational age. If there is no evidence of proteinuria, the diagnostic of pre-eclampsia can be suggested by intense sweating, kidney or liver dysfunction, thrombocytopenia, pulmonary edema, ankle edema, cerebral or visual disturbances. Severe pre-eclampsia can be correlated with organ dysfunction.

To predict risks of pre-eclampsia, the placenta formation can be followed during pregnancy. An early biomarker for pre-eclampsia could be the presence of podocytes ('highly differentiated cell located in the outer space of the glomerular basement membrane that deals with many different functions' Trimarchi, 2015) in urine (Craici et al., 2013). Identification of medium and high risks patients is essential to allow a quality of care adapted to the pregnant woman.

It is admitted that preeclampsia is related to maternal endothelial dysfunction due to the excess or lack of angiogenic factors such as sFlt-1 (soluble Fms-like tyrosine kinase 1) and PlGF (placental growth factor) into maternal circulation (Sibiude et al., 2012). sFlt-1 is the soluble form of VEGF (Vascular Endothelial Growth Factor) and PlGF receptor. sFlt-1 binds to free VEGF and PlGF in the maternal circulation, and reduces their bioavailability for their membrane receptor (Tsatsaris et al., 2003). It inhibits the role of VEGF and PlGF in the maternal endothelium such as endothelial survive, angiogenesis and vasodilatation (Ferrara, 2004).

Clinical studies have shown that the sFlt-1/PlGF ratio is highly correlated with preeclampsia severity (Verlohren et al., 2012). This approach has been validated clinically and led to the creation of hospital devices for usual tests, such as Elecsys® Preeclampsia from Roche and Cobas.

As shown in Figure 87, the concentration of sFlt-1 increases during normal pregnancy while the concentration of PlGF decreases. However, women with clinical pre-eclampsia show a distinguished behavior with higher concentration of sFlt-1 and lower concentration of PlGF than normal (Levine and Karumanchi, 2005).

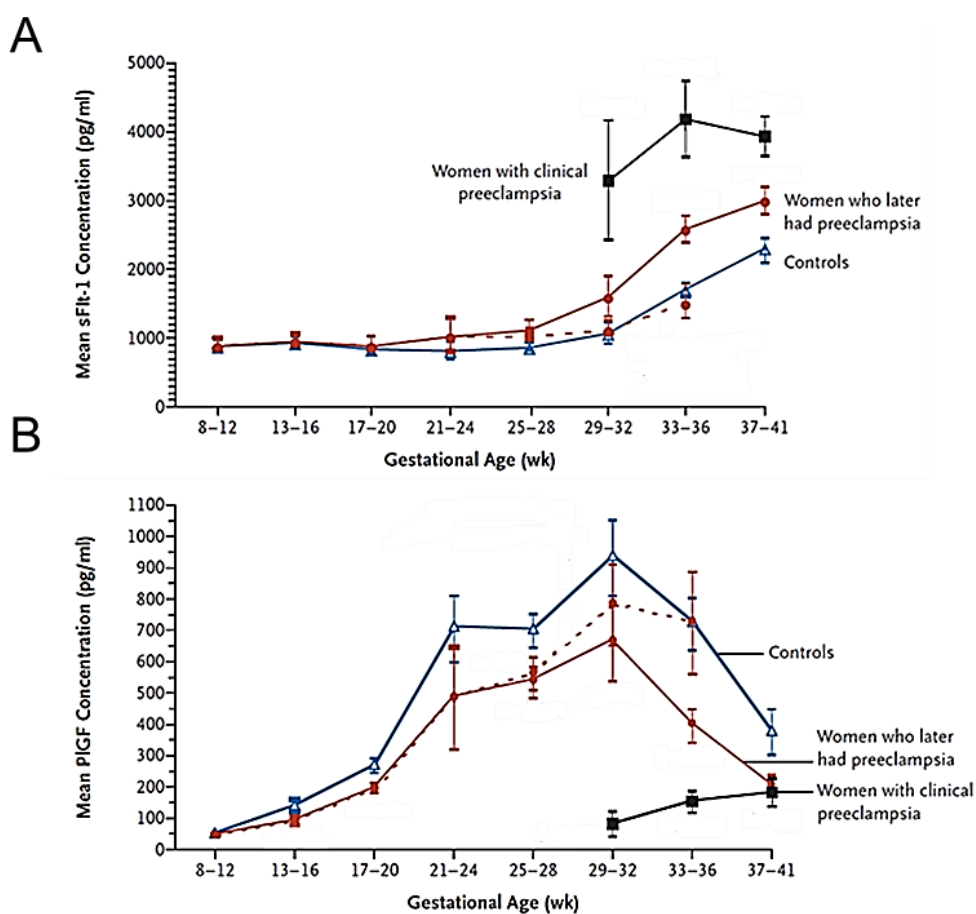


**Figure 87** Graphic representation of the evolution of mean concentrations of two growth factors sFlt-1 (A) and PlGF (B) as function of the gestational age of the fetus (Levine and Karumanchi, 2005)

### c) Pre-eclampsia treatment and sFlt-1 depletion

As previously mentioned, there is no efficient drug to treat preeclamptic patients. Drug developments are poor, limited by 1) the possibility of exchanges between the mother and

the fetus and 2) the difficulties to obtain the right authorizations for perinatal medical trials. In this context, restoring the angiogenic balance could be a solution to delay the birth of an extremely preterm infant by one week. This delay is critical and may increase from 10% to 30% his or her chances of survival without sequelae. In order to delay the childbirth, different solutions have been considered to assuage the mother and protect the fetus. To face the risks and overcome the inefficiency of previous solutions a strategy recently developed relies on modifying the balance of growth factors with an extracorporeal technique.

This approach aims to change directly the concentration of the growth factors in order to restore the angiogenic balance. An approach based on extra-corporeal circulation coupled to extraction on columns is currently under clinical investigation to delay the birth of extremely preterm infants (Liu et al., 2014). The first apheresis columns that have been developed are able to capture sFlt-1 through electrostatic interactions. The solid phase in the columns is negatively charged (dextran sulfate cellulose) allowing an electrostatic-based capture of sFlt-1 positively charged. As its isoelectric point calculated using ExPasy software is 9.51, at physiological pH sFlt-1 is positively charged (Thadhani et al., 2011). Thanks to this approach, the sFlt-1 concentration present in the mother's blood can be reduced by 14 to 28 %. However, the capture being based on electrostatic interaction is not specific and many other molecules are extracted from the blood without any control. This can lead to the depletion of essential blood constituents of the mother, and even to the capture of PlGF as well if it binds to sFlt-1 (free PlGF has an isoelectric point 6.27 calculated by Protein isoelectric point calculator so it cannot be capture by its own).

To reduce the non-specific adsorption, a new generation of preeclampsia columns is currently under development, sFlt-1 antibodies being grafted on the solid phase. This technique is highly specific. However, it only reduces the concentration of Sflt-1 while it does not affect the bioavailability of PlGF. The sFlt-1/PlGF ratio is lower but not as much as if we could play with the concentration of PlGF at the same time.

In order to balance the mismatch of concentration in growth factors, we present here a new competitive approach allowing both capture sFlt-1 and release the PlGF bound to sFlt-1. We expect this approach to decrease drastically the sFlt-1/PlGF ratio, without disturbance of the initial matrix.



#### d) Fluidized bed as a test platform

In this context, we used the microfluidic fluidized bed in order to mimic the extracorporeal circulation technology and to evaluate the performances of an innovative strategy to restore the angiogenic balance.

We have already demonstrated that the microfluidic magnetic fluidized bed system can be efficiently used to capture and extract biomolecules thanks to functionalized magnetic particles. Its configuration enhances the interactions between a fluid and the beads surface, with low back-pressure and reduced risks of clogging making this platform an ideal miniaturized design of extracorporeal circulation. By grafting specific ligands on the beads surface, we can use this asset to capture a target present in the sample flowing through the bed. Our aim is to use the fluidized bed as a miniaturized extra-corporeal approach in order to evaluate new strategies to restore the angiogenic balance at high throughput and low cost. In particular we will investigate a competitive bioassay that allows capturing the sFlt-1 protein in excess while releasing its ligand PlGF in default.

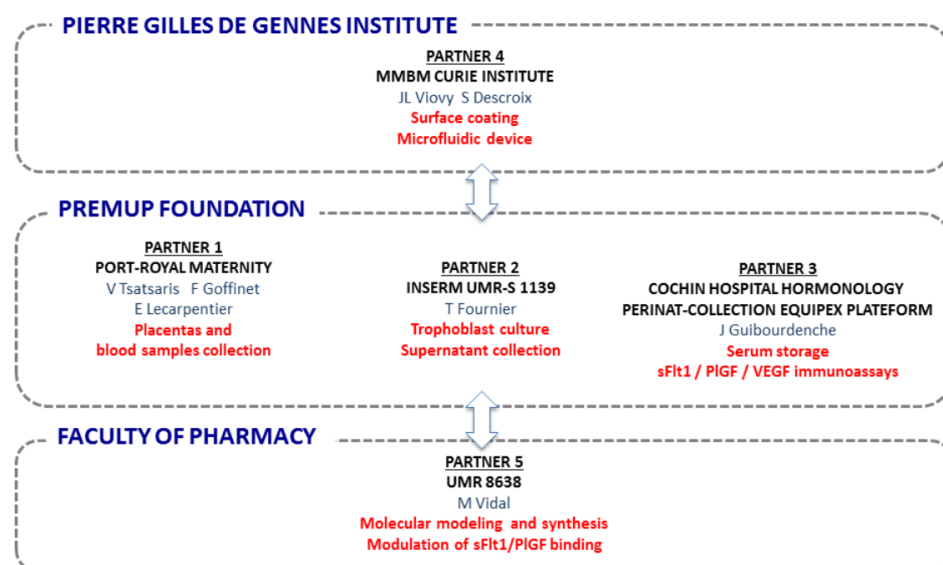


**Figure 88 Organization chart of the ANR project: New therapeutic strategy against preeclampsia: Specific extra-corporeal removal of sFlt-1 in order to restore the angiogenic balance**

This project was created in collaboration between the Port-Royal maternity, the Inserm UMR s-1139, the Cochin hospital hormonology perinat-collection Equipex platform, the UMR 8638 of the Faculty of Pharmacy and our team (Figure 88).

### e) New ligands to restore the angiogenic balance

The strategy developed in this project is a competitive bioassay to capture sFlt-1 using VEGF (vascular endothelial growth factor) as specific ligand. VEGF has a high affinity towards sFlt-1 ( $K_d$  around 1 nM), which is higher than the PlGF – sFlt-1 affinity ( $K_d$  around 22 pM). The VEGF/sFlt-1 and VEGF/PlGF interactions take place at the same site on VEGF, therefore we expect a capture of free sFlt-1 as well as of complexed sFlt-1 and thus a release of PlGF in the maternal circulation.

After grafting VEGF on the surface of the micro-beads introduced in the fluidized bed, the sample will be flown through the bed. To come back to normal balance, the concentration of sFlt-1 needs approximately to be divided by two or three, whereas the concentration of PlGF needs to be multiplied by five.

## 2. Preliminary proof of concept

### a) Materials and method

Magnetic beads Dynabeads M-280 Streptavidin were purchased from Thermofisher, and grafted at 60% with VEGF using a house-made protocol in the UMR 8638 of the Faculty of Pharmacy of Paris. Capture was performed with a solution of human recombinant sFlt-1 (rhVEGF R1/Flt-1 Fc Chimera, Ser27-His687) from R&D systems (321-FL, d1d3). The washing buffer contained Dulbecco's Phosphate Buffered Saline 'PBS' (Sigma Aldrich) and Bovine Serum Albumine 'BSA' (1%, Sigma Aldrich). Secondary antibody was a mouse anti-human IgG1 Fc-Alexa Fluor488. Elution was achieved with a solution of citric acid at pH 2.

The experimental setup is similar to the one presented in chapter 1. Excitation light is produced by a mercury lamp, and a FITC filter is interspersed.

The colorimetric immunoassay was performed using human VEGF R1/Flt-1 & Quantikine ELISA kit from R&D system. The range of detection was between 31 and 2 000 pg/mL and the minimum detectable dose was around 1.5-13.3 pg/mL  $\pm$  3.5 pg/mL

### b) Proof of concept of the detection by immunoassay in chip

The approach proposed here aims to capture sFlt-1 and release PlGF. To demonstrate this ability, we first performed quantification of the sFlt-1 capture and measured the release of PlGF.

sFlt-1 is a tyrosine kinase protein able to bind to free VEGF and PlGF in human blood. In order to save precious human blood samples, preliminary experiments have been performed with sFlt-1 synthesized by bacteria (*spodoptera frugiperda*, baculovirus): the human antibody recombinant (called R1), dissolved at a chosen concentration in PBS and BSA 1%.

In order to quantify the R1 capture level, we used an antibody conjugated with a fluorophore targeting R1. This secondary antibody can specifically bind to R1, and allows its detection.

The protocol of capture and detection is described on Figure 89:

- A. A first step of calibration is performed with a solution at known concentration of secondary antibody. The solution is flown at the same flowrate as the one used during the detection step. The intensity of the fluorescent signal is called  $I_0$  and used to calibrate the fluorescence.
- B. 50  $\mu\text{g}$  of streptavidin Dynabeads coated with VEGF are introduced inside the PDMS chip
- C. The sample (10  $\mu\text{L}$ ) composed of PBS, BSA (1%) and human recombinant R1 (at 16 pmol/mL) is flown at 0.5  $\mu\text{L}/\text{min}$  through the matrix of beads
- D. A washing step is performed at 1.5  $\mu\text{L}/\text{min}$  with 20  $\mu\text{L}$  of PBS, BSA 1% and Tween 20 0.1%
- E. A solution of secondary antibody is flowed through the matrix of beads at 0.5  $\mu\text{L}/\text{min}$  at different concentrations (between 0.026 pmol/mL and 0.26 pmol/mL)
- F. A second washing step is performed at 1.5  $\mu\text{L}/\text{min}$  with 30  $\mu\text{L}$  of PBS, BSA 1% and Tween 20 0.1%
- G. Citric acid is injected inside the matrix of beads (0.7  $\mu\text{L}$ ) at low flow rate (0.1  $\mu\text{L}/\text{min}$ ), followed by an incubation of ten minutes
- H. Washing buffer (PBS, BSA 1% and Tween 20 0.1%) is injected inside the chip at 0.1  $\mu\text{L}/\text{min}$  to push the detached fluorophore to the detection area. The detection is then performed by measure of the fluorescent signal at the output channel of the chip.

All steps are performed at 37°C.

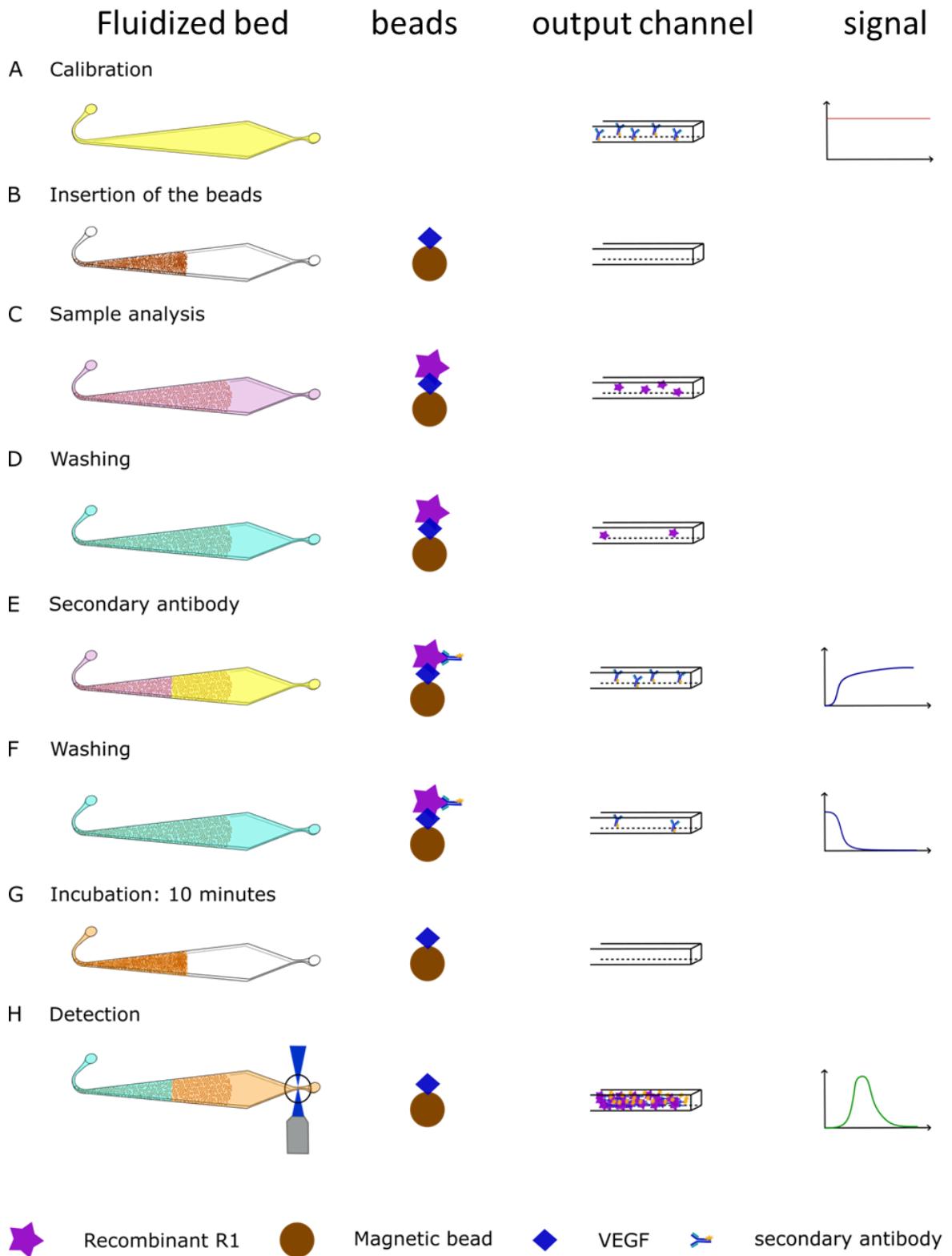


**Figure 89** Protocol of capture and detection of the human recombinant R1 in fluidized bed with from left to right a schematic representation of the fluidized bed, of the capture on the magnetic

*beads, the detection area on the output channel and the intensity of the signal measured. A calibration step (A) is first performed, then beads are inserted inside the PDMS chip (B). The sample preparation is injected inside the matrix of beads (C). The beads are washed (D) then the solution of secondary antibodies is injected (E). Beads are again washed (F). 0.7  $\mu$ L of acid citric acid is injected inside the beads, followed by ten minutes of incubation at stopped flow ? (G). The detection is performed on the output channel of the chip when the incubated volume is pushed by washing buffer (H)*

### **c) Preliminary results**

#### ***Proof of concept***

Using an elution step as previously described, we were able to detect a peak of fluorescence in the output channel, as pictured in Figure 6. This peak proves that VEGF grafted on the beads surface can capture sFlt-1 and the capture can be detected by fluorescence thanks to the use of a conjugated secondary antibody.

#### ***Toward optimization of the parameters***

This protocol needed optimization of several parameters. First of all, the quantity of secondary antibody had to be optimized to ensure the detection of all the human recombinant.

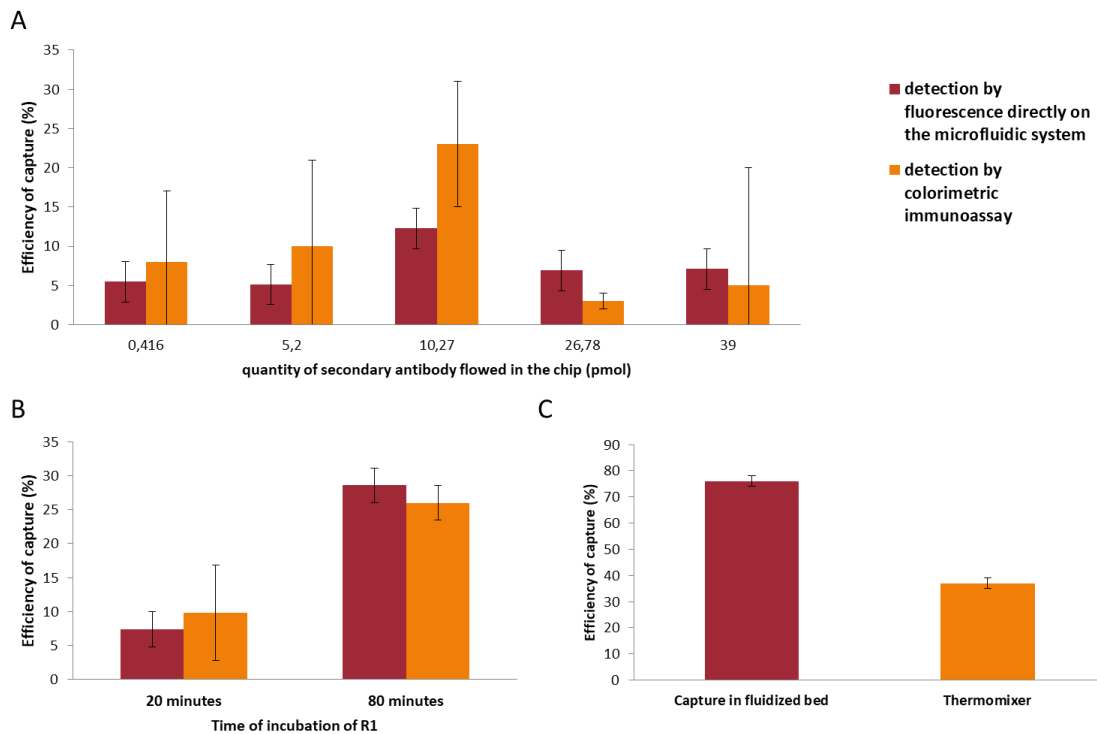


**Figure 90** Capture efficiency of sFlt-1 measured either by fluorescent detection in chip (red) or by colorimetric immunoassay (orange) for different quantities of secondary antibody(A) or different times of incubation of the human recombinant(B). For same parameters, the capture in the fluidized bed and in tube (thermomixer)(C)

Optimization of the parameter of the immunoassay was realized in parallel on the fluidized bed and on a colorimetric immunoassay using human VEGF R1/Flt-1 Quantikine ELISA kit (as described in the materials and methods). The colorimetric immunoassay was developed by the partner laboratory of the Faculty of Pharmacy. We observed that the results obtained by detection of fluorescence inside the fluidized bed are comparable to the ones obtained by colorimetric immunoassay (Figure 5).

The concentration of the solution of secondary antibody had to be optimized, as well as the flowrate of injection (Figure 5). However, the high quantity of expensive secondary antibody needed for detection limited the number of achievable experiments.

This protocol was used to show that for the same quantity and concentration of human recombinant, a smaller flow rate of work (in fluidized bed) and a longer incubation time (in static) increased the efficiency of capture (Figure 90 B). It is directly related to the binding kinetics between VEGF and sFlt-1. Finally, the capture in fluidized bed seemed to have a

higher efficiency than the capture with the same beads in tube (Figure 90 C). This was an encouraging result that needed confirmation.

#### **Acidic treatment to reuse the beads**

The previously described protocol was also applied to evaluate if an acidic treatment can be used to release all the molecules trapped, wash the surface of the beads and leave them ready for a new capture. We thus investigate the conditions in which the beads could be reused.

Citric acid has been used to elute R1 and the secondary antibody by disrupting the Ag/Ab interaction at acidic pH. This operation leaves the beads with only VEGF on the surface. We decided to test if those beads could be reused to capture R1 a second time after a washing step. As shown on Figure 6, the peak of fluorescence obtained during the second capture is similar to the first one demonstrating that the beads after being in contact with citric acid can still be reused for R1 capture.

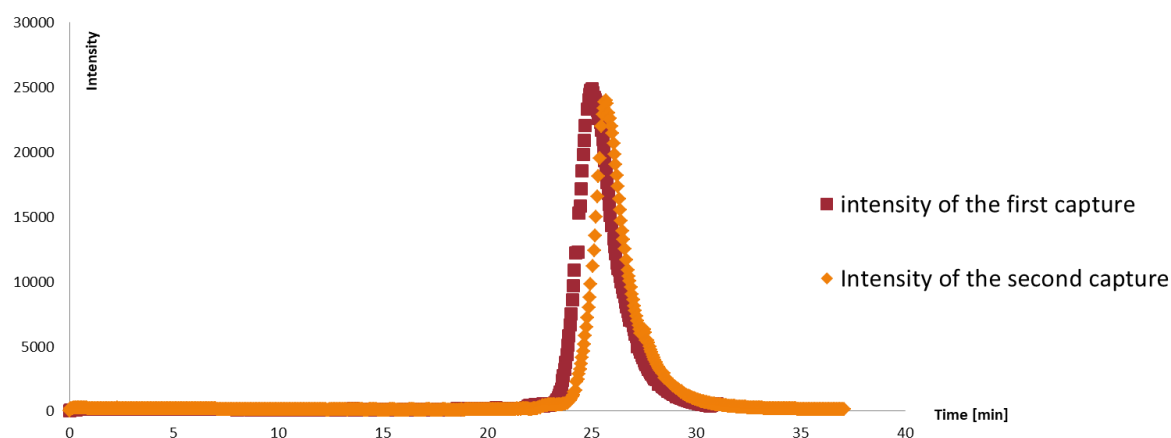


**Figure 6** Elution of R1 and the secondary antibody after a first capture (red) and for a second one (orange) after an acidic treatment. Both signals were recorded in the same conditions.

#### **d) Going forward to optimization and clinical samples test**

Those first results constitute a first proof of concept for the capture of recombinant target on the beads coated with VEGF. The detection using a fluorescent secondary antibody was interesting to demonstrate the feasibility of the capture as well as to evidence the different parameters to be adjusted. However it is quite far from the final setting as human sFlt-1 will be the target and the quantification will be performed off line to avoid any interference. We thus decided to continue this work by detection of sFlt-1 and PlGF concentration before and

after the fluidized bed process with an off line conventional immunoassay. These immunoassays have been performed by the Team of J. Guibourdenche, a partner of the project. They have been using a Roche immunoassay to measure the PlGF concentration in a range from 3 to 10 000 pg/mL and sFlt-1 concentration from 10 to 85 000 pg/mL. The main results achieved in this project are reported in the following manuscript submitted to Clinical Chemistry.

### **3. Article**



# VEGF FUNCTIONALIZED MAGNETIC BEADS IN A MICROFLUIDIC DEVICE TO IMPROVE THE ANGIOGENIC BALANCE IN PREECLAMPSIA

## Authors and Affiliations

Laura TRAPIELLA-ALFONSO<sup>a,§</sup>, Lucile ALEXANDRE<sup>b,§</sup>, Camille FRAICHARD<sup>c,e</sup>, Kelly PONS<sup>a,c</sup>, Simon DUMAS<sup>b</sup>, Jean-François GAUCHER<sup>d</sup>, Marylise SCHUSTER-HEBERT<sup>c,e</sup>, Jean GUIBOURDENCHE<sup>c,e</sup>, Thierry FOURNIER<sup>c</sup>, Michel VIDAL<sup>a</sup>, Laurence LECOMTE-RACLET<sup>h</sup>, Stéphanie DESCROIX<sup>b</sup>, Vassilis TSATSARIS<sup>c\*</sup>, Nathalie GAGEY-EILSTEIN<sup>a,†</sup>, Edouard LECARPENTIER<sup>c,f,g,†</sup>

<sup>a</sup> UMR 8638 CNRS Université Paris Descartes, Faculté des Sciences Pharmaceutiques et Biologiques, Sorbonne Paris Cité, 4 avenue de l'Observatoire, 75006 Paris, France

<sup>b</sup> UMR 168 CNRS Institut Curie, PSL Research University, Institut Pierre Gilles de Gennes; 75005 Paris, France

<sup>c</sup> Cochin Hospital, Assistance Publique-Hôpital de Paris, DHU Risques et grossesse, Paris Descartes University, INSERM UMR 1139, PremUP Foundation, 53 avenue de l'Observatoire, 75014 Paris, France

<sup>d</sup> UMR 8015 CNRS Université Paris Descartes, Faculté des Sciences Pharmaceutiques et Biologiques, Sorbonne Paris Cité, 4 avenue de l'Observatoire, 75006 Paris, France

<sup>e</sup> Cochin Hospital, UF Biologie du médicament, toxicologie, 27 rue du Faubourg Saint Jacques, 75014 Paris, France

<sup>f</sup> Université Paris Est Créteil and CHI Créteil, Créteil, France

<sup>g</sup> INSERM, U955, Institut Mondor de Recherche Biomédicale, Equipe 4, Créteil, France

<sup>h</sup> URC - CIC P1419, Cochin Hotel-Dieu Hospital, Assistance Publique – Hôpitaux de Paris, Paris, 75014 France;

§ Both authors contribute equal to this work (co-first authors)

† Both authors contribute equal to this work (co-last authors)

## \*Corresponding author:

Prof. Vassilis Tsatsaris

E-mail: [vassilis.tsatsaris@aphp.fr](mailto:vassilis.tsatsaris@aphp.fr)

## Sources of Funding

The study was funded by the Agence Nationale pour la recherche (ANR-15-CE17-0005-01)

KP received a grant from the Fondation pour la Recherche Médicale (FRM - DEA 40994)

## Abstract

**Background:** Preeclampsia is a hypertensive disease of pregnancy due to massive increase of sFlt-1 in maternal circulation responsible of angiogenic imbalance and endothelial dysfunction. Non-specific apheresis systems are experimented to remove sFlt-1 from maternal circulation with potential adverse effects due to the capture of many other molecules. Here, we propose a specific and competitive apheresis approach to capture sFlt-1 while releasing endogenous PlGF, potentiating the proangiogenic effects on maternal endothelial functions.

**Methods:** A ligand based approach was used. Magnetic beads were functionalized with VEGF to capture sFlt-1. Experiments were carried out in PBS, conditioned media from human trophoblastic cells and human plasma. The proof of concept was validated in dynamic conditions in a microfluidic device as an approach mimicking real apheresis.

**Results:** Magnetic beads were functionalized with VEGF and characterized to evaluate the surface ligand density and the recognition capabilities. Afterwards, VEGF-coated magnetic beads have been demonstrated as an efficient support to capture sFlt-1 and release PlGF. In static conditions, sFlt-1 concentration decreased by  $33 \pm 13\%$  whereas PlGF concentration increased by  $27 \pm 10\%$ . When dynamic conditions were applied, the performances were improved with a sFlt-1 capture around 40% and an increase up to two times of the initial concentration for free PlGF. The sFlt-1/PlGF ratio was reduced by 63% in the plasma of preeclamptic patients.

**Conclusions:** A ligand based approach using VEGF-coated beads is an effective selective approach to capture sFlt-1 and release the endogenous PlGF, offering new perspectives for the treatment of preeclampsia.

## Keywords

Apheresis, Preeclampsia, sFlt-1/PlGF ratio, microfluidic magnetic fluidized bed

## **Introduction**

Preeclampsia is a hypertensive disorder of pregnancy associated with important maternal and perinatal mortality and morbidity(1). There is currently no curative treatment of preeclampsia, and only childbirth and delivery of the placenta alleviate maternal symptoms. The development of therapeutic strategies for preeclampsia is one of the highest priorities in perinatal medicine.

During preeclampsia massive amounts of sFlt-1, the soluble form of the Vascular Endothelial Growth Factor Receptor 1 (sVEGFR1), are released by the placenta in maternal circulation resulting in an inhibition of the proangiogenic effects of the VEGF-A and the Placental Growth Factor (PlGF) on the maternal endothelium(2). These angiogenic factors are essential for the survival of endothelium, thus explaining the endothelial dysfunction during preeclampsia(3,4).

On the basis of compelling evidence that circulating sFlt-1 is a critical and potentially rate-limiting step in the pathobiology of preeclampsia, it is supposed that by reducing its circulating concentrations with an extracorporeal device, the disease progression could be limited. Based on the positive charge of sFlt-1, dextran sulfate columns have been used to remove the excess of circulating maternal sFlt-1 during preeclampsia(5). Thadhani *et al.* have shown the potential of this unspecific method of apheresis for women with preterm preeclampsia, to reduce sFlt-1 concentrations by 18%(6). Currently, a proof of concept trial on selective removal of sFlt-1 in health volunteers and preeclamptic women using a sFlt-1 antibody specific adsorption column is ongoing to test the safety and the efficacy of this procedure(7).

The objective of this study was to develop and make the proof of concept of a selective apheresis approach to reduce circulating sFlt-1 while increasing free PlGF in order to restore the physiologic angiogenic balance in maternal circulation (Figure S1). To shift the equilibrium of sFlt-1/PlGF binding, we have grafted magnetic beads with VEGF, which has a greater affinity than PlGF for sFlt-1(8). This competitive biomimetic binding approach would capture the circulating sFlt-1 while releasing endogenous PlGF thereby increasing the bioavailability of PlGF and potentiating its proangiogenic effects on maternal endothelial function. To validate on step

further the potential of our approach, it has been integrated in a microfluidic device mimicking a miniaturized extra-corporeal circulation system.

## Material and Methods

Magnetic beads Dynabeads M-280 streptavidin, magnetic support Dynal™ Dynabeads® MPC-DynaMag™-96 Side Skirted Magnet and DynaMag™-5 Magnet were obtained from Invitrogen. Bovine serum albumin fraction IV (BSA) and PBS without Ca<sup>2+</sup> and Mg<sup>2+</sup> were obtained from Eurobio. Tween 20 was from Sigma-Aldrich. Human recombinant sFlt-1 (*rh*VEGFR1/Fc Chimera, Ser27-His687) and human recombinant PlGF (*rh*PlGF) were obtained from R&D Systems. Kits from R&D systems (Quantikine®) or from Roche Diagnostics (Elecsys®) were employed for the dosage of freePlGF and sFlt-1.

### Beads functionalization and characterization

Dynabeads M-280 streptavidin were functionalized with homemade biotinylated VEGF (see SI for VEGF<sub>95</sub>-AVI-biotin expression and purification) or with human anti-Flt-1 biotinylated antibody (R&D Systems). The functionalization was made following the supplier information with slight modifications (see SI).

After beads functionalization, two tests have been performed for their characterization. One to assess the ligand surface density and the other to ensure the ability of the grafted ligand to bind sFlt-1 (see SI).

### Proof of concept with recombinant protein

#### *Formation and dosage of sFlt-1/PlGF complexes*

Increasing concentrations of *rh*VEGFR1/Fc (from 0 to 1000 ng/mL) in PBS/0.1% BSA were added to the same volume of a solution at 4 ng/mL of *rh*PlGF in PBS/0.1% BSA and the mixture was incubated 1h at 37°C. The quantification of complexes formation was obtained after dosage of free *rh*PlGF with the Quantikine® kits. The maximum signal of absorbance ( $S_{\max}$ ) was given

by the solution of *rhPIGF* without *rhVEGFR1/Fc*. The amounts of free and complexed *rhPIGF* were obtained using equations 1 and 2:

$$\%rhPIGF_{free} = \frac{S}{S_{max}} \times 100 \quad \text{Equation 1}$$

$$\%rhPIGF_{complexed} = \frac{S_{max}-S}{S_{max}} \times 100 \quad \text{Equation 2}$$

#### *Capture of rhVEGFR1/Fc and release of rhPIGF with VEGF-beads*

200  $\mu\text{L}$  of the solution of *rhVEGFR1/Fc/rhPIGF* complexes (see 2.2.1) were incubated in a tube with 5  $\mu\text{L}$  (50  $\mu\text{g}$ ) of VEGF coated beads (V-beads) at 105 pmol of bt-VEGF/mg beads. For negative control, non-functionalized beads (C-beads) were used. After 1h incubation at 37°C under stirring, concentration of free *rhPIGF* and *rhVEGFR1/Fc* were measured with Quantikine® kits.

#### Ethics statements and biological samples

The local ethics committee (Comité de Protection des Personnes Ile de France 3) has approved both the human primary cell culture studies from placenta tissue (Perinat Collection ANR-10-EQPX-0010) and the human plasma sample from the APHERESE case/control prospective study (NCT03188900). All patients gave written consent for participation in these studies. For the primary cell culture, cytotrophoblasts (CTs) were isolated as previously described(9) and the conditioned media were collected after 72 hours of culture and then stored at -80°C.

#### Microfluidic experiments

The characteristics and procedures for the chip fabrication and the microfluidic set-up were previously described and are summarized in the SI(10). PBS containing 1% Bovine Serum Albumine, from Sigma Aldrich, were used for the conditioning of the chip.

#### *Sample treatment*

The system of chip and tubing was initially filled with the washing buffer and the temperature was adjusted at 37°C thanks to an indium tin oxide glass slide with feed-back regulation from a

voltage controller (Eurotherm 3508) via a thermocouple gauge installed inside a slot in the PDMS chip. When using plasma samples, preliminary 3 min spin centrifugation was performed to remove eventual solid aggregates and only supernatant was then collected.

The sample (150  $\mu\text{L}$ ) was flown inside the chip chamber at 1  $\mu\text{L}/\text{min}$ . A Tygon<sup>®</sup> tube (Saint Gobain AAD04103 Tygon Non-DEHP Medical Microbore Tubing, 0.020" ID, 0.060" OD) connected at the outlet was used to collect the passed through solution.

## Results

### Functionalization and characterization of streptavidin magnetic beads

#### *Functionalization*

In order to study the impact of the VEGF density on the beads to the sFlt-1 binding capacity, it was necessary to estimate precisely the surface saturation of the magnetic beads since steric hindrance, repulsion or interactions may play a role in the protein recognition(11,12). Based on a previous work(13), 4 different grafted V-beads with ligand densities between  $11.7 \cdot 10^3$  to  $158 \cdot 10^3$  VEGF/ $\mu\text{m}^2$ , have been prepared by changing the initial quantity of VEGF and characterized (Table S1).

#### *Binding of sFlt-1*

To evaluate how the VEGF grafted on the beads was still able to recognize human recombinant sFlt-1 with a good affinity, a binding assay was developed and gave access to the dissociation constant of the immobilized VEGF/*rh*VEGFR1/Fc complex (Fig.S2). The binding assay was performed with the 35% saturated beads (105 pmol VEGF/mg of beads) and revealed a  $K_d$  value of  $1.0 \pm 0.4$  nM (n=5). This value is in good agreement with the value obtained when VEGF is coated in a plate performing a classical ELISA test(14) and confirms the high ligand-receptor affinity.

Proof of concept

Capture and release of recombinant proteins

The ability of V-beads to perform simultaneously the capture of sFlt-1 and the release of PIGF was first demonstrated in static conditions with recombinant proteins.

Formation of *rh*VEGFR1/Fc /*rh*PIGF complexes

The first step was to produce artificial samples with varying composition of complexed and free proteins. To do so it was necessary to control the formation of recombinant *rh*VEGFR1/Fc/*rh*PIGF complexes (Fig.1A). To estimate the initial amount of each protein required to form the complex, a theoretical study was performed (see SI). Taking into account these calculations, the initial concentration of *rh*PIGF was kept constant at 6.9 pM and the selected range of initial *rh*VEGFR1/Fc concentrations ranged from 0 to 500 pM. The estimated  $K_d$  value for *rh*PIGF/*rh*VEGFR1/Fc complex was found at  $22 \pm 3$  pM (n=3) (Fig.S3).

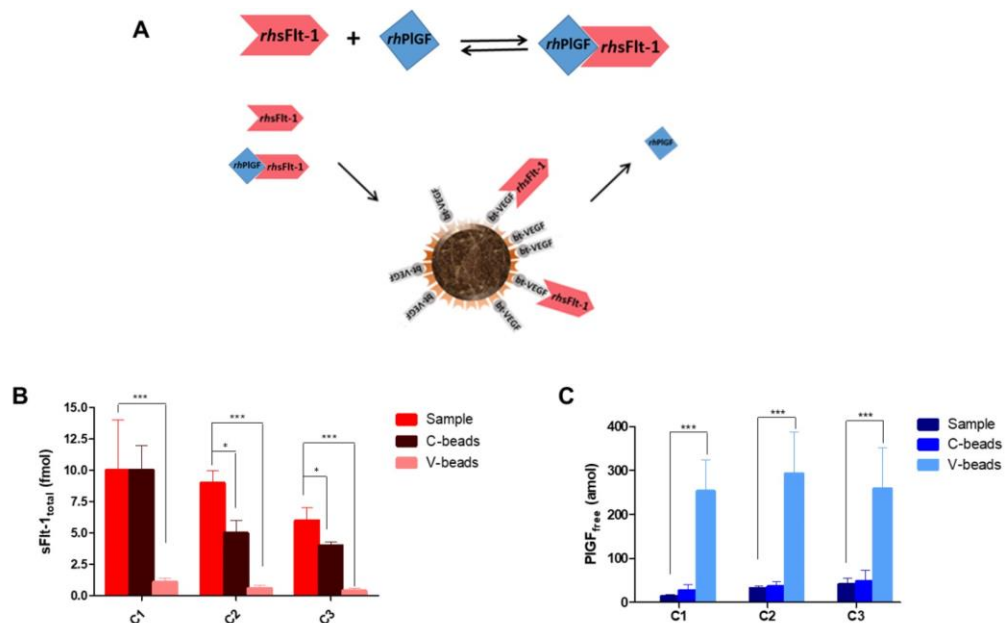


**Figure 1:** Proof of concept of the specific and competitive apheresis approach using recombinant proteins in physiological buffer medium (PBS at pH 7.4). A/ schematic representation of the *rh*VEGFR1/Fc/*rh*PIGF complex formation and its interaction with V-beads; B/ Evolution of the concentration of *rhs*Flt-1 after being incubated with V-beads; C/ Evolution of the concentration of *rh*PIGF after incubation with V-beads.

Please note that in B/ and C/: i- C1, C2 and C3 are 3 solutions of complexes with different initial concentrations of *rhVEGFR1/Fc* (i.e. 52.3; 43.7; and 29.2 pM, respectively); (\*  $p < 0.1$ ; \*\*\*  $p < 0.001$ )

Abbreviations: bt-VEGF: biotinylated VEGF; *rh*sFlt-1: recombinant human sFlt-1; *rh*PIGF: recombinant human PIGF; IgG AP: Alkaline Phosphatase linked IgG; pNPP: para-nitrophenylphosphate; pNP: 4-nitrophenol; Sample: initial *rhVEGFR1/Fc/rhPIGF* formed complexes; C-beads: non-functionalized beads; and V-beads: VEGF grafted beads.

#### sFlt-1 capture and PIGF release

The second step of the proof of concept was to evaluate the ability of V-beads to capture *rh*sFlt-1 and to disrupt the *rhVEGFR1/Fc/rhPIGF* complex (Fig.1A). Thus, three different complexes solutions (C1, C2 and C3) obtained with three different initial concentrations of *rhVEGFR1/Fc* (ranging from 52.3 to 29.2 pM), were incubated with non-functionalized beads (C-beads) as negative control and V-beads. The final concentration of *rhVEGFR1/Fc* and *rhPIGF* were thus determined in the supernatants. Figures 1B and 1C show the molar quantity of total *rhVEGFR1/Fc* and free *rhPIGF* in each solution before (sample bar) and after incubation (C- and V-beads bars). A moderate non-specific interaction of the C-beads with *rhVEGFR1/Fc* was observed in some cases while C-beads had no effect regarding PIGF. In contrast, a significant decrease in *rhVEGFR1/Fc* concentration accompanied by an increase of PIGF concentration in presence of V-beads was observed in all the samples tested. In addition, since the total amount of *rhPIGF* used to form the complexes is known (6.9 pM), the % of PIGF initially and finally complexed could be calculated. While around 90% of initial *rhVEGFR1/Fc* was captured only 20% of initial *rhPIGF* complexed to *rhVEGFR1/Fc* was released. This could be explained by the great difference in the amounts of proteins used to form the complexes (Table S2). Note that, in this study, we have chosen conditions where almost all the *rhPIGF* was complexed (> 90%) and *rhVEGFR1/Fc* was in high excess, which is the case during severe preeclampsia.

These results, with recombinant proteins demonstrate our competitive approach for the capture of sFlt-1 and the release of PIGF proposed in this work allowing to move on more complex media to validate the strategy.



*Impact of the saturation rate on the capture of sFlt-1 and release of PlGF*

The efficiency of sFlt-1 capture and PlGF release has been assessed according to the surface ligand density of the V-beads. The amount of bt-VEGF coated on streptavidin Dynabeads® has been evaluated from 30 to 259 pmol/mg of beads corresponding to a surface ligand density ranging from  $11.7 \cdot 10^3$  to  $102 \cdot 10^3$  VEGF/ $\mu\text{m}^2$  (Table S1). To investigate how our system was able to accommodate complex samples, these experiments were performed with conditioned media obtained from human trophoblastic primary cells in which the initial concentrations of sFlt-1<sub>total</sub> and PlGF<sub>free</sub> were 0.27 pmol/ml (20868 pg/ml) and 0.015 pmol/ml (292 pg/ml) respectively. 200  $\mu\text{L}$  of this conditioned media (CM) was incubated with the necessary amount of beads to ensure the required VEGF excess compared to initial sFlt-1 in the sample. The amount of sFlt-1 captured increased when the ligand surface density decreased, going from 30% of capture at  $100 \cdot 10^3$  VEGF/ $\mu\text{m}^2$  to 60% of capture at  $12 \cdot 10^3$  VEGF/ $\mu\text{m}^2$  for the case of 500 molar excess of VEGF (Fig.2A). This could be explained by a high steric hindrance at higher saturation rate limiting the capture(12). Then, at constant surface ligand density, the effect of VEGF in excess compared to initial concentration of sFlt-1 has been evaluated. We increased the mass of beads in order to obtain a 10 to 500 molar excess of VEGF. As expected, the capture increased with the excess of VEGF. However, over 100 molar excess, only a slight improvement of capture was observed. For PlGF release the excess of VEGF plays a more important role than for sFlt-1, since this molecule is initially complexed to sFlt-1 and has to be displaced. In addition, the levels of PlGF are considerable lower than sFlt-1 (sometimes more than one order of magnitude). For example, in the CM used for this study the initial quantity of free PlGF in solution was 3 fmol while the total quantity of sFlt-1 was 54 fmol, corroborating the great difference in concentration between both molecules and the fact that most of the PlGF will be complexed. Thus, we can observe in Figure 2B how at least a molar excess of 100 is required to have a significant release of PlGF.

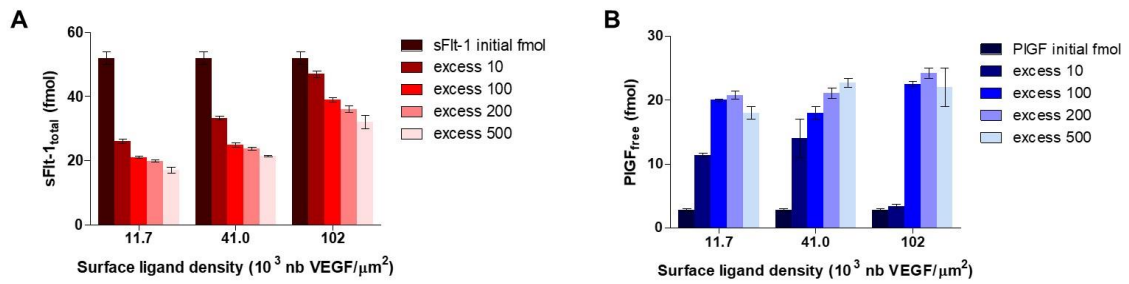


**Figure 2:** Impact of the grafting rates of V-beads on their capture/release performances in conditioned media of human trophoblastic cells. A/ sFlt-1 capture and B/ PIGF release after 2h30 of incubation at 37°C. Note that the marked excess are molar excess of VEGF compared to initial concentration of sFlt-1.

Based on these series of experiments, the selected surface ligand density for further experiments was fixed at  $41 \cdot 10^3$  VEGF/ $\mu\text{m}^2$  ( $105$  pmol VEGF/mg of beads; 35% saturation rate) as the better compromise in terms of beads and VEGF consumption and performance of capture/release. In patient samples the quantities of these factors are considerably variable and consequently the VEGF excess from beads may be different affecting the efficiency of the apheresis. Nevertheless, previous experiments shown that this efficiency will not be negatively affected if we ensure at least a 100 molar excess (VEGF/sFlt-1).

#### *Valorization of the competitive strategy*

To emphasize the features of this new specific and competitive strategy for restoring the angiogenic balance in preeclampsia, we aimed to compare the performances of the proposed approach with the specific strategy based on the use of antibodies for the capture of sFlt-1. Magnetic beads were functionalized either with VEGF or with anti-sFlt-1 antibody and their performances for restoring the angiogenic balance in complex media (culture cell supernatants and mixed plasma of pregnant women) were compared. In the Figure 3, we can observe that both systems capture sFlt-1 in the same range. However, the competitive approach, by releasing PIGF, is more efficient for the final objective of restoring the angiogenic balance.

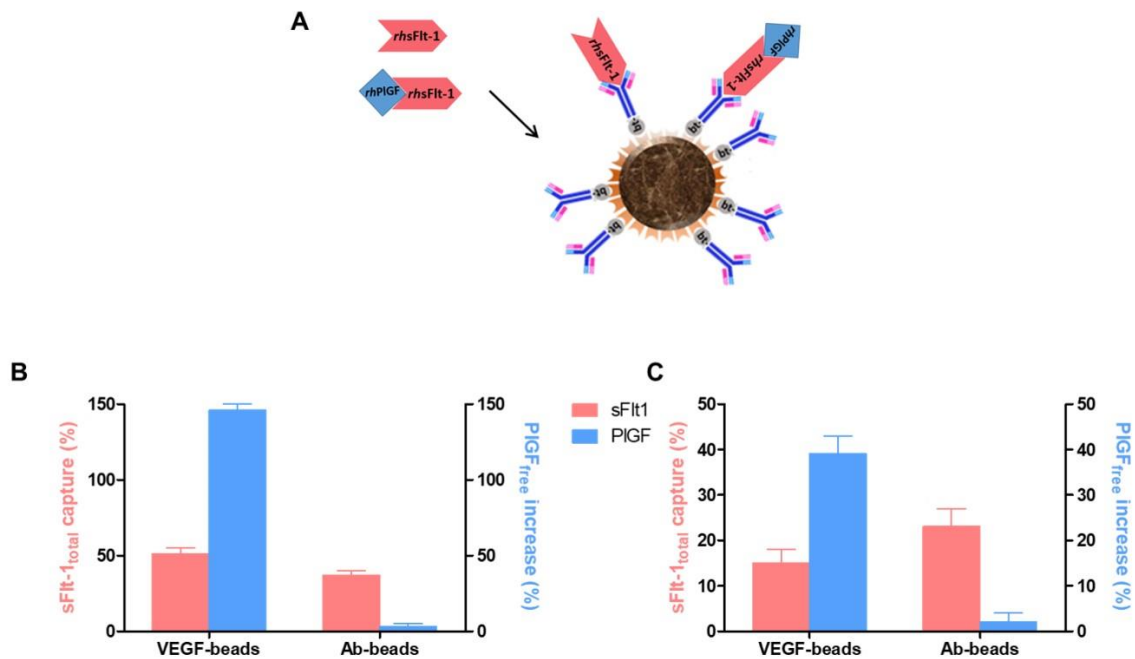


**Figure 4:** Evolution of concentrations of sFlt-1 and PIGF with A) the capture of sFlt-1 and the release of free PIGF and B) the comparison between the initial and final sFlt-1/PIGF ratio as function of the residence time of each molecules inside the matrix of magnetic beads in the microfluidic device. The abscissa 0 represents a control experiment realized with Streptavidin Dynabeads M-280©. Evolution of the concentration of molecules were evaluated as  $\Delta = \frac{[C]_{fin} - [C]_{init}}{[C]_{init}}$  where concentrations measured in pmol/mL (\* p < 0.001)

It should also be mentioned that both systems suffer a loss of efficiency in the capture of sFlt-1 when the sample matrix is more complex. Thus, Ab-beads capture 37% of sFlt-1 in CM and 23% in plasma whereas V-beads capture 51% in CM and 15% in plasma capture. This fact could be explained by the complexification of the sample matrix.

#### Optimization of the microfluidic conditions

In order to test this approach in a dynamic setting, a microfluidic PDMS chip of the magnetic fluidized bed previously described(14) has been used to increase the surface to volume interactions during the treatment of the CM and the plasma samples with the functionalized beads. Here, the solid phase constituted of V-beads is in a continuous recirculation (fluidization) during

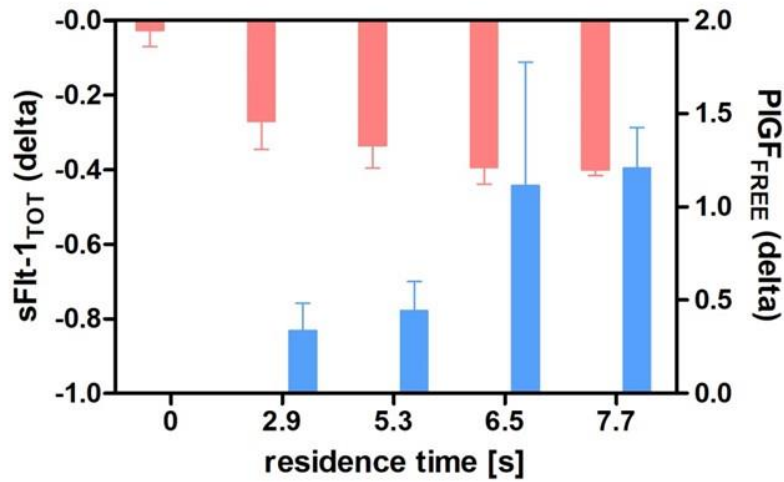
the percolation of a liquid phase (the biological samples). In the following sections, we present the different steps of the optimization of the microfluidic device-based approach.

*Time of residence of the sample inside the bed*

We assessed the impact of the sample residence time inside the bed of magnetic beads. This residence time is directly correlated with the flowrate and the bed porosity. We used a CM of primary human trophoblastic cells where concentrations of sFlt-1 and PlGF were respectively at 0.26 pmol/mL and 0.013 pmol/mL. Experiments with 150  $\mu$ L of biological samples were performed at a flow rate ranging from 0.5  $\mu$ L/min (residence time of 7.7 s) to 3  $\mu$ L/min (residence time of 2.9 s). As shown in Fig 4A, increasing the residence time of each molecule inside the chip improved the capture of sFlt-1 and the release of PlGF in a non-linear way since optimum capture/release mechanism is reached at 6.5 seconds of residence time, representing a flowrate of 1  $\mu$ L/min and a total experiment of 2h30. This residence time is in agreement with the results obtained in static conditions (Fig.S4). As shown on Fig. 4B, 6.5 seconds of residence time is enough to reach a final sFlt-1/PlGF ratio at a physiological level below 38 for a sample with an initial ratio around 80.

For the following experiments a flowrate of 1  $\mu$ L/min has been chosen to percolate the sample through the bed, which means a residence time of 6.5 seconds of the biological sample inside the chip. Note that when the experiment is performed with C-beads (the abscissa 0 in Fig.4) no capture and no release could be measured and the sFlt-1/PlGF ratio was not affected by the sample percolation through the bed of beads.

A



B

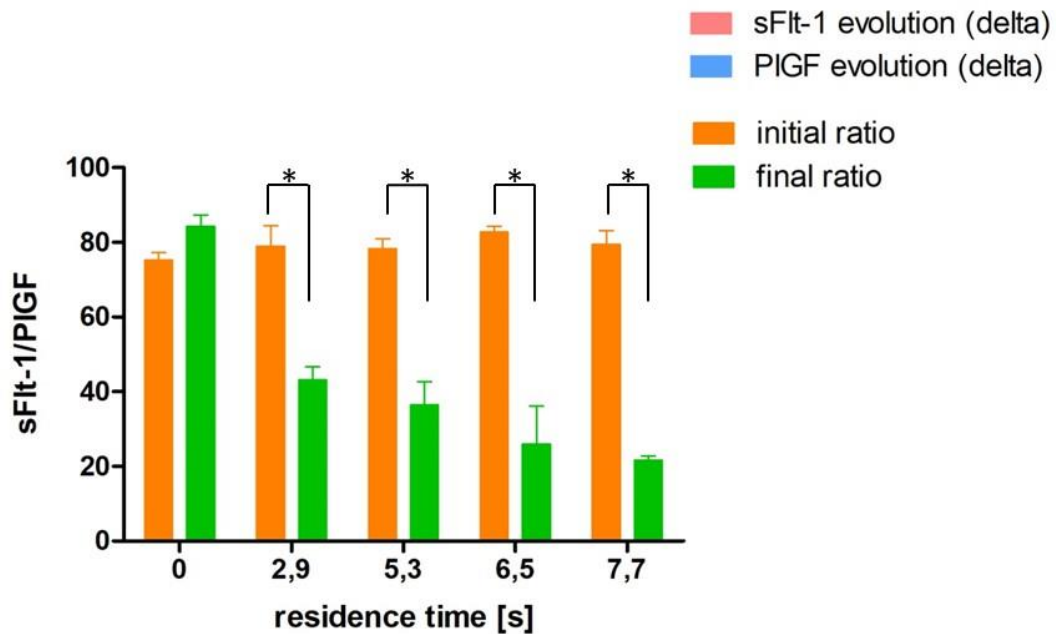


**Figure 4:** Evolution of concentrations of sFlt-1 and PIGF with A) the capture of sFlt-1 and the release of free PIGF and B) the comparison between the initial and final sFlt-1/PIGF ratio as function of the residence time of each molecules inside the matrix of magnetic beads in the microfluidic device. The abscissa 0 represents a control experiment realized with Streptavidin Dynabeads M-280©. Evolution of the concentration of molecules were evaluated as  $\text{delta} = \frac{[C]_{fin} - [C]_{init}}{[C]_{init}}$  where concentrations measured in pmol/mL (\* p < 0.001)

*Surface ligand density of the beads*

The performance of capture/release of sFlt-1/PlGF in the microfluidic device has been evaluated considering the surface ligand density of the magnetic beads. The amount of bt-VEGF coated on Streptavidin Dynabeads® has been evaluated from  $11.7 \cdot 10^3$  to  $158 \cdot 10^3$  VEGF/ $\mu\text{m}^2$ . We showed that increasing the VEGF surface density on the beads from 11.7 to  $41.0 \cdot 10^3$  VEGF/ $\mu\text{m}^2$  beads increased the capture of sFlt-1. However, large ligand surface densities induced a decrease of capture of sFlt-1 (Figure S5). Thus,  $41.0 \cdot 10^3$  VEGF/ $\mu\text{m}^2$  was the final surface ligand density selected for the experiments. These findings are in agreement with the static experiments (Fig.2).

*Validation of the approach in complex matrices: from cell culture to human plasma*

To validate our system, we used two types of biological samples, CM of human trophoblastic cells (n=3) and plasma from pregnant women with preeclampsia (n=3). The details concerning these samples are summarized in Table S3.

First we tested our device with CM from human primary trophoblastic cells. For each of the samples tested, we were able to capture sFlt-1, release PlGF and consequently decrease the sFlt-1/PlGF ratio. As shown on Fig.5A, we captured more than 70% of the sFlt-1 of the sample, and released from half to more than the double of the initial quantity of PlGF. The final ratio sFlt-1/PlGF in CM was significantly reduced and systematically below the physiologic level of 38 (Fig.5C).

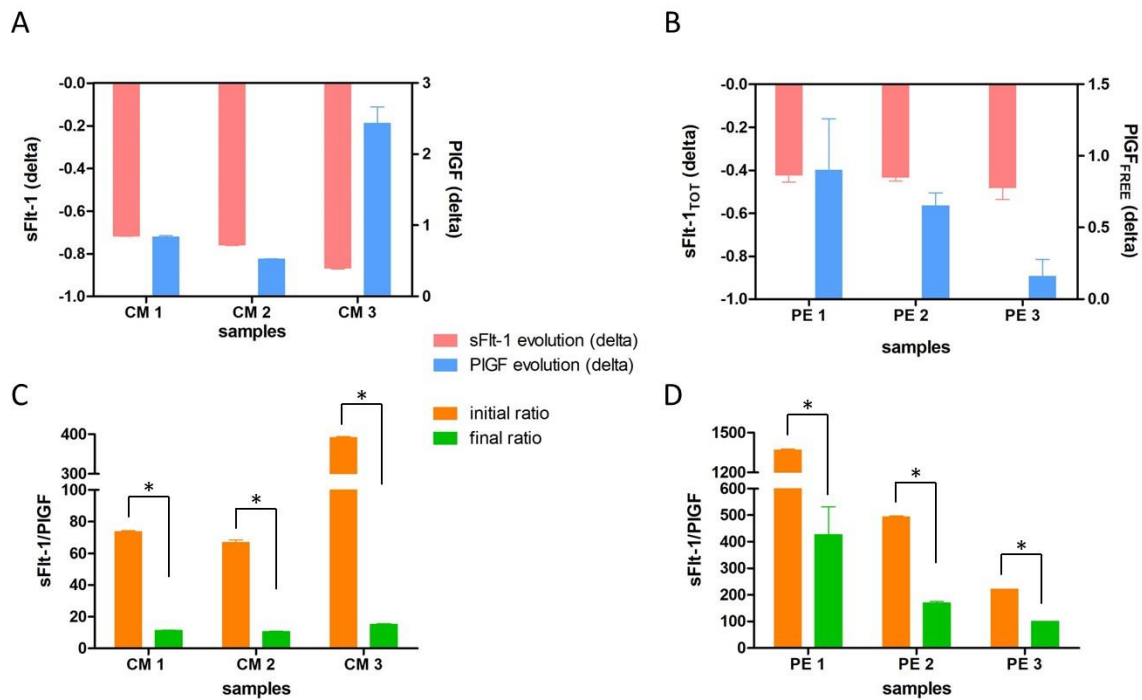


**Figure 5:** Performance of sFlt-1 capture and PIGF release in conditioned media from human trophoblastic primary cell culture (A) and human plasma from pre-eclamptic women (B) after passage through the microfluidic device. Evolution of the sFlt-1/PIGF ratio in conditioned media (C) and plasma samples (D) after passage through the microfluidic device. Performances are evaluated as  $\text{delta} = \frac{[C]_{fin} - [C]_{init}}{[C]_{init}}$  with concentrations measured in pmol/mL (\*  $p < 0.001$ )

Finally, with plasma samples from pregnant women with preeclampsia (Fig.5B) we observed a reduction of sFlt-1 around 40% and an increase of free PIGF concentration from one sixth to more than double in all the tested samples. Thus, our microfluidic system with V-beads decreased the sFlt-1/PIGF ratio in plasma samples by 63% in average (Fig.5D).

## Discussion

Extracorporeal strategies are evaluated to treat preeclampsia for three main reasons: (1) the suspected primary role of the circulating sFlt-1 in the pathogeny of the disease, (2) the development of drugs that act specifically on the soluble form and not on the membrane form is particularly complex and (3) apheresis methods avoid the adverse effects of molecules that cross the placenta. We have decided to target sFlt-1 because of the mounting evidence of its

involvement in the pathogenesis of preeclampsia(15–18). The soluble Flt-1 has been postulated to exert inhibitory effects on angiogenic signaling via two mechanisms: direct sequestration of angiogenic ligands such as VEGF and PlGF and/or dominant-negative heterodimerization with surface VEGFRs(19).

Our sFlt-1 capture strategy consists on a specific and competitive approach between the VEGF coated on the beads and the PlGF bound to the sFlt-1. The decline in total sFlt-1 is therefore as important as the increase in free PlGF for our study endpoint, reason why we used the ratio sFlt-1/PlGF for the expression of our results. To capture *in vitro* the sFlt-1 in static and dynamic conditions we used streptavidin magnetic beads, which are easy to functionalize with specific ligands (e.g. biotinylated VEGF, Fig.S2). Before application, several tests to evaluate the surface ligand density (Table S1) and the ability to recognize sFlt-1 by the grafted ligand (Fig.S2) as well as the time-stored stability of the V-beads (up to 2 weeks at 4°C, Fig.S6) have been performed. Then, the sFlt-1 capture combined with PlGF release was proven mainly by two series of experiments. First, with the recombinant human *rh*VEGFR1/Fc/*rh*PlGF complexes in static conditions, enabling to control the total amount of PlGF used in the experiments, which is not possible with more complex media (CM, plasma) since human PlGF ELISA kits only measure the free PlGF. These experiments demonstrated the ability of V-beads to capture *rh*VEGFR1/Fc and also to release significantly *rh*PlGF (20% of the initial complexed PlGF). Second, our approach was compared with another specific capture strategy based on beads coated with a sFlt-1 antibody. We demonstrated an equivalent capture rate of sFlt-1 but with the addition of an increase of free PlGF in solution, which proves the potential interest of our competitive approach. The increase in free PlGF in solution after incubation with the V-beads may be caused by the combination of two phenomena. The initially free sFlt-1, is trapped by the V-beads, resulting in a shift of the biochemical equilibrium towards free PlGF (see equilibrium equation in Fig.1A). In addition, the V-beads, competes with the PlGF bound to the sFlt-1, and due to the excess of VEGF used for the incubation we can displace the bound PlGF (Fig.2 and S5).



The second part of our work was performed under dynamic conditions. The fluidized bed model allows the use of the same magnetic beads than for the static conditions. Moreover, the magnetic fluidized bed brings, to applications involving fluid-solid exchanges, advantages such as high surface to volume ratio, constant mixing, low flow resistance(19). Our results demonstrate the proof of concept of a significant sFlt-1 capture combined with the release of PlGF in dynamic conditions, being able to reduce by 68% the sFlt-1/PlGF ratio in plasma from preeclamptic women. The flowrates and the fluid volumes are low in such conditions and not compatible with an application in pregnant woman (50-60 mL/min)(6) but these microscale techniques are interesting to test different molecules to capture the sFlt-1 in preeclamptic plasmas because of the limited amount of human material as well as performing the proof of concept of our approach in animal models.

In conclusion, our work brings the proof of concept of a new strategy to capture the circulating sFlt-1 and release endogenous PlGF. The originality of our approach is based on a competitive and biomimetic strategy to bind sFlt-1 with its natural ligand (VEGF) and release part of the PlGF trapped by sFlt-1. This technique enables to rebalance the ratio of anti/pro angiogenic molecules in maternal circulation offering new perspectives for the treatment of preeclampsia.

### **Acknowledgements**

We would like to acknowledge the financial support provided by the Agence National de la Recherche (ANR-15-CE17-0005-01). The Paris Descartes University, INSERM and CNRS are also acknowledged.

We would also thank to the UMR 8258-CNRS for sharing the TECAN SAFIRE and MULTISKAN EX plate-readers.

### **References**

1. Tranquilli AL, Dekker G, Magee L, Roberts J, Sibai BM, Steyn W, et al. The classification, diagnosis and management of the hypertensive disorders of pregnancy: A revised statement from the ISSHP. *Pregnancy Hypertens Int J Womens Cardiovasc Health*. 2014; 4(2):97-104.
2. Maynard S, Epstein FH, Karumanchi SA. Preeclampsia and angiogenic imbalance. *Annu Rev Med*. 2008; 59:61-78.
3. Wu FTH, Stefanini MO, Mac Gabhann F, Kontos CD, Annex BH, Popel AS. A systems biology perspective on sVEGFR1: its biological function, pathogenic role and therapeutic use. *J Cell Mol Med*. 2010; 14(3):528-52.
4. Maharaj ASR, Walshe TE, Saint-Geniez M, Venkatesha S, Maldonado AE, Himes NC, et al. VEGF and TGF-beta are required for the maintenance of the choroid plexus and ependyma. *J Exp Med*. 2008; 205(2):491-501.
5. Thadhani R, Kisner T, Haggmann H, Bossung V, Noack S, Schaarschmidt W, et al. Pilot study of extracorporeal removal of soluble fms-like tyrosine kinase 1 in preeclampsia. *Circulation*. 2011; 124(8):940-50.
6. Thadhani R, Haggmann H, Schaarschmidt W, Roth B, Cingoz T, Karumanchi SA, et al. Removal of Soluble Fms-Like Tyrosine Kinase-1 by Dextran Sulfate Apheresis in Preeclampsia. *J Am Soc Nephrol JASN*. 2016; 27(3):903-13.
7. Proof-of-Concept Trial on Selective Removal of sFlt-1 in Pregnant Women With Preeclampsia Via Apheresis - Full Text View - ClinicalTrials.gov [Internet]. [cité 24 juill 2018]. Disponible sur: <https://clinicaltrials.gov/ct2/show/NCT02923206>
8. Autiero M, Lutun A, Tjwa M, Carmeliet P. Placental growth factor and its receptor, vascular endothelial growth factor receptor-1: novel targets for stimulation of ischemic tissue revascularization and inhibition of angiogenic and inflammatory disorders. *J Thromb Haemost JTH*. 2003; 1(7):1356-70.
9. Alsat E, Haziza J, Evain-Brion D. Increase in epidermal growth factor receptor and its messenger ribonucleic acid levels with differentiation of human trophoblast cells in culture. *J Cell Physiol*. 1993; 154(1):122-8.
10. Pereiro I, Tabnaoui S, Fermigier M, du Roure O, Descroix S, Viovy J-L, et al. Magnetic fluidized bed for solid phase extraction in microfluidic systems. *Lab Chip*. 2017; 17(9):1603-15.
11. Jennings TL, Rahman KS, Fournier-Bidoz S, Chan WCW. Effects of microbead surface chemistry on DNA loading and hybridization efficiency. *Anal Chem*. 2008; 80(8):2849-56.
12. Teste B, Vial J, Descroix S, Georgelin T, Siaugue J-M, Petr J, et al. A chemometric approach for optimizing protein covalent immobilization on magnetic core-shell nanoparticles in view of an alternative immunoassay. *Talanta*. 2010; 81(4-5):1703-10.
13. Bouzas-Ramos D, Trapiella-Alfonso L, Pons K, Encinar JR, Costa-Fernández JM, Tsatsaris V, et al. Controlling Ligand Surface Density on Streptavidin-Magnetic Particles by a Simple, Rapid, and Reliable Chemiluminescent Test. *Bioconj Chem*. 2018; DOI:10.1021/acs.bioconjchem.8b00347

14. Trapiella-Alfonso L, Broussy S, Liu W-Q, Vidal M, Lecarpentier E, Tsatsaris V, et al. Colorimetric immunoassays for the screening and specificity evaluation of molecules disturbing VEGFs/VEGFRs interactions. *Anal Biochem.* 2018; 544:114-20.
15. Maynard SE, Min J-Y, Merchan J, Lim K-H, Li J, Mondal S, et al. Excess placental soluble fms-like tyrosine kinase 1 (sFlt1) may contribute to endothelial dysfunction, hypertension, and proteinuria in preeclampsia. *J Clin Invest.* 2003; 111(5):649-58.
16. Rana S, Powe CE, Salahuddin S, Verlohren S, Perschel FH, Levine RJ, et al. Angiogenic factors and the risk of adverse outcomes in women with suspected preeclampsia. *Circulation.* 2012; 125(7):911-9.
17. Levine RJ, Maynard SE, Qian C, Lim K-H, England LJ, Yu KF, et al. Circulating angiogenic factors and the risk of preeclampsia. *N Engl J Med.* 2004; 350(7):672-83.
18. Kim MY, Buyon JP, Guerra MM, Rana S, Zhang D, Laskin CA, et al. Angiogenic factor imbalance early in pregnancy predicts adverse outcomes in patients with lupus and antiphospholipid antibodies: results of the PROMISSE study. *Am J Obstet Gynecol.* 2016; 214(1):108.e1-108.e14.
19. Wu FTH, Stefanini MO, Mac Gabhann F, Popel AS. A compartment model of VEGF distribution in humans in the presence of soluble VEGF receptor-1 acting as a ligand trap. *PloS One.* 2009; 4(4):e5108.

## 4. Perspectives

### a) Conclusion on the first results

We demonstrated an alternative way to restore the angiogenic balance of the growth factors sFlt-1 and PlGF in case of pre-eclampsia. By taking advantage of the fluidized bed disposition, we were able to validate the competitive approach. In presence of VEGF, the concentration of sFlt-1 decreases whereas the bio-availability of free PlGF increases.

We showed that this competitive bioassay can be adapted to the dynamics of fluidized bed. This technology can mimic at small scale an apheresis system. It allows new strategies to be tested at low-cost, with small amounts of reagents and small volumes of samples. This technology is fully adapted to experiments on precious samples such as maternal pre-eclamptic plasma.

We demonstrated that the fluidized bed can be adapted to complex media such as cell culture supernatant or maternal plasma. Its efficiency stays comparable to those obtained in batch in both matrices. The system offers the possibility to balance both sFlt-1 and PlGF concentrations and to control the non-specific absorption compared to apheresis columns.

To continue this work, the system must prove its efficiency on a more complex model from real sample (such as whole blood) up to living animal.

### b) Going to extracorporeal blood- cleaning: the strategy of animal model

In a next future, we aim to evaluate the potential of the microfluidic platform previously described on a model in-vivo of mice. To implement this project, we will work with Pr Pierre Louis Tharaux from the cardiovascular center of Paris. He developed a model of non gestating mice expressing sFlt-1 and PlGF rates similar to the ones of pre-eclamptic women.

A first study should prove the feasibility to work with whole blood (already demonstrated with human whole blood) and evaluate the efficiency of the system in this sample matrix. Blood sample will be collected from the mice and injected in the system. This step will allow us to elucidate all the issues related to the biocompatibility of our system.

Then we will adapt the system to connect it directly to the animal. All explorations will be first controlled by the ethical comity of animal experimentation of Paris Descartes. All fluidic

connections need to be developed. Another microfluidic system already showed its efficiency in blood cleaning using a apheresis structure (Kang et al., 2014). Pathogens (bacteria *Staphylococcus aureus*) were continuously removed from the blood using magnetic nanobeads. Beads were coated with lectins with high affinity for the pathogens. They were mixed with the blood and extracted using a magnet (Figure 7 A). The cleaned (> 90% removal) blood could then re-enter the animal (rats). The system was directly connected to the jugular veins of the anesthetized rats. The treatment lasted 5h without affecting the animal or creating coagulation. They showed a significant improvably of the survival rate through the 5 hours of treatment (14% of untreated rats against 89% of animals treated with the blood-cleansing device survived for the entire experiment as shown on Figure 7 C)

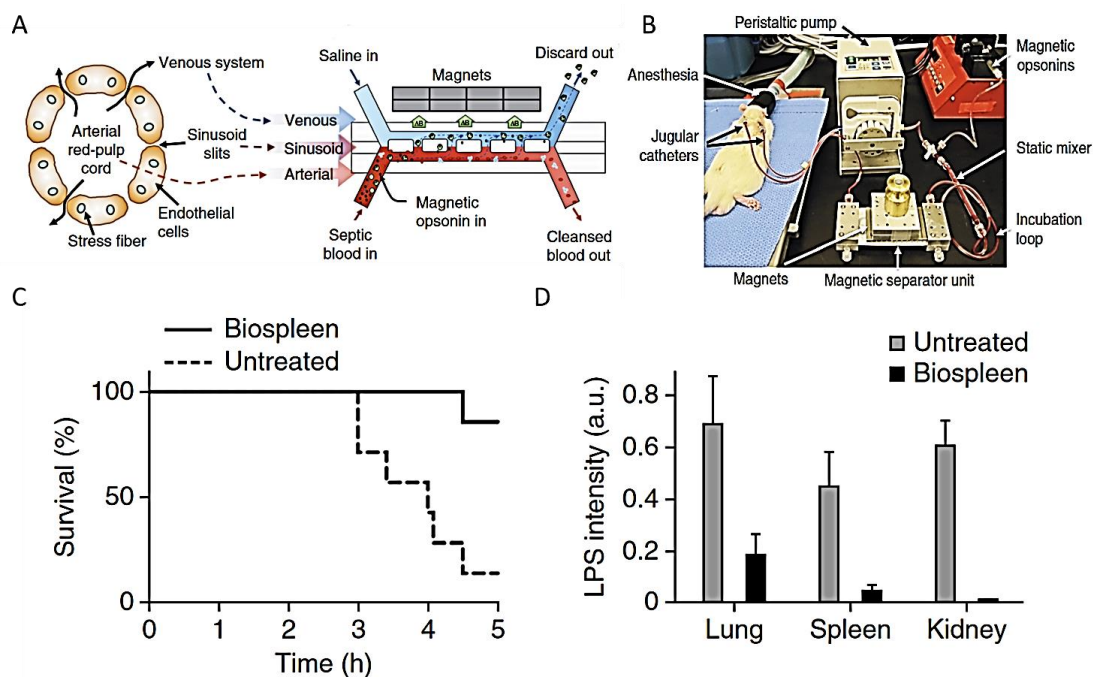


**Figure 7A Schematics of a venous sinus in the red pulp of the spleen (left) and a longitudinal view of the biospleen (right) B photograph of the system implemented on a rate C Plot showing the increase of survival in rats treated D Quantitative analysis of immunostained histological sections of lung spleen and kidney (Kang et al., 2014)**

The evaluation of the efficiency of the system will be related to the improvement of the living conditions of the mice. Mainly dosages of sFlt-1 and PlGF, measures of proteinuria, arterial pressure and weight of the animal, and analysis of renal lesions will be performed.

Those new experiments could lead us to the construction of a mobile platform dedicated to pre-eclampsia treatment in vivo.

## Bibliography

- Arngrimsson, R., Björnsson, S., Geirsson, R.T., Björnsson, H., Walker, J.J., and Snaedal, G. (1990). Genetic and familial predisposition to eclampsia and pre-eclampsia in a defined population. *Br. J. Obstet. Gynaecol.* *97*, 762–769.
- Brazdova, A., Keprova, A., Zidkova, J., and Madar, J. (2014). Pre-eclampsia: a life-threatening pregnancy syndrom. *Braz. Arch. Biol. Technol.* *57*, 701–705.
- Craici, I.M., Wagner, S.J., Bailey, K.R., Fitz-Gibbon, P.D., Wood-Wentz, C.M., Turner, S.T., Hayman, S.R., White, W.M., Brost, B.C., Rose, C.H., et al. (2013). Podocyturia predates proteinuria and clinical features of preeclampsia: longitudinal prospective study. *Hypertens. Dallas Tex 1979* *61*, 1289–1296.
- Ferrara, N. (2004). Vascular Endothelial Growth Factor: Basic Science and Clinical Progress. *Endocr. Rev.* *25*, 581–611.
- Kang, J.H., Super, M., Yung, C.W., Cooper, R.M., Domansky, K., Graveline, A.R., Mammoto, T., Berthet, J.B., Tobin, H., Cartwright, M.J., et al. (2014). An extracorporeal blood-cleansing device for sepsis therapy. *Nat. Med.* *20*, 1211–1216.
- Khan, K.S., Wojdyla, D., Say, L., Gülmezoglu, A.M., and Look, P.F.V. (2006). WHO analysis of causes of maternal death: a systematic review. *The Lancet* *367*, 1066–1074.
- Khvorova, A., Moore, M., Turanov, A.A., and Karumanchi, A. (2018). Oligonucleotide compounds for treatment of preeclampsia and other angiogenic disorders.
- Levine, R.J., and Karumanchi, S.A. (2005). Circulating angiogenic factors in preeclampsia. *Clin. Obstet. Gynecol.* *48*, 372–386.
- Liu, L.-C., Wang, Y.-C., Yu, M.-H., and Su, H.-Y. (2014). Major risk factors for stillbirth in different trimesters of pregnancy—A systematic review. *Taiwan. J. Obstet. Gynecol.* *53*, 141–145.
- Nafee, T.M., Farrell, W.E., Carroll, W.D., Fryer, A.A., and Ismail, K.M.K. (2008). Review article: Epigenetic control of fetal gene expression. *BJOG Int. J. Obstet. Gynaecol.* *115*, 158–168.
- Plouin, P.F., Bréart, G., Rabarison, Y., Sureau, C., Rumeau-Rouquette, C., and Ménard, J. (1982). [Incidence and fetal impact of hypertension in pregnancy: study of 2996 pregnancies]. *Arch. Mal. Coeur Vaiss.* *75 Spec No*, 5–7.

Roberts, J.M., and Cooper, D.W. (2001). Pathogenesis and genetics of pre-eclampsia. *The Lancet* 357, 53–56.

Sibiude, J., Guibourdenche, J., Dionne, M.-D., Le Ray, C., Anselem, O., Serreau, R., Goffinet, F., and Tsatsaris, V. (2012). Placental Growth Factor for the Prediction of Adverse Outcomes in Patients with Suspected Preeclampsia or Intrauterine Growth Restriction. *PLoS ONE* 7.

Thadhani, R., Kisner, T., Hagmann, H., Bossung, V., Noack, S., Schaarschmidt, W., Jank, A., Kribs, A., Cornely, O.A., Kreyssig, C., et al. (2011). Pilot study of extracorporeal removal of soluble fms-like tyrosine kinase 1 in preeclampsia. *Circulation* 124, 940–950.

Trimarchi, H. (2015). Podocyturia: What is in a name? *J. Transl. Intern. Med.* 3, 51–56.

Tsatsaris, V., Goffin, F., Munaut, C., Brichant, J.-F., Pignon, M.-R., Noel, A., Schaaps, J.-P., Cabrol, D., Frankenne, F., and Foidart, J.-M. (2003). Overexpression of the Soluble Vascular Endothelial Growth Factor Receptor in Preeclamptic Patients: Pathophysiological Consequences. *J. Clin. Endocrinol. Metab.* 88, 5555–5563.

Verlohren, S., Herraiz, I., Lapaire, O., Schlembach, D., Moertl, M., Zeisler, H., Calda, P., Holzgreve, W., Galindo, A., Engels, T., et al. (2012). The sFlt-1/PlGF ratio in different types of hypertensive pregnancy disorders and its prognostic potential in preeclamptic patients. *Am. J. Obstet. Gynecol.* 206, 58.e1-58.e8.

Walker, J.J. (2000). Pre-eclampsia. *The Lancet* 356, 1260–1265.

## Chapter 7

# Extraction, preconcentration and detection of proteic biomarker by immunoassay in continuous flow

### 1. Introduction

Biological marker (biomarker) can be defined as an entity '*that is objectively measured and evaluated as an indicator of normal biological processes, pathogenic processes, or pharmacologic responses to a therapeutic intervention*' (Biomarkers Definitions Working Group., 2001) or as '*any substance, structure or process that can be measured in the body or its products and influence or predict the incidence of outcome or disease*' (World Health Organization, 2001). Biomarker analysis is used as a noninvasive diagnostic tool for diseases and anomalies. It is also a clinical tool to follow the progression of a disease, but also the effects of the interventions (surgery), drugs and treatments. Biomarkers provide guidance for new medicines. They also provide information on the molecular and cellular mechanisms involved in diseases.

The increase of interest on biomarkers has been followed by the development of screening technologies such as combinatorial chemistry, mass spectrometry and high throughput screening and different micro-assays. The global biomarkers market is supposed to reach \$53.34 billion in 2021 from \$ 27.95 billion in 2016 (MarketsandMarkets, 2017).



Among the different biomarkers (cellular, molecular, vesicular), proteins have already demonstrated their potential; in particular protein concentrations are significantly affected by pathologies. For instance, among the numerous protein biomarkers, cytokines are used as indicators for disease progression (Mack, 2007) such as tumor progression (Yamazaki et al., 2017), liver diseases (Deng et al., 2015; Tilg et al., 1992), hepatic inflammations and fibrosis (Neuman et al., 2007). They are glycoproteins from organisms that can be synthesized by several immune-cells and can regulate the immune response to face an infection. Monitoring cytokines is thus significant for a wide range of diseases. However, cytokines detection by immunoassay is usually challenging due to very low concentration in biological samples (Ridker et al., 2000).

In this context, a large range of immunoassays have been developed such as ELISA methods (Enzyme-Linked Immunosorbent Assay) which have a huge impact on quantitative determination of proteins in clinical biotechnology (Ekins, 1999). Immunoassays are fast, sensitive, selective and cost effective methods to detect and quantify protein in different media. They rely on antibody-antigen interaction providing high specificity to the bioassay. In case of the addition of a secondary antibody conjugated with an enzyme, the method is named ELISA sandwich. This method has been widely adapted in microfluidic (Fichorova et al., 2008; Mirasoli et al., 2014; Novo et al., 2011). Microfluidics is indeed an interesting tool for immunoassays. It allows to work at low cost, with small amount of reagents in a system at micro-scale. Miniaturization and integration offer a unique opportunity to decrease the time of analysis and the limits of detection. Immunoassay on chip has first been designed as miniaturization of conventional microtiter plate ELISA, the antibody being functionalized on the surface of the microchannel. To further improve the specific surface of interaction, solid supports have thus been inserted in the microdevices starting with mechanical trapping of micrometric polystyrene beads functionalized with antibody (Sato et al., 2000). Based on these first encouraging approaches, many other strategies have been proposed that could be based for instance, on electrokinetics or magnetism (Augustin et al., 2007; Mirasoli et al., 2014). For example, ELISA on chip for bacterial detection has shown a great improvement using microfluidics channel as support. Li et al. evaluated a limit of detection of 10-100 CFU/mL with a total procedure of 2h (Li and Su, 2005) whereas the conventional method of plating can reach 5 days for this limit of detection and even PCR-based techniques have difficulties to go below 6h. Microfluidics also makes the automation easier and the portability of the device reachable.

Among the miniaturized immunoassay, two technologies based on microfluidics have emerged as leaders on the technological advances: Quanterix's SiMoA and DLISA.

Thus, Quanterix 's SiMoA (Single Molecule Array) is a digital ELISA-based immunoassay dedicated to proteins detection in samples such as blood, plasma, serum (Heiden, 2017). This system is already available on the market. The ELISA process is made following a digital protocol. Samples are mixed with subpopulation of encoded capture beads, with specific antibodies grafted on the surface. The antigens are specifically captured on the surface of beads and a second antibody, coupled to an enzyme, is used to build a sandwich (Figure 91). The whole complex is loaded in the Simoa disc of 120 mm diameter with more than 5 billions of microwells, each of the size of a bead and a volume of 50 femtoliters (Kan et al., 2012). Beads enter the microwells by gravity and the excess is removed. Each well is filled with the fluorogenic substrate of the enzyme, and sealed using fluorocarbon oil. Fluorescence images are acquired to determine the fraction of wells associated with enzyme activity. The system of imaging and analysis has been progressively improved over the years. Its multiplexing ability has also been demonstrated. (Rissin et al., 2013) As the antigen capture is performed on the magnetic beads, this approach can be adapted for complex matrices easily and the capture support is movable (no clogging issue). They demonstrate a dynamic range of detection for Interleukine 6 (Il6) from 0.006 to 100 pg/mL (Pleil et al., 2015). Thus, the analysis time of each experiment is 6 hours (Rissin et al., 2010).

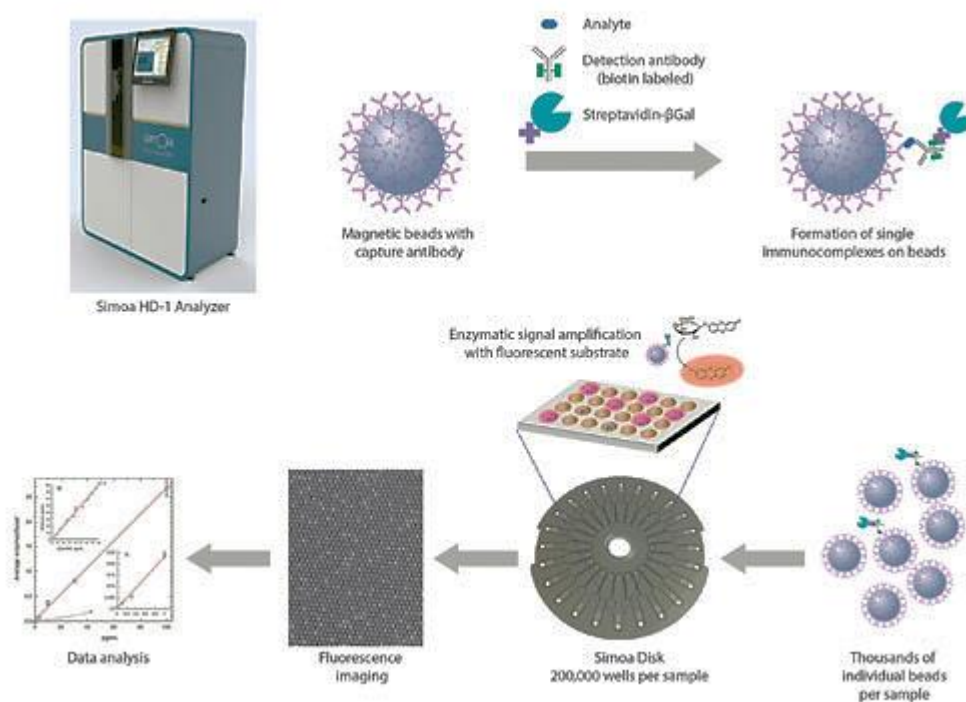


**Figure 91** The Quanterix Simoa HD-1 Analyzer has a workflow in which single protein molecules are captured and labeled on beads using standard ELISA reagents. Individual beads are isolated in femtoliter-sized wells, and single enzyme-labeled proteins on these beads are detected by fluorescence imaging. Only a fraction of the beads possess catalytic enzyme activity. The concentration of protein in bulk solution is correlated to the percentage of beads that carry a protein molecule (Heiden, 2017)

A second example of immunoassay relying on a sandwich ELISA is the system named DLISA (Hu et al., 2015). To improve the sensibility in comparison with standard ELISA system, the secondary antibody is conjugated with nanoparticles and the detection is based on 1) a combination of a cation exchange reaction (CX reaction) and 2) a catalytic and molecular beacon system (CAMB) as explained in Figure 92. Antigens are captured on a 96-well plate. A second ZnS-conjugated antibody is added and  $Zn^{2+}$  ions are released using an  $Ag^+$ -induced CX reaction. The fluorescence is due to the cleavage of a molecular beacon, triggered by a  $Zn^{2+}$ -dependent DNAzyme. This method frees itself from protein modification, which can be a sensitive issue for stability of the process. This system can be adapted to multiplexing as shown in the Figure 92.

The combination of those methods allows the usual limit of detection to go below (LOD). In the study of Hu et al (Hu et al., 2015) they reached a LOD of 2 fg/mL for human IgG detection in a PBS buffer with 5% BSA. It means that they are able to detect as few as 1800

molecules (human IgG and prostate specific antigen) in 100  $\mu\text{L}$  of sample. It is compatible with a complex matrix such as human serum, with an increase of the LOD of 10 times.

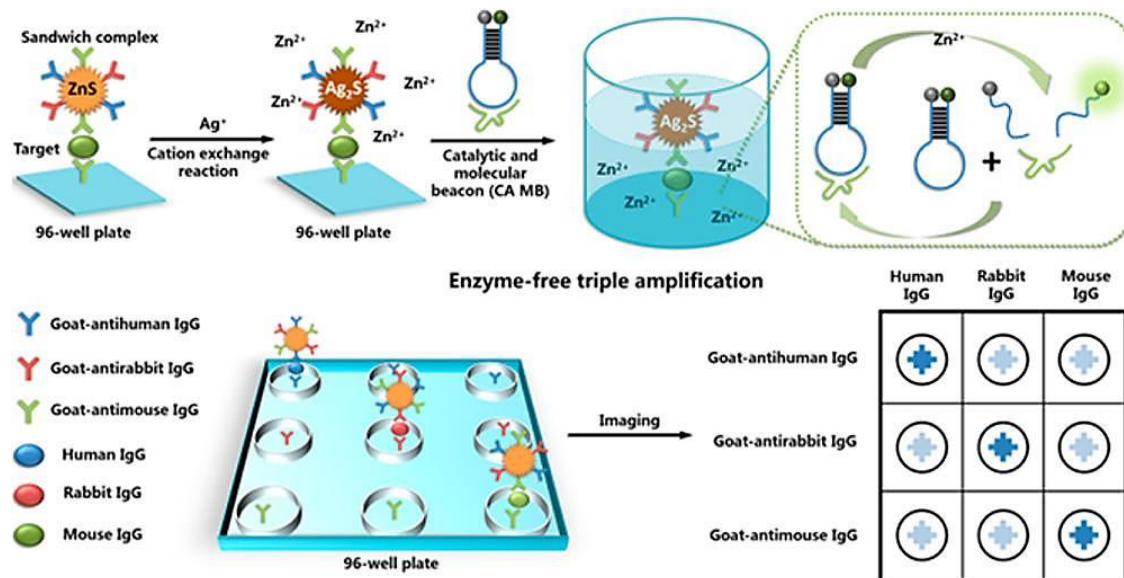


**Figure 92** Schematic illustration of the DLISA strategy. A DNzyme-based ELISA, termed DLISA, was developed for ELISA detection. After CX reaction, DNzyme with a molecular beacon (CMB) allowed to multiple enzymatic turnovers in the presence of  $\text{Zn}^{2+}$  (Hu et al., 2015)

The above mentioned technologies show that working with small volumes can bring shorter time of analysis, higher sensitivity, possibility of multiplexing and reduction of size, of costs and of sample / reagents volumes. However, several issues are not already solved. For instance, the latter approach induces an increase of heat during the CX reaction that can't be controlled and could damage the sample. More importantly, the analysis time is around 24h. An overnight incubation was needed to coat the walls of the 96-well plate. Another overnight incubation was required for the capture of the target by the primary antibody. This is exactly the step that a capture in fluidized bed could improve.

Not mentioned earlier is also the nonspecific adsorption on PDMS-based micro-channels (Butler et al., 1997). That's why surface treatments were developed as strategies to avoid nonspecific adsorption of biomolecules on the surface of microchannels (Eteshola and Leckband, 2001). Our team developed a surface treatment (PDMA-AGE as described previously) to avoid those nonspecific adsorptions (Poitevin et al., 2009). It allows us to adapt immunoassays in PDMS devices.

As demonstrated in this manuscript, microfluidic magnetic fluidized beds can be used to extract and pre-concentrate molecules of interest in a complex matrix. In this chapter, we

aim to demonstrate how the system can be also used for protein detection. An integration of a complete ELISA from capture to detection within the fluidized bed will be performed. Bruno Teste et al. already demonstrated that the kinetics of target analyte capture is improved by working with micro-magnetic beads compared to standard microtiter plates (Teste et al., 2011a, 2011b).

Our demonstration will focus on the capture of the interleukin 6 (IL-6). It is a multifunctional protein of 26 kDa involved in responses of the human immune system to infection and cellular injury. IL-6 is secreted by T cells and macrophages into the serum in case of acute and chronic inflammation to stimulate an immune response. It is also involved in the fight against infection.

A first antibody (monoclonal anti-Human IL-6) was coated on magnetic beads to capture IL-6. A detection antibody (anti-human IL-6 biotin) conjugated with an enzyme Alkaline Phosphatase by a streptavidin – biotin bonding (Bayer and Wilchek, 1990) was used to form a sandwich complex. Detection was performed by the reaction of the enzyme with a fluorogenic substrate.

Our ambition was also to benefit from the automation capabilities of the process and from the high efficiency of the fluidized bed system to perform the capture of antibodies with a high selectivity and in short time (~2h).

## **2. Materials and methods**

### **Reagents and chemicals**

The washing buffer was prepared with Tris HCl (200mM, Sigma Aldrich), Bovine Serum Albumine “BSA” (1%, Sigma Aldrich) and Tween 20 (0.1%, Sigma Aldrich). The pH was adjusted at 7.5. The washing buffer was stored at -4°C.

The substrate MUP (Methylumbelliferyl phosphate, Thermofischer Scientific) used for the enzymatic reaction was dissolved in the washing buffer at 10 mM, pH adjusted at 8.0. The substrate was kept at -20°C.

Tosylactivated beads (Dynabeads™ M-280 Tosylactivated, Thermofisher Scientific) were grafted as described on the Dynabeads datasheet with anti-IL6 human antibodies (Thermofischer Scientific). They were shaken and incubated with anti-IL6 antibodies, Tris

buffer and ammonium sulfate (3M) at 37°C for 18 hours. Then, the beads were washed and resuspended in PBS with BSA 0.1% at a final concentration of 5 mg/mL.

### Chip fabrication

Microfluidic chips were designed based on micro-milled molds. These molds were machined in brass piece of 5cm x 5cm. The designs were a positive replica of the chip. The chips were fabricated by pouring polydimethylsiloxane (PDMS, Sylgard184, Dow Corning) on the molds, and were bonded to a PDMS cover of 4 mm by oxygen plasma (O<sub>2</sub>, 40 mbar, 30 sec, 200W). A surface treatment of PDMA-AGE 0.5% was incubated inside the chip chamber for 2 hours then rinsed with distilled water and dried with compressed air.

### Microfluidic Setup

The liquid flow was controlled by a pressure controller connected to the sample reservoir (MFCS™, Fluigent). The outlet of the chip was connected to a flowrate controller (Flowunit S, Fluigent), which allowed precise flowrate measurement and feedback control on the pressure based on the Maesflo software (Fluigent). Peek tubing (Tube Peek 1/32"x0.25mm, Cil Cluzeau Info Labo) were used to connect the microfluidic chip to the other elements of the experimental setup. The resistance (12 cm PEEK tubing of 0.063 mm diameter) was positioned at the entrance of the chip. A NdFeB 1.47T (N52, size 20mm x 20mm x 30mm, magnetization direction through the thickness, by ChenYang technologies) permanent magnet was aligned with the chamber axis at a 1.5mm distance from the chip inlet.

### Operating process

Manual batchwise in-solution labeling ELISA: The sample (50µL) and the detection antibodies (50µL, 0.5µg/mL) were incubated off chip at room temperature for 50 min. This mix (50µL) was flowed inside the chip chamber at a 1 µL/min flowrate. The beads were then rinsed with the washing buffer for 30 minutes at 2µL/min inside the chip.

Sequential injection in continuous mode ELISA: The sample (50µL) was flown inside the chip chamber at 1 µL/min then the detection antibodies (50µL, 0.5 µg/mL, Tris HCl 200 mM buffer) were injected at 1 µL/min. The beads were rinsed with the washing buffer for 30 minutes at 2µL/min within the chip.

Specific experiment: experiment where the sample was a solution of antigens at a given concentration

Non-specific experiment: experiments where the sample used was a solution of buffer instead of antigens

All experiments were performed at room temperature.

### Fluorescence detection

“Stop and go” reading operating process: the chamber was filled with 0.7  $\mu\text{L}$  of MUP substrate at 10 mM at a flowrate of 400 nL/min. This step was followed by a 10-min incubation at zero flow rate. The fluorescence signal was acquired while 6 $\mu\text{L}$  of buffer Tris HCl 200 mM pH 7.5 BSA at 1% and Tween 20 at 0.1% (all percentages are weight/volume) was flown through the beads at 1  $\mu\text{L}/\text{min}$ . The signal was read on the output channel by fluorescence (Mercury lamp Nikon intensilight C-HGFIE, FITC filter)

Continuous inflow reading process: The signal was acquired as 6 $\mu\text{L}$  of MUP at 10 mM was flown through the beads bed at 1  $\mu\text{L}/\text{min}$  using the same fluorescence measurement method as described above.

## 3. Optimization of the support

As previously mentioned, the ELISA immunoassay first relies on the specific interaction between a molecule of interest and a specific capture antibody (antigen/antibody interaction). In the fluidized bed, the support of the immune-capture is the surface of the magnetic beads used to create the fluidized bed. Microbeads increase the probability of interactions by increasing the surface to volume ratio as compared to a straight microchannel.

During the development of the fluidized bed technology, a first proof of concept of the extraction of biomolecules in the dynamic matrix of beads had been performed. This proof of concept was performed with 2.8  $\mu\text{m}$  Dynabeads grafted with antibody targeting a model biomolecule fluorescent IgG with an efficiency of capture of 60% (Tabnaoui, 2012). S. Tabnaoui investigated the possibility to work at different flowrates, from 0.5 to 2  $\mu\text{L}/\text{min}$  with large volumes of sample, up to 200  $\mu\text{L}$ . We will investigate here the possibility to perform a complete ELISA immunoassay, from capture to detection directly in the fluidized bed.

## a) Optimization of the immune-capture support functionalization

The support of the immunoassay presented in this chapter is the magnetic beads. As discussed earlier, micro-fluidized beds use magnetic beads with diameter ranging from 1 to 5  $\mu\text{m}$ . The surface of those beads has first to be functionalized by grafting the capture antibody.; To do so, different approaches can be considered. To functionalize the antibody on the surface of magnetic beads, many protocols exist depending on the initial beads functionalization (amino group, carboxylic acid, streptavidin, protein A...) (Arshady, 1991; Li et al., 2005; Mirasoli et al., 2014; Nilsson et al., 2009; Rödiger et al., 2014). Based on other studies performed in the team (Mai et al., 2015a), we decided to compare two types of beads both based on covalently antibody bond using either tosyl-activated surface or carboxylic acid modified surfaces.

On one hand, the grafting of protein on tosyl-activated beads takes place as described below in the materials and method section. On the other hand, COOH beads carbodiimide-based functionalization has been widely used in microfluidics (Figure 3) (Conde et al., 2014; Gilles et al., 1990; Nakajima and Ikada, 1995; Sehgal and Vijay, 1994; SzajANI et al., 1991) and is represented in Figure 93 (Al-Warhi et al., 2012).

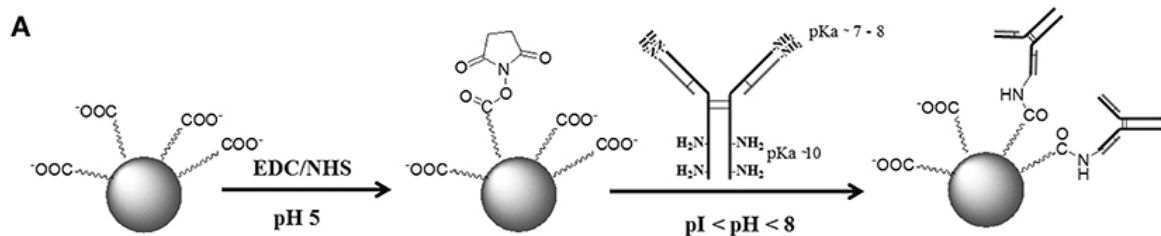


**Figure 93 Mechanism of peptide bond formation through carbodiimide (Conde et al., 2014)**

The two protocols for bead grafting are described in the materials and methods. They have been first compared in batch, outside from the microfluidic system. Capacity of grafting was evaluated as 20  $\mu\text{g}$  of antibody per mg of beads for the tosyl-activated beads, and to 4  $\mu\text{g}$  of antibody per mg of beads for the MyOne Carboxylic beads. For both types of beads, the antibody grafting is performed in a non-oriented way.

To characterize the different beads functionalization, both specific (experiment with a solution of antigens) and non-specific (experiments with a solution of buffer instead of antigens) signals were acquired (Table 5). With the tosyl-activated Dynabeads® a higher specific signal was obtained compared with the one achieved with the MyOne Carboxylic



Dynabeads™. Moreover, the low non-specific signal obtained with the tosyl-beads allowed reaching the best specific to nonspecific signal. Both signals had to be compared to reach the best signal to noise ratio. Therefore, for the following experiments, we selected tosyl-activated Dynabeads™ as solid phase.

**Table 5 Specific and nonspecific signal as function of the beads used for the experiment**

Beads used	Specific signal (u.a.)	Nonspecific signal (u.a.)
Tosyl-activated Dynabeads™	5797	375
MyOne Carboxylic Dynabeads™	2279	1003

Those tests were performed in a Tris HCl buffer at 200 mM. The composition of the buffer was optimized in a second part.

#### **b) Optimization of the buffer composition**

The buffer solution was not only used to prepare the solutions needed for the experiment, but also to prepare the beads suspension, to fill the chip and the tubing prior the beginning of the experiment, and finally to wash the system right after the capture. Risks of non-specific adsorption and contamination had to be examined along the entire fluidic pathway as well as on the surface of the beads. We have thus investigated how the nature of the buffer can affect and limit the nonspecific adsorption.

Several buffer compositions, NaHCO<sub>3</sub> (pH=8, 100mM), Tris EDTA (pH=8, 100mM), Tris HCl (pH=8, 200 mM), and PBS (pH=7, 150mM), have been considered. To evaluate their effect on the fluidized bed-based ELISA test, we have measured the nonspecific signal achieved using these different buffers. Tris HCl buffer was selected as it presented the lowest non-specific signal (data not shown).

The influence of BSA and Tween 20 as additives in the buffer has also been evaluated (Table 6). BSA is a hydrophobic protein that acts as a passivation agent limiting the protein adsorption on the surface of the chip and of the beads. The Tween 20, a nonionic surfactant, is expected to limit beads aggregation and beads interaction with the surface of the chip.

Our results (Table 2) confirmed the necessity to have both BSA and tween in solution. A final concentration of 1% and 0.1% (w/v) has been selected.

**Table 6 Nonspecific signal as function of composition of the buffer**

Buffer (% w/v)	Nonspecific signal (u.a.)
Tris HCl 200 mM pH 8 BSA 1% TWEEN 0.1%	375
Tris HCl 200 mM pH 8 BSA 0.5% TWEEN 0.1%	404
Tris HCl 200 mM pH 8 BSA 0.5% TWEEN 0.05%	706
Tris HCl 200 mM pH 8 BSA 0.1% TWEEN 0.1%	397
Tris HCl 200 mM pH 8 BSA 0% TWEEN 0%	537

Besides, the pH is also an important parameter as ELISA tests rely on hydrogen bond, Van Der Waals or dipolar interactions. A range of pH close to the physiological pH has been evaluated regarding its effect on nonspecific signal (Table 7). The lowest non-specific signal was achieved at pH 7.5, indicator of a higher specificity. We decided to set the buffer solution at Tris HCl at 200 mM pH 7.5 BSA at 1% and Tween 20 at 0.1% as it optimized the ratio signal to noise.

**Table 7 Influence of the pH on the nonspecific signal**

pH of the solution	Nonspecific signal (u.a.)
pH 8.5	350
pH 8	315
pH 7.5	210

#### **4. Two methods of operation: manual in-tube labeling versus sequential injection**

A recent paper by Tai et al. (Mai et al., 2015b) has demonstrated the possibility to perform immunocapture on chip in two modes: manual in-tube labeling and sequential injection. In order to determine the most efficient way to perform the fluidized bed-based immunoassay, these two processes have been compared in our setting. In the manual in-tube labeling mode, the sample and the secondary antibody were pre-incubated in tube before being flowed inside the chip chamber for the capture (to create directly the sandwich during the immunocapture) while in the sequential mode all the reagents were injected one by one directly on chip following the conventional ELISA sequence (sample/buffer/secondary antibody...).

In the case of the manual in-tube labeling, the sample, detection antibody and the enzyme were incubated together prior to their on-chip injection (Figure 94 A and B). The enzyme (Alkaline Phosphatase) was conjugated with the detection antibody thanks to an interaction streptavidin/biotin simultaneously the complex IL-6/antibody formation in solution. This incubation step was performed at room temperature with continuous shaking (Thermomixer® C, eppendorf) for 50 minutes. The solution that contains the immuno-complex was then injected in the fluidized bed to be captured on the magnetic beads (Figure 94 C). After a washing step to remove the excess of detection antibody and enzyme, the enzymatic substrate was injected in the bed to perform the detection step.

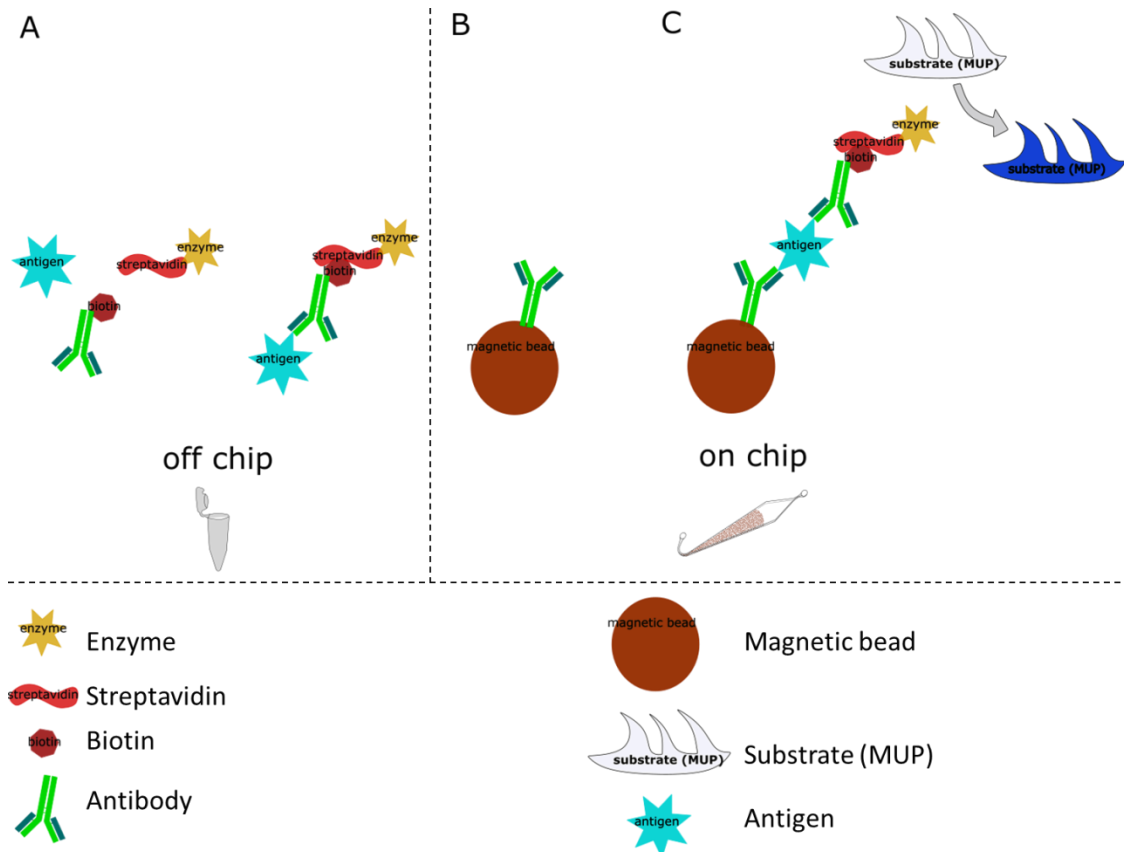


**Figure 94** Protocol of sequential mode with ligation of the antigen, the secondary antibody and the enzyme off chip (A and B) then the sample is flown through the matrix of magnetic beads and the complex is captured on the surface of beads (B and C). When substrate is flown through the chip the enzyme uses the substrate resulting in an increase of the fluorescence signal

In the case of sequential injection, only the conjugation of the detection antibody by the enzyme was performed in tube prior to the injection on the chip (Figure 95 A). Then, as in a conventional ELISA in microtiter plate, each step was performed sequentially by injection in the fluidized bed of each ELISA solution as follows: the sample was first injected in the matrix of beads, a washing step was performed, conjugated detection antibody was injected inside the chip, a washing step was repeated, and then the enzymatic substrate was finally injected to perform the detection (Figure 95 B,C and D).

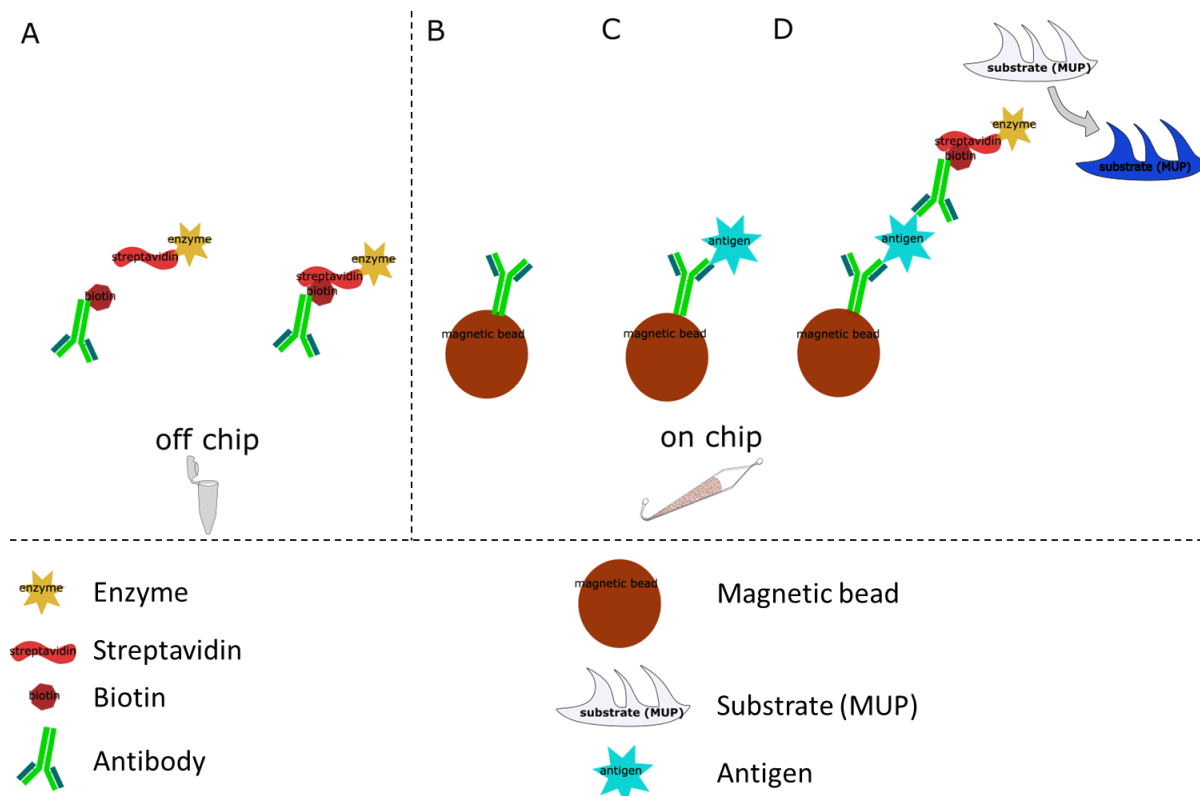


**Figure 95 Protocol of continuous mode with ligation of the secondary antibody and the enzyme off chip (A) then the sample is flown through the matrix of magnetic beads (B) and captured on the surface of beads (C). The complex formed off chip is then flown through the beads and captured too (D). When substrate is flown through the chip the enzyme reacted to create fluorescence.**

A series of preliminary experiments have been conducted to compare these two approaches in terms of sensitivity in similar conditions. Even if the ELISA by sequential injection had many advantages such as full integration, simplified automation, and low non-specific signal, the results achieved show that for a given antigen concentration a higher signal to noise ratio is achieved with manual in-tube labeling (Table 8).

**Table 8 Influence of the process of injection on the specific and nonspecific signal**

Mode of injection	Specific signal (u.a.)	Nonspecific signal (u.a.)
manual in-tube labeling	8680	187

sequential injection

4450

112

A first pre-incubation seemed to enhance the efficiency of capture of the complex antigen-detection antibody. The same results were obtained in previous studies (Mohamadi et al., 2010; Svobodova et al., 2012). Therefore, the following experiments have been performed in manual in-tube labeling mode.

### 5. Influence of the enzymatic step: “stop and go” versus “continuous in flow” processes

The detection step was performed thanks to the enzymatic reaction of the substrate: methylumbelliferoneb (7-hydroxy-4-methylcoumarin or MUP) monitored by epifluorescence microscopy (Figure 96) (Obayashi et al., 2015). In this substrate, the product of the enzymatic reaction used to detect the analyte of interest, had an excitation peak at 372 nm and an emission peak at 445 nm.

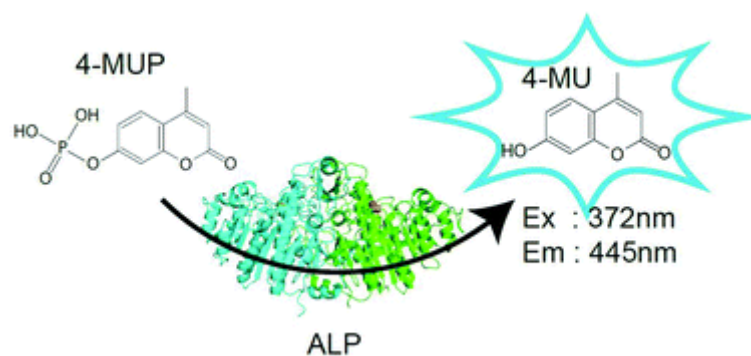


*Figure 96 Fluorogenic assay of alkaline phosphatase (ALP) which hydrolyzes 4-methylumbelliferyl phosphate (4-MUP) to 4-methylumbelliferon (4-MU) and inorganic phosphate (Obayashi et al., 2015).*

#### a) Detection protocol

Performing the enzymatic reaction inside the fluidized bed offers the possibility to consider and compare two modes of detection. Indeed, after injecting the enzymatic substrate in the bed, the fluorescent signal can be read either continuously (in flow method) or sequentially by changing the inlet pressure (stop and go method).

In the continuous in-flow detection approach, the enzymatic substrate was perfused continuously inside the chamber at  $1\mu\text{L}/\text{min}$ . The bed was, at this flow rate, in a fluidized bed regime; the enzymatic product generated at the surface of the beads was thus continuously flown through the bed to reach the detection area.

In the stop and go method, a given volume of enzymatic substrate ( $0.7\mu\text{L}$ ) was first flown through the bed at  $0.4\mu\text{L}/\text{min}$ . The substrate and the magnetic beads were thus incubated together in a packed bed regime (without any flow) for 10 min (Figure 97 A). The volume of substrate was set so that the molecules generated at the surface of the beads could not reach during the incubation the area of detection by diffusion. This incubation time had been optimized to reach a significant signal of fluorescent product (to be distinguished above the noise even at low concentration) in the shortest time possible. After 10 minutes of incubation the solution was pushed towards the area of detection by flowing at  $1\mu\text{L}/\text{min}$  the buffer solution from the inlet of the chamber. A peak of fluorescence was thus obtained (Figure 97 B). By this process, a high quantity of fluorescent product could be accumulated inside the bed of beads before reaching the detection area while switching on the flow rate. With this approach, we aimed to increase the sensibility of our method and be able to decrease the limit of detection of the system.

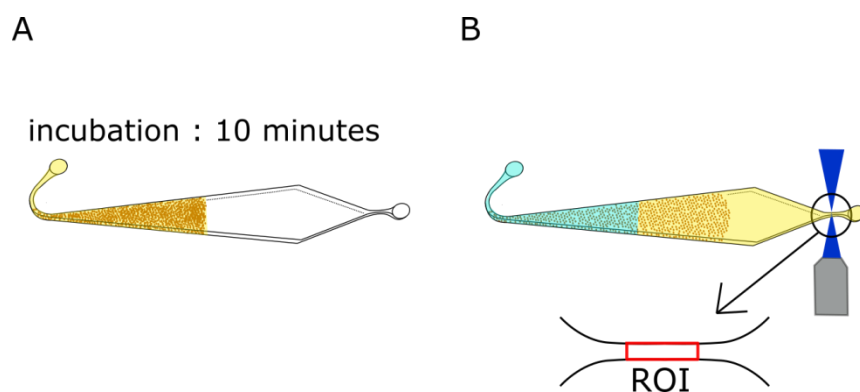


**Figure 97 Schematic of the signal visualization for an acquisition 'stop and go'. The matrix of beads is filled with the substrate solution. An incubation of ten minutes at RT is performed then the liquid is pushed by the buffer to the exit channel where the fluorescence is measured (B)**

#### **b) Signal analysis**

For both methods, the signal of fluorescence was recorded during 6 minutes. It was enough to flow 6 times the volume of the chamber through the beads, and to reach a stable signal. In

the case of a measurement in in-flow mode, the signal had the shape of an asymptotic curve (Figure 98). The value of interest was the height of the plateau ( $I_1$ ) once the stability zone had been reached. This value depended on the initial number of molecules of interest in the sample.

In the case of stop and go mode, the signal had the shape of a peak, as expected, the quantity of product obtained during the 10 minutes of incubation being a finite quantity. The value of interest could be both the height ( $I_2$ ) and the area of the peak. The height of the peak can be directly linked to highest concentration of the fluorescent product flowing in the detection area. It has the advantage of offering high values of fluorescence. The area under the curve was related by integration through time to the quantity of fluorescent product obtained during the incubation. It gives an estimation related to the full 6 min signal recording.

Both of those values are related to the physical properties of fluidization of the bed. In particular the opening of the bed after the 10 minutes of incubation is a critical step which could affect the shape and dimensions of the peak.

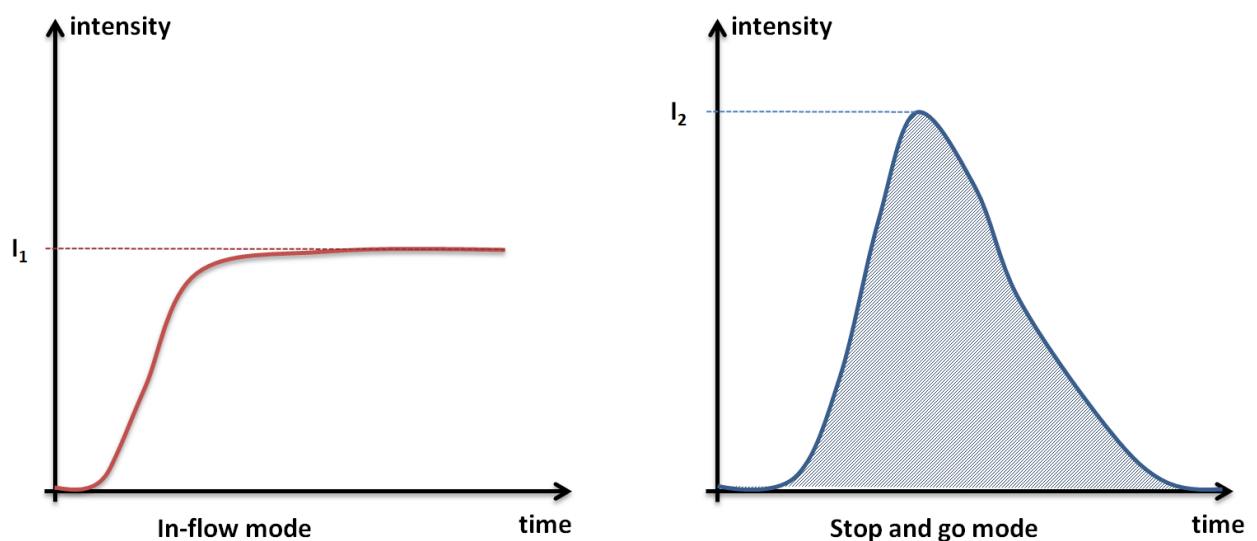


**Figure 98** Forms of the fluorescent signal recorded in in-flow and stop and go modes

As these experiments have been performed in parallel on two experimental set-ups, we have normalized the signal to avoid discrepancy due to the mercury lamp and to the optical setting. A first approximation can be done concerning the dependence of the signal to the lamp used and to optical factors of the set-up by writing the intensity of fluorescence  $I(t)$  as:

$$I(t) = k_{lamp} * N + C_{ext}$$



Equation 27

Where  $k_{lamp}$  and  $C_{ext}$  are constants related to the lamp used and to the optical factors,  $N$  is the number of excited molecules (Guiot, 2005). The constant  $C_{ext}$  can easily be evaluated for each experiment as the signal of fluorescence in absence of fluorescent molecule.

For each experiment performed with a sample at a chosen concentration, a similar experiment is simultaneously performed with a blank as a control to evaluate the nonspecific signal. Comparison and optimization are based on the value:

$$Value\ of\ interest = \frac{N_{spe} - N_{non\ spe}}{N_{non\ spe}} = \frac{(I_{spe} - C_{ext\ spe}) - (I_{non\ spe} - C_{ext\ non\ spe})}{(I_{non\ spe} - C_{ext\ non\ spe})}$$

Equation 28

Where  $I_{spe}$  and  $I_{non\ spe}$  are the specific and non-specific signal.

For each condition, the value of interest was  $\frac{N_{spe} - N_{non\ spe}}{N_{non\ spe}}$ . We worked with this expression in order to free the results from parameters linked to the lamp or the set-up. This value can thus be used to compare results of two different experiments in order to optimize the fluidized bed-based ELISA.

## 6. Evaluation of the bioassay performances

Prior to a complete evaluation of the fluidized bed-based ELISA, several parameters, such as the secondary antibody concentration, the flow rate of work and the sample volume, were first optimized.

### a) Optimization of the concentration of detection antibody on the immunoassay performances

As in conventional ELISA, we first optimized the detection antibody concentration. To detect the target molecules, this concentration needed to be comparatively high (compared to the antigen concentration). However, to maintain low costs of development and mainly to limit the non-specific signal, the detection antibody concentration had to be optimized as a compromise between sensitivity and specificity.

The detection antibody was an anti-human IL-6 biotin antibody conjugated with an Alkaline Phosphatase enzyme. The 1X concentration corresponds to an antibody concentration of 0.5 µg/mL. The results obtained with 1x detection antibody have been compared to experiments with concentrations of 5µg/mL (10X) and 25 µg/mL (50X). This choice limits the detection of IL-6 to concentrations below 0.5µg/mL, which is not an issue as the clinical range of IL-6 is below 1ng/mL (Todd et al., 2013).

As expected, the specific signal increased with the concentration of detection antibody. However for a concentration higher than 1X, the nonspecific signal was affecting the signal to noise ratio, so the value  $\frac{N_{spe} - N_{non\ spe}}{N_{non\ spe}}$  decreases with the increase of detection antibody (Figure 99).

Based on our results (Figure 99), we chose to work at a concentration of detection antibody set at 0.5 µg/mL (concentration 1X). Those first results were also used to compare in-flow method to the stop and go method. As shown on the results Figure 99, the highest signal to noise ratio for a concentration 1X was obtained with the stop and go detection mode. Between the area and the peak height, the first value presented the highest signal. We decided to work with this parameter; however the peak height was also evaluated as confirmation.

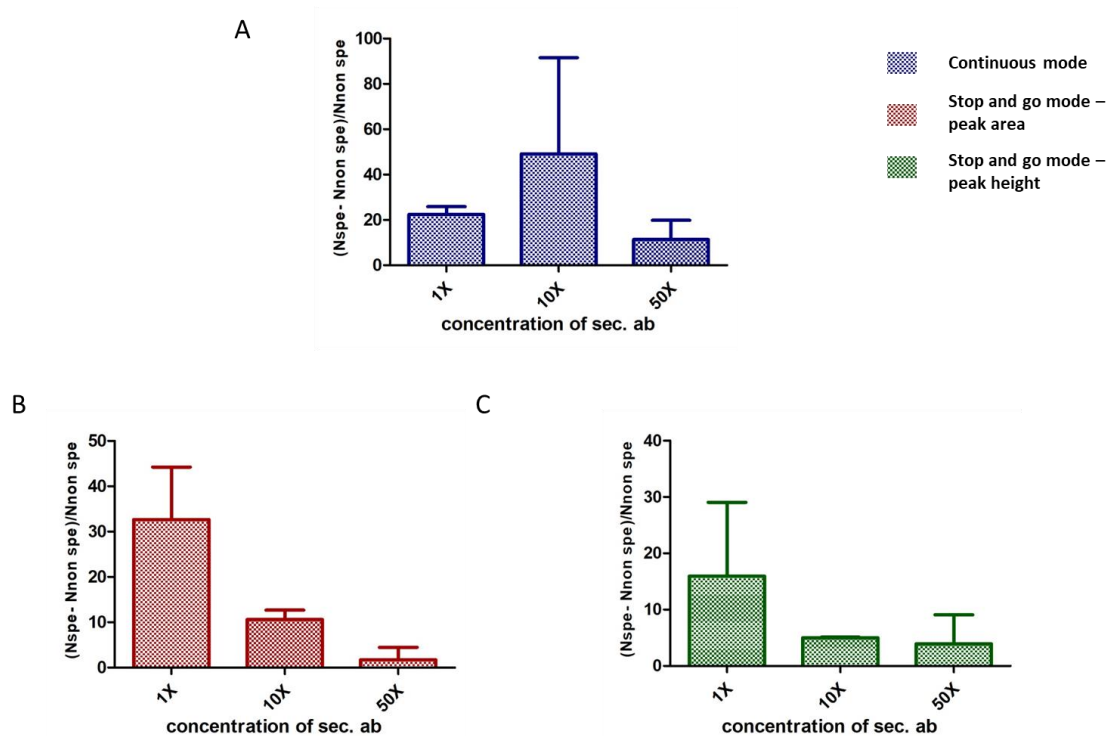


**Figure 99 Optimization of the concentration of secondary antibodies: Representation of the signal obtained for solution of 0.5 $\mu$ g/mL (1X), 5  $\mu$ g/mL (10X) and 25 $\mu$ g/mL (50X) of secondary antibodies conjugated to enzyme for continuous (A), or stop and go considering the peak area (B) or the peak height (C) for a sample of 50  $\mu$ L at 10 ng/mL**

#### b) Influence of the capture flow rate on the immunoassay performances

We investigated the impact of the flowrate of the injection of the sample on the immunoassay performances. Three flowrates of sample injection were considered: 0.5  $\mu$ L/min, 1  $\mu$ L/min and 1.5  $\mu$ L/min.

As discussed in the previous chapters, modifying the processing flow rate had a direct impact on the residence time of a target molecule inside the matrix of beads and on the bed porosity. For a flowrate of 1  $\mu$ L/min we estimated the residence time of a molecule at 6.5 seconds inside the volume of beads. The surface of the beads available for capture was estimated at 98.5  $\mu$ m<sup>2</sup>. At each instant, for a sample at 10 ng/mL, the concentration of antigens to be captured could be evaluated at 0.5 amol/ $\mu$ m<sup>2</sup> relatively to the surface of capture offered by the beads. As the grafting of the capture antibody was evaluated at 0.01 $\mu$ g/ $\mu$ m<sup>2</sup>, 0.5 amol of antigens could interact with 0.01  $\mu$ g of capture antibody.

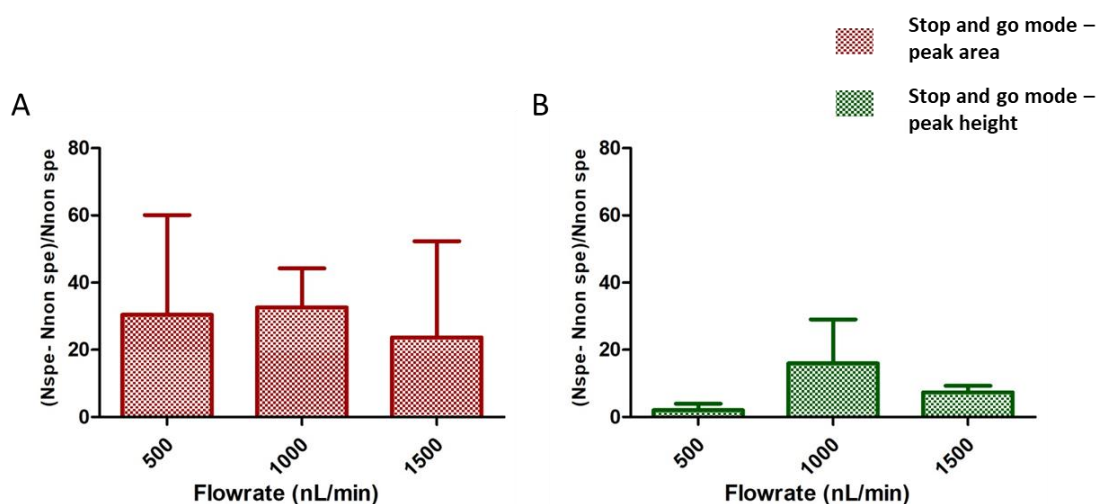


**Figure 100** Comparison of the effect of the flowrate measured at the exit of the chip: Representation of the signal obtained for a flowrate of 500, 1000 and 1500 nL/min for the peak area (A) and the peak height analysis (B) for a sample of 50  $\mu$ L at 10 ng/mL

For stop and go detection method (Figure 100 A and B), taking into account the standard deviations, there is no striking difference between the different flow rate conditions. As a compromise, we selected 1  $\mu$ L/min as flow rate of work.

### c) Influence of the volume of the sample on the immunoassay performances

Moreover, we were able to show that, as expected, the volume injected inside the system correlated with the intensity of the resulting signal at the output of the fluidized bed. Indeed, as we have been working at a fixed concentration, if we increased the volume of sample, we were supposed to increase proportionally the number of molecules captured at the surface of the beads and increase then the fluorescent signal (this before reaching the beads saturation). An increase of processed sample volume could lead to a lower limit of detection and therefore higher assay sensitivity. However, it would also increase the analysis time.

From 50  $\mu$ L to 100  $\mu$ L samples, IL6 being at 10 ng/mL concentration, the ELISA signal increased whatever the detection method used. However, no increase appeared for a sample volume of 200  $\mu$ L. New trials have to be performed at lower concentrations to investigate the possibility of saturation of the system.

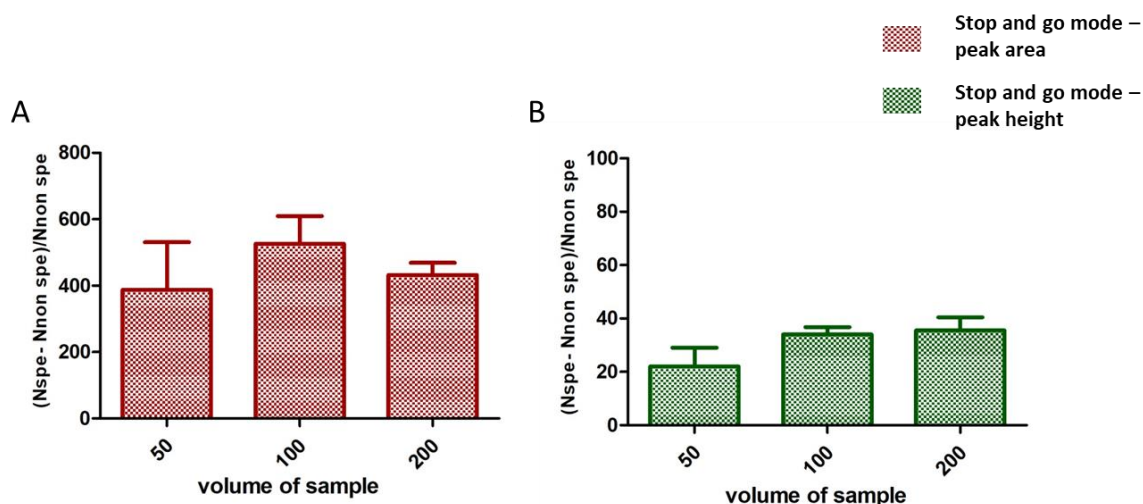


**Figure 101 Influence of the volume of the sample on the signal of detection for the peak area (A) and the peak height analysis (B) for a sample at 10 ng/mL**

#### d) Calibration curve

To highlight the detection range that can be achieved with the fluidized bed-based ELISA, we established a calibration curve. A series of experiments was performed with IL6 concentration ranging from 10 pg/mL to 10 ng/mL in Tris HCl buffer 200 mM (at pH 7.5 with BSA at 1% and Tween 20 at 0.1%) (Figure 102). The 50  $\mu$ L sample was pre-incubated with the detection antibody (0.5  $\mu$ g/mL) at room temperature for 50 min and flowed in the matrix of beads at 1  $\mu$ L/min.

Results are presented here as raw signal (in astronomical unit) with subtraction of the constant linked to external factors. The intensity is:

$$I_{conc}(t) = k_{lamp} * N_{conc}$$

Equation 29

Where  $I_{conc}(t)$  and  $N_{conc}$  are the intensity and the number of molecules relative to a chosen concentration.

The ELISA in fluidized bed was performed with IL6 concentration ranging from 10 pg/mL to 10 ng/mL. The assay range of our approach is competitive with those of devices reported in the literature (Hu et al., 2015; Pleil et al., 2015). A linearity of the signal as a function of IL6 concentration was obtained with the continuous mode of detection ( $r^2 = 0.9844$ ) as well as with the stop and go detection considering the peak area ( $r^2 = 0.9370$ ). When the detection

was based on peak height (stop and go mode), the linearity was not satisfying ( $r^2 = 0.6734$ ). We are investigating the possible . Specially, the re-opening of the bed in the case of an incubation of the substrate could lead to unreproducibility.

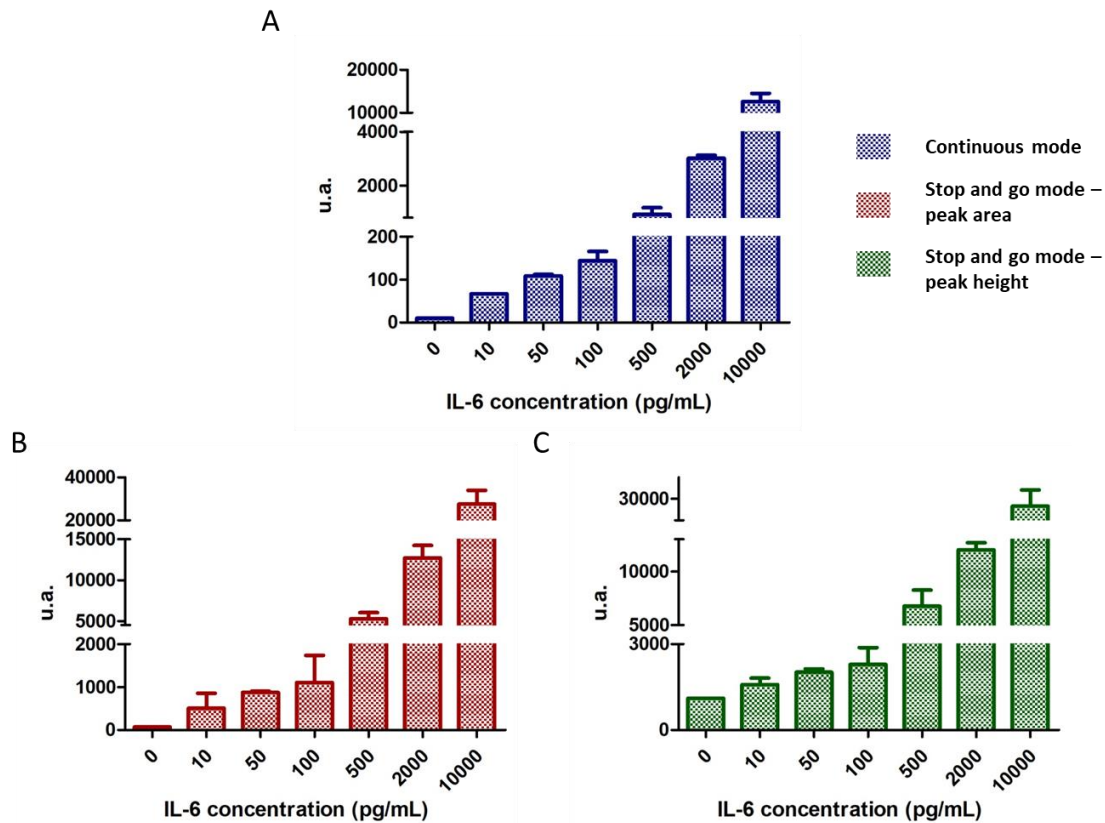


**Figure 102** Calibration curve of the fluorescent signal as function of the concentration of IL-6 (pg/mL) in the sample for continuous (A), maximum of the peak (B) and area of the peak analysis (C)

Limit of detection (LOD) and limit of quantification (LOQ) have thus been determined to further characterize our approach. As described in the literature (Thomsen et al., 2003), those limits can be evaluated as:

$$LOD = 3 h_{max} R$$

$$LOQ = 10 h_{max} R$$

Where  $h_{max}$  is the maximum of height of the noise and R is the ratio between the maximum signal of the quantity detect and the height of the signal recorded.

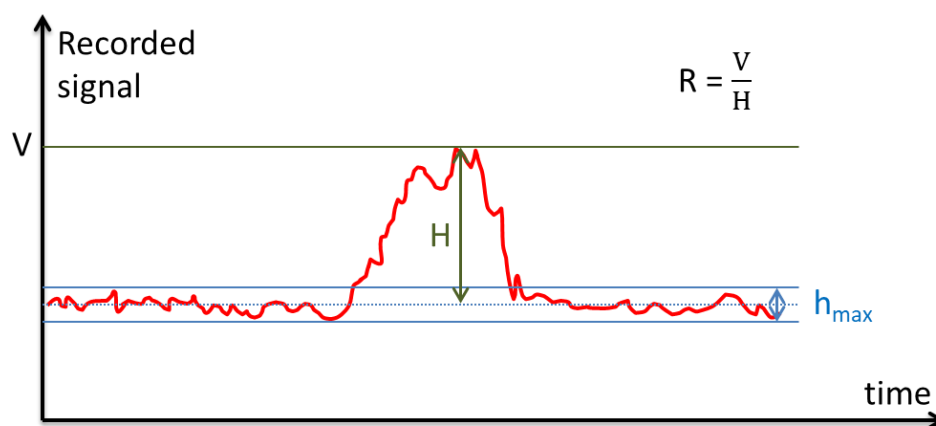


**Figure 103** Schematic representation of the constants needed to estimate the LOD and the LOQ

For the experiments previously proposed, LOD and LOQ can be estimated as:

$$LOD_{max} = 0.12 \text{ pg/mL} = 5.7 \text{ fM}$$

$$LOQ_{max} = 0.40 \text{ pg/mL} = 19 \text{ fM}$$

## 7. Perspectives

This study has focused on the development of a fluidized bed-based ELISA and it has been exemplified by detection a specific cytokine (IL-6). It has been shown that really small change of IL6 concentration can be correlated to development of disease. For example, in (Ridker et al., 2000) a change from 1.46 to 1.81 pg/mL was associated to higher risks of myocardial infarction. It means that a system able to measure at low concentration and with high precision the concentration of IL-6 could be highly useful for clinicians. Each steps of the ELISA has to be fully controlled, especially the extraction as condition of sampling, matrix and pH can affect the measure (Fichorova et al., 2008)

**Table 9 Comparison of different immunoassay for two cytokines IL-1 $\beta$  and IL-6 (<sup>a</sup>Value of the smallest dose that is not zero with 95% CI, typically calculated as the mean signal + 2 SD of the zero standard read from standard curve. <sup>b</sup>Range provided by manufacturer, if commercially available assay kit, or by testing laboratory, if in-house assay)( Fichorova et al., 2008)**

assay name	kit manufacturer	sensitivity <pg/mL <sup>a</sup>	assay range pg/mL <sup>b</sup>
<b>IL-1<math>\beta</math></b>			
BioSource ELISA	Invitrogen	1	3.9–250
Endogen EH2 ELISA	Pierce Biotechnology	1	10.24–400
Quantikine ELISA	R&D Systems	1	3.9–250
QuantiGlo ELISA	R&D Systems	0.4	0.5–5000
Beadlyte Luminex	Millipore	0.5	10–7500 <sup>d</sup>
in-house Luminex <sup>e</sup>			4.57–3333
MSD Small Spot	Meso Scale Discovery	0.1	2.44–10 000
<b>IL-6</b>			
BioSource ELISA	Invitrogen	2	19–2024 <sup>d</sup>
Endogen EH2 ELISA	Pierce Biotechnology	1	10.24–400
Quantikine ELISA	R&D Systems	0.7	3.12–300
QuantiGlo ELISA	R&D Systems	0.4	0.48–1500
Beadlyte Luminex	Millipore	1	11–8000 <sup>d</sup>
in-house Luminex			4.57–3333
MSD Small Spot	Meso Scale Discovery	0.1	0.6–2500

We put forward in this chapter a new approach of ELISA on magnetic beads. This configuration allows a full control of each step of the analysis. The limits of detection and quantification of the system are comparable to existing systems (Table 9), and the assay range is increased from 5 to 10 000 pg/mL. Compare to the SiMoA and DLISA systems (Table 10), the fluidized bed is a low cost opportunity, able to realize quick analyzes (~ 2 hours). The assay range goes from 1 to 10 000 pg/mL, with high specificity.



**Table 10 Comparison of Quanterix SiMoA DLISA and fluidized bed performances for immunoassay (in buffer solution)**

	<b>Quanterix SiMoA</b>	<b>DLISA</b>	<b>Fluidized bed</b>
<b>Cost</b>	+++	++	+
<b>Analysis time</b>	~ 6 h	~ 24 h	~ 2 h
<b>LOD</b>	< 5 pg/mL	2 fg/mL	0.12 pg/mL
<b>Assay range</b>	0.006 to 100 pg/mL	10 fg to 1 µg/mL	1 pg/mL to 10 ng/mL
<b>Specificity</b>	++	+++	++

Our system allows a dynamic detection of biomarkers, and this method can be adapted to complex matrices. However, our approach is potentially limited by the possible functionalization of magnetic beads and their efficiency. The proof of concept in serum or a complex matrix is ongoing to complete this study.

## Bibliography

Al-Warhi, T.I., Al-Hazimi, H.M.A., and El-Faham, A. (2012). Recent development in peptide coupling reagents. *J. Saudi Chem. Soc.* *16*, 97–116.

Arshady, R. (1991). Beaded polymer supports and gels: II. Physico-chemical criteria and functionalization. *J. Chromatogr. A* *586*, 199–219.

Augustin, V., Proczek, G., Dugay, J., Descroix, S., and Hennion, M.-C. (2007). Online preconcentration using monoliths in electrochromatography capillary format and microchips. *J. Sep. Sci.* *30*, 2858–2865.

Bayer, E.A., and Wilchek, M. (1990). Application of avidin—biotin technology to affinity-based separations. *J. Chromatogr. A* *510*, 3–11.

Biomarkers Definitions Working Group. (2001). Biomarkers and surrogate endpoints: preferred definitions and conceptual framework. *Clin. Pharmacol. Ther.* *69*, 89–95.

Butler, J.E., Navarro, P., and Lü, P. (1997). Comparative studies on the interaction of proteins with a polydimethylsiloxane elastomer. II. The comparative antigenicity of primary and secondarily adsorbed IgG1 and IgG2a and their non-adsorbed counterparts. *J. Mol. Recognit.* *10*, 52–62.

Conde, J., Dias, J.T., Grazú, V., Moros, M., Baptista, P.V., Fuente, D.L., and M, J. (2014). Revisiting 30 years of biofunctionalization and surface chemistry of inorganic nanoparticles for nanomedicine. *Front. Chem.* *2*.

Deng, Y.-Q., Zhao, H., Ma, A.-L., Zhou, J.-Y., Xie, S.-B., Zhang, X.-Q., Zhang, D.-Z., Xie, Q., Zhang, G., Shang, J., et al. (2015). Selected Cytokines Serve as Potential Biomarkers for Predicting Liver Inflammation and Fibrosis in Chronic Hepatitis B Patients With Normal to Mildly Elevated Aminotransferases. *Medicine (Baltimore)* *94*, e2003.

Ekins, R.P. (1999). Immunoassay, DNA Analysis, and Other Ligand Binding Assay Techniques: From Electropherograms to Multiplexed, Ultrasensitive Microarrays on a Chip. *J. Chem. Educ.* *76*, 769.

Eteshola, E., and Leckband, D. (2001). Development and characterization of an ELISA assay in PDMS microfluidic channels. *Sens. Actuators B Chem.* *72*, 129–133.

Fichorova, R.N., Richardson-Harman, N., Alfano, M., Belec, L., Carbonneil, C., Chen, S., Cosentino, L., Curtis, K., Dezzutti, C.S., Donoval, B., et al. (2008). Biological and Technical Variables Affecting Immunoassay Recovery of Cytokines from Human Serum and Simulated Vaginal Fluid: A Multicenter Study. *Anal. Chem.* *80*, 4741–4751.

Gilles, M.A., Hudson, A.Q., and Borders, C.L. (1990). Stability of water-soluble carbodiimides in aqueous solution. *Anal. Biochem.* *184*, 244–248.

Guiot, E. (2005). microscopie de fluorescence par excitation à deux photons: application à des études de corrélations et de déclin de fluorescence en milieu biologique. 215.

Heiden, L. (2017). Tumor Biomarkers Guide Immunotherapy.

Hu, R., Liu, T., Zhang, X.-B., Yang, Y., Chen, T., Wu, C., Liu, Y., Zhu, G., Huan, S., Fu, T., et al. (2015). DLISA: A DNzyme-Based ELISA for Protein Enzyme-Free Immunoassay of Multiple Analytes. *Anal. Chem.* *87*, 7746–7753.

Kan, C.W., Rivnak, A.J., Campbell, T.G., Piech, T., Rissin, D.M., Mösl, M., Peterça, A., Niederberger, H.-P., Minnehan, K.A., Patel, P.P., et al. (2012). Isolation and detection of single molecules on paramagnetic beads using sequential fluid flows in microfabricated polymer array assemblies. *Lab Chip* *12*, 977–985.

Li, Y., and Su, X.-L. (2005). Microfluidics-Based Optical Biosensing Method for Rapid Detection of Escherichia Coli O157:h7. *J. Rapid Methods Autom. Microbiol.* *14*, 96–109.

Li, Y., Cu, Y.T.H., and Luo, D. (2005). Multiplexed detection of pathogen DNA with DNA-based fluorescence nanobarcodes. *Nat. Biotechnol.* *23*, 885–889.

Mack, C.L. (2007). Serum cytokines as biomarkers of disease and clues to pathogenesis. *Hepatology* *46*, 6–8.

Mai, T.D., Pereiro, I., Hiraoui, M., Viovy, J.-L., Descroix, S., Taverna, M., and Smadja, C. (2015a). Magneto-immunocapture with on-bead fluorescent labeling of amyloid- $\beta$  peptides: towards a microfluidized-bed-based operation. *Analyst* *140*, 5891–5900.

Mai, T.D., Pereiro, I., Hiraoui, M., Viovy, J.-L., Descroix, S., Taverna, M., and Smadja, C. (2015b). Magneto-immunocapture with on-bead fluorescent labeling of amyloid- $\beta$  peptides: towards a microfluidized-bed-based operation. *Analyst* *140*, 5891–5900.

MarketsandMarkets (2017). Biomarkers Market by Product, Type & Applications - 2021 | MarketsandMarkets.

Mirasoli, M., Guardigli, M., Michelini, E., and Roda, A. (2014). Recent advancements in chemical luminescence-based lab-on-chip and microfluidic platforms for bioanalysis. *J. Pharm. Biomed. Anal.* *87*, 36–52.

Mohamadi, M.R., Svobodova, Z., Verpillot, R., Esselmann, H., Wiltfang, J., Otto, M., Taverna, M., Bilkova, Z., and Viovy, J.-L. (2010). Microchip Electrophoresis Profiling of A $\beta$  Peptides in the Cerebrospinal Fluid of Patients with Alzheimer's Disease. *Anal. Chem.* *82*, 7611–7617.

Nakajima, N., and Ikada, Y. (1995). Mechanism of Amide Formation by Carbodiimide for Bioconjugation in Aqueous Media. *Bioconjug. Chem.* *6*, 123–130.

Neuman, M.G., Benhamou, J.-P., Marcellin, P., Valla, D., Malkiewicz, I.M., Katz, G.G., Trepo, C., Bourliere, M., Cameron, R.G., Cohen, L., et al. (2007). Cytokine—chemokine and apoptotic signatures in patients with hepatitis C. *Transl. Res.* *149*, 126–136.

Nilsson, J., Evander, M., Hammarström, B., and Laurell, T. (2009). Review of cell and particle trapping in microfluidic systems. *Anal. Chim. Acta* *649*, 141–157.

Novo, P., Prazeres, D.M.F., Chu, V., and Conde, J.P. (2011). Microspot-based ELISA in microfluidics: chemiluminescence and colorimetry detection using integrated thin-film hydrogenated amorphous silicon photodiodes. *Lab. Chip* *11*, 4063–4071.

Obayashi, Y., Iino, R., and Noji, H. (2015). A single-molecule digital enzyme assay using alkaline phosphatase with a coumarin-based fluorogenic substrate. *Analyst* *140*, 5065–5073.

Pleil, J.D., Angrish, M.M., and Madden, M.C. (2015). Immunochemistry for high-throughput screening of human exhaled breath condensate (EBC) media: implementation of automated quanterix SIMOA instrumentation. *J. Breath Res.* *9*, 047108.

Poitevin, M., Shakalisava, Y., Miserere, S., Peltre, G., Viovy, J.-L., and Descroix, S. (2009). Evaluation of microchip material and surface treatment options for IEF of allergenic milk proteins on microchips. *Electrophoresis* *30*, 4256–4263.

Ridker, P.M., Rifai, N., Stampfer, M.J., and Hennekens, C.H. (2000). Plasma Concentration of Interleukin-6 and the Risk of Future Myocardial Infarction Among Apparently Healthy Men. *Circulation* *101*, 1767–1772.

Rissin, D.M., Kan, C.W., Campbell, T.G., Howes, S.C., Fournier, D.R., Song, L., Piech, T., Patel, P.P., Chang, L., Rivnak, A.J., et al. (2010). Single-Molecule enzyme-linked immunosorbent assay detects serum proteins at subfemtomolar concentrations. *Nat. Biotechnol.* *28*, 595–599.

Rissin, D.M., Fournier, D.R., Piech, T., Kan, C.W., Campbell, T.G., Song, L., Chang, L., Rivnak, A.J., Patel, P.P., Provuncher, G.K., et al. (2011). Simultaneous Detection of Single Molecules and Singulated Ensembles of Molecules Enables Immunoassays with Broad Dynamic Range. *Anal. Chem.* *83*, 2279–2285.

Rissin, D.M., Kan, C.W., Song, L., Rivnak, A.J., Fishburn, M.W., Shao, Q., Piech, T., Ferrell, E.P., Meyer, R.E., Campbell, T.G., et al. (2013). Multiplexed single molecule immunoassays. *Lab. Chip* *13*, 2902.

Rödiger, S., Liebsch, C., Schmidt, C., Lehmann, W., Resch-Genger, U., Schedler, U., and Schierack, P. (2014). Nucleic acid detection based on the use of microbeads: a review. *Microchim. Acta* *181*, 1151–1168.

Sato, K., Tokeshi, M., Odake, T., Kimura, H., Ooi, T., Nakao, M., and Kitamori, T. (2000). Integration of an Immunosorbent Assay System: Analysis of Secretory Human Immunoglobulin A on Polystyrene Beads in a Microchip. *Anal. Chem.* *72*, 1144–1147.

Sehgal, D., and Vijay, I.K. (1994). A Method for the High Efficiency of Water-Soluble Carbodiimide-Mediated Amidation. *Anal. Biochem.* *218*, 87–91.

Svobodova, Z., Reza Mohamadi, M., Jankovicova, B., Esselmann, H., Verpillot, R., Otto, M., Taverna, M., Wiltfang, J., Viovy, J.-L., and Bilkova, Z. (2012). Development of a magnetic immunosorbent for on-chip preconcentration of amyloid  $\beta$  isoforms: Representatives of Alzheimer's disease biomarkers. *Biomicrofluidics* *6*, 024126.

SzajANI, B., Südi, P., KlamAR, G., JÀszay, Z.M., PetnehÀzy, I., and TÓke, L. (1991). Effects of carbodiimide structure on the immobilization of enzymes. *Appl. Biochem. Biotechnol.* *30*, 225.

Tabnaoui, S. (2012). Magnetic fluidized bed for sample preconcentration and immunoextraction in microfluidic systems (Paris 6).

Teste, B., Kanoufi, F., Descroix, S., Poncet, P., Georgelin, T., Siaugue, J.-M., Petr, J., Varenne, A., and Hennion, M.-C. (2011a). Kinetic analyses and performance of a colloidal magnetic

nanoparticle based immunoassay dedicated to allergy diagnosis. *Anal. Bioanal. Chem.* *400*, 3395–3407.

Teste, B., Malloggi, F., Siaugue, J.-M., Varenne, A., Kanoufi, F., and Descroix, S. (2011b). Microchip integrating magnetic nanoparticles for allergy diagnosis. *Lab. Chip* *11*, 4207–4213.

Thomsen, V., Schatzlein, D., and Mercurio, D. (2003). *Limits of Detection in Spectroscopy*. 3.

Tilg, H., Wilmer, A., Vogel, W., Herold, M., Nölchen, B., Judmaier, G., and Huber, C. (1992). Serum levels of cytokines in chronic liver diseases. *Gastroenterology* *103*, 264–274.

Todd, J., Simpson, P., Estis, J., Torres, V., and Wub, A.H.B. (2013). Reference range and short- and long-term biological variation of interleukin (IL)-6, IL-17A and tissue necrosis factor-alpha using high sensitivity assays. *Cytokine* *64*, 660–665.

World Health Organization (2001). *Biomarkers In Risk Assessment: Validity And Validation (EHC 222, 2001)*.

Yamazaki, N., Kiyohara, Y., Uhara, H., Iizuka, H., Uehara, J., Otsuka, F., Fujisawa, Y., Takenouchi, T., Isei, T., Iwatsuki, K., et al. (2017). Cytokine biomarkers to predict antitumor responses to nivolumab suggested in a phase 2 study for advanced melanoma. *Cancer Sci.* *108*, 1022–1031.



---

## Conclusion

Fluidization of particles has been intensively used in industry to enhance reactions based on contact between a solid surface and a fluid. This concept is ingenious as the contact is enhanced by the suspension of the particles inside the solution. Fluidized bed approaches can bypass clogging issues while the solid phase is continuously recirculating and high flow rate can be applied thanks to the low backpressure generated. This system has been recently adapted to microfluidics by working with magnetic particles actuated by permanent magnet. Its efficiency as a solid phase extraction system was shown for the capture of fluorescent immunoglobulin G (IgG). Despite very promising results, this device is still limited in flow rate (1  $\mu\text{L}/\text{min}$ ). To overcome these limitations and to make this technology suitable for trace analysis, larger samples volumes have to be analyzed to detect lower concentrations of biomarkers in a reasonable time scale.

This PhD work presents an approach of the microfluidic magnetic fluidized bed able to accommodate high flow rates (up to 15  $\mu\text{L}/\text{min}$ ). A new module has been developed by scaling up the size of the main chamber. It allowed to increase the flow rate and the amount of beads involved in the extraction. In order to reach a good homogeneity of beads inside the microfluidic chamber, a vibration motor and a bimodal support have proved their efficiency and enabled the system to reach higher rate of extraction and pre-concentration of molecules of interest. A proof of concept has been performed for extraction of protein and DNA samples.

Based on existing technologies and improvements developed during my PhD, a large part of this work has been dedicated to answer new analytical challenges exploiting the power of this technology.

1) First, our approach has been performed in the context of food safety by extracting, pre-concentrating and detecting bacteria on chip. We were able to detect down to 4 bacteria in 50  $\mu\text{L}$  sample in only half of the time needed with usual detection methods. New perspectives can be investigated on the development of a platform to test drug resistance.

2) A second project has use the fluidized bed as miniaturized extracorporeal circulation approach to change the blood composition of preeclamptic patients. In particular, we have developed a on chip competitive bioassay to restore the angiogenic



balance in case of pre-eclampsia. The performances were evaluated on complex matrices such as cell media and plasma, and the angiogenic balance could be brought back to values closer to healthy profile. The next step is to work with a model of non gestating mice expressing sFlt-1 and PlGF rates similar to the ones of pre-eclamptic women.

3) Our last work has shown the possibility to fully integrate an ELISA in the fluidized bed platform with promising preliminary results. This work is on going.

All these approaches have shown the versatility of the microfluidic magnetic fluidized bed. It can easily be integrated as a first step for extraction inside a more complex device, actions can be performed directly on the surface of the beads where the molecule is captured, and can be used as a system to test at low cost the efficiency of capture of certain ligands with small amounts of samples.

The main limitation of the system remains its full automation. As a matter of facts, the first step of insertion of the beads is still manually performed. We are currently investigating innovative automation strategies, using for example encapsulation of beads in an hydrogel matrix.

Overall, the microfluidic magnetic fluidized bed appeared as a breakthrough for extraction and pre-concentration at high throughput, demonstrating interesting skills like high solid/liquid contact, continuous mixing, low back pressure and non-clogging. These aspects, together with the high versatility of the solid phase support, allowed to push forward the limits of the fluidized bed with for example, implementation of on-chip detection, in-flow competitive bioassay and high sensitive immuno-assay.

## Appendixes



## Awards

- 2018 **Prizewinner of the French fellowship l'Oréal-UNESCO For Women in Science**, Paris, France.

## Publications in refereed journals

- 2017 **A new microfluidic approach for the one-step capture, amplification and label-free quantification of bacteria from raw samples**, *Iago Pereiro, Amel Bendali\**, *Sanae Tabnaoui\**, *Lucile Alexandre\**, *Jana Srbova, Zuzana Bilkova, Shane Deegan, Lokesh Joshi, Jean-Louis Viovy, Laurent Malaquin, Bruno Dupuy and Stéphanie Descroix*, *Chemical Science*, 2017, 8, 1329.  
\*equal contribution
- 2014 **Conference MicroTas 2014 : “la microfluidique un domaine en essor”**, *Lucile Alexandre*, Scientific watch in Science, Technology and Innovation.

## Conference proceedings

- 2018 **Microfluidic platform to restore the angiogenic balance in preeclampsia**, *L. Alexandre, Laura Trapiella Alfonso, Nathalie Eilstein, Jean Guibourdenche, Edouard Lecarpentier, Vassilis Tsatsaris, Jean-Louis Viovy, Laurent Malaquin, Stéphanie Descroix*, *Pregnancy Hypertension*.
- 2017 **New generation of microfluidic magnetic fluidized bed for high throughput sample pretreatment**, *L. Alexandre, I. Pereiro, A. Bendali, J.-L. Viovy, L. Malaquin and S. Descroix*, *MicroTas*.
- 2014 **Microfluidic magnetic fluidized bed for bacteria extraction, growth and detection**, *I. Pereiro, J. Kucerova, L. Alexandre, B. Dupuy, Z. Bilkova, J.-L. Viovy, L. Malaquin and S. Descroix*, *MicroTas*.

## Papers in preparation

- submitted **VEGF functionalized beads in microfluidic device to restore the physiological sFlt-1/PlGF balance in preeclampsia**, *Laura Trapiella-Alfonso\**, *Lucile Alexandre\**, *Kelly Pons, Camille Fraichard, Jean-François Gaucher, Marylise Shuster Hebert, Jean GUIBOURDENCHE, Thierry Fournier, Stéphanie Descroix, Vassilis Tsatsaris, Nathalie Gagey-Eilstein, Edouard Lecarpentier*, *Nature Communications*.  
\*equal contribution
- in preparation **Protein biomarker detection in an innovative and integrated microfluidic approach**, *Lucile Alexandre, Madad Azmani, Amel Bendali, Iago Pereiro, Thanh Duc Mai, Stéphanie Descroix*, *Lab Chip*.

## Book chapter

- 2018 **A microfluidic fluidized bed to capture, amplify and detect bacteria from raw samples**, *L. Alexandre, I. Pereiro, A. Bendali, Sanae Tabnaoui, Jana Srbova, Zuzana Bilkova, Shane Deegan, Lokesh Joshi, J.-L. Viovy, L. Malaquin and S. Descroix*, *Methods in Cell Biology*.

## Patent

- 2014 **“Procédé de détection d’organismes dans un échantillon dilué”**, French patent number FR1460246 published under the number FR3027678.

## National and international conferences

- 2018 **Microfluidic platform to restore the angiogenic balance in preeclampsia**, *L. Alexandre, L. Trapiella Alfonso, N. Eilstein, J. Guibourdenche, E. Lecarpentier, V. Tsatsaris, J.-L. Viovy, L. Malaquin, S. Descroix*, *MicroNanoFluidic 2018*.  
oral presentation
- 2017 **New generation of microfluidic magnetic fluidized bed for high throughput sample pretreatment**, *L. Alexandre, I. Pereiro, A. Bendali, J.-L. Viovy, L. Malaquin and S. Descroix*, *MicroTas*.  
poster
- 2017 **Lit fluidisé microfluidique magnétique comme outil d’action sur la balance sFlt-1/PlGF pour le contrôle et le suivi de la pré-éclampsie**, *L. Alexandre, L. Trapiella-Alfonso, K. Pons, C. Fraichard, E. Lecarpentier, M. Shuster Hebert, J. Guibourdenche, N. Gagey-Eilstein, V. Tsatsaris, S. Descroix*, *Journée de la pré-éclampsie*.  
oral presentation
- 2017 **New design of microfluidic magnetic fluidized bed for high throughput**, *L. Alexandre, I. Pereiro, A. Bendali, J.-L. Viovy, L. Malaquin, and S. Descroix*, *Flow17*.  
oral presentation
- 2016 **Microfluidic Magnetic Fluidized Bed: its application to capture and culture of bacteria**, *L. Alexandre, I. Pereiro, A. Bendali, J.-L. Viovy, L. Malaquin, S. Descroix*, *Circle meeting*.  
poster



## Supporting information:

# VEGF functionalized magnetic beads in a microfluidic device to improve the angiogenic balance in preeclampsia

### Authors and Affiliations

Laura TRAPIELLA-ALFONSO<sup>a,§</sup>, Lucile ALEXANDRE<sup>b,§</sup>, Camille FRAICHARD<sup>c</sup>, Kelly PONS<sup>a,c</sup>, Simon DUMAS<sup>b</sup>, Jean-François GAUCHER<sup>d</sup>, Marylise HEBERT-SCHUSTER<sup>c,e</sup>, Jean GUIBOURDENCHE<sup>c,e</sup>, Thierry FOURNIER<sup>c</sup>, Michel VIDAL<sup>a</sup>, Laurence LECOMTE-RACLET<sup>h</sup>, Stéphanie DESCROIX<sup>b</sup>, Vassilis TSATSARIS<sup>c\*</sup>, Nathalie GAGEY-EILSTEIN<sup>a,†</sup>, Edouard LECARPENTIER<sup>c,f,g,†</sup>

<sup>a</sup> UMR 8638 CNRS Université Paris Descartes, Faculté des Sciences Pharmaceutiques et Biologiques, Sorbonne Paris Cité, 4 avenue de l'Observatoire, 75006 Paris, France

<sup>b</sup> UMR 168 CNRS Institut Curie, PSL Research University, Institut Pierre Gilles de Gennes; 75005 Paris, France

<sup>c</sup> Cochin Hospital, Assistance Publique-Hôpital de Paris, DHU Risques et grossesse, Paris Descartes University, INSERM UMR 1139, Fondation PremUp, 53 avenue de l'Observatoire, 75014 Paris, France

<sup>d</sup> INSERM, UMR-S1139, Faculté de Pharmacie de Paris, Université Paris Descartes, Sorbonne Paris Cité, Fondation PremUp, 75006, Paris, France

<sup>e</sup> Cochin Hospital, UF d'Hormonologie, Service de Biologie Automatisée, 27 rue du Faubourg Saint Jacques, 75014 Paris, France

<sup>f</sup> Université Paris Est Créteil and CHI Créteil, Créteil, France

<sup>g</sup> INSERM, U955, Institut Mondor de Recherche Biomédicale, Equipe 4, Créteil, France

<sup>h</sup> URC - CIC P1419, Cochin Hotel-Dieu Hospital, Assistance Publique – Hôpitaux de Paris, Paris, 75014 France;

§ Both authors contribute equal to this work (co-first authors)

† co-last authors

**\*Corresponding author:**

Prof. Vassilis Tsatsaris MD, PhD

E-mail: [vassilis.tsatsaris@aphp.fr](mailto:vassilis.tsatsaris@aphp.fr)

## **TABLE OF CONTENTS**

### **Supplementary Materials & Methods**

VEGF<sub>95</sub>-AVI-Biotin: protein expression and purification

Functionalization of magnetic beads

Tests for the characterization of functionalized magnetic beads

Theoretical calculations for the formation of sFlt-1/PlGF complex

Microfluidic experiments

### **Supplementary Figures**

Figure S1: Schematic representation of the specific and competitive apheresis approach and the microfluidic device

Figure S2: Functionalization and characterization of magnetic beads

Figure S3: Curve of rh-sFlt-1/rhPlGF complex formation

Figure S4: Kinetic study of the sFlt-1 capture and PlGF release

Figure S5: Evolution of concentrations of sFlt-1 and PlGF as function of the ligand surface density in dynamic conditions

Figure S6: VEGF-beads stability

### **Supplementary tables**

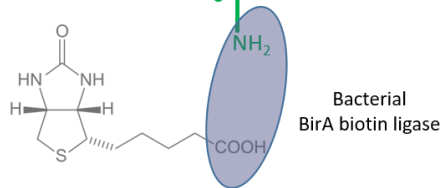
Table S1: Concentration of the ligand, surface saturation rates and ligand surface density of VEGF-beads

Table S2: Initial concentrations of rh-PlGF and rh-sFlt-1 used for the complex formation as well as the concentrations of each molecule after the complexation reaction and incubation with VEGF-beads

Table S3: Different types of biological samples used for the final experiment

**Supplementary Material & Methods***1. VEGF<sub>95</sub>-AVI-Biotin: protein expression and purification*VEGF<sub>95</sub>-**Avi**-biotin

MEVVKFMDVYQRSYCHPIETLVDIFQEYPDEIEYIFKPSCVPLMRCG  
 GCCNDEGLECVPTTEESNITMQIMRIKPHQGHIGEMSFLQHMKCEC  
 RPKVD**GGGLNDIFEAQKIEWHE**



Human VEGF-A (residue 39-133) was cloned (NdeI/SalI) into a pET15b expression vector (Novagen) previously modified to express a C-terminus Avitag sequence (GLNDIFEAQKIEWHE). The final plasmid encoding for His6-VEGF-A-AviTag was transformed in *E. coli* Rosetta-gami (DE3) pLysS bacterial strain (Novagen) for protein expression. Growth was performed at 37°C in LB supplemented with 100 µg/mL ampicillin and 100 µg/mL chloramphenicol and protein expression was induced by the addition of 0.5 mM isopropyl β-D-1-thiogalactopyranoside when the cell density reached an OD<sub>600nm</sub> of 0.4. After 4 h, cells were harvested by centrifugation (8,000g, 30 min) and frozen. The protein was expressed only in an insoluble form in inclusion bodies. Thawed cells were re-suspended in lysis buffer containing Tris/Hepes 50 mM/50 mM pH 8.0 (TH buffer) and Triton X100 0.5% (w/v). Cells were disrupted by sonication for 10 min. Inclusion bodies were isolated by centrifugation at 10,000 g for 10 min at 4°C. The pellet was submitted to this treatment (re-suspension, sonication and centrifugation) two additional times: first in TH buffer, NaCl 1M, and then in TH buffer alone. 1 mg of dried pellet was suspended by sonication in 2 mL of TH buffer and incubated for 10 min with DTT 50 mM. The suspension was diluted in 500 mL of urea 8 M, NaCl 1 M, TH buffer, imidazole 25 mM, prior to purification on 5 mL Ni-NTA columns (GE Healthcare). After one-step 500 mM imidazole elution, 20 mg of unfolded protein purified in urea was obtained from 1 L of culture. Refolding was performed as follows: Purified His6-VEGF-A-Avitag was incubated with DTT 10 mM and concentrated by ultrafiltration (cutoff 3 kDa) to exchange the buffer for Na<sub>3</sub>Citrate 50 mM, reduced



cysteine 1 mM, Tris/HCl 25 mM pH 8.0. Protein at 0.5 mg/mL was further dialyzed overnight against 11 volumes of the same buffer. Dialysis was repeated against 20 volumes of reduced cysteine 10 mM, Tris/HCl 25 mM pH 8.0 for 4 hours then overnight against 20 volumes of Tris/HCl 25 mM pH 8.0, CuCl<sub>2</sub> 10 μM at 20°C with air bubbling to oxidize disulfides. (NH<sub>4</sub>)<sub>2</sub>SO<sub>4</sub> 0.6 M was added to the dialysis buffer to precipitate misfolded protein and then discarded by centrifugation at 16,000 g for 10 min. The soluble protein was concentrated by ultrafiltration and the buffer was progressively exchanged against H<sub>2</sub>O. The protein was concentrated at 50 mM prior to biotinylation by 1.5 μg/mL of BirA biotin-protein ligase in bicine/NaOH 50 mM pH 8.3, ATP 10 mM, MgOAc 10 mM, d-biotin 50 mM, at 37°C for 1 h. The His<sub>6</sub> tag was cleaved overnight at 4° C using 0.1 U of thrombin for 10 μg of protein in NaH<sub>2</sub>PO<sub>4</sub>/NaOH 100 mM pH 7.2. The biotinylated and cleaved protein was finally purified on a Source 15Q column equilibrated with Hepes/NaOH 20 mM pH 7.0 buffer (H buffer) and eluted with a 6 CV linear gradient up to NaCl 1 M in H buffer. The biotinylated and cleaved protein appeared as a single and focused 28 kDa band in non-reduced SDS-PAGE. The protein was finally frozen in liquid nitrogen and lyophilized for long-term storage. The overall yield is around 1 mg of protein per liter of culture.

## *2. Functionalization of magnetic beads*

Typically for functionalization of 0.6 mg of Dynabeads, the beads were re-suspended in the vial (vortex for 30 s), and then 60 μL of stock solution was transferred to a tube. Dynabeads were washed 2 times with 200 μL of PBS and re-suspended at the initial concentration (60 μL of PBS). The desired amount of the biotinylated molecule was added to the Dynabeads and incubated for 1 h at room temperature with gentle shaking of the tube. Functionalized Dynabeads were washed 4 times with 300 μL of PBS/0.1% BSA (w/v) and re-dispersed to the initial concentration (60 μL, 10 mg/mL) in PBS/0.1% BSA. To eliminate non-specific grafting, 3 successive short incubations (10 min) in 300 μL of acidic buffer (100 mM citric acid/ 200 mM Na<sub>2</sub>HPO<sub>4</sub> buffer, pH 3) were performed. After washing with 300 μL of PBS, a last blocking step was done (300 μL PBS/0.1% BSA, 30 min at RT). Finally, the beads were re-suspended in 60 μL PBS/0.1% BSA and stored at 4°C until use.

### 3. Tests for the characterization of functionalized magnetic beads

#### 3.1.1. Grafting rate: bt-HRP assay

The grafting rate of functionalized magnetic beads was evaluated as previously described [REF Diego]. Briefly, functionalized magnetic beads and solution of bt-HRP (Invitrogen) were mixed. After incubation and washing, SuperSignal West Pico Substrate (Pierce) was added. The chemiluminescence (as relative light units, RLU) was read on a Tecan Infinite ® 200 PRO plate reader. Chemiluminescence signal (S) was compared to the maximum signal of control beads without functionalization (S<sub>max</sub>) and percentage of grafting was calculated using equation 1:

$$\%grafting = 100 \times \left( \frac{S_{max} - S}{S_{max}} \right) \quad \text{Equation 1}$$

Where S is the chemiluminescence signal from the grafted beads and S<sub>max</sub> is the maximum signal from non-grafted beads used as reference.

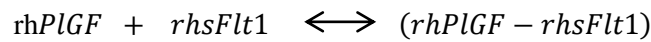
#### 3.1.2. Binding test

The ability of VEGF-functionalized magnetic beads (VEGF-beads) to bind rhsFlt-1 was evaluated. Briefly, a transparent high-binding 96 well-plate (Costar 9018) was blocked for 2 h at 37°C with 200 µL/well of blocking buffer (PBS containing 3% BSA (w/v)). The plate was then washed 3 times with 200 µL/well of buffer A (PBS containing 0.1% Tween 20 (v/v)). Then, after dilution of the functionalized beads stock, 20 µL of diluted beads (1 pmol of grafted VEGF) was added to each well. Increasing concentrations of rhsFlt-1 (from 100 pg/mL to 10 µg/mL) in buffer B (PBS containing 0.1% BSA (w/v), 0.01% Tween (v/v)) were added to the wells (60 µL final volume). After 1-h incubation at 37°C with continuous agitation, the beads were kept subject to a magnetic field and washed 3 times with 200 µL of buffer A. Then, 100 µL/well of IgG-AP, directed against Fc fragment of rhsFlt-1 (Dako, Santa Clara, US) in buffer B (dilution 1/1000 from commercial stock solution), was added and incubated for 1 h at 37°C. Again, the beads were washed 3 times with buffer A and 100 µL/well of pNPP solution (1 mg/mL in diethanolamine pH 9.8, from Sigma-Aldrich) was added. The

absorbance was measured at 405 nm on a MULTISKAN EX plate-reader spectrophotometer (MTX Lab Systems, Bradenton, US) after 20 min of incubation at 37°C. For the measurement, the beads were kept on the well side with the magnet to avoid light diffraction. Saturation curves corresponding to the specific signal (total signal – non-specific signal) of rhsFlt-1 bound to VEGF were analyzed using a nonlinear regression function in Prism (version 5.01, GraphPad Software, USA). Non-specific signals were obtained by non-functionalized magnetic beads. All experiments were performed in triplicate.

#### 4. Theoretical calculations for the formation of the sFlt-1/PlGF complex

Considering the PlGF and sFlt-1 complexation equilibrium, its dissociation constant was an estimated 170 pM (25). The dynamic range of the Quantikine ELISA human PlGF of 2 ng/mL (50 pM), the initial concentration of rhPlGF at 2 ng/mL (50 pM) and the theoretical initial rhsFlt-1 concentrations were calculated to obtain various amounts of complex rhsFlt-1/rhPlGF.



$$K_d = \frac{[\text{rhPlGF}_{free}][\text{rhsFlt1}_{free}]}{[\text{rhPlGF} - \text{rhsFlt1}]}$$

During the complexation,  $\text{rhPlGF}_{free} = \text{rhPlGF}_0 - x$ , being  $x$  the concentration of rhPlGF/rhsFlt-1 complex

$$\text{And } [\text{rhsFlt1}_{free}] = \frac{K_d \times x}{[\text{rhPlGF}_{free}]}$$

$$\text{Then, } [\text{rhsFlt1}_0] = [\text{rhsFlt1}_{free}] + x = x \left( 1 + \frac{K_d}{[\text{rhPlGF}_0] - x} \right)$$

#### 5. Microfluidic experiments

##### 5.1. Chip fabrication

The design comprised an optimized rhombic chamber geometry ([Pereiro et al., 2017b](#)) with an aperture angle of 13° and 25° at the inlet and outlet, respectively, 13 mm in length and 2.6 mm at its maximum width. The inlet channel was 100 μm wide and all the structures 50 μm high. Microfluidic

chips were designed based on micro-milled molds. These molds were machined in brass pieces of 5 cm x 5 cm. The designs were a positive replica of the chip. The chips were fabricated by pouring polydimethylsiloxane (PDMS, Sylgard184, Dow Corning) on the molds, and were bonded by oxygen plasma. A surface treatment of PDMA-AGE 0.5% was incubated inside the chip chamber for 2 hours then rinsed with distilled water and dried with compressed air. The chips were stored at RT until use.

## 5.2. Microfluidic setup

The liquid flow was produced by pressurization of the sample reservoir by a pressure controller (MFCS<sup>TM</sup>, Fluigent, from 1 to 1 000 mbar). The outlet of the chip was connected to a flowrate controller (Flowunit S, Fluigent, from 1 to 7700 nL/min), which allowed both precise flow rate measurement and feedback control on the pressure based on the Maesflo software (Fluigent). The system can be controlled either in pressure or flow rate. Peek tubing (IDEX, IDXOD 0.010''X1/32 and IDXOD 0.0025''X1/32) was used to connect the microfluidic chip to the other elements of the experimental set-up. The entrance of the chip was the main resistance of the system (12 cm peek tubing of 0.063 mm diameter). An NdFeB 1.47T permanent magnet was aligned with the chamber axis 1.5 mm from the chip inlet.

**Supplementary Figures**

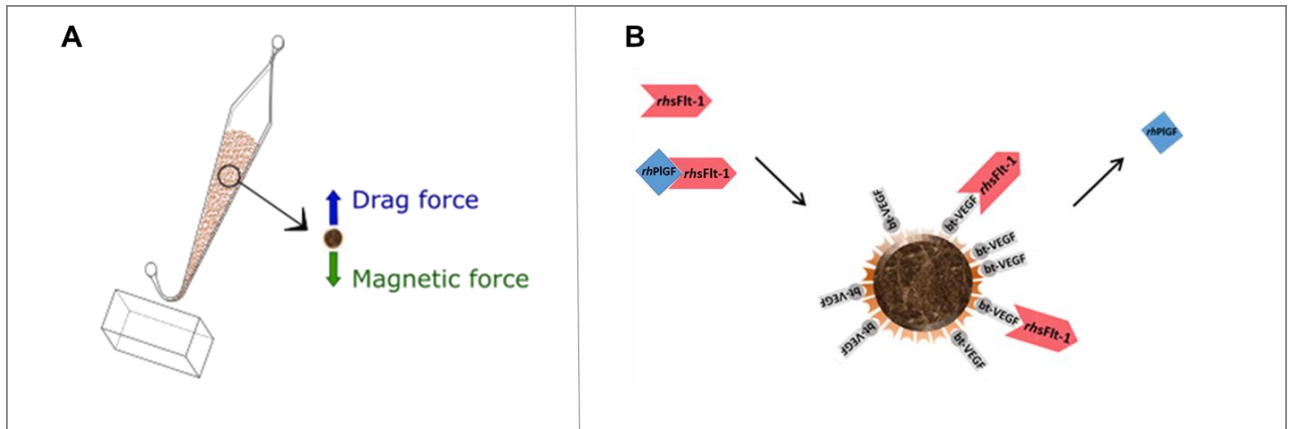


**Figure S1:** Schematic representation of the specific and competitive apheresis approach. A/ Microfluidic device based on magnetic fluidized bed; B/ Streptavidin-magnetic beads functionalized with biotinylated VEGF capturing the sFlt-1 and displacing the PlGF.

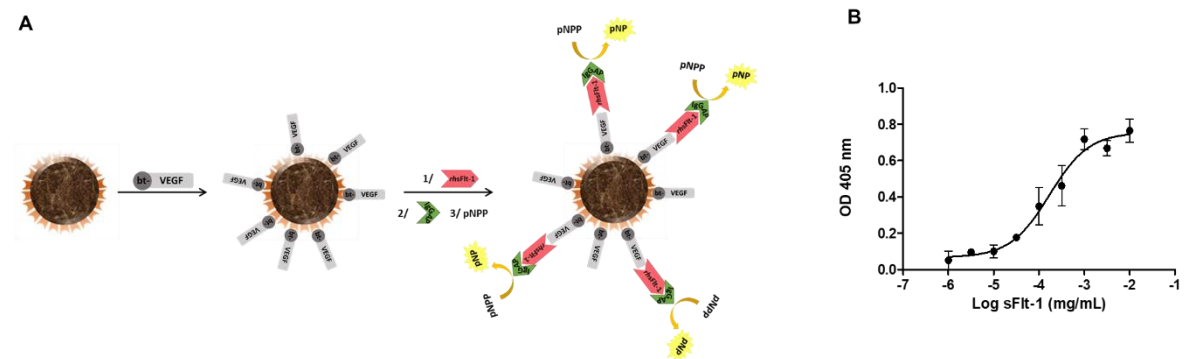


**Figure S2:** Functionalization and characterization of magnetic beads. A/ Schematic representation of functionalization of magnetic beads with bt-VEGF followed by the *rhFlt-1* binding colorimetric immunoassay; B/ Binding curve showing the interaction between VEGF-beads and *rhFlt-1* ( $K_d = 1$  nM). Abbreviations: bt-VEGF: biotinylated VEGF, *rhFlt-1*: recombinant human sFlt-1, IgG AP: alkaline phosphatase linked IgG, pNPP: para-nitrophenylphosphate, pNP: 4-nitrophenol

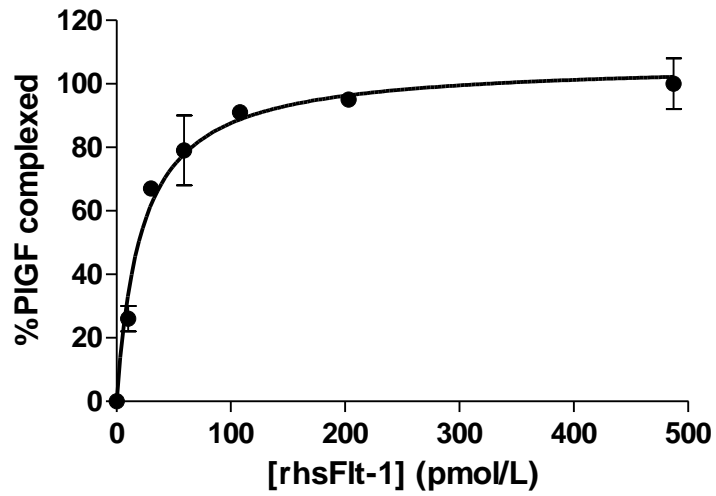


**Figure S3:** Curve of *rhsFlt-1*/*rhPIGF* complex formation

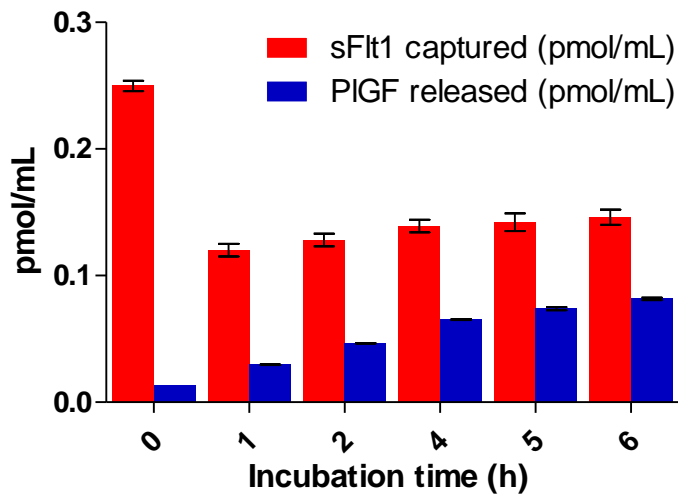


**Figure S4:** Kinetic study of the sFlt-1 capture (red) and PIGF release (blue). The graph shows incubations of the culture cell supernatant (0.26 pmol/mL sFlt-1 and 0.013 pmol/mL PIGF) with 105 pmol/mg VEGF-beads at different times. After 2 h of incubation, no significant variations were observed that justify a prolonged incubation time.

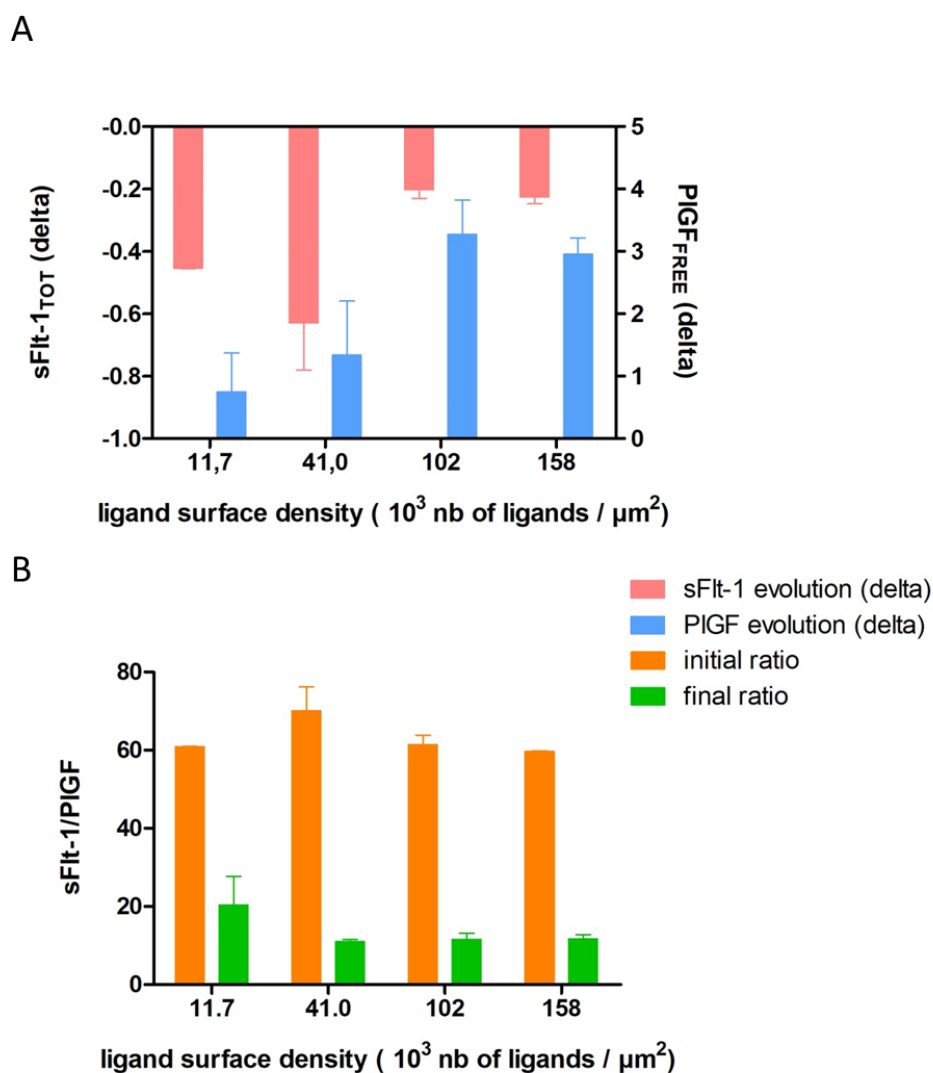


**Figure S5:** Evolution of concentrations of sFlt-1 and PIGF with A) the capture of total sFlt-1 and release of free PIGF and B) the comparison between the initial and final ratio sFlt-1/PIGF in placenta cellular conditioned media evaluated as the final concentration minus the initial concentration divided by the initial concentration of the molecule in a sample with an initial concentration of 0.26 pmol/mL for sFlt-1 and 0.013 pmol/mL for PIGF as a function of the ligand surface density expressed in  $\cdot 10^3$  number of ligands per square micrometer.

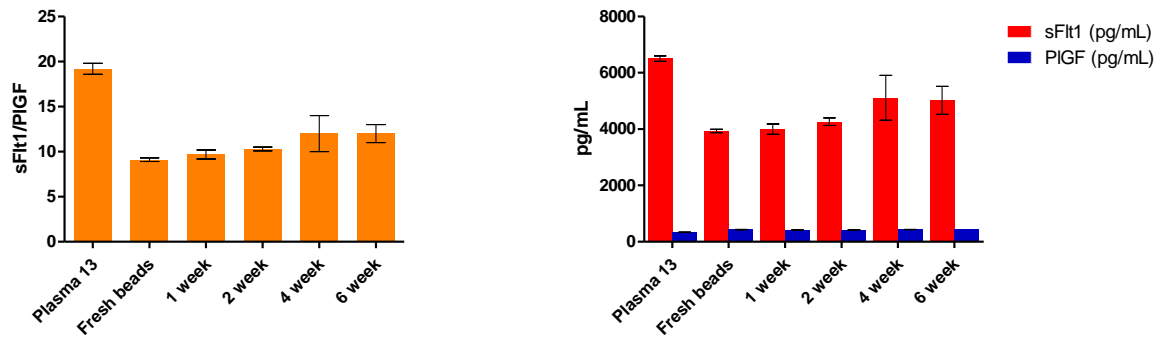


**Figure S6:** VEGF-beads stability. A/ stability after storage at 4 °C measured by the shift in the sFlt-1/PIGF ratio after incubation in a pool of plasma from preeclamptic women; B/ stability measured by the shift in sFlt-1 capture and PIGF release.



**Supplementary Tables**

**Table S1:** Concentration of the ligand, surface saturation rates and ligand surface density of VEGF-beads

<b>bt-VEGF (pmol/mg beads)</b>	<b>Surface saturation rate (%)</b>	<b>Ligand surface density* (no. of ligands x10<sup>3</sup>/μm<sup>2</sup>)</b>
<b>30</b>	20 ± 5	11.7 ± 1.2
<b>105</b>	35 ± 3	41.0 ± 2.0
<b>259</b>	64 ± 2	101.9 ± 1.3
<b>400</b>	91 ± 4	158.1 ± 1.6

\*  $\sigma = \left( \frac{Y \times W_{ligand}}{W_{particle}} \right) \times \left( \frac{N_A \times d_{particle} \times \rho_{particle}}{6MW_{ligand}} \right)$  (23), where Y is the grafting yield, W are the ligand or particle masses,  $N_A$  is Avogadro's number,  $d_{particle}$  is the diameter of the particle,  $\rho_{particle}$  is the particle density.

**Table S2.** Initial concentrations of rh-PlGF and rh-sFlt-1 used for the complex formation as well as the concentrations of each molecule after the complexation reaction and incubation with VEGF-beads.

Complex	PlGF <sub>initial</sub> (pg/mL)	PlGF <sub>free</sub> (pg/mL)	PlGF <sub>complexed</sub> <sup>*</sup> (pg/mL)	%PlGF complexed	PlGF <sub>free</sub> , after incubation (pg/mL)	Δ(PlGF), after incubation (pg/mL)	%PlGF released <sup>**</sup>
C1	167 ± 45	2 ± 1	165 ± 46	99 ± 1	37 ± 10	35 ± 11	21 ± 3
C2	167 ± 45	5 ± 1	162 ± 46	97 ± 1	43 ± 14	38 ± 15	23 ± 3
C3	167 ± 45	6 ± 2	161 ± 47	96 ± 1	38 ± 13	32 ± 15	20 ± 3
Complex	sFlt-1 <sub>total</sub> (pg/mL)	sFlt-1 <sub>free</sub> <sup>***</sup> (pg/mL)	sFlt-1 <sub>complexed</sub> <sup>***</sup> (pg/mL)	sFlt1 <sub>total</sub> /PlGF <sub>free</sub> initial ratio	sFlt-1 <sub>total</sub> , after incubation (pg/mL)	%sFlt-1 captured	sFlt1 <sub>total</sub> /PlGF <sub>free</sub> final ratio
C1	10471 ± 2281	9333 ± 2598	1138 ± 317	5235 ± 2855	1110 ± 265	88 ± 57	30 ± 11
C2	8735 ± 1236	7618 ± 1553	1117 ± 317	1747 ± 428	615 ± 214	93 ± 21	14 ± 7
C3	5844 ± 652	4734 ± 976	1110 ± 324	974 ± 342	443 ± 180	92 ± 18	12 ± 6

\* PlGF<sub>initial</sub> – PlGF<sub>free</sub>; \*\* PlGF released with respect to the PlGF<sub>complexed</sub>; \*\*\* Calculated concentrations: (i) sFlt-1<sub>complexed</sub> comes from the fact that the interaction PlGF-sFlt-1 is equimolar and MW (rh-PlGF): 29 kDa and MW (rh-sFlt-1): 200 kDa; and (ii) sFlt-1<sub>free</sub> = sFlt-1<sub>total</sub> – sFlt-1<sub>complexed</sub>

**Table S3:** Different types of biological samples used for the final experiment

<b>Sample</b>	<b>Type</b>	<b>Gestational age</b> <b>(weeks of gestation,</b> <b>WG)</b>	<b>sFlt-1</b> <b>(pmol/mL)</b>	<b>PlGF</b> <b>(pmol/mL)</b>
<b>CM1</b>	Conditioned media of trophoblastic cells	Term, normal pregnancy	0.22	0.014
<b>CM2</b>	Conditioned media of trophoblastic cells	Term, normal pregnancy	0.21	0.012
<b>CM3</b>	Conditioned media of trophoblastic cells	Term, normal pregnancy	0.30	0.0029
<b>PE1</b>	Plasma, preeclampsia	23 WG	0.17	0.00049
<b>PE2</b>	Plasma, preeclampsia	30 WG	0.23	0.0018
<b>PE3</b>	Plasma, preeclampsia	33WG	0.20	0.0034

## **Résumé en français**

**Développement (et compréhension) de lits fluidisés magnétiques  
en microfluidique :**

**Application à la détection ultrasensible en bio-analyse**



## 1. Introduction générale

La microfluidique a déjà démontré son potentiel en tant que plate-forme d'analyse à petite échelle, avec des coûts limités et une consommation de réactifs réduite. Dans ce contexte, l'utilisation de microparticules semble une approche intéressante pour améliorer le ratio surface sur volume et augmenter ainsi les interactions entre une surface solide et un volume de liquide. Ces microparticules peuvent être facilement manipulées et possèdent une haute capacité de charge. Elles peuvent alors être utilisées pour faire face aux nouveaux défis de l'analyse de traces. Pour automatiser le mouvement de particules, plusieurs techniques ont été développées ayant recours à la mécanique, la chimie, l'optique, la di-électrophorèse, l'acoustique, les gouttes ou le magnétisme. Dans cette étude, nous avons choisi de nous concentrer sur les billes magnétiques présentant des propriétés super-paramagnétiques. Ces billes sont facilement manipulées avec un champ magnétique. Pour les utiliser comme support analytique, leur surface peut être fonctionnalisée (Figure 104) avec des molécules biologiques. Ces propriétés font des billes magnétiques un candidat de choix pour relever les nouveaux défis de l'analyse de traces. D'autre part, les billes magnétiques peuvent être impliquées dans l'extraction et la détection de très faibles concentrations. Les billes peuvent être soit le support de production du signal, soit directement l'outil de reconnaissance et mesure.

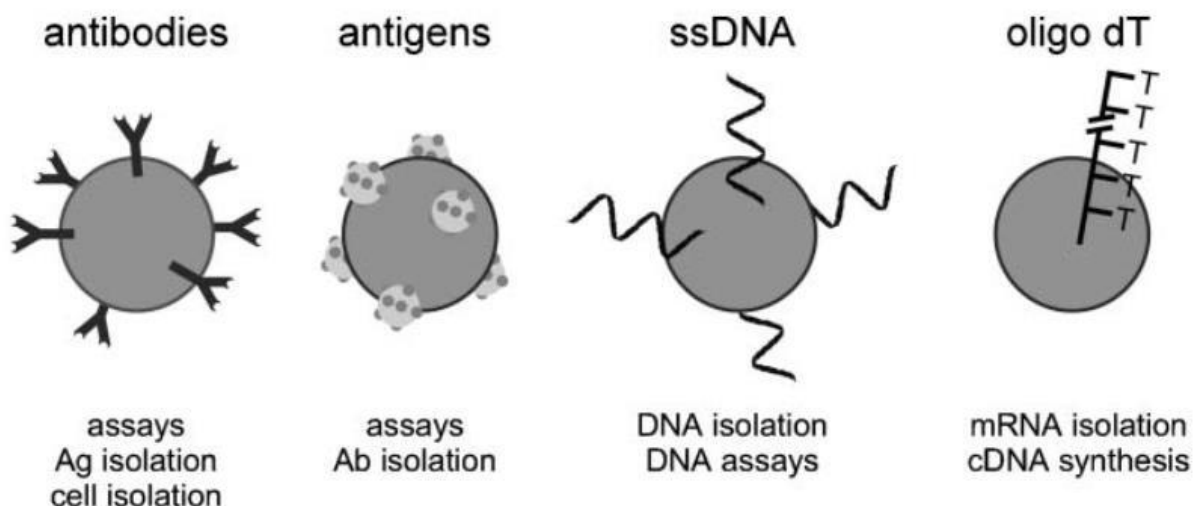


Figure 104 Présentation de plusieurs fonctionnalisations de billes magnétiques (Pamme, 2006)

Le lit fluidisé microfluidique et magnétique est un outil développé dans l'équipe Macromolécules et Microsystèmes pour la Biologie et la Médecine. Cette technologie permet de réaliser une extraction sur une phase solide à débit modéré, mais avec une efficacité très élevée directement en puce microfluidique.

Au cours de ma thèse, j'ai inventé et caractérisé une nouvelle génération de lits fluidisés permettant de travailler à haut débit et capables d'analyser de larges volumes d'échantillons en un temps raisonnable. Le développement de cette nouvelle technique m'a poussée à faire face à de nouveaux défis, en particulier concernant l'homogénéisation des billes dans la puce.

Ainsi, dans un premier temps seront décrites plusieurs approches différentes permettant d'améliorer le mouvement des billes dans la puce, qu'elles soient passives ou actives. La deuxième partie de ce résumé mettra l'accent sur les applications bio-analytiques en lit fluidisé. Nous étudierons d'abord la capture et détection de bactéries, puis la capture de biomolécules dans le cas de pré-éclampsie, et enfin l'intégration d'un immuno-dosage sur billes magnétiques.

## **2. Description du système de lit fluidisé microfluidique et magnétique**

Les lits fluidisés sont utilisés à l'échelle macroscopique pour maximiser le contact entre une surface solide et une phase liquide ou gazeuse. Pour optimiser ce contact, la phase solide est divisée en particules qui sont dispersées dans le flux de la phase liquide/gazeuse. Plusieurs avantages accompagnent cette configuration tels qu'un mélange continu des particules, une résistance interne très faible qui permet de travailler à haut débit, et une réduction des risques de colmatage du système. La dispersion de particules est réalisée grâce à un équilibre général entre la force de traînée créée par le liquide ou le gaz passant à travers les particules et la gravité qui les retient à l'intérieur du réservoir, comme décrit sur la figure 105.

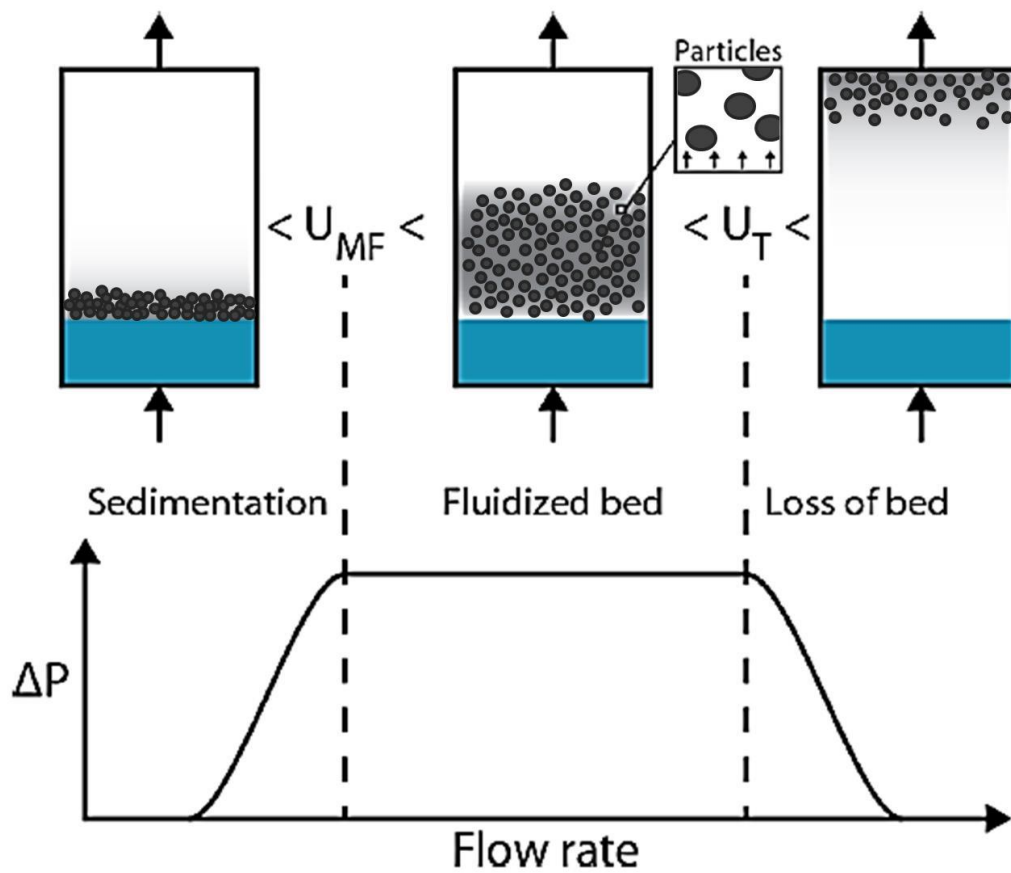


Figure 105 Description des systèmes de lit fluidisé à l'échelle macro

Afin de tirer avantages de ces caractéristiques, l'équipe Macromolécules et Microsystèmes pour la Biologie et la Médecine a décidé de créer un système de lit fluidisé à l'échelle microscopique, comme montré sur la figure 106. A cette échelle, pour des sphères avec des diamètres de l'ordre du micromètre, la gravité n'est plus prépondérante. Cette force est remplacée par une force magnétique dont l'ordre de grandeur est le même que pour la force de traînée.



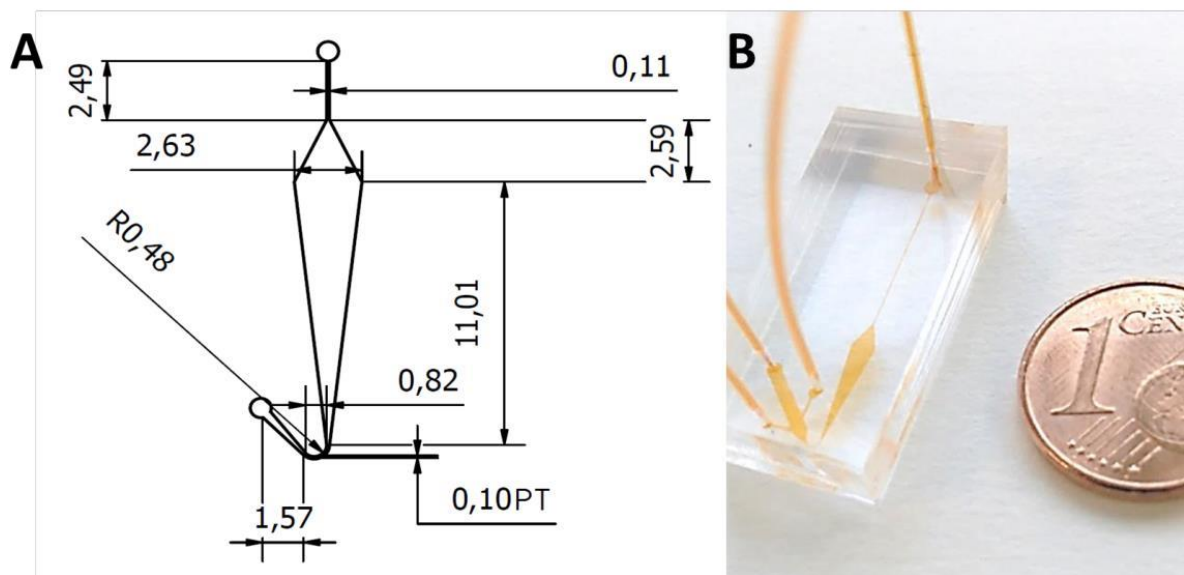


Figure 106 Schéma du système de lit fluidisé (A) et photographie de la puce en PDMS (B)

L'équilibre des forces est représenté sur le schéma ci-dessous :

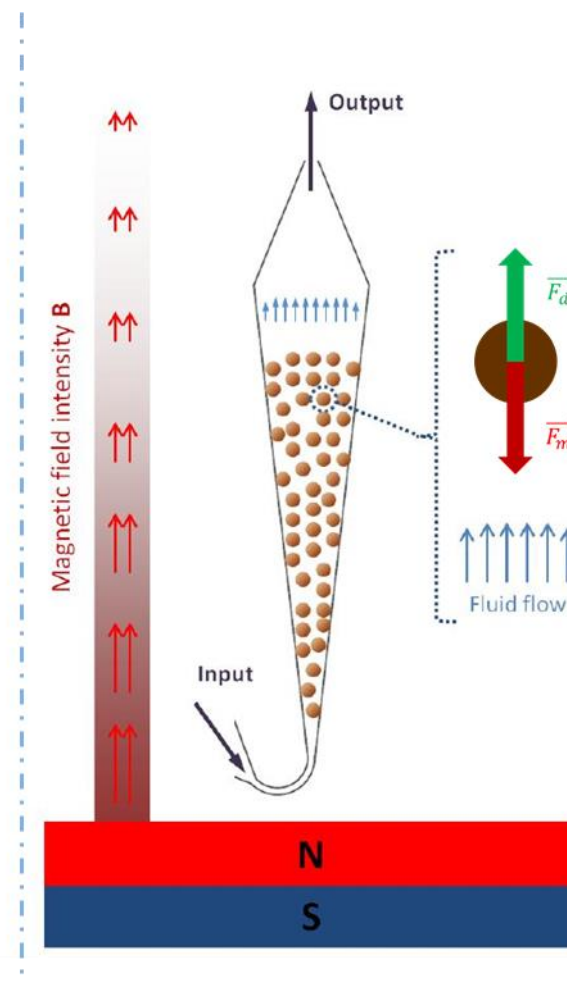


Figure 107 Schéma de fonctionnement du lit fluidisé

La forme évasée de la chambre centrale permet d'équilibrer la décroissance de la force magnétique lorsqu'on s'éloigne de l'aimant. Sans écoulement, les billes sont rassemblées les unes contre les autres à l'entrée de la chambre principale. Lorsqu'un écoulement est mis en place, une fluidisation des particules peut être observée. Un mouvement de re-circulation a été observé dans la puce : les billes sont poussées par l'écoulement à l'entrée et au centre de la puce, puis ramenées sur les côtés par la force magnétique.

### 3. Développement des aspects physiques du lit fluidisé en vue de travailler à haut débit

Le débit de travail dans le lit fluidisé microfluidique est limité par la perte des billes en fin de lit. La force de traînée est trop forte, et la force magnétique n'est pas suffisante pour contrebalancer cette augmentation au-delà d'une certaine limite (au-delà de 3  $\mu\text{L}/\text{min}$ ). Afin de travailler à plus haut débit, la géométrie doit être modifiée. Comme l'optimisation de la géométrie 2D a déjà été entièrement optimisée au cours d'une précédente thèse, le paramètre modifié est la hauteur de la chambre en PDMS. Une nouvelle structure a été créée avec une hauteur de 250 $\mu\text{m}$ .

La perte de confinement des billes sur l'axe vertical a une conséquence directe sur l'homogénéité des billes dans la puce, comme présenté sur la figure 108. A l'intérieur de la matrice de billes, on voit se former un chemin préférentiel dans lequel une grande partie du liquide s'écoule sans avoir la possibilité de percoler le reste des billes. Ce phénomène limite les interactions entre la phase solide et la phase liquide, et donc réduit l'efficacité de notre système.

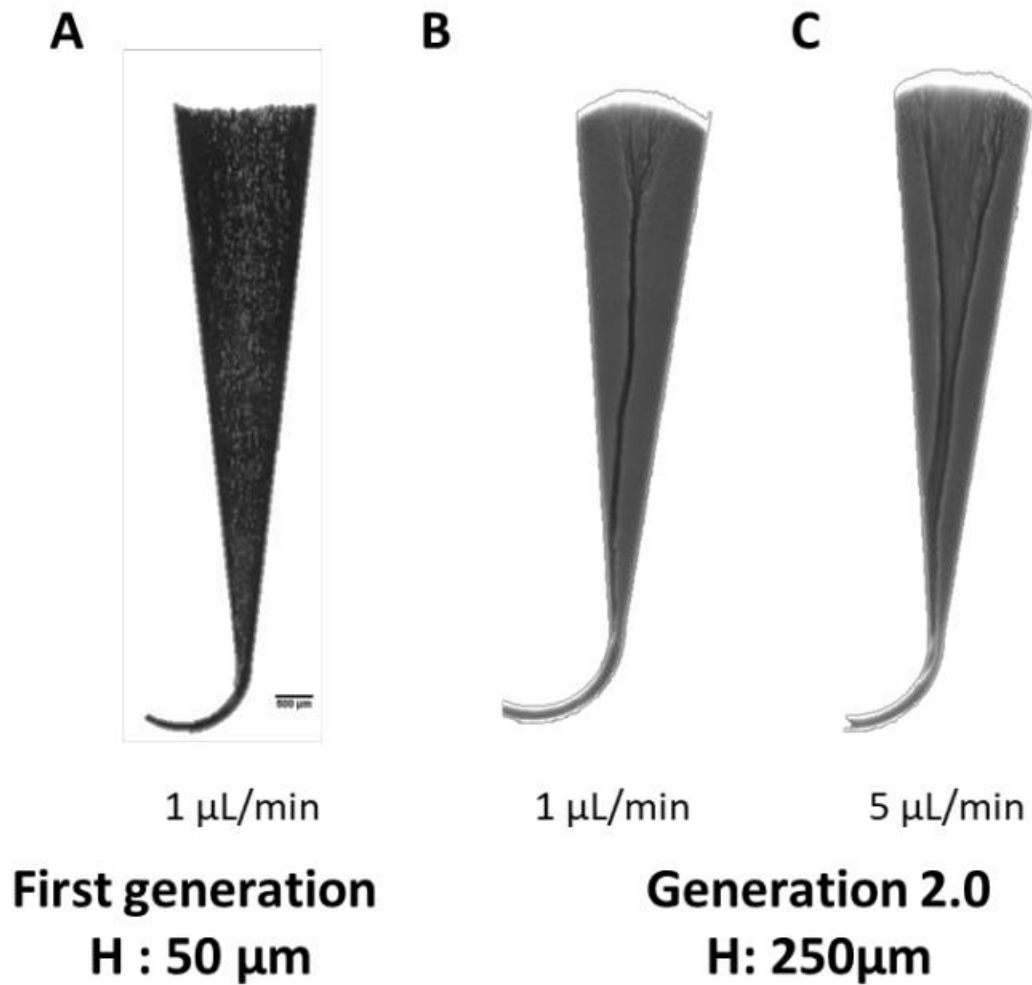


**Figure 108 Photographies de matrices de billes**

Mon travail de thèse s'est focalisé sur la mise en œuvre de différentes solutions qui permettent d'améliorer l'homogénéité de répartition des billes dans la puce. Le but est d'avoir un système efficace à haut débit. Trois solutions ont fait l'objet d'un examen approfondi: l'implémentation de rainures, l'ajout d'un système de vibration et l'utilisation d'une matrice magnétique bimodale.

### **1. Implémentation de rainures de type « Herringbones »**

Dans cette thèse, des rainures de types « herringbones » ont été implémentées au système microfluidique de lit fluidisé. Si la plupart des mélangeurs passifs sont difficiles à implémenter au système de lit fluidisé, les rainures de types « Herringbones » présentent l'avantage de la simplicité et ont démontré leur effet sur la distribution de fluides circulant dans la puce (Figure 109). Les premiers tests ont été réalisés sur la base des travaux publiés

par Stroock (2002, Sciences) ; puis des optimisations ont été réalisées à la fois sur le dessin des rainures, mais aussi sur leur taille et leur placement géométrique (Figure 110).

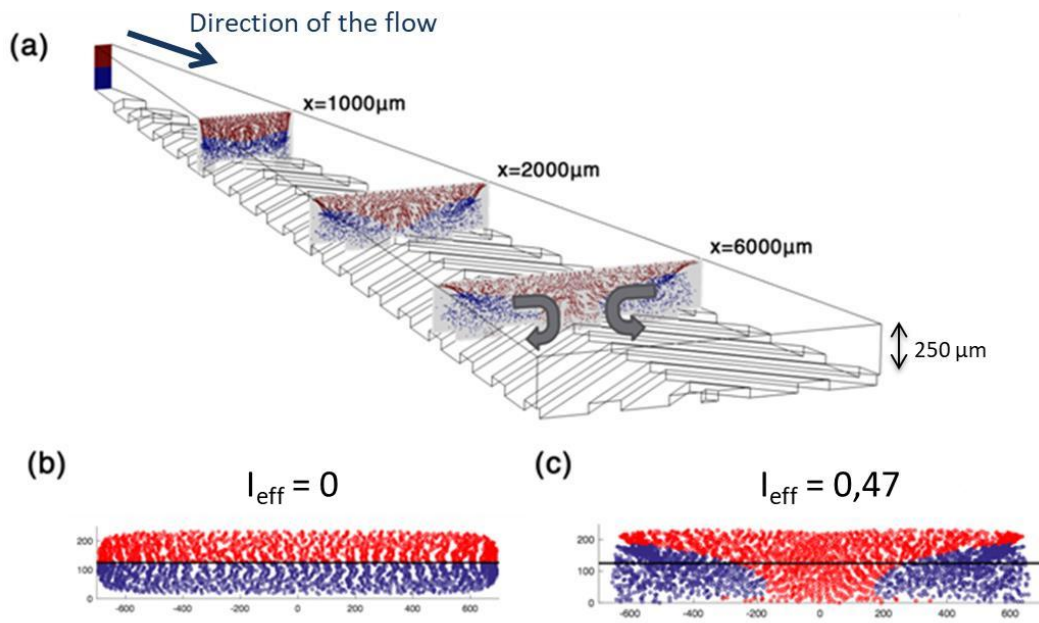
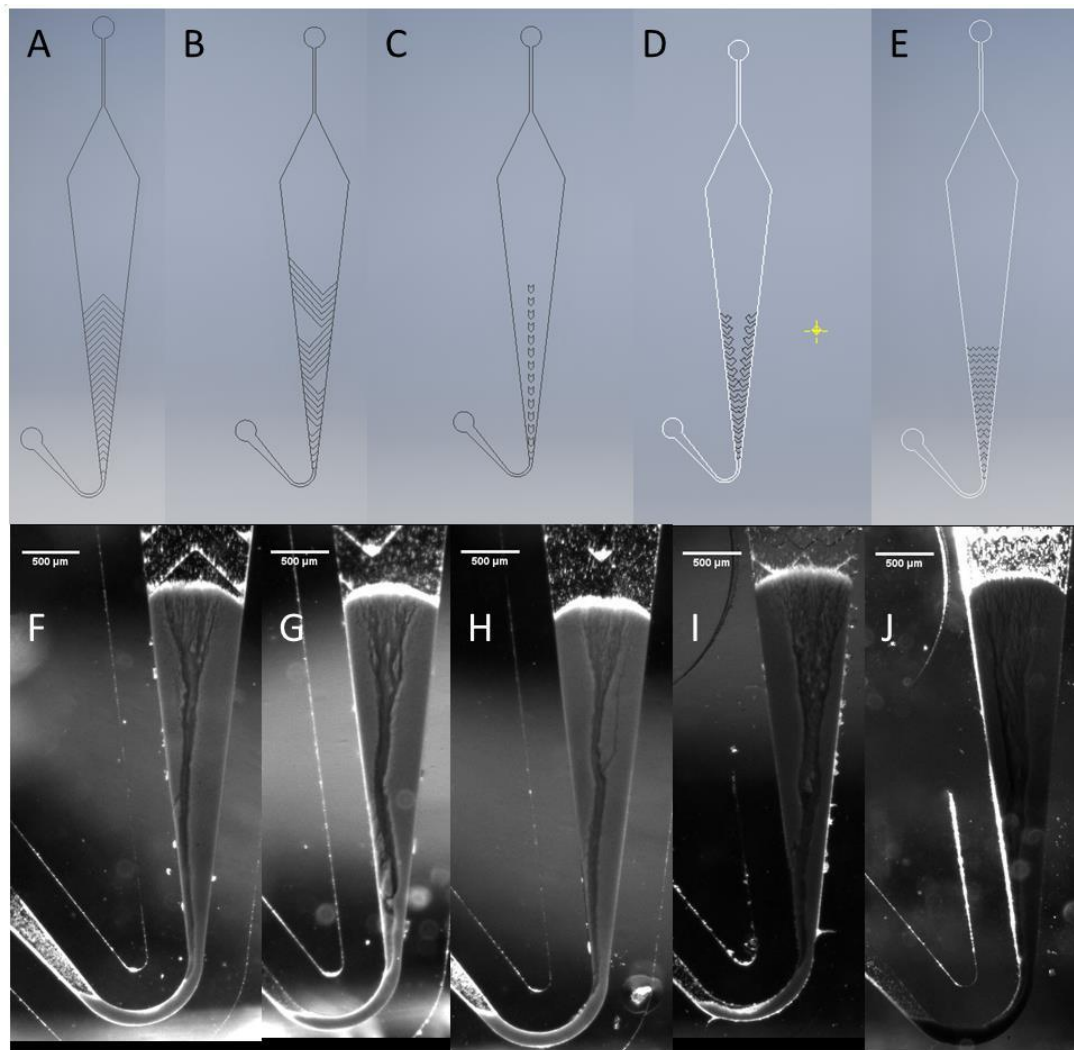


Figure 109 Représentation des rainures de types Herringbones (a) et simulation sur écoulement (b)



**Figure 110** Schémas et photographies des dessins testés

Cependant, nous n'avons pas été en capacité d'observer une influence significative sur le mouvement des billes à l'intérieur de la puce, ni sur l'efficacité de capture. Plusieurs explications à cette difficulté peuvent se présenter. Il est hautement probable que les mouvements induits sur les distributions de liquides dans la puce ne soient pas suffisants pour perturber l'organisation initiale et le mouvement des billes magnétiques.

Les simulations Comsol® ont montré que les vitesses perpendiculaires à l'écoulement principal sont dix fois plus faibles que celles qui se font dans la direction principale. Ainsi un facteur dix peut être identifié entre les forces de traînée dues à la présence des rainures et celles générées par l'écoulement entre l'entrée et la sortie de la puce. Comme les forces magnétiques sont du même ordre de grandeur que ces dernières, cela peut expliquer les difficultés à observer un effet sur les billes magnétiques.

Nous avons donc décidé d'augmenter le mélange en agissant, soit directement sur la matrice de billes magnétiques, soit par addition d'un mélangeur actif.

## 2. Ajout de vibrations par système actif

Afin d'améliorer le contact entre la phase solide et la phase liquide, des perturbations peuvent être créées par un module externe au système.

Tout d'abord, nous nous sommes intéressés à une configuration permettant l'alternance de cycles d'ouverture et de fermeture du lit fluidisé pour réinitialiser la position des billes dans la matrice à différents moments de l'expérience. Les premiers résultats de quantification obtenus avec cette méthode sur un modèle de capture n'ont cependant pas été satisfaisants (Figure 111)

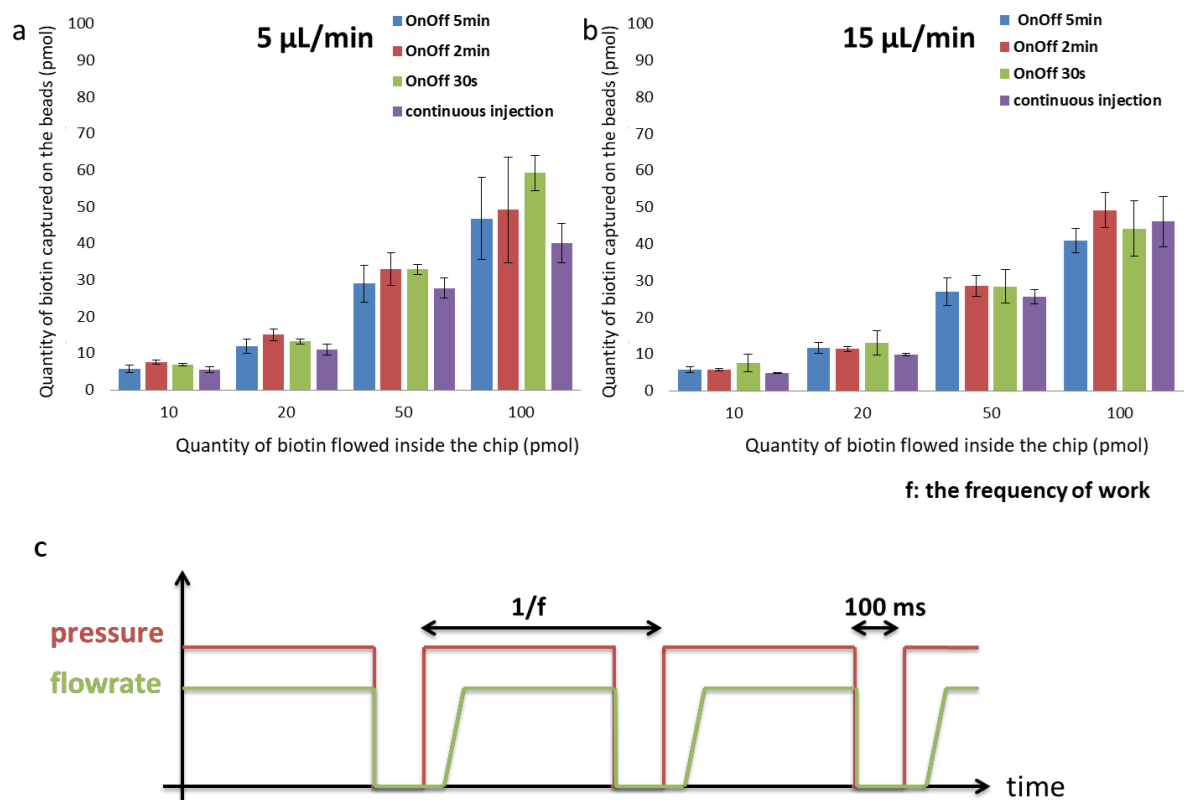
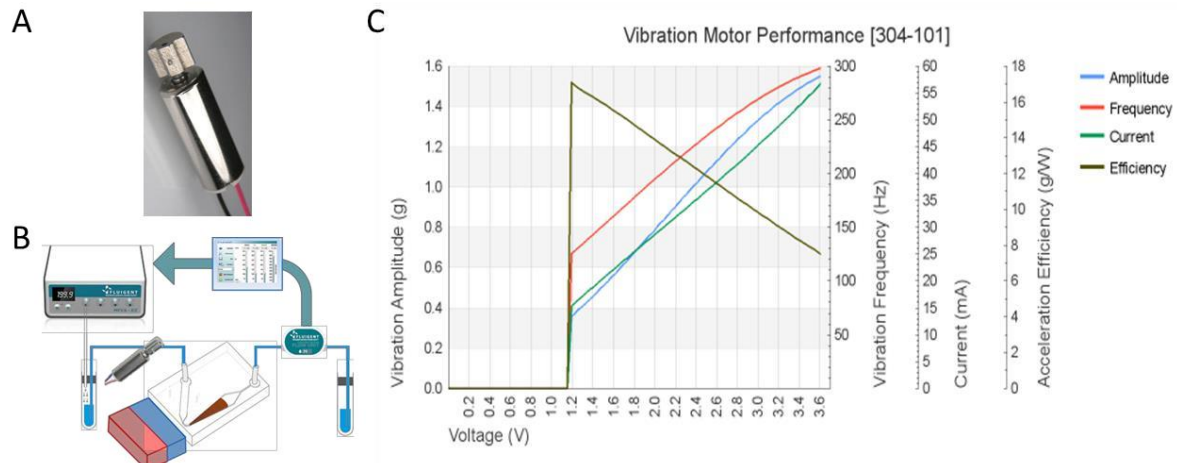


Figure 111 Représentation de l'efficacité de capture à 5µL/min (a) et 15 µL/min(b) Représentation de la pression et du débit en entrée de puce

En deuxième approche, un vibreur, inspiré de celui des téléphones portables et présenté en figure 112, a été ajouté sur le tube d'entrée du lit fluidisé. Accolé à celui-ci, il permet la transmission de perturbations à l'écoulement de liquide qui pénètre dans la matrice de billes.



**Figure 112 Photographie du vibreur (A) et sa position sur le système de lit fluidisé (B) ainsi que ses principales caractéristiques (C)**

Les deux approches ont permis d'améliorer l'efficacité de capture, comme démontré dans cette thèse sur un modèle de capture streptavidin-biotine et sur un modèle d'hybridation d'ADN pour la détection d'ADN tumoral circulant dans le cas de biopsie liquide. Le système de vibration automatisé a présenté de meilleurs résultats pour une fréquence de travail contrôlée. En effet, travailler avec un système de vibrations entièrement contrôlé permet de générer des fluctuations périodiques sur le débit autour d'une valeur moyenne. Cette solution nous a permis d'augmenter l'efficacité de capture d'ADN tumoral de 10% à 80% en travaillant à 5 ou 15  $\mu\text{L}/\text{min}$ .

Afin d'avoir une meilleure compréhension du système, des développements futurs du système sont envisagés. En particulier, nous aimerions travailler avec un meilleur contrôle de la fréquence et de l'amplitude des fluctuations. Pour cela, nous voudrions créer des vibrations grâce à une membrane de haut-parleur.

Une autre proposition se base sur l'utilisation d'ultrasons pour créer du mouvement à l'intérieur de la matrice de billes. Des premiers travaux ont été réalisés avec l'équipe de Thomas Laurel, comme montré sur l'image 113



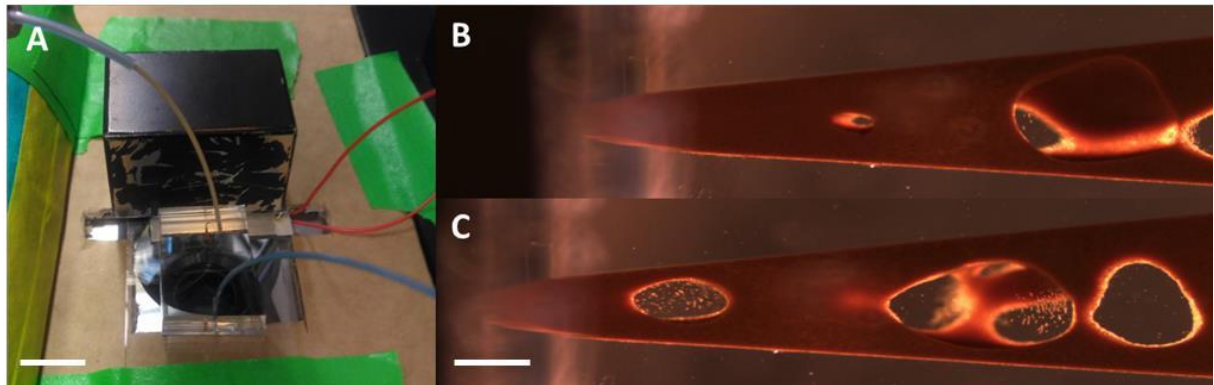


Figure 113 Photographie de la puce en PDMS de lit fluidisé avec ajout de transducteurs (A) Photographies des billes magnétiques sous effet des ultrasons (B) et (C)

### 3. Travail avec un support magnétique bimodal

Dans les lits fluidisés macroscopiques, le mélange de particules de différentes tailles peut mener à créer soit une ségrégation, soit une amplification du mélange. Cette idée a été transposée au lit fluidisé microfluidique magnétique en jouant avec des billes au diamètre compris entre 1 et  $4.5\mu\text{m}$ .

Ce nouveau concept, nommé support magnétique bimodal, a été adapté pour augmenter l'efficacité de capture de la nouvelle génération de lit fluidisé. La composition optimale des billes de la matrice est le mélange en proportion égale de deux tailles de billes : des billes de 1 et de  $2.8\mu\text{m}$  de diamètre.

L'utilisation d'un support bimodal semble modifier significativement la morphologie du lit fluidisé : on observe une augmentation du volume du lit fluidisé, ainsi qu'une meilleure uniformité, à la fois dans la distribution des particules mais aussi dans celle de l'écoulement (Figure 114). Notre hypothèse est que la présence de deux populations de billes modifie la façon dont les billes interagissent à l'intérieur du lit, favorise la mobilité des particules en diminuant la stabilité des colonnes et en remplissant l'espace vide induit par la formation de ces colonnes.



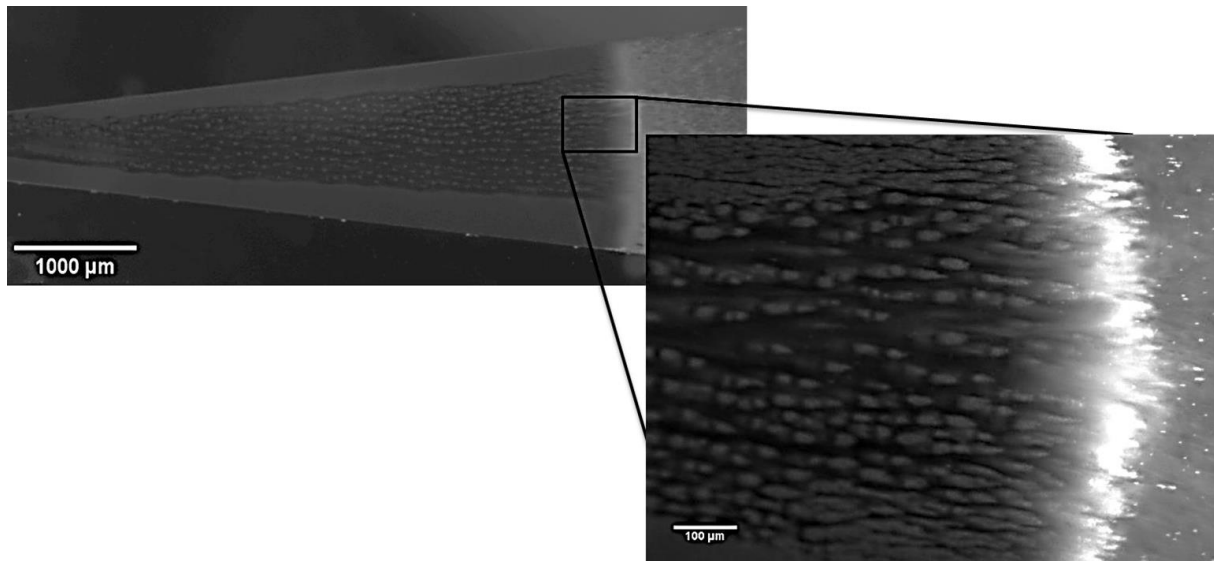


**Figure 114 Photographies du lit fluidisé avec support bimodal**

Pour mieux comprendre comment les améliorations physiques peuvent affecter les performances de l'extraction sur phase solide, une première évaluation de l'efficacité de capture a été réalisée sur un modèle streptavidin-biotine. Nous avons démontré que l'utilisation d'une matrice bimodale couplée avec l'ajout d'un système de vibration à l'entrée de la puce permet d'augmenter significativement la capture. Ainsi, une efficacité de 65% de capture à 15  $\mu\text{L}/\text{min}$  a été obtenue contre une capture à 46% dans un système standard. Un modèle plus réaliste a ensuite été proposé, avec pour cible de l'ADN tumoral circulant. La capture est réalisée par hybridation directement sur les billes magnétiques. : 80% de capture contre 10% en système standard ont été obtenus.

Nous souhaitons continuer ce travail avec une approche différente portant sur la forme des particules magnétiques. Des premiers travaux ont été réalisés avec les équipes de Gaëlle Charron et d'Olivia Du Roure.

La combinaison des deux dernières approches: vibrations et matrice bimodale, est la meilleure configuration pour réaliser une extraction et pré-concentration tout en travaillant à haut débit, et en maintenant une haute efficacité de capture.

#### **4. Applications biologiques du système de lits fluidisés microfluidiques magnétiques**

Les différents avantages du lit fluidisé peuvent être utilisés pour plusieurs applications dans le domaine bio-médical.

#### a. Capture et culture de bactéries in situ

Le lit fluidisé magnétique microfluidique peut être utilisé pour extraire, pré-concentrer et détecter des bactéries dans un milieu complexe tel que le lait. Il permet de détecter jusqu'à 10 bactéries dans un millilitre d'échantillon, en moins de 8 heures. Cette performance est comparable aux nouvelles stratégies développées pour améliorer la méthode de référence qui reste l'ensemencement sur milieu nutritif en boîte de Pétri. De plus, cette technique permet l'accès à de nouvelles informations sur les effets des antibiotiques, telles que le développement de résistance ou le changement de temps de division des bactéries.

L'étude présentée dans cette thèse se base sur des billes de 2.8  $\mu\text{m}$  de diamètre fonctionnalisées avec des anticorps spécifiques à la Salmonelle Typhonium. Celles-ci ont été utilisées pour démontrer la capture en lit fluidisé. La détection de la présence de bactéries a été réalisée directement à l'intérieur de la puce en PDMS, en réalisant une culture en puce. Une quantification peut être atteinte en liant le temps pour une expansion du lit de 200  $\mu\text{m}$  avec la concentration initiale en bactéries, comme montré sur l'image ci-dessous.

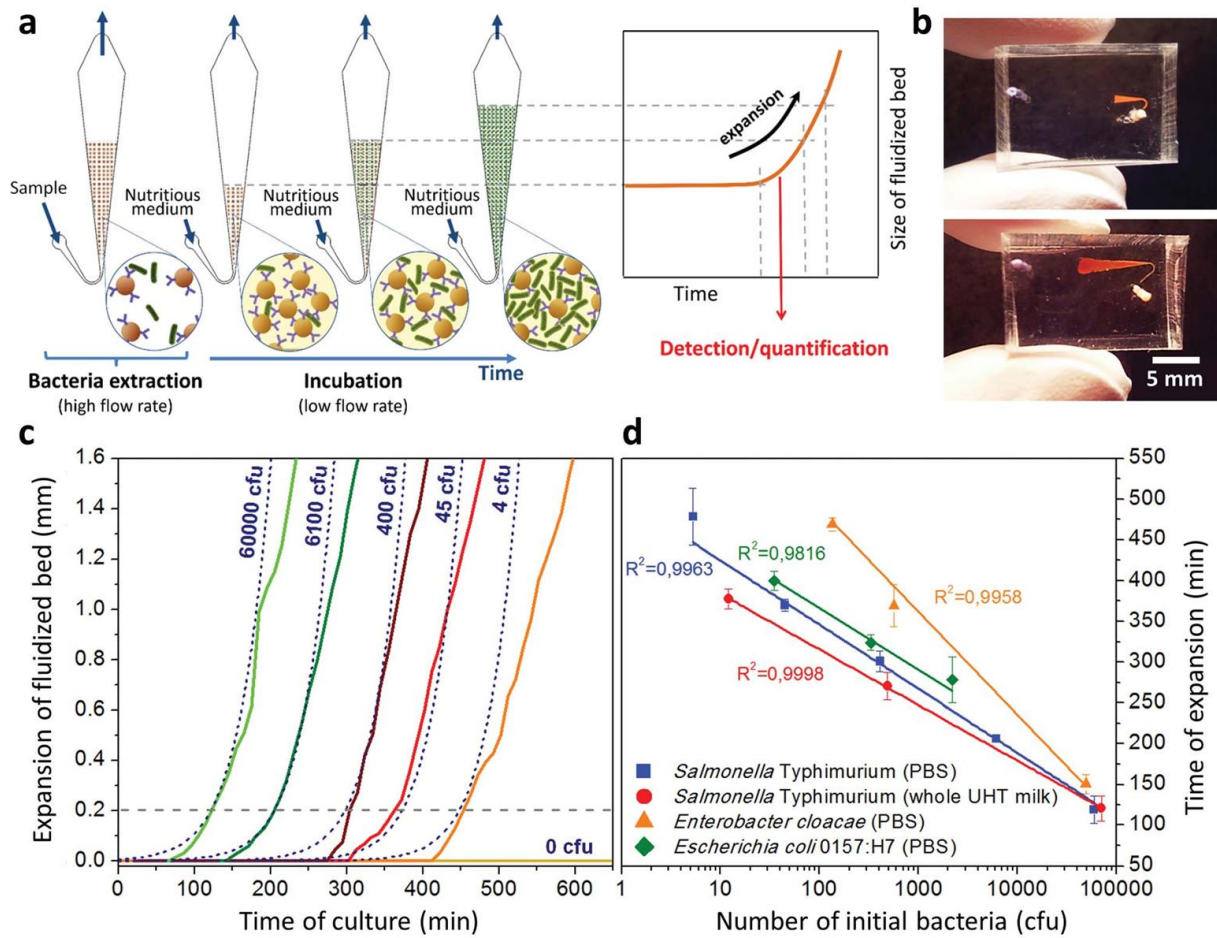


Figure 115 Protocole et résultats de la capture, culture et détection en lit fluidisé de *Salmonella Typhimurium*

Une version automatisée du système de lit fluidisé a mené à la création d'une plateforme transportable permettant la détection et la quantification de bactéries en milieu complexe, comme présenté sur la figure 116. Dans ce système, l'appareil dont seules les puces en PDMS doivent être changées pour toute nouvelle expérience permet de travailler à bas coût, sans nécessité d'un personnel formé, et surtout à grande vitesse, sans besoin de temps longs d'incubation. De plus, cette plateforme peut s'adapter à différentes souches de bactéries. La première plateforme mobile a été réalisée en coopération avec la société Fluigent.

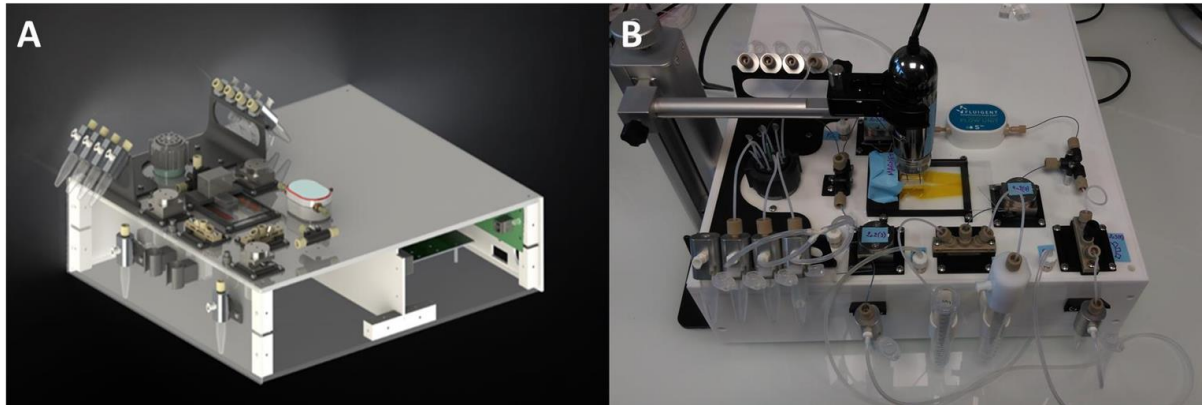


Figure 116 Plateforme mobile et transportable de lit fluidisé

### b. Traitement par aphérèse de la pré-éclampsie

La pré-éclampsie est une pathologie associée à une hypertension artérielle qui survient au cours de la grossesse et qui résulte d'un dysfonctionnement du placenta. Ce syndrome touche entre 5 et 10 pour cent des maternités dans le monde. La pré-éclampsie, si elle n'est pas traitée, entraîne de nombreuses complications et peut même entraîner la mort de la mère ainsi que celle de l'enfant. Cette maladie est liée à environ 18% des décès survenant lors de la naissance.

Pour le moment, les causes n'ont pas été identifiées, ce qui rend le traitement difficile. L'étendue et la diversité des symptômes en fait une maladie difficilement détectable. Le développement de médicaments est limité par un besoin de protéger l'enfant dans le ventre de la mère. La solution qui est aujourd'hui la plus prometteuse est la mise en place d'un filtre sanguin permettant d'enlever du sang de la mère les éléments reconnus comme dangereux pour elle.

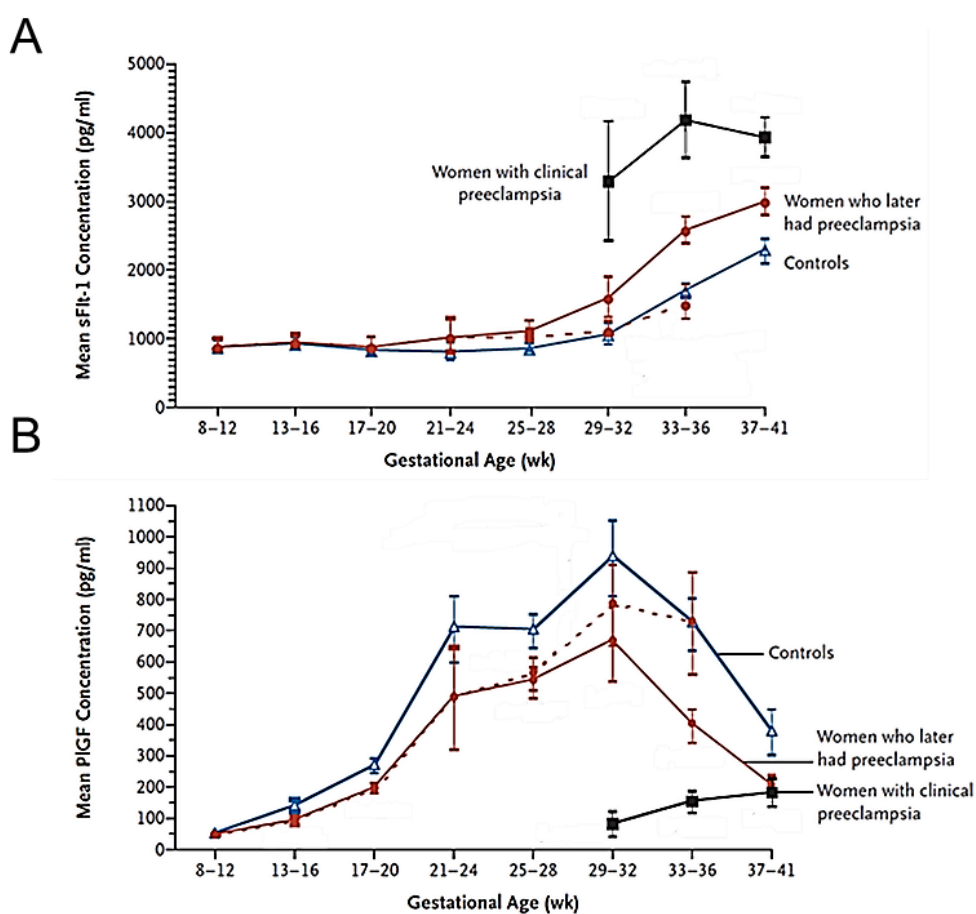


Figure 117 Evolution de la sFlt-1 et du PlGF au cours de la grossesse (Levine and Karumanchi, 2005)

Un élément en particulier, la protéine sFlt-1 (Soluble fms-like tyrosine kinase-1) est impliquée dans la maladie. Des études cliniques ont révélé son importance dans le développement de la pré-éclampsie (Figure 117). Les premières études cliniques ont été lancées sur des prototypes de colonnes d'aphérèse permettant la capture par interactions électrostatiques des composants chargés positivement du sang. Ces systèmes permettent de réduire de 14 à 28% la concentration en sFlt-1 dans le sang de la mère. Pour améliorer la spécificité des systèmes, la capture par anticorps a permis de réduire la concentration en sFlt-1 uniquement dans le sang des patientes. Cependant, les résultats montrent que cette capture entraîne une réduction de la concentration en PlGF (le facteur de croissance placentaire). Cette diminution est défavorable pour la patiente. Des études cliniques ont mis en avant la corrélation entre le ratio sFlt-1/PlGF et l'avancée de la pré-éclampsie chez la femme enceinte.

Pour faire face à ce problème, nous proposons une approche innovante basée sur un immuno-dosage compétitif. Le lit fluidisé est alors utilisé comme plateforme extra-corporelle mimant la percolation du sang dans un filtre dynamique composé de billes

magnétiques. Le système microfluidique permet de tester à petite échelle, sur des volumes d'échantillons réduits, les différentes approches. L'aspect percolation dynamique du lit fluidisé a été utilisé pour mimer un système de filtrage sanguin dans des cas de pré-éclampsie pendant la grossesse. Cette approche est particulièrement intéressante pour travailler directement avec des femmes enceintes et malades.

La stratégie développée est la capture du sFlt-1 en utilisant un ligand spécifique : le VEGF (le facteur de croissance endothélial vasculaire). L'interaction VEGF/sFlt-1 se trouve au même endroit géographique que l'interaction PlGF/sFlt-1, mais avec une affinité bien supérieure. Ainsi la capture du sFlt-1 par le VEGF permet de relâcher du PlGF et diminue drastiquement le ratio sFlt-1/PlGF. Le greffage de VEGF à la surface des billes utilisées dans le lit fluidisé permet alors de réajuster la balance angiogénique.

Une première preuve de concept a été tout d'abord testée en tube, puis réalisée en lit fluidisé. La détection a été réalisée grâce à l'implémentation d'une détection par anticorps secondaire fluorescent, comme présenté sur la figure 118. Ces premiers résultats ont permis de montrer que la capture de sFlt-1 était possible en lit fluidisé.

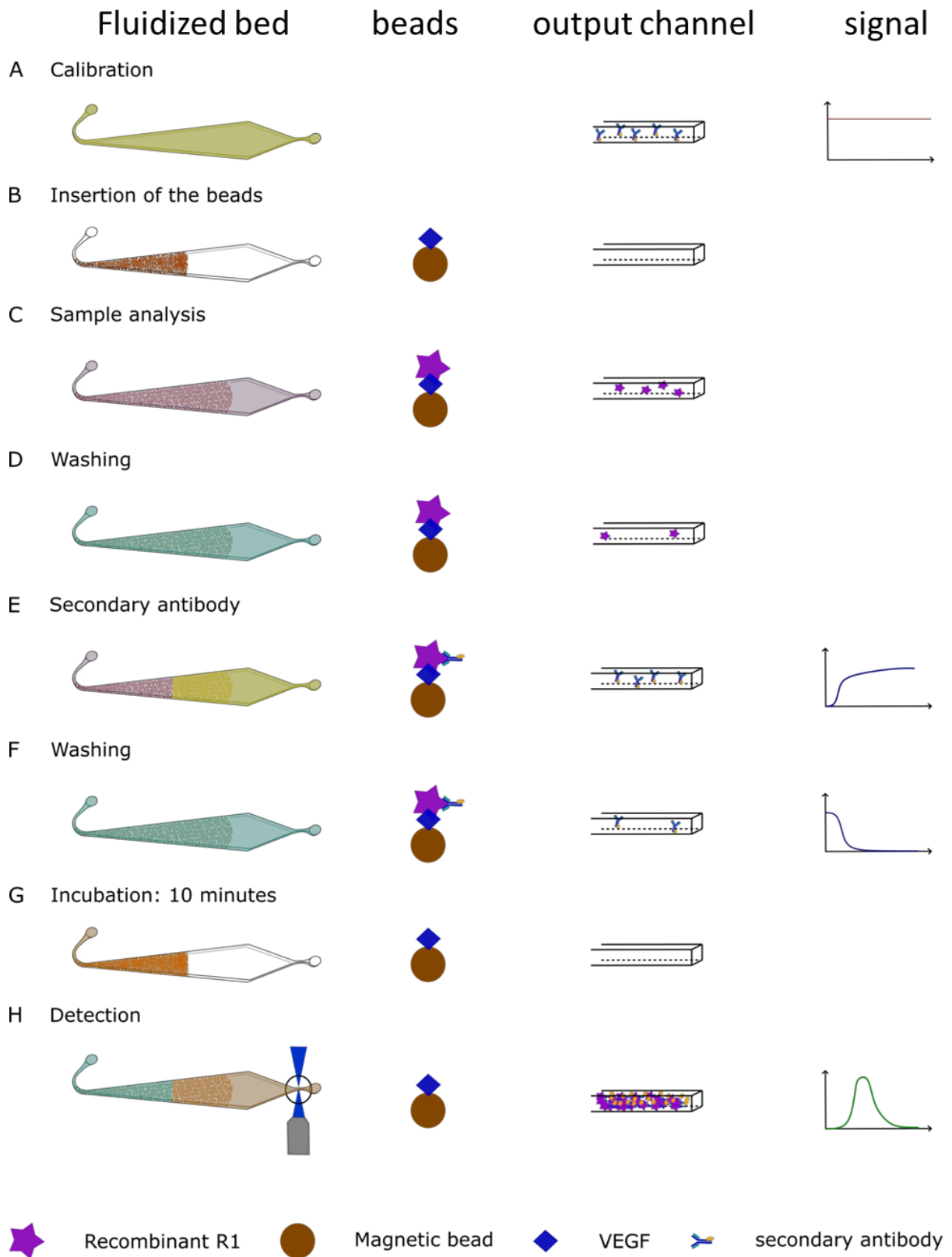


Figure 118 Protocole de capture et détection en lit fluidisé

Les résultats de cette étude ont ensuite été rassemblés sous forme d'un article. Nous avons validé l'approche par dosage compétitif adapté au système dynamique de lit fluidisé. Cette technologie permet de mimer à petite échelle un système d'aphérèse, avec possibilité de s'adapter aux matrices complexes telles que le plasma de femme enceinte. Cela permet de tester à bas coût, sur des petits volumes d'échantillons et avec une consommation faible de réactifs, de nouvelles stratégies. Cette technologie est parfaitement adaptée au travail avec des échantillons précieux tels que le plasma de femme enceinte.

### c. Intégration d'un test ELISA en puce

Le système de lit fluidisé a été utilisé pour réaliser un test de détection de la molécule IL-6 par dosage immuno-assay, nommé ELISA (enzyme-linked immunosorbent assay).

L'exemple choisi pour ce travail est celui d'une cytosine spécifique, l'IL-6. Il a été montré par des études cliniques que même un changement très faible de concentration en IL-6 peut être corrélé avec le développement de pathologies, telles que l'infarctus du myocarde. Cela dénote toute l'importance pour le milieu médical du développement d'un système capable de mesurer de très faibles concentrations d'IL-6, avec une haute précision. Chaque étape du protocole d'ELISA doit être entièrement contrôlée, en particulier l'extraction, car la matrice, l'échantillon et le pH peuvent affecter la mesure.

Nous avons évoqué dans cette thèse une nouvelle approche permettant de réaliser un protocole ELISA sur billes magnétiques. Cette configuration permet un contrôle total de chaque étape du protocole, comme décrit sur la Figure 104.



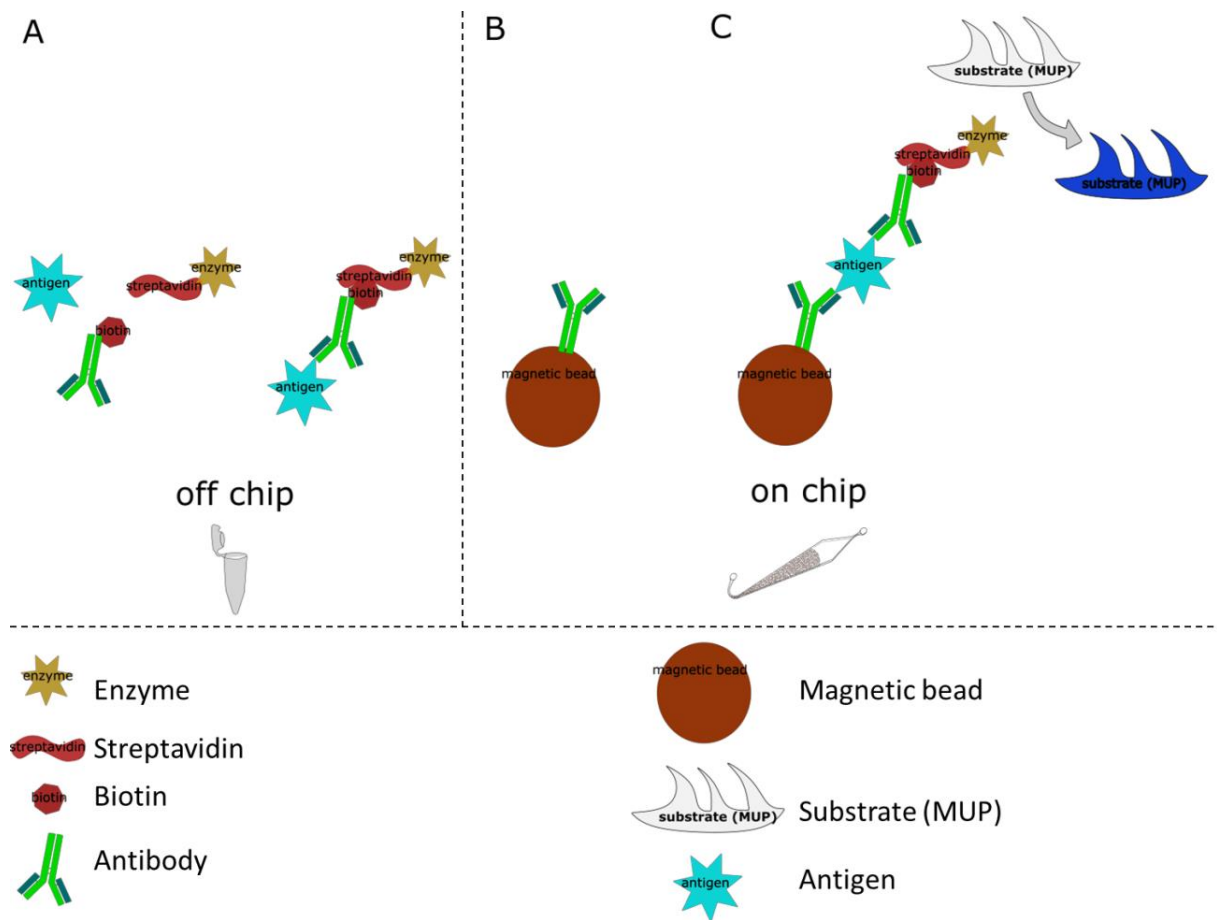


Figure 204 Protocol d'extraction par ELISA sur billes magnétiques en lit fluidisé

Les limites de détection et de quantification du système sont comparables aux systèmes existants, et la gamme de travail de ce dosage va de 5 à 10 000 pg/mL. Comparé aux systèmes SiMoA et DLISA de la littérature, le lit fluidisé offre l'opportunité de travailler à bas coût, de réaliser des analyses courtes, sur une gamme de travail large et avec une haute spécificité.

Notre système permet la détection en dynamique de biomarqueurs, et cette méthode peut être adaptée à des matrices complexes. Cependant, notre approche risque d'être limitée par les possibilités de fonctionnalisation des billes magnétiques et leur efficacité de capture. La preuve de concept en sérum ou dans une matrice plus complexe doit être réalisée pour compléter cette étude.

## 5. Conclusion

Ce travail de thèse a eu pour but de présenter l'élaboration et la réalisation d'une nouvelle génération de lits fluidisés permettant de travailler à haut débit grâce à l'ajout d'un système de vibrations et l'utilisation d'un support magnétique bimodal. D'autre part, cette thèse a révélé l'efficacité de ce système de fluidisation dans différentes applications biologiques, telles que l'extraction et la détection de bactéries, la capture de molécules biologiques d'intérêt dans le cas de la pré-éclampsie, et l'implémentation d'un dosage de type ELISA sur billes magnétiques.



## Résumé

Un système de lit fluidisé magnétique microfluidique a été développé pour répondre aux besoins d'extraction et de pré-concentration nécessaire comme première étape de bio-analyse. Ce système se base sur le même concept que les lits fluidisés macroscopiques en remplaçant la gravité par une force magnétique. Un nouveau module a été développé au court de ma thèse afin d'aborder de nouveaux défis en terme de détection à très basse concentration. Une augmentation de la hauteur de la puce nous a permis de travailler à hauts débits (15 $\mu$ L/min). Un premier travail sur l'homogénéisation de la répartition des billes à l'intérieur de la puce microfluidique a été effectué grâce à l'implémentation d'un système de vibration et d'une matrice bimodale. Cette approche a prouvé son efficacité sur des modèles de capture de protéines et d'ADN.

En parallèle, une seconde partie de mon travail a porté sur l'application du système de lit fluidisé à différents défis analytiques. Dans un premier temps, nous avons montré son potentiel pour l'analyse bactérienne. Le lit fluidisé peut aussi être utilisé comme plateforme de tests pour ligands pour la prise en charge de patientes souffrant de pré-éclampsie au cours de leur grossesse. Enfin un immuno-dosage de type ELISA a été réalisé entièrement dans ce système de lit fluidisé.

Ces résultats montrent l'adaptabilité de ce système au-delà de ses capacités à travailler à haut débit, bas coût, en consommant peu d'échantillon, et avec une grande sensibilité.

## Abstract

To tackle new challenges in trace analysis, a new generation of microfluidic magnetic fluidized has been developed. This system is based on a suspension of magnetic beads inside a microfluidic channel. Particles are in suspension between two forces: the drag force created by the flow of liquid and the magnetic force due to addition of a permanent magnet to the system. In order to increase the flow rate of work, the height of the chip has been increased five times. We were able to work at 15 $\mu$ L/min and the efficiency of the new system was improved by addition of a vibrator motor and a bimodal support. A proof of concept was performed on capture of biotin and DNA.

A second part of my PhD work was dedicated to the application of the fluidized bed module for bioanalysis. First, extraction, pre-concentration and detection of bacteria on chip have been performed with a significant decrease of the limit of detection and of the time scale compared to usual methods. Then the system of fluidized bed was used as a platform to tests new ligands in order to perform a competitive bioassay in the context of preeclampsia. Finally, an ELISA was integrated on the fluidized bed with promising results.

Those results proved the efficiency of the microfluidic magnetic fluidized bed to work as a module for extraction, pre-concentration and detection of target of low concentration.

## Mots Clés

Microfluidique  
lits fluidisés magnétiques  
bioanalyse  
pre-éclampsie

## Keywords

Microfluidics  
magnetic fluidized beds  
bioanalysis  
pre-eclampsia